CYTOCHROME P450 2J2 MEDIATED METABOLISM OF OMEGA-6 AND OMEGA-3 ENDOCANNABINOIDS

BY

DANIEL R. MCDOUGLE

DISSERTATION

Submitted in partial fulfillment of the requirements
for the degree of Doctor of Philosophy in VMS - Comparative Biosciences
in the Graduate College of the
University of Illinois at Urbana-Champaign, 2016

Urbana, Illinois

Doctoral Committee:

Assistant Professor Aditi Das, Chair and Research Director
Professor Indrani Bagchi
Associate Professor Jing Yang
Professor Claudio Grosman

ABSTRACT

Cytochrome P450 2J2 (CYP2J2) is membrane bound enzyme that is highly expressed in the cardiovascular system and brain where it mediates the metabolism of polyunsaturated fatty acids into oxygenated bioactive metabolites. This enzyme is most well-known for the conversion of arachidonic acid into epoxyeicosatrienoic acids (EETs) regioisomers, 14,15-, 11,12-, 8,9-, and 5,6-EET that mediate vasodilatory, pro-angiogenic and anti-inflammatory effects. More recently, CYP2J2 has been identified as a key enzyme for the metabolism of omega-3 fatty acids, such as eicosapentanoic acid (EPA) and docosahexaenoic acid (DHA), producing epoxygenated metabolites that provide cardioprotective benefits.

The biochemical study of the CYP2J2 mediated metabolism of xenobiotics and endogenous fatty acids have been difficult due to challenges with protein expression and solubilization. To circumvent these issues, a series of N-terminal modifications were introduced in the CYP2J2 N-terminus that enabled heterologous expression in *E. coli*. Importantly, to address the propensity of CYP2J2 to aggregate in solution, each construct was incorporated into the native membrane bilayers of nanodiscs for rigorous spectroscopic and functional studies. Notably, all N-terminal constructs were stably bound within the nanodisc bilayers, which prompted efforts to elucidate additional motifs that impart membrane binding. These observations were further explored in a study using molecular dynamics simulations which revealed CYP2J2 membrane insertion at the F-G loop, through hydrophobic residues Trp-235, Ille-236, and Phe-239. To explore the role of these residues, three F-G loop mutants were prepared from the truncated CYP2J2 construct (Δ34), which included Δ34-I236D, Δ34-F239H and Δ34-I236D/F239H. Interestingly, the expression of the CYP2J2 F-G loop mutants in *E. coli* were shown to be localized to the cytosolic fraction at a greater percentage relative to construct Δ34 while functional characterization revealed that the double mutant, Δ34-I236D/F239H, exhibited the greatest solubility while maintaining native-like enzymatic activity. Further, the membrane insertion characteristics were examined by monitoring CYP2J2 Trp-quenching fluorescence spectroscopy upon binding nanodiscs containing pyrene phospholipids. Relative to the Δ34 construct, all three F-G loop mutants exhibited lower Trp quenching indicating reduced membrane insertion.

The original CYP2J2 expression and characterization studies enabled metabolic screening of endogenous polyunsaturated fatty acid (PUFA) derived substrates that included derivatives of AA,

EPA and DHA. Notably, these efforts resulted in the discovery of the CYP2J2-nanodisc mediated oxygenation of omega-6 derived endocannabinoids, thereby revealing a previously unknown metabolic pathway. The endocannabinoids, anandamide (AEA) and 2-arachidonylglycerol (2-AG), are endogenous lipid mediators that are agonists of cannabinoid receptor-1 (CB1) and cannabinoid receptor-2 (CB2) with effects similar to the active ingredient of marijuana. Reactions of CYP2J2 with AEA formed four AEA-epoxyeicosatrienoic acids, whereas incubations with 2-AG yielded detectable levels of only two 2-AG epoxides. Additionally, 2-AG was shown to undergo enzymatic oxidative cleavage to form AA through a NADPH-dependent reaction with CYP2J2 and cytochrome P450 reductase.

The demonstrated ability of CYP2J2 to oxygenate AEA and 2-AG raised questions whether CYP2J2 could also accommodate the omega-3 derived endocannabinoids, eicosapentaenoic ethanolamide (EPEA) and docosahexaenoic ethanolamide (DHEA), as substrates. Indeed, subsequent metabolism studies of CYP2J2 with EPEA/DHEA revealed the production of a new class of ω-3 derived metabolites that we termed the omega-3 endocannabinoid epoxides – epoxyeicosatetraenoic-ethanolamide (EEQ-EA) and epoxydocosapentaenoic-ethanolamide (EDP-EA). These newly discovered endogenous metabolites share structural similarity to both their endocannabinoid and epoxide parent compounds, with potential to exert physiological effects mediated through both signaling pathways. Both EEQ-EAs and EDP-EAs were endogenously present in rat brain and peripheral organs as determined via LC-MS/MS with 19,20-EDP-EA also detectable in pooled human plasma. Using LC-MS/MS we demonstrated the direct production of these lipids by recombinant human CYP2J2 epoxygenase, rat brain microsomes and activated BV-2 microglia cells when supplemented with the parent EPEA or DHEA lipids. The discovery of these metabolites prompted a panel of *in vitro* assays to provide a first ever examination of their biological effects. Most notably, upon LPS stimulation of BV-2 microglia cells, both 17,18-EEQ-EA and 19,20-EDP-EA decreased pro-inflammatory IL-6 and nitric oxide whilst increasing anti-inflammatory IL-10. Additional studies revealed that these metabolites exerted anti-angiogenic effects in HMVEC cells, vasodilatory properties in bovine coronary arteries and reciprocally regulated platelet aggregation in washed human platelets. Taken together, the following thesis details new methods for the study of CYP2J2 within the membrane bilayers of nanodiscs. These techniques were used to reveal a new role for CYP2J2 in the metabolism of endocannabinoids into novel endocannabinoid metabolites with important physiological functions in the heart and brain.

To my Grandparents, Mother, Father, Siblings, and Katie

ACKNOWLEDGEMENTS

A great network of people have aided in the work that is presented in the following dissertation. I am deeply thankful for both the scientific assistance as well as a many number of lifelong friendships made at University of Illinois at Urbana-Champaign. Foremost, I would like to acknowledge my mentor, Prof. Das, for introducing me to the world of P450s and Nanodiscs and giving me the opportunity to conduct challenging and rewarding research within her lab. I sincerely appreciate the significant investment of time and effort on a multitude of projects over the past four years. I am also very fortunate for her help for searching and securing three very accomplished scientists to act as members on my doctoral committee. Specifically, Prof. Claudio Grosman, Prof. Jing Yang and Prof. Indrani Bagchi provided great support and guidance during the development of my PhD dissertation project. I offer my sincere thanks to these four individuals for helping to shape how I think and approach scientific problems and questions.

I am very thankful to have had a great number of lab mates and collaborators that helped throughout the past four years. First, although we have yet to meet, I would like to acknowledge Amrita Palaria for first cloning the CYP2J2 mutants which continue to be a staple for my research work and conceptualizing the CYP2J2 N-terminal construct project that we would act as co-authors on. Secondly, Dr. Daryl Meling aided in the construction of F-G loop mutants of CYP2J2 that was used in one of my publications. Additionally, I thank Snehita SriVarma for her kindness and teaching me how to use software such as Origin, VMD and Matlab. Importantly, I was very lucky to get to help train and work with an undergraduate student, Mr.Amogh Kambalyal, who aided in completing the endocannabinoid work and in the development of the membrane binding fluorescence assay. In a serendipitous twist of fate we are now in the same medical school cohort and will be in Urbana-Champaign School of Medicine the next 3 years. I am very grateful for the diversity of PhD students that have joined the lab with specialties and viewpoints different from my own. Particularly, Mr. William Arnold and Ms. Jahnabi Roy are current PhD students that are part of the Biochemistry and Chemistry Departments, respectively. Both individuals have keen insights due to their backgrounds that have aided in the lab work. I would like to acknowledge all other members of our lab including the undergraduate students such as Mr. Eric Magnetta and Mr. John Krapf that are co-authors in my paper and helped to drive research as well as the newest PhD students, Hannah Huff and Josephine Watson.

I would like to acknowledge all the immense support that I received from the Comparative Biosciences Department. Specifically, I am deeply indebted to the Bagchi, Yang, Bunick, Ferguson and Ko labs for their consultation and sharing of resources when developing new methods and experiments. More specifically, within Prof. Jay Ko's lab, Dr. Joe Cacioppo's training on the myograph instrument allowed me to pursue a very difficult experiment that otherwise would not have been possible. In addition to Dr. Cacioppo, I offer my sincerest thanks to Patrick Lin as well as Prof. Jay Ko for helping me to accomplish these experiments. I am also appreciative of the friendship and help provided by Dr. Patrick Hannon as well as Dr. Juan Davila over the years.

Importantly, I acknowledge the American Heart Association for awarding me a Predoctoral Fellowship [14PRE20130015] and AHA SDG [15SDG25760064] to Prof. Das that allowed me to finish my PhD and work on CYP2J2. I am also very grateful to my adviser and previous mentors that wrote recommendation letters to secure this funding. I also appreciate the support of Dr. Zhong Li at the UIUC Roy J. Carver Biotechnology Center. I thank Dr. Kevin Tucker of the UIUC School of Chemical Sciences. I extend my thanks to Dr. Javier Baylon and Dr. Emad Tajkhorshid for the MD simulation studies.

I would like to offer my sincere thanks to the administrators and faculty that are part of the Medical Scholars Program (MD/PhD). Specifically, Dr. Hall, Nora Few, Heather Wright and Prof. Slauch have provided essential oversight and sage advice in navigating a very rigorous dual degree

I would like to thank my previous mentors that also provided significant time in helping to learn how to think and providing challenging scientific problems. Firstly, I am deeply indebted to Prof. Gregory Bulaj for taking me on as a lab manager at the University of Utah and brining me in to work at NeuroAdjuvants with Dr. Erika Dr. Adkins Scholl, Dr. Cameron Metcalf, Dr. Misty Smith, Dr. Brian Klein and Prof. Steve White. Being the only employee without a doctorate and working on such advanced science was an exhilarating and rewarding endeavor.

Lastly, I would like to thanks my parents, siblings, cousins, grandparents, close friends and Dr. Katie Magerko for providing unwavering support and love.

"*If I have seen further than others, it is by standing upon the shoulders of giants.*"
-Sir Isaac Newton, 1676, Letter to Robert Hooke

TABLE OF CONTENTS

LIST OF ABBREVIATIONS

CYP	cytochrome P450
CYP2J2	cytochrome P450 2J2
COX	cyclooxygenase
LOX	lipoxygenase
CPR	cytochrome P450 reductase
ND	nanodisc
PUFA	polyunsaturated fatty acids
EDHFs	endothelium derived hyperpolarizing factors
AA	arachidonic acid
EPA	eicosapentaenoic acid
DHA	docosahexaenoic acid
EET	epoxyeicosatrienoic acid
EEQ	epoxyeicosatetraenoic acid
EDP	epoxydocosapentaenoic acid
HETE	hydroxyeicosatetrenoic acid
DHET	dihydroxyeicosatrienoic acid
DiHETE	dihydroxyeicosatetraenoic acid
DiHDPA	dihydroxydocasapentaenoic acid
AEA	anandamide
2-AG	2-arachidonoylglycerol
EPEA	eicosapentaenoyl ethanolamide
DHEA	docosahexaenoyl ethanolamide
EET-EA	epoxyeicosatrienoic ethanolamide
EEQ-EA	epoxyeicosatrienoic-ethanolamide
EDP-EA	epoxydocosapentaenoic-ethanolamide
EET-G	epoxyeicosatrienoic glycerol
PYR	pyrene
PYR-PC	pyrene phosphatidylcholine
PYR-ND	pyrene nanodiscs
MD	Molecular dynamics
HMMM	Highly mobile membrane mimetic
CB1	cannabinoid receptor 1
CB2	cannabinoid receptor 2
MS-PPOH	N-(methylsulfonyl)-2-(2-propynyloxy)-benzenehexanamide

POPC	1-palmitoyl-2-oleoyl-sn-glycero-3-phosphocholine
POPS	1-hexadecanoyl-2-(9Z-octadecenoyl)-sn-glycero-3-phospho-L serine
sEH	soluble epoxide hydrolase
FAAH	fatty acid amide hydrolase
ER	endoplasmic reticulum
cAMP	cyclic adenosine monophosphate
MOE	molecular Operating Environment
NADPH	nicotinamide adenine dinucleotide phosphate
PPARα	peroxisome proliferator-activated receptor alpha
PPARγ	peroxisome proliferator-activated receptor gamma

CHAPTER I: DISSERTATION OVERVIEW

In biology, membrane proteins are embedded within the cell membrane bilayer. These membrane bound proteins are broadly classified into signaling receptors, ion channels and metabolic enzymes that are utilized throughout all kingdoms of life. Traditionally, membrane proteins have constituted one of the most difficult classes of proteins to characterize due to issues with stability, extraction, expression, functionality and data reproducibility. Thus, continual and incremental improvements in the methodologies necessary to probe the characteristics of these membrane proteins are an active area of research. Additionally, the structural differences among the different types of membrane proteins (e.g. enzyme vs. receptor) require targeted efforts to elucidate the nuances of each particular class of membrane proteins.

The following dissertation explores the biochemical, biophysical and metabolic pathway of human cytochrome P450 2J2 (CYP2J2), a membrane bound enzyme. This heme containing enzyme is the most highly expressed cytochrome P450 in the cardiovascular system and provides essential homeostatic functions via the metabolism of polyunsaturated fatty acids (PUFAs) into bioactive metabolites. Due to the intransigent nature of this enzyme, considerable efforts were expended to develop the methods that would later enable screening for previously unknown endogenous substrates of CYP2J2, thus providing new insights into the mechanisms by which CYP2J2 maintains homeostatic balance.

The dissertation is divided into a total of seven chapters with the corresponding figures, tables and references located at the end of each chapter. In Chapter II, I briefly review the literature that is relevant to what is known about the biochemistry and physiological significance of CYP2J2. Chapter III is an original research article that probes how the hydrophobic N-terminal membrane anchoring domain affects CYP2J2 expression in *E. coli* and functional activity in the membrane bilayers of nanodiscs [PMID: 23661295]. Importantly, this chapter provided the method to express the proteins that facilitated the other studies in this thesis. Of particular note we find that the native membrane bilayer and not the enzyme N-terminus is important for native-like activity. In Chapter IV, we show that additional hydrophobic residues of the F-G loop also are important for membrane binding capabilities of CYP2J2 [PMID: 26232558]. Using pyrene-phospholipids incorporated into the membrane bilayers of nanodiscs, we were able to experimentally demonstrate that hydrophilic mutation of key residues in the F-G loop significantly decrease the depth of insertion of CYP2J2 and impart peripheral binding membrane protein characteristics.

In Chapters V and VI, we show that CYP2J2 rapidly oxygenates a particular class of lipids known as the endocannabinoids into bioactive metabolites. Endocannabinoids are PUFA derived signaling molecules 2that have similar effects as Δ9-tetrahydrocannabinol, the active ingredient of cannabis. Specifically, in Chapter V we demonstrate that the omega-6 endocannabinoids, anandamide and 2-arachidonoylglycerol, are substrates for CYP2J2 [PMID: 25277139]. In short, CYP2J2 produced 2-AG and AEA epoxides that were previously demonstrated have greater binding affinity to cannabinoid receptors, thus revealing an unknown metabolic pathway in the heart. In Chapter VI, we demonstrated that CYP2J2 also oxygenates the omega-3 endocannabinoids, EPEA and DHEA, to produce a newly discovered class of metabolites with unknown functions. In addition to the biosynthetic routes of formation of these metabolites, another major focus of this chapter was to determine the biological effects of the primary metabolites produced by CYP2J2.

Chapter VII includes methods employed in our lab in two successful collaborations with Prof. Andrew Smith and Prof. Michael Malkowski that utilized membrane scaffold protein and phospholipids to solubilize nanoplatelets and nanodiscs to solubilize and stabilize cyclooxygenase-2, respectively.

Taken together, the following dissertation reports on the expression and solubilization of recombinant human CYP2J2 and the capacity of this enzyme to metabolize endogenous substrates such as polyunsaturated fatty acids and endocannabinoids. All three published original research articles utilize innovative nanodisc technology that were used to incorporate CYP2J2 in discoidal (~10 nm diameter) membrane bilayers as well as be employed in fluorescence applications. The two original projects on endocannabinoid metabolism comprise efforts to map the CYP2J2 metabolic pathway using targeted lipidomics. While the physiological significance of these pathways have yet to be fully explored, these studies provide the critical basis for which additional animal studies are to be built upon as well as new targets for pharmacological intervention in disease pathologies.

CHAPTER II: INTRODUCTION TO CYP2J2 EPOXYGENASE

2.1 CYP2J2 overview. Cytochrome P450s (CYPs) are a superfamily of heme containing enzymes that are widespread throughout all kingdoms of life (*1*). In humans, these enzymes mediate oxidation of xenobiotics, hormones and fatty acids which provide essential detoxifying, reproductive and homeostatic functions, respectively (*2*). Historically, the mechanism and specificity of CYPs located in the liver (hepatic) were investigated due to their relevance in drug pharmacokinetics and pharmacodynamics. More recently, the role(s) of extrahepatic CYPs, especially those in the brain and heart, has become an active area of research as their physiological effects are critical in states of health and disease. One particular enzyme, human CYP2J2 epoxygenase, has emerged as an essential regulator of cardiovascular health, vascular tone and hemostasis (*3, 4*). Notably, the dysregulation of this enzyme is implicated in a wide-range of pathophysiological conditions such as cancer (*5*), obesity (*6*) and heart disease (*4*).

2.2 CYP2J2 endogenous expression. CYP2J2 was successfully cloned and expressed by Zeldin and co-workers in 1996 (*7*), and since has emerged as a critical extrahepatic CYP for general homeostasis in the human body. CYP2J2 is the only member of the CYP2J subfamily expressed in humans. Moreover, there are few existing CYP2J2 single nucleotide polymorphisms (SNPs), thus suggesting that alteration of the enzyme's typical functions significantly decreases overall fitness (*8*). This supposition is supported by studies that showed CYP2J2 overexpression promotes preeclampsia (*9*), and cancer (*5, 10*) whereas under expression is implicated in obesity (*6, 11, 12*). As mentioned above, CYP2J2 is the most highly expressed CYP in the cardiomyocytes that comprise the myocardium and is most well recognized for its role in controlling cardiovascular function (*7, 8, 13*). CYP2J2 is also highly expressed within the aortic arch and more generally within the epithelium that lines the vascular system with levels comparable to CYPC28 and CYP2C9 epoxygenase. Together these P450s comprise the CYP epoxygenase pathway in the cardiovascular system. In addition to the cardiovascular system, CYP2J2 was found within adipocytes (*6*), reproductive tissues (*9*), renal vasculature (*14*) and gastrointestinal tracts (*15*). Additionally, a recent report found that CYP2J2 is one of the primary CYPs in the brain with high expression in astrocytes as well as the hippocampus and total mRNA transcripts accounting for 20% of total brain CYP transcripts (*16*).

2.3 CYP2J2 biochemistry and metabolism of dietary fatty acids. The general biochemical mechanism of CYP2J2 is thought to follow that of the classical P450 catalytic cycle. In short,

substrate binds to a heme prosthetic group in the enzymatic active site, resulting in ferrous (Fe^{II}) conversion to a high spin state (Fe^{III}) and subsequent transfer of the first electron transfer via cytochrome P450 reductase (CPR) and NADPH. This step is followed by molecular oxygen (O_2) binding and a second reduction, mediated by CPR and NADPH, to form a ferric-peroxo species (Fe^{III}-O_2^{2-}) that undergoes two protonation steps to form an unstable Fe-OOH_2 reactive species that enables catalytic oxidation of carbon (*17*). Notably, the interactions of CYP2J2 and CPR are of interest as there are important protein-protein interactions that are thought to regulate enzyme activity and kinetics (*18*). During the P450 cycle there is potential for generation of reactive oxygen species (ROS) through catalytic shunts that can result in tissue damage and disease. Notably, CYP2J2 exhibits protection against ROS damage when compared to other cardiovascular P450s such as CYP2C8 and CYP2C9 (*19, 20*). Many questions persist concerning the biochemical mechanisms by which CYP2J2 mediates these protective properties through regulation of ROS. Particularly, whether CYP2J2 affords these benefits through differential CYP-CPR interactions, more efficient regulation of the P450 catalytic cycle or generation of anti-oxidant metabolites remain unknown.

CYP2J2 exerts its effects by converting dietary polyunsaturated fatty acids (PUFAs) into bioactive monooxygenated eicosanoids that, along with CYP2C8 and CYP2C9, comprise the third branch of the eicosanoid cascade (*21*). Eicosanoids are bioactive lipid signaling molecules generated by enzymes of the cyclooxygenase (COX), lipoxygenase (LOX) and CYP epoxygenase pathways (*21*). Collectively, the eicosanoids constitute one of the most complex pathways in the human body, with hundreds of known interrelated bioactive lipid species (*22*).

Recent attention has shifted towards elucidating the epoxide metabolites of CYP2J2 due to their potency, biological actions and physiological significance. Importantly, there is strong evidence that suggests this mechanism is mediated, in part, through an unknown GPCR receptor, thus the identification of the 'epoxyeicosanoid' receptor is an active area of research (*23*). The class of metabolites produced by CYP2J2 and their known pharmacology are discussed below.

2.4 CYP2J2 metabolism of dietary omega-6 arachidonic acid. Arachidonic acid (AA) is an omega-6 dietary PUFA that is found at high levels in meats, cheese, eggs and vegetable oil (*24*). Notably, the eicosanoid cascade is commonly referred to as the 'arachidonate cascade' due to the reflection that AA is the predominant substrate for enzymes of this metabolic pathway. Upon dietary consumption, AA is esterified in membrane phospholipids until cytosolic phospholipase

A_2 ($cPLA_2$) is activated to catalyze AA hydrolysis from the phospholipid bilayer (*23*). AA can be oxygenated into a diverse range of metabolites that are generally pro-inflammatory when metabolized by enzymes of the COX and LOX pathways and anti-inflammatory when utilized by enzymes of the CYP pathway (*4*). Of particular focus are the metabolites produced by CYP2J2 due their maintenance of homeostasis and potential for pharmacological interventions.

CYP2J2 utilizes molecular oxygen and two NADPH electrons to convert AA into 10 unique regio- and stereo-isomers that exhibit differing biological actions (Figure 2.1A-B). When considering regioselectivity, CYP2J2 exhibits catalytic preference for the terminal olefin of AA resulting in the predominant production of the (±) 14,15-EET regioisomer followed by the sequential production of (±) 11,12-EET, 8,9-EET and 5,6-EET (Figure 2.1A). Importantly, the EET regioisomers are comprised of R,S and S,R epoxide enantiomers that have different bioactivities and are also differentially produced by CYP epoxygenase enzymes (*25*). For instance, CYP2J2 was shown to produce the active R,S 14,15-EET stereoisomer at 72% whereas the remaining EETs were produced in a ~50:50 racemic mixture (R,S vs S,R) (*7*).

Upon production by CYP2J2, EETs are either re-incorporated in the plasma membrane or remain in solution to exert autocrine and paracrine biological actions until inactivation via hydrolysis (*26*). The re-incorporation of EETs into the plasma membrane is mediated by isozymes of the fatty acid binding protein (FABP) family, which esterify EETs within phospholipids for long-term storage and sequestration of their bioactivity (*27*). Importantly, it has been estimated that at rest, approximately 80-90% of total EETs are stored within the membrane until a signaling event triggers it release by PLA_2 (*28*). Upon EET enzymatic production or release from the membrane, EET inactivation is primarily mediated by soluble epoxide hydrolase (sEH), which acts to hydrolyze the epoxide bond producing vicinal diols. While the vicinal diols have been shown to retain some biological activity, their potency is greatly diminished as compared to the epoxides (*29*).

2.5 EETs pharmacology and biological effects. EETs are autocrine and paracrine lipid mediators that elicit vasodilatory, anti-inflammatory and pro-angiogenic effects that provide beneficial cardiovascular effects (*26, 29*). These actions are thought be facilitated through a number of extracellular and intracellular channels and receptors. One of the primary pathways involves an omega-6 epoxy eicosanoid g-coupled protein receptor (GPCR) that remains undetermined and controversial within the CYP epoxygenase field of research (*23*). Accumulating

evidence suggests that this putative EET receptor is a $G_{\alpha s}$-coupled GPCR that activates adenylyl cyclase resulting in cyclic adenosine monophosphate (cAMP) accumulation and secondary signaling events (*25, 30, 31*). Additional direct modes of action are mediated through nuclear receptors such as peroxisome proliferator-activated receptor gamma (PPARγ) (*32*) as well as transient vanilloid receptor 4 (TRPV4) (*33*). While the complex pleiotropic signaling pathways of EETs are far being elucidated, the ultimate biological effects have been the focus of rigorous physiological studies.

One common biological effect of all EET regioisomers is the ability to activate large-conductance Ca^{2+}-activated K^+ channels (BK_{Ca}), effectively hyperpolarizing the membrane and mediating vasodilation (*29*). Importantly, because the EETs are stored the plasma membrane and released as a result of phospholipase activation, they are classified as endothelium-derived hyperpolarizing factors (EDHFs) (*33*). Notably, there is mounting evidence to support the cross-talk of the EETs with other EDHFs (e.g. adenosine and nitric oxide), to act in concert to properly maintain vascular tone in response to changes in blood pressure, heart rate and sympathetic and parasympathetic regulation (*34, 35*). Additionally, vasodilatory mechanisms of EETs include direct activation of TRPV4 resulting in Ca^{2+} influx and complex formation with BK_{Ca} channels (*36, 37*). However, it should be noted that direct EET (14,15-, 11,12-, 8,9- and 5,6-) activation of BK_{Ca} channels have also been shown to potentiate the Ca^{2+} mediated activation of these channels. These physiological effects have been elicited with pharmaceutical agents to inhibit sEH to prolong EET *in vivo* half-life for the treatment of cardiovascular disease and other vascular disorders (*21*).

EETs exert potent anti-inflammatory effects in the endothelium, heart and brain via inhibition of nuclear factor kappa-light-chain-enhancer of activated B cells (NF-κB), and heme oxygenase-1 (HO-1) (*29, 38*). Importantly, it is likely that the anti-inflammatory effects are dependent on the tissue and expression of the diverse range of receptors thought to mediate EET activity (Figure 2.1B) (*39*). Thus, given the importance of the CYP epoxygenase pathway in the heart and vasculature, most studies have focused on EET anti-inflammatory effects in endothelial cells and myocytes. For example, in endothelial cells EETs were shown to inhibit leukocyte migration through potent inhibition of VCAM-1 and to a lesser extent inhibition of E-selectin and ICAM-1 expression after LPS stimulation (*38*). Interestingly, these effects are independent of the vasodilatory effects mediated by BK_{Ca} inhibition providing evidence of EET pleiotropic activity

(*38*). The anti-inflammatory effects have also been confirmed in neonatal cardiomyocytes after LPS stimulation, in part, through activation of the PPARγ nuclear receptor (*40*).

Angiogenesis is important for normal homeostatic functions as well as pathological tumor growth and cancer metastasis. The mechanisms by which the EETs promote angiogenesis are far from being fully understood. A previous study demonstrated that the pro-angiogenic effects are mediated, in part, through EET binding and cleavage of heparin-binding epidermal growth factor-like growth factor (HB-EGF) (*41*). More specifically, 14,15-EET activation of metalloproteinase cleavage resulted in epidermal growth factor (EGF) ligand release and EGFR mediated angiogenesis that was reversible with metalloproteinase inhibitors (*41*).

Not surprisingly, it is tempting to generally group the EETs as a single class of lipid mediators. However, this is an inaccurate assumption as the pharmacology between stereo- and regioisomers exhibits subtle differences in potency and effects depending on the target tissue/organ. For example, for activation of the putative EET receptor, the 14,15-EET R,S-stereoisomers are active whereas the S,R-stereoisomers are inactive (*25*). Moreover, differences between EET regioisomer anti-inflammatory activity have been demonstrated, with 11,12-EET showing the greatest inhibition of TNF-alpha induced vascular cell adhesion molecule (VCAM-1) in endothelial cells followed by 8,9-EET, 5,6-EET and 14,15-EET (*38*). It should also be considered that the EETs may demonstrate cross-talk with other eicosanoid pathways. Specifically, 5,6-EET is a substrate for enzymes of the COX pathway which produce thromboxane-like metabolites with vasoconstrictive properties (*42*).

2.6 CYP2J2 metabolism of dietary omega-3 fatty acids. The capacity of CYP2J2, and other CYP epoxygenases, to directly convert EPA and DHA into potent vasodilatory and anti-arrhythmic metabolites is thought to provide many of the beneficial cardiovascular effects associated with dietary omega-3 fatty acids (*43*). As shown in Figure 2.2B-C, CYP2J2 converts EPA and DHA into EEQ and EDP regio-and stereoisomers, respectively. Relative to AA the substrate preference for EPA and DHA were reported at 17-fold and 4-fold greater, respectively (*43*). The preferred site of oxygenation is the terminal PUFA olefin, predominantly producing, 17,18-EEQ from EPA and 19,20-EDP from DHA (Figure 2.2B-C). The physiological significance of this pathway was further highlighted in a study where EPA and DHA supplementation in humans resulted in significant increase of EEQ and EDP metabolites with no apparent increase in metabolites from the COX and LOX pathways (*44*). Taken together, there is significant biochemical and clinical

evidence to support that dietary supplementation with omega-3 fatty acids alters the eicosanoid profile in the body, in part, through interactions with CYP2J2. Many of these metabolites are yet to be identified and characterized. As discussed in Chapter VI, we characterized a new class of omega-3 derived bioactive metabolites produced by CYP2J2 thereby revealing a previously unknown metabolic pathway.

2.7 EEQ and EDP pharmacology and biological effects. The details concerning the pharmacology of the EEQ and EDP metabolites are poorly understood relative to the EETs. Initial assumptions that these epoxy-containing PUFAs would have similar actions as their EET counterparts have generally proved inaccurate. More specifically, the EEQ and EDP metabolites have vastly different potencies and sometimes even opposing biological effects when compared to the EETs. For example, while the EETs have been shown to produce pro-angiogenic effects, the EEQs and EDPs are anti-angiogenic and blocked cancer growth and metastasis (*45*). Even when considering instances where the general biological effects are the same, there are significant differences in the efficacy among PUFA epoxide classes. For instance, both 17,18-EEQ and 19,20-EDP are profoundly anti-arrhythmic whereas 14,15-EET exhibits much weaker activity (*43*). Given, the contrary effects of the EETs relative to EEQs/EDPs it is tempting to hypothesize that there is unidentified omega-3 epoxide receptor, yet studies attempting to elucidate this receptor are lacking. This notion is supported by evidence that the 14,15-EEZE inhibitor does not block the actions of the 17,18-EEQ and required EEQ specific antagonists (*46*). Moreover, the EDPs were shown to exhibit the most potent vasodilatory activities, with the 13,14-EDP metabolite activating BK_{Ca} channels with 1000-fold greater potency than 14,15-EET (*47*).

2.8 CYP2J2 roles in health and disease. The potential significance of CYP2J2 expression in the cardiovascular system and other tissues of the body can be reasonably deduced by understanding the general biological actions of the EET, EEQ and EDP metabolites. However, it is necessary to demonstrate the CYP2J2 physiological significance *in vivo* to fully understand the role of CYP2J2 in states of health and disease. When examining related isozymes across species there are 'CYP2J2-like' isozymes in larger animals such as porcine and bovine. Bovine and sheep CYP2J isoforms share 75% and 77% homology with human CYP2J2, respectively (*48*). Moreover, microsomes prepared from bovine and porcine myocardium as well as recombinant human CYP2J2 nanodiscs all were shown to epoxygenate AA as well as arachidonate containing endocannabinoids (*48*). Interestingly, sheep CYP2J preferentially hydroxylates AA into 20-, 19-

and 18-HETES (~86% of total product) followed by 14,15-, 11,12-, 8,9- and 5,6-EET (~14% of total product) (*49*). In contrast, rodent species such as rats and mice have 10 subfamily CYP2J isozymes (CYP2J-5,6,7,8,9,11,12,13,14,15) but lack a comparable CYP2J2 isozyme, making comparative species studies more difficult (*50*). This limitation has largely been overcome with the use of a transgenic mice with localized over-expression of CYP2J2 in the cardiomyocytes (α-MHC-CYP2J2) as well as within the cardiovascular endothelium (Tie-CYP2J2) for use in various models of disease (*13, 19*). Additional approaches include the use of primary human myocyte cultures as well as the use of CYP2J2 specific inducers and inhibitors as a model of CYP2J2 cardiotoxicity (*51*). Further approaches have included the transfection and subsequent expression of CYP2J2 into specific cellular systems (*52*).

The importance of CYP2J2 for the maintenance of cardiovascular homeostasis became apparent upon the FDA approval of a new non-brain penetrating H1 antagonist (Terfenadine) with off-target effects that included ventricular arrhythmias (*53*). One of these effects included potent inhibition of CYP2J2 which efficiently hydroxylates terfenadine to form hydroxyl-terfenadine (*54*). Terfenadine was ultimately pulled from the market due to cardiotoxicity related side effects which prompted many to hypothesize it was due in part to inhibition of CYP2J2 mediated metabolism of PUFAs. Notably, the CYP2J2 metabolite hydroxyl-terfenadine was later released and is devoid of the cardiotoxic effects of its predecessor. The cardioprotective benefits of CYP2J2 have been explored in several models of cardiotoxicity (*51*). For example, transgenic mice with the cardiac-specific overexpression of CYP2J2 ameliorated doxorubicin-induced cardiotoxicity (*55*). In a separate study these transgenic mice were shown to provide treatment of ischemia-reperfusion injury in the heart through increased expression of phosphor-p42/p44 mitogen-protein kinase (MAPK) pathway (*13*). In another cardioprotective pathway CYP2J2 overexpression counteracted electrical remodeling in mechanical and chemically induced cardiac hypertrophy (*56*). These effects are postulated to be due to EETs collective regulation of Ca^{2+}, K^{+} and Na^{+}-channels which provided electrical stability in part through maintaining gap junction integrity resulting in anti-arrhythmic effects (*56, 57*).

Not surprisingly, CYP2J2 expression provides anti-inflammatory effects, presumably through the production of EET, EEQ and EDP metabolites. This was demonstrated in mouse aortic endothelial cells transfected with the pcDNA3.1/CYP2J2 plasmid which inhibited homocysteine induced metalloproteinase-9 activation of NFκB (*52*). Subsequent studies showed that CYP2J2 expression

promotes activation of peroxisome proliferator activated receptor-alpha (PPARα) in monocyte derived macrophages (*58*). The profound influence of CYP2J2 on macrophages was recently confirmed in a study that utilized adenovirus to overexpress CYP2J2 in mice to ameliorate LPS-induced cardiac dysfunction (*59*). Mechanistic studies demonstrated that 11,12-EET promotes macrophage polarization from the pro-inflammatory M1 phenotype to the anti-inflammatory M2 phenotype (*59*). As previously mentioned, CYP2J2 produces significantly fewer pro-inflammatory reactive oxygen species (ROS) when compared with CYP2C8 and CYP2C9. This characteristic has pathophysiological implications as the CYP2C9 production of ROS caused inflammation and CYP2C8 production of ROS increased susceptibility to ischemia-reperfusion injury despite the CYP production of EETs that theoretically oppose these events (*19, 20*). Thus, the production of bioactive epoxide metabolites by CYP2J2 likely proceeds much more efficiently with fewer side products that may counteract the beneficial effects of EETs, EEQs and EDPs.

The recognition of CYP2J2 and its metabolites' anti-inflammatory effects have far reaching implications as nearly every disease pathology involves some component of inflammation. For instance, excess adipose tissue in obesity is associated with increased pro-inflammatory cytokines that have been shown to confer insulin resistance (*60*). Strikingly, CYP2J2 expression ameliorated inflammatory cytokines and insulin resistance associated with type II diabetes in mice (*11*). These reports were consistent with additional literature that revealed the expression of CYP2J2 in endothelial cells reversed vessel fat deposits and vascular disease in part by attenuation of heme oxygenase-1 (HO-1) (*61*). Interestingly, CYP2J2 is down-regulated in subcutaneous adipose tissue in obese people and may contribute to low levels of 25-hydroxy-vitamin D in these patients (*6*). Moreover, overexpression of CYP2J2 in mice fed a high fat diet resulted in significant decrease of hyperlipidemia in part through activation of AMPK and PPARα pathways (*12*).

Despite the apparent ameliorating benefits provided by CYP2J2 over-expression in pathologies that involve inflammatory and hypertensive characteristics, there are a number of diseases that are exacerbated by CYP2J2 overexpression. Most notably, CYP2J2 has been identified as an enzyme that drives tumor growth and metastasis. This was first reported in a study that found upregulation of CYP2J2 in 77% of human carcinoma tissues and shown to promote the neoplastic phenotype (*62*). The importance of CYP2J2 was further confirmed through synthesis of CYP2J2 specific terfenadone inhibitors that potently inhibited cancer growth using MDA-MB-435 cancer cells *in vitro* and in an *in vivo* murine tumor xenograft models of cancer (*63*). The CYP2J2 antagonist

mechanisms were found to be a result of caspase-3 activity and enhanced tumor cell apoptosis which inhibited growth and prevented metastasis (*63*). The effects are not surprisingly attributed to the mitogenic and pro-angiogenic effects of the EETs that are produced by a number of CYP epoxygenses. A separate disease in which CYP2J2 has been specifically implicated is in preeclampsia (*9*). As previously mentioned CYP2J2 is highly expressed in reproductive tissues such as the placenta, likely due to its production of pro-angiogenic and pro-growth metabolites. A recent report found that CYP2J2 overproduction of 5,6-EET and its subsequent conversion by COX-2 is largely responsible for the hypertensive and potentially life-threatening characteristics of preeclampsia (*9*).

2.9 CYP2J2 summary. Studies examining the physiological role(s) of CYP2J2 epoxygenase in health and disease have continually increased since the discovery of this extrahepatic CYP in 1996. Many characteristics set CYP2J2 apart from the traditional detoxifying hepatic CYPs, with the major being that CYP2J2 contains a significantly narrower hydrophobic active site that confers unique regioselectivity relative to the major liver CYPs (*64*). Additionally, liver CYPs generally exhibit much faster xenobiotic and endogenous substrate turnover with greater production of ROS than CYP2J2. However, despite the relatively slow turnover of the metabolism of endogenous fatty acids by CYP2J2, the scientific community has come to appreciate that this enzyme regulates complex homeostatic function through the generation of EETs that require enzymatic precision. Thus, the formation of these metabolites most likely represents a far more elegant mechanism for control of the many delicate homeostatic processes within organs, such as the heart, kidneys and brain. Therefore, similar to the steroid-synthesizing P450s, the enzymatic expression levels rather than the catalytic turnover are likely the prominent mechanism for metabolic control in each respective organ.

2.10 FIGURES

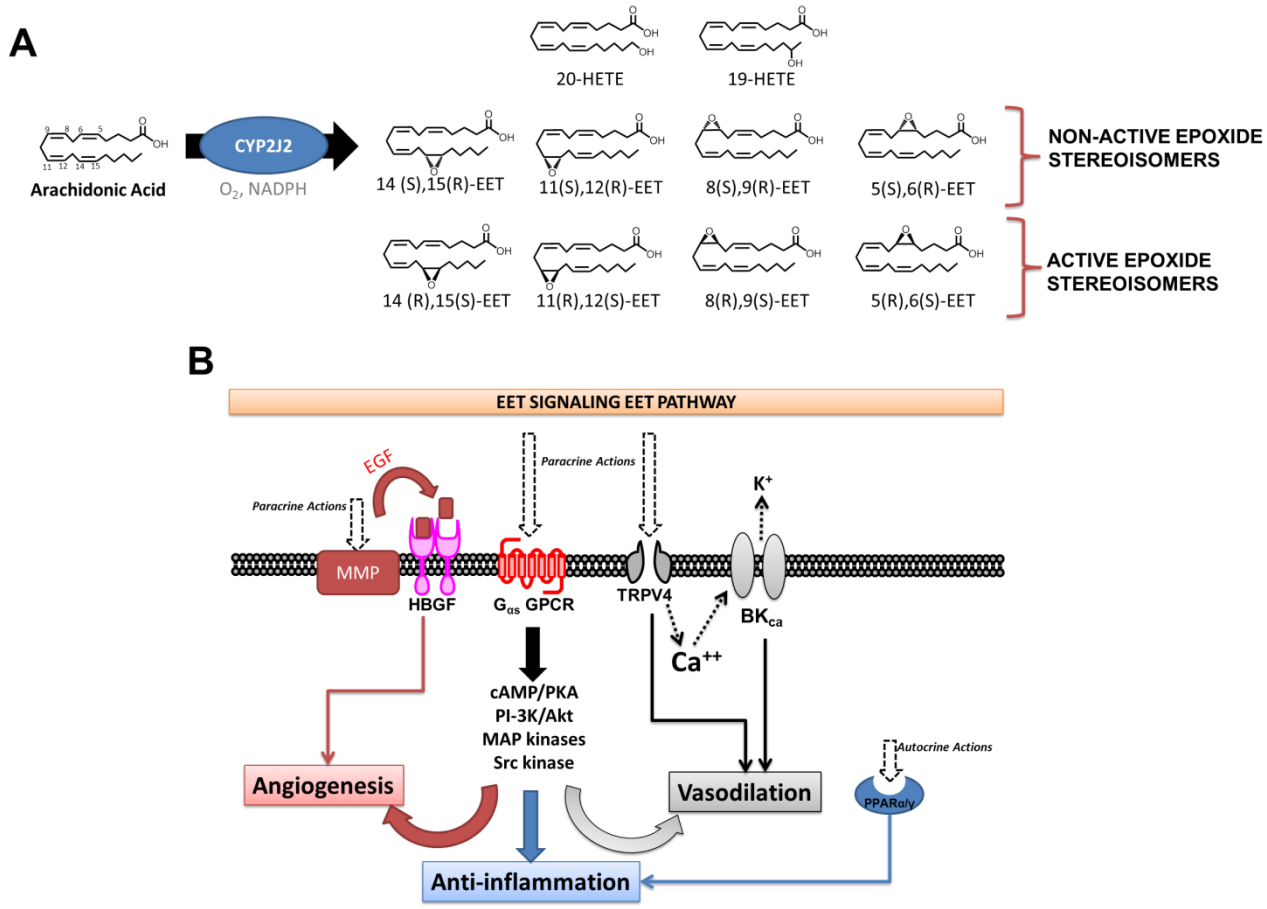

Figure 2.1. CYP2J2 mediated metabolism of arachidonic acid into bioactive EETs. **(A)** Using molecular oxygen and NADPH, CYP2J2 converts arachidonic acid (AA) as a substrate to form 10 different metabolites consisting of two hydroxylated regioisomers (20-, and 19-HETE) as well as 8 different epoxide stereo- and regioisomers (S,R and R,S) 14,15-, 11,12-, 8,9-, and 5,6-EET. **(B)** (R,S) EET regioisomers are autocrine and paracrine pleiotropic lipid mediators with biological effects that include angiogeneis (*red pathway*), anti-inflammation (*blue pathway*) and vasodilation (*grey pathway*). The mechanisms of angiogenesis (*red pathway*) are mediated through activation of metalloproteinases (MMPs) which produce EGFRs and activate heparin binding growth factor (HGFR) and/or via the putative EET receptor. The vasodilatory actions (*grey pathway*) are mediated by multiple mechanisms that include activation of transient receptor potential cation channel 4 (TRPV4) and calcium influx, direct or indirect activation of large conductance calcium gated potassium channels (BK_{ca}), and/or activation of the putative EET receptor. The anti-inflammatory effects (*blue pathway*) are mediated through activation of nuclear receptors such as the peroxisome-proliferator activated recetor gamma (PPARγ) and/or activation of the putative EET receptor).[29,30,31,32,33,41]

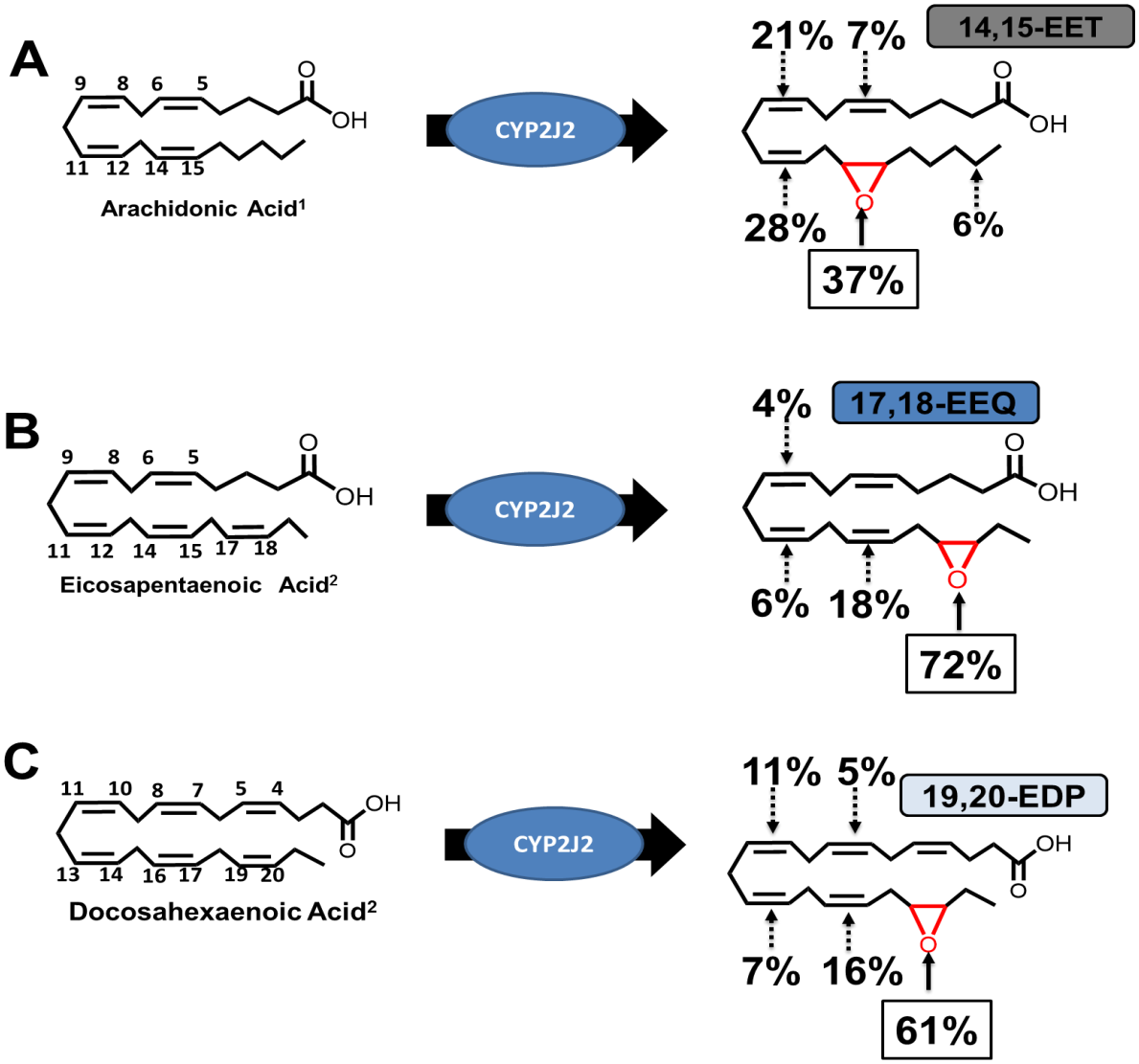

1. AA regioselectivity experimentally determined in-house via LC-MS/MS.
2. EPA and DHA regioselectivity as previously reported by Arnold et. al.[43]

Figure 2.2. CYP2J2 oxygenation regioselectivity of omega-6 and omega-3 fatty acids. (A) The omega-6 arachidonic acid is oxygenated by recombinant CYP2J2 with specific regioselectivity dependent on olefin position. The 14,15-EET metabolite is the predominant product and is formed through epoxygenation of the 14,15-olefin as shown in red. **(B)** The omega-3 eicosapentaenoic acid is oxygenated by recombinant CYP2J2 to form at least 4 different epoxide metabolites. The predominant metabolite, 17,18-EEQ is formed through epoxygenation of the 17,18-olefin as shown in red. (C) The omega-3 docosahexaenoic acid is a substrate for CYP2J2 and was reported to form at five regioisomers with the predominant isomer epoxygenated at the 19,20-olefin as shown in red.

2.11 REFERENCES

1. Nelson, D. R., Koymans, L., Kamataki, T., Stegeman, J. J., Feyereisen, R., Waxman, D. J., Waterman, M. R., Gotoh, O., Coon, M. J., Estabrook, R. W., Gunsalus, I. C., and Nebert, D. W. (1996) *Pharmacogenetics 6*, 1-42.
2. Niwa, T., Murayama, N., and Yamazaki, H. (2009) *Curr Drug Metab 10*, 700-12.
3. Zeldin, D. C. (2001) *J Biol Chem 276*, 36059-62.
4. Deng, Y. M., Theken, K. N., and Lee, C. R. (2010) *Journal of Molecular and Cellular Cardiology 48*, 331-341.
5. Jiang, J. G., Ning, Y. G., Chen, C., Ma, D., Liu, Z. J., Yang, S., Zhou, J., Xiao, X., Zhang, X. A., Edin, M. L., Card, J. W., Wang, J., Zeldin, D. C., and Wang, D. W. (2007) *Cancer Res 67*, 6665-74.
6. Wamberg, L., Christiansen, T., Paulsen, S. K., Fisker, S., Rask, P., Rejnmark, L., Richelsen, B., and Pedersen, S. B. (2013) *Int J Obes (Lond) 37*, 651-7.
7. Wu, S., Moomaw, C. R., Tomer, K. B., Falck, J. R., and Zeldin, D. C. (1996) *J Biol Chem 271*, 3460-8.
8. Zordoky, B. N. M., and El-Kadi, A. O. S. (2010) *Pharmacology & Therapeutics 125*, 446-463.
9. Herse, F., Hubel, C. A., Huppertz, B., Park, J. K., LaMarca, B., Sargent, I. L., Luft, F. C., Staff, A. C., Schunck, W. H., Muller, D. N., and Dechend, R. (2010) *Hypertension 56*, E91-E91.
10. Chen, C., Wei, X., Rao, X. Q., Wu, J., Yang, S. L., Chen, F. Q., Ma, D., Zhou, J. F., Dackor, R. T., Zeldin, D. C., and Wang, D. W. (2011) *Journal of Pharmacology and Experimental Therapeutics 336*, 344-355.
11. Li, R., Xu, X., Chen, C., Wang, Y., Gruzdev, A., Zeldin, D. C., and Wang, D. W. (2015) *Am J Physiol Endocrinol Metab 308*, E270-82.
12. Zhang, S., Chen, G., Li, N., Dai, M., Chen, C., Wang, P., Tang, H., Hoopes, S. L., Zeldin, D. C., Wang, D. W., and Xu, X. (2015) *Obesity (Silver Spring) 23*, 1401-13.
13. Seubert, J., Yang, B., Bradbury, J. A., Graves, J., Degraff, L. M., Gabel, S., Gooch, R., Foley, J., Newman, J., Mao, L., Rockman, H. A., Hammock, B. D., Murphy, E., and Zeldin, D. C. (2004) *Circulation Research 95*, 506-14.
14. Capdevila, J. H., Falck, J. R., and Imig, J. D. (2007) *Kidney Int 72*, 683-9.
15. Thelen, K., and Dressman, J. B. (2009) *Journal of Pharmacy and Pharmacology 61*, 541-558.
16. Dutheil, F., Dauchy, S., Diry, M., Sazdovitch, V., Cloarec, O., Mellottee, L., Bieche, I., Ingelman-Sundberg, M., Flinois, J. P., de Waziers, I., Beaune, P., Decleves, X., Duyckaerts, C., and Loriot, M. A. (2009) *Drug Metab Dispos 37*, 1528-38.
17. Denisov, I. G., Makris, T. M., Sligar, S. G., and Schlichting, I. (2005) *Chem Rev 105*, 2253-77.
18. Meling, D. D., McDougle, D. R., and Das, A. (2015) *J Inorg Biochem 142*, 47-53.
19. Edin, M. L., Wang, Z., Bradbury, J. A., Graves, J. P., Lih, F. B., DeGraff, L. M., Foley, J. F., Torphy, R., Ronnekleiv, O. K., Tomer, K. B., Lee, C. R., and Zeldin, D. C. (2011) *FASEB J 25*, 3436-47.
20. Fleming, I., Michaelis, U. R., Bredenkotter, D., Fisslthaler, B., Dehghani, F., Brandes, R. P., and Busse, R. (2001) *Circulation Research 88*, 44-51.
21. Imig, J. D., and Hammock, B. D. (2009) *Nature Reviews Drug Discovery 8*, 794-805.

22. Mietla, J. A., Wijesinghe, D. S., Hoeferlin, L. A., Shultz, M. D., Natarajan, R., Fowler, A. A., 3rd, and Chalfant, C. E. (2013) *J Lipid Res 54*, 1834-47.
23. Spector, A. A., and Kim, H. Y. (2015) *Biochim Biophys Acta 1851*, 356-65.
24. Taber, L., Chiu, C. H., and Whelan, J. (1998) *Lipids 33*, 1151-7.
25. Wong, P. Y., Lin, K. T., Yan, Y. T., Ahern, D., Iles, J., Shen, S. Y., Bhatt, R. K., and Falck, J. R. (1993) *J Lipid Mediat 6*, 199-208.
26. Spector, A. A. (2009) *J Lipid Res 50 Suppl*, S52-6.
27. Widstrom, R. L., Norris, A. W., Van Der Veer, J., and Spector, A. A. (2003) *Biochemistry 42*, 11762-7.
28. Karara, A., Dishman, E., Falck, J. R., and Capdevila, J. H. (1991) *J Biol Chem 266*, 7561-9.
29. Spector, A. A., Fang, X., Snyder, G. D., and Weintraub, N. L. (2004) *Prog Lipid Res 43*, 55-90.
30. Ding, Y., Fromel, T., Popp, R., Falck, J. R., Schunck, W. H., and Fleming, I. (2014) *Journal of Pharmacology and Experimental Therapeutics 350*, 14-21.
31. Nithipatikom, K., Brody, D. M., Tang, A. T., Manthati, V. L., Falck, J. R., Williams, C. L., and Campbell, W. B. (2010) *Cancer Sci 101*, 2629-36.
32. Liu, Y., Zhang, Y., Schmelzer, K., Lee, T. S., Fang, X., Zhu, Y., Spector, A. A., Gill, S., Morisseau, C., Hammock, B. D., and Shyy, J. Y. (2005) *Proc Natl Acad Sci U S A 102*, 16747-52.
33. Kotlikoff, M. I. (2005) *Circulation Research 97*, 1209-10.
34. Cheng, M. K., Doumad, A. B., Jiang, H., Falck, J. R., McGiff, J. C., and Carroll, M. A. (2004) *Br J Pharmacol 141*, 441-8.
35. Liu, X., Li, C., Falck, J. R., Roman, R. J., Harder, D. R., and Koehler, R. C. (2008) *Am J Physiol Heart Circ Physiol 295*, H619-31.
36. Watanabe, H., Vriens, J., Prenen, J., Droogmans, G., Voets, T., and Nilius, B. (2003) *Nature 424*, 434-438.
37. Earley, S., Heppner, T. J., Nelson, M. T., and Brayden, J. E. (2005) *Circulation Research 97*, 1270-1279.
38. Node, K., Huo, Y., Ruan, X., Yang, B., Spiecker, M., Ley, K., Zeldin, D. C., and Liao, J. K. (1999) *Science 285*, 1276-9.
39. Imig, J. D. (2012) *Physiol Rev 92*, 101-30.
40. Samokhvalov, V., Vriend, J., Jamieson, K. L., Akhnokh, M. K., Manne, R., Falck, J. R., and Seubert, J. M. (2014) *Frontiers in Pharmacology 5*.
41. Chen, J. K., Capdevila, J., and Harris, R. C. (2002) *Proceedings of the National Academy of Sciences of the United States of America 99*, 6029-6034.
42. Imig, J. D., Navar, L. G., Roman, R. J., Reddy, K. K., and Falck, J. R. (1996) *J Am Soc Nephrol 7*, 2364-70.
43. Arnold, C., Markovic, M., Blossey, K., Wallukat, G., Fischer, R., Dechend, R., Konkel, A., von Schacky, C., Luft, F. C., Muller, D. N., Rothe, M., and Schunck, W. H. (2010) *Journal of Biological Chemistry 285*, 32720-32733.
44. Fischer, R., Konkel, A., Mehling, H., Blossey, K., Gapelyuk, A., Wessel, N., von Schacky, C., Dechend, R., Muller, D. N., Rothe, M., Luft, F. C., Weylandt, K., and Schunck, W. H. (2014) *J Lipid Res 55*, 1150-1164.
45. Zhang, G., Panigrahy, D., Mahakian, L. M., Yang, J., Liu, J. Y., Stephen Lee, K. S., Wettersten, H. I., Ulu, A., Hu, X., Tam, S., Hwang, S. H., Ingham, E. S., Kieran, M. W.,

Weiss, R. H., Ferrara, K. W., and Hammock, B. D. (2013) *Proc Natl Acad Sci U S A 110*, 6530-5.
46. Falck, J. R., Wallukat, G., Puli, N., Goli, M., Arnold, C., Konkel, A., Rothe, M., Fischer, R., Muller, D. N., and Schunck, W. H. (2011) *Journal of Medicinal Chemistry 54*, 4109-4118.
47. Ye, D., Zhang, D., Oltman, C., Dellsperger, K., Lee, H. C., and VanRollins, M. (2002) *Journal of Pharmacology and Experimental Therapeutics 303*, 768-76.
48. McDougle, D. R., Kambalyal, A., Meling, D. D., and Das, A. (2014) *J Pharmacol Exp Ther 351*, 616-27.
49. Messina, A., Nencioni, S., Gervasi, P. G., Gotlinger, K. H., Schwartzman, M. L., and Longo, V. (2010) *Xenobiotica 40*, 109-18.
50. Zhou, G. L., Beloiartsev, A., Yu, B. L., Baron, D. M., Zhou, W. H., Niedra, R., Lu, N. F., Tainsh, L. T., Zapol, W. M., Seed, B., and Bloch, K. D. (2013) *Plos Genetics 9*.
51. Evangelista, E. A., Kaspera, R., Mokadam, N. A., Jones, J. P., 3rd, and Totah, R. A. (2013) *Drug Metab Dispos 41*, 2087-94.
52. Moshal, K. S., Zeldin, D. C., Sithu, S. D., Sen, U., Tyagi, N., Kumar, M., Hughes, W. M., Jr., Metreveli, N., Rosenberger, D. S., Singh, M., Vacek, T. P., Rodriguez, W. E., Ayotunde, A., and Tyagi, S. C. (2008) *J Cell Physiol 215*, 771-81.
53. Thompson, D., and Oster, G. (1996) *Jama-Journal of the American Medical Association 275*, 1339-1341.
54. Hashizume, T., Imaoka, S., Mise, M., Terauchi, Y., Fujii, T., Miyazaki, H., Kamataki, T., and Funae, Y. (2002) *Journal of Pharmacology and Experimental Therapeutics 300*, 298-304.
55. Zhang, Y., El-Sikhry, H., Chaudhary, K. R., Batchu, S. N., Shayeganpour, A., Jukar, T. O., Bradbury, J. A., Graves, J. P., DeGraff, L. M., Myers, P., Rouse, D. C., Foley, J., Nyska, A., Zeldin, D. C., and Seubert, J. M. (2009) *Am J Physiol Heart Circ Physiol 297*, H37-46.
56. Westphal, C., Spallek, B., Konkel, A., Marko, L., Qadri, F., DeGraff, L. M., Schubert, C., Bradbury, J. A., Regitz-Zagrosek, V., Falck, J. R., Zeldin, D. C., Muller, D. N., Schunck, W. H., and Fischer, R. (2013) *PLoS One 8*, e73490.
57. Ke, Q., Xiao, Y. F., Bradbury, J. A., Graves, J. P., Degraff, L. M., Seubert, J. M., and Zeldin, D. C. (2007) *Mol Pharmacol 72*, 1063-73.
58. Bystrom, J., Wray, J. A., Sugden, M. C., Holness, M. J., Swales, K. E., Warner, T. D., Edin, M. L., Zeldin, D. C., Gilroy, D. W., and Bishop-Bailey, D. (2011) *PLoS One 6*, e26591.
59. Dai, M., Wu, L., He, Z., Zhang, S., Chen, C., Xu, X., Wang, P., Gruzdev, A., Zeldin, D. C., and Wang, D. W. (2015) *J Cell Physiol 230*, 2108-19.
60. Greenberg, A. S., and Obin, M. S. (2006) *Am J Clin Nutr 83*, 461S-465S.
61. Abraham, N. G., Sodhi, K., Silvis, A. M., Vanella, L., Favero, G., Rezzani, R., Lee, C., Zeldin, D. C., and Schwartzman, M. L. (2014) *Hypertension 64*, 1352-61.
62. Jiang, J. G., Chen, C. L., Card, J. W., Yang, S. L., Chen, J. X., Fu, X. N., Ning, Y. G., Xiao, X., Zeldin, D. C., and Wang, D. W. (2005) *Cancer Research 65*, 4707-4715.
63. Chen, C., Li, G., Liao, W., Wu, J., Liu, L., Ma, D., Zhou, J., Elbekai, R. H., Edin, M. L., Zeldin, D. C., and Wang, D. W. (2009) *Journal of Pharmacology and Experimental Therapeutics 329*, 908-18.
64. Lafite, P., Andre, F., Zeldin, D. C., Dansette, P. M., and Mansuy, D. (2007) *Biochemistry 46*, 10237-47.

CHAPTER III: FUNCTIONAL STUDIES OF N-TERMINALLY MODIFIED CYP2J2 EPOXYGENASE IN NANODISCS

3.1 ABSTRACT

CYP2J2 epoxygenase is a membrane bound cytochrome P450 that converts omega-3 and omega-6 fatty acids into physiologically active epoxides. In this chapter, we present a comprehensive comparison of the effects of N-terminal modifications on the properties of CYP2J2 with respect to the activity of the protein in model lipid bilayers using Nanodiscs. We demonstrate that the complete truncation of the N-terminus changes the association of this protein with the *E.coli* membrane but does not disrupt incorporation in the lipid bilayers of Nanodiscs. Notably, the introduction of silent mutations at the N-terminus was used to express full length CYP2J2 in *E. coli* while maintaining wild-type functionality. We further show that lipid bilayers are essential for the productive use of NADPH for ebastine hydroxylation by CYP2J2. Taken together, it was determined that the presence of the N-terminus is not as critical as the presence of a membrane environment for efficient electron transfer from cytochrome P450 reductase to CYP2J2 for ebastine hydroxylation in Nanodiscs. This suggests that adopting the native-like conformation of CYP2J2 and cytochrome P450 reductase in lipid bilayers is essential for effective use of reducing equivalents from NADPH for ebastine hydroxylation.

[1]Reprinted, with permission, from McDougle DR[§], Palaria A[§], Magnetta E, Meling DD, Das A*. Functional studies of N-terminally modified CYP2J2 epoxygenase in model lipid bilayers. Protein Sci. 2013 Jul;22(7):964-79. PMID: 23661295

3.2 INTRODUCTION

Eicosanoids are signaling molecules that mediate inflammation in the body and are implicated in many disorders including cancer, arthritis and cardiovascular disease (*1*). One class of eicosanoid synthesizing cytochrome P450s, known as the CYP epoxygenases catalyzes the epoxidation and/or hydroxylation of various dietary polyunsaturated fatty acids (PUFAs) and xenobiotics (*2, 3*). CYP2J and CYP2C are the two primary mammalian subfamilies that comprise the CYP epoxygenases. In humans, CYP2J2 is highly expressed in cardiac myocytes and the endothelium of coronary arteries where it plays significant roles in cardiovascular diseases and inflammation (*4-7*). This enzyme catalyzes the metabolism of arachidonic acid (AA) into epoxyeicosatrienoic acids (EETs). These metabolites are stereo- and regio-isomers that exert isomer specific anti-inflammatory, vasodilatory and pro-angiogenic effects (*8, 9*). Additionally, CYP2J2 catalyzes the conversion of the omega-3 fatty acids into physiologically active products (*5*). Both the omega-3 and omega-6 fatty acid metabolites are known dilators of the microvasculature and are essential for heart homeostatic equilibrium (*5, 10*).

Recently, CYP2J2 has also been found to be relevant in both cancer and preeclampsia pathophysiology (*11-14*). EETs are recognized as major promoters of angiogenesis and consequently enhance tumor cell survival (*12, 13, 15, 16*). In a study by Jiang and coworkers CYP2J2 was found to be predominantly localized in tumor cells when compared to the adjacent normal tissue samples (*16*). Additionally, Zeldin and co-workers recently found that EETs stimulate extensive multiorgan metastasis and escape from tumor dormancy in several cancer models (*12*). In preeclampsia, CYP2J2 was found to be highly upregulated in placental tissues and administration of CYP2J2 inhibitors reversed preeclampsia-associated symptoms in women (*11*). Hence, the development of drugs inhibiting CYP2J2 has tremendous pharmaceutical potential for the prevention of cancer metastasis and preeclampsia (*11, 14, 17, 18*).

CYP2J2 also plays an important role in the first pass metabolism of astemizole, terfenadine and ebastine and is essential for understanding the pharmacokinetic and pharmacodynamic relationships of these drugs in the body (*19, 20*). Thus, to begin to elucidate the structure-function relationships of pharmaceutically relevant CYP2J2, we expressed the protein with high yields in *E. coli* and focused on understanding the role of the N-terminus of CYP2J2 in association with lipid bilayers and in ebastine hydroxylation activity.

The N-termini of membrane bound cytochrome P450s have been shown to play an important role in lipid association, protein-protein interactions and substrate access. There are many reports of the hydrophobic N-terminal domain mediating the P450 membrane binding association (*21-24*). Based on this observation, a soluble and monomeric form of CYP2C5 was engineered by deleting the N-terminal membrane-spanning region (*25, 26*). Additionally, the N-terminus of CYP1A2 was shown to be involved in membrane anchoring and N-terminal modifications had an effect on the catalytic activity (*27*). Interestingly, it was also demonstrated that membrane insertion of CYP1A2 was promoted by the presence of anionic phospholipids and this association with membrane is dependent on the N-terminus of CYP1A2 (*28*). In addition to playing a role in association with membrane, the N-terminus can be involved in P450-P450 interactions (*29*). Tracy and coworkers demonstrated that the hydrophobic N-terminus binding domains of CYP2C9 and CYP3A4 are involved in heterodimer complex formation and truncation of the N-terminus of CYP2C9 led to the abolition of inhibition by CYP3A4 (*30*). In separate studies it was hypothesized that the N-terminal domain might be critical for orientation of the protein into the lipid bilayer (*31*). Thus, the N-terminus affects the localization on the membrane and can influence orientation and activity. Although the N-terminus is considered to be responsible for membrane association, one cannot always obtain a soluble protein by simply truncating the N-terminus. This is likely due to the presence of additional hydrophobic residues, which contribute to membrane association. The other regions thought to be involved in membrane anchoring are the F′ and G′ helices and F-G loop. Hence, it is strongly believed that membrane lipid molecules may play an important role in gating the entrance of substrates and/or release of products implying that the ligand entrance pathways are likely partially immersed in the membrane (*32, 33*).

Here we use Nanodiscs for rigorous biochemical interrogation of CYP2J2 and the role of N-terminus in membrane association and activity. Nanodiscs are nanoscale lipid bilayers that are surrounded by a membrane scaffold protein (*34-36*). Incorporation of a CYP protein into Nanodiscs mimics the endogenous membrane environment of the protein, producing a macromolecule amenable to several important biochemical and biophysical assays hitherto reserved for soluble proteins. Nanodiscs have proven to be excellent for the solubilization and mechanistic investigation of many diverse membrane protein systems. Moreover, this technology has enabled the stabilization of membrane proteins both in solution (*37-41*) and on surfaces (*40, 42-45*).

Herein we functionally characterize CYP2J2 in model lipid bilayer Nanodiscs. We demonstrate the role of the N-terminus in association with the *E.coli* membrane and with the lipid bilayers of Nanodiscs. We further evaluate whether lipid bilayers are essential for the productive use of NADPH and product formation by CYP2J2.

Notably, we introduce silent mutations at the N-terminus to express full length CYP2J2 in *E. coli* while maintaining wild-type functionality (*46*). The full-length CYP2J2 provides a nearly identical wild-type construct for comparison to the N-terminus truncated constructs being explored in this work. While some of the results corroborate more anecdotal results for other P450s, this present study presents a more thorough and comprehensive comparison of the effects of N-terminal modifications on the properties of CYP2J2 in native-like lipid bilayers with respect to membrane association and activity.

3.3 MATERIALS AND METHODS

Materials. Human CYP2J2 cDNA was obtained from OriGene (Catalog No. SC321730). PCR reagents and other enzymes for molecular biology were purchased from Invitrogen. Qiagen kits were used to purify the plasmid DNA from bacterial cells and from agarose gels. The bacterial strains used were *E.coli* XL1 Blue obtained from Agilent and DH5α from Invitrogen. Ampicillin, arabinose, chloramphenicol, IPTG and Ni-NTA resin were bought from Gold Biotechnology. δ-Aminolevulinic acid was bought from Frontier Scientific. NADPH and NADP were obtained from P212121.com. 3-[(3-cholamidopropyl) dimethylammonio]-1-propanesulfonate (CHAPS) was acquired from BioVision Inc. 1-palmitoyl-2-oleoyl-sn-glycero-3-phosphocholine (POPC) was purchased from Avanti Polar Lipids, Inc. Amberlite XAD 2 was acquired from Supelco. Nanosep MF (0.2 µM) and Amicon Ultra (10,000 MWCO) centrifugal filters were procured from Millipore. Arachidonic acid and ebastine were obtained from Cayman Chemical. The protein standards – thyroglobulin, ferritin, bovine serum albumin and cytochrome c were purchased from Sigma. All other materials and reagents used were purchased from Sigma and Fisher Scientific.

***Design of CYP2J2 constructs and cloning into pCWori+ vecto*r.** CYP2J2 cDNA obtained from OriGene was cloned into the pCWori vector. All the constructs were grown in the presence of chaperonin system hence "G" is used for all constructs. Construct 1-M2G: The amino acid sequence of this construct is similar to the wild type amino acid sequence except for the substitution of the second amino acid residue leucine (CTC) by alanine (GCT). Construct 2-M2SMG: The sequence of this construct is similar to M2G with the introduction of silent mutations

in the 3rd, 4th and 6th codons to make them AT rich and thereby minimizing the free energy of the mRNA secondary structure formation. The ΔG of first 7 codons at N terminus of M2SMG is -1.69, ΔG of WT = -4.27 and ΔG of construct M2G = -3.94. Values were obtained using RNAFold WebServer (*47, 48*). Note that M2G and M2SMG share identical primary sequences but differ in N-terminus codon usage. Construct 3-M2D5HG – This construct was designed not only to increase the yields of expression of human CYP2J2 but also for maintaining the association of this protein with lipid bilayers. Therefore in this construct we have replaced the first five amino acids from the N-terminus with a hydrophilic sequence AKKTSS and maintained most of the original hydrophobic sequence (*49*). Construct 4-M2D19HG – In order to optimize and enhance the expression while preserving some part of the hydrophobic region to interact with membranes we deleted codons, 2 to 19, from the N-terminus and inserted the hydrophilic sequence AKKTSS. Insertion of a hydrophilic sequence in combination with truncation of a major part of the native hydrophobic sequence has been shown to give higher protein expression. Construct 5-M2D34G was engineered with the goal of enhancing yield and making the protein soluble and suitable for crystallization and structural determination by X-ray diffraction studies (*50, 51*). It has been shown previously that deletion of the first 34 amino acids with a hydrophilic region naturally following this deletion increases the yields of CYP2J2 protein in *E. coli*. (52). In all the constructs we added a penta-his tag to the C-terminus to facilitate purification using metal chelating affinity columns.

The different constructs of the CYP2J2 gene were prepared and amplified by PCR using the appropriate sets of primers listed in supplementary material (Table 3.2). The PCR conditions are also mentioned. CYP2J2 gene has an internal NdeI site. Hence, an AseI site was introduced within the forward primer. AseI site overhangs are compatible with the overhang produced from digesting NdeI site in the vector. Therefore all of the constructs had an AseI restriction site in the forward primer along with the various N-terminal modifications. The reverse primer incorporated a penta His tag and an XbaI restriction site at the C-terminus. The amplified CYP2J2 genes were digested with AseI-XbaI and then ligated with the NdeI-XbaI digested pCWori vector and co-transformed with chaperonin plasmid pTGro7 into DH5α competent cells. pTGro7 encodes for the GroEL-GroES gene and is selected via chloroamphenicol resistance. Transformed colonies were confirmed for the presence of the respective constructs by DNA sequencing.

***Expression and purification of CYP2J2*.** Double transformant colonies containing the CYP2J2 gene and pTGro7 gene were cultured in 30 mL of Luria Bertani (LB) media with chloroamphenicol

(20 µg/ml) and ampicillin (100 µg/ml) at 37°C and 250 rpm overnight. 5 mL of this culture was used to inoculate 500 mL of Terrific Broth (TB) media supplemented with trace elements, ampicillin (100 µg/ml) and chloramphenicol (20 µg/ml). The culture was grown for 2.5 hours at 37°C and 220 rpm. Delta-aminolevulinic acid (500 µl of 0.5 mM) was then added and the culture was grown for another 2h at 26°C and 160 rpm. After reaching a target absorption (A_{600} = 1.2), 1 mM of Isopropyl β-D-1-thiogalactopyranoside (IPTG) was added to induce protein expression. In addition 2g of arabinose was added to each 500 mL culture (*53*). The cultures were grown for 44 h and then the cells were harvested by centrifugation. The cell pellet was resuspended in buffer 1 (100 mM potassium phosphate pH 7.4, 20% glycerol, 6mM magnesium chloride, 0.1mM dithiothreitol (DTT) and 0.2 mM phenylmethanesulfonylfluoride (PMSF), approximately 1mg each of DNase and RNase). The cells were sonicated on ice for 6 cycles of 1 minute with breaks of 1 minute at an output of 4, 40% duty cycle with a Heat Systems Ultrasonics (Qsonica, Newtown, CT) sonicator. This was followed by centrifugation at 35,000 RPM at 4°C for 45 min using a Beckman ultracentrifuge (Beckman Coulter, Brea, CA). The supernatant was collected to quantitate protein in the soluble fraction. The membrane fraction pellet was resuspended in a solubilization buffer 2 (100mM potassium phosphate pH 7.4, 20% glycerol, 200 mM sodium chloride, 0.1mM dithiothrietol and 1% CHAPS) for 3-5 h at 4°C. This was further centrifuged at 4°C and 35,000 RPM for 45 min to obtain the supernatant, which contained the target membrane protein. The supernatant was then loaded onto a Ni-NTA column equilibrated with the column buffer 3 (100 mM potassium phosphate pH 7.4, 20% glycerol and 0.5% CHAPS). The column was washed with 5 column volumes of the wash buffer (100 mM potassium phosphate pH 7.4, 20% glycerol, 0.5% CHAPS and 20 mM imidazole). It was further washed with 4 column volumes of ATP containing buffer 4 (100 mM potassium phosphate pH 7.4, 20% glycerol and 0.5% CHAPS, 5 mM ATP, 10 mM magnesium chloride, 150 mM potassium chloride) to remove the GroEL which may be bound to the CYP proteins (*54*). Finally the protein was eluted with 4 column volumes of the elution buffer (100mM potassium phosphate pH 7.4, 20% glycerol, 0.5% CHAPS and 200 mM imidazole). The eluted protein was concentrated and buffer exchanged to remove imidazole using Amicon centrifugal filters (10,000 MWCO) and stored at -80°C.

Characterization of CYP2J2. CYP2J2's purity was analyzed using 10% SDS-PAGE where it separated as a single band with an Rz ratio (A417 nm/A280 nm) of 1.3 or higher obtained by measuring the UV-Visible spectra. CYP2J2 concentration was measured by carbon monoxy

difference spectra as described previously by Omura and Sato using an extinction coefficient of 91 mM^{-1} cm^{-1} (*55*). The protein content from both cytosol and membrane fractions were quantified. For CO analysis we modified the Omura and Sato method by purging a 500µl aliquot of the buffer exchanged sample with nitrogen for 20 min and then adding 10-20 µL of dithionite solution anaerobically. This was then used for CO addition and monitored using a Cary Bio 300 UV-Vis spectrophotometer (Agilent Technologies, Santa, Clara CA). The difference spectra were recorded to quantify the protein as well as to assess the quality of the protein.

Oligomerization States of detergent solubilized CYP2J2 using size exclusion chromatography. Size exclusion chromatography (SEC) was performed using a Superdex 200 10/300 column (GE Life Sciences, Piscataway NJ) coupled with a high performance liquid chromatography (HPLC) system consisting of an Alliance 2695 analytical separation module (Waters, Milford MA) and a Waters 996 photodiode diode array detector (Waters, Milford MA). The different CYP2J2 constructs were loaded individually at 15 µM on the SEC column and were run with an isocratic mobile phase consisting of 100 mM of potassium phosphate buffer (pH 7.4) containing 150 mM sodium chloride and 0.1 mM EDTA at 0.5ml/min flow rate. The oligomerization states of the CYP2J2 constructs were estimated using a standard curve plotted using thyroglobulin (669 kDa), ferritin (440 kDa), BSA (67 kDa) and cytochrome c (14 kDa) as standards.

Expression and purification of cytochrome p450 reductase. A 10 ml volume of starter culture (grown from a single colony for 18-20 hours at 37°C and 220 rpm) was used to inoculate 1L of LB media supplemented with ampicillin and riboflavin. The culture was grown at 37°C and 220 rpm for 4 h (O.D. was 0.8-1). Expression of the reductase was induced by adding IPTG (1 ml of 1 mM) and growing the culture at 30-33°C and 220 rpm for 18-20 h. Cells were harvested by centrifuging at 4000 rpm for 15 min. in a JA-10 rotor (Beckman Coulter, Brea, CA) at 4°C. The pellet was resuspended in 500 ml of cold lysozyme buffer (75 mM Tris pH 8.0, 0.25 M sucrose, 0.25 mM EDTA and 0.02 mg/ml lysozyme) and allowed to stir at 4°C for 30min. The spheroplasts were obtained by centrifuging at 4000 rpm for 30 min. in the JA-10 rotor at 4ºC and then resuspended in 40 ml of lysis buffer (50 mM Tris pH 8.0 and 1mM PMSF) at 4ºC for 30min. Sonication was carried out on ice with 5 cycles of 30 seconds with 1 minute breaks. Membranes were isolated by centrifuging at 30000 rpm for 30 min. at 4ºC in a Ti-45 rotor. This membrane pellet was then solubilized in 40 ml of column buffer (50 mM Tris pH 7.7, 0.1 mM EDTA 0.1 mM DTT and 20% glycerol) containing 0.2% Triton for an hour at 4ºC. Subsequent centrifugation at 30000 rpm for

30 min. at 4ºC in a Ti-45 rotor (Beckman Coulter, Brea, CA) gave the protein in the supernatant fraction which was then loaded onto a 2'5'ADP Agarose column equilibrated with the column buffer. The column was then washed with 10 column volumes (c.v.) of the wash buffer (100ml of column buffer containing 2 mM adenosine) and eluted with 5 c.v. of the elution buffer (50ml of column buffer containing 2 mM NADP or 2 mM AMP). To remove the detergent and obtain high purity of protein, the eluate was passed through a DEAE column equilibrated with the wash buffer, washed with 10 column volumes of the wash buffer and eluted with 5 column volumes of the elution buffer. The final eluate was concentrated and the CPR concentration was measured with a Cary Bio 300 UV-Vis spectrophotometer (Agilent Technologies, Santa, Clara CA) at 456 nm. Purified CPR was characterized by measuring the cytochrome c reduction for 10 min. at 550nm in a solution of 1 ml of 0.3 M potassium phosphate buffer pH 7.4 containing 50 µM cytochrome c, 50 µM NADPH and 2 µM of the purified CPR. The purified reductase was stored at -80ºC.

***Assembly of CYP2J2-Nanodiscs*.** The lipid, 1-palmitoyl-2-oleoyl-sn-glycero-3-phosphocholine (POPC) solubilized using 100 mM cholate, was added to the membrane scaffold protein MSP1D1 (65:1 ratio) and allowed to mix at 4ºC for 1 hour. To assemble the Nanodiscs with the protein, CYP2J2 in 100 mM potassium phosphate pH 7.4, 20% glycerol, 0.5% CHAPS was added to the mixture at a CYP:MSP ratio of 1:15 and allowed to mix for an additional hour. Amberlite beads were then added to the final mixture to remove the detergent overnight at 4ºC. The mixture was separated from the beads by filtration. The resulting solution was concentrated, loaded onto a SEC column and the protein incorporated Nanodiscs peaks were collected and concentrated. The concentrated CYP2J2-ND complex was stored at -80ºC in the presence of 10% glycerol.

***Assembly of CYP2J2-CPR Nanodisc complex for activity assay*.** The assembly the CYP2J2 and CPR into a single macromoleculer complex was achieved following previously described methods (*56*). Briefly, CYP2J2 and CPR was incubated in a 1:1.5 ratio in 0.1% (v/v) cholate for one hour at 4ºC prior to being added to the detergent solubilized MSP1E3D1- and POPC mixture described above. The final molar ratio of the mixture contained a CYP2J2/CPR/MSP1E3D1(-)/POPC ratio of 0.1:0.15:1:130. Amberlite beads were then added to the final mixture to remove the detergent overnight at 4ºC. For the isolation of Nanodiscs containing both CPR and CYP2J2 the filtered solution was passed through an ADP agarose column to selectively bind CPR and eluted with 2.5 mM NADP phosphate buffer (7.4). The eluent was then passed through a Ni-NTA column to selectively bind the his-tagged CYP2J2 protein and eluted phosphate buffer (7.4) containing 200

mM imidazole. The eluent was concentrated and then loaded on a SEC column where the relatively large Nanodisc containing both CPR and CYP was confirmed by the elution time at ~21.5 minutes. The final reconstitution molar ratio of all components was 0.1:0.2:240:120:1 CYP2J2/CPR/cholate/POPC/MSP1E3D1(–)). The 1:1 ratio of CYP2J2 and CPR was confirmed with a UV-Vis scan using the respective absorbance of CYP2J2 at 417 nm (ε = 110 mM^{-1} cm^{-1}) and CPR at 456 nm (ε = 24 mM^{-1} cm^{-1}).

Preparation of CYP2J2 and CPR in a 1-palmitoyl-2-oleoyl-sn-glycero-3-phosphocholine (POPC) reconstituted system. The *in vitro* activity of CYP2J2 and the redox partner CPR were assessed in a standard phospholipid reconstituted system following previously described methodology (*57*). The lipids were prepared by reconstituting POPC in 100 mM phosphate buffer (pH 7.4) containing 100 mM sodium cholate to a final lipid stock concentration of 10 mM. The solution was then dispersed by sonication until clarity was achieved prior to mixing with the proteins. The detergent solubilized POPC stock was then added at a final concentration of 50 µM into a cuvette containing 0.6 µM CPR and 0.2 µM CYP2J2 and incubated at 37ºC for five minutes prior to use in the NADPH oxidation and ebastine hydroxylation assay.

Stability of CYP2J2-Nanodiscs. The effect of N-terminal modifications on association of CYP2J2 with lipid bilayers of Nanodiscs was investigated by monitoring the stability of CYP2J2-Nanodiscs at 4ºC using SEC-HPLC. Samples containing CYP2J2 N-terminal mutants incorporated into Nanodiscs were prepared with 50 mM POPC, 290 nmol of MSP1T2(-) (MSP1T2 His-tag was cleaved using TEV protease) (*58*) and 29 nmol of CYP2J2 as described above. Ni-NTA affinity column was used to remove empty Nanodiscs from CYP2J2-Nanodiscs mixture since the CYP2J2 constructs contained a His-tag but the MSP1T2(-) did not. Samples were aliquoted and stored in 100 mM phosphate buffer (pH 7.4) at 4ºC and analyzed over a period of 7 days with an isocratic gradient consisting of a 100 mM phosphate buffer (pH 7.4) mobile phase over a 60 minute period. The CYP2J2-ND assembly was monitored at 417 nm and 280 nm. Overall stability of M2SMG-ND, M2D5HG-ND, M2D19HG-ND and M2D34G-ND were calculated from the integrated areas of each time point relative to the initial injection for each respective construct. The day 0 and day 7 samples were also evaluated for stability using a CO binding assay as described above.

Binding titration of CYP2J2-Nanodiscs with ebastine. The binding of ebastine to CYP2J2 constructs was calculated by monitoring the spin state shift using a Cary Bio 300 UV-Vis spectrophotometer (Agilent Technologies, Santa, Clara CA). Two constructs, M2SMG and

M2D19HG, were incorporated into Nanodiscs and purified using methods listed above. Samples contained 2-5 µM of CYP2J2-ND, 100 mM phosphate buffer (pH 7.4) and ebastine. Ebastine was added incrementally from a 10 mM ethanol stock with the final concentration of ethanol not exceeding 1%. The absorption spectra were measured between 800 and 200 nm after each ebastine titration. Spectra were plotted and analyzed in Origin Lab (Origin Lab Inc., Northhampton, MA) For each titration the characteristic Type I spectral shift difference, from a low spin to a high spin state, were calculated (by measuring difference A_{386}-A_{417}) and plotted against the ebastine concentration. The data were then fitted using the Hill equation (Eq. 1). Additionally, the percent of high spin was calculated using a standard MATLAB subroutine.

(**Equation 1**) $\Delta A = A_{max} S^n / (K_s^n + S^n)$

Where ΔA is the absorbance difference at 386 nm and 417 nm, A_{max} is the amplitude corresponding to maximal spin shift, K_s is the spectral dissociation constant, S is the substrate concentration and n is the Hill coefficient. The ebastine binding data fit n=1 better than n=2, therefore for final fitting a single binding isotherm was used. The calculated spectral binding constants are averages of three independent experiments.

***NADPH activity assays*.** CYP2J2 NADPH oxidation rates were examined native-like in membrane bound systems (Nanodiscs) and detergent solubilized systems (0.1% CHAPS). The NADPH oxidation rates were measured using kinetics mode in a Cary 300 UV-Vis spectrometer (Agilent Technologies, Santa Clara, CA). Incubation mixtures were calculated in the presence of saturating concentrations of substrate (arachidonic acid or ebastine) and electron donor (NADPH). The incubation mixtures contained 100 mM phosphate buffer (pH 7.4), 150 pmol CPR, 50 pmol of CYP2J2 N-terminal mutant and either arachidonic acid (70 µM) or ebastine (50 µM). Samples were equilibrated at 37˚C for 5 minutes prior to reaction initiation with 200 µM NADPH (total volume 250 µL). NADPH oxidation was monitored for ten minutes at 340 nm and the slope was used to determine the absorption change over time. The NADPH consumption rate was calculated using an extinction coefficient of 6.22 $mM^{-1}cm^{-1}$. Reactions were quenched and products of the reaction were further analyzed as given in the next section (*59*).

***Ebastine hydroxylation assay*.** CYP2J2 N-terminal mutant ebastine metabolism rates were examined in membrane bound systems (Nanodiscs) and detergent solubilized systems (0.1% CHAPS). Saturating concentrations of the substrate (ebastine) and electron donor (NADPH) were used to calculate the reaction V_{max} (nmol/min/nmol of CYP) for each respective CYP2J2 N-

terminus mutant. The incubation mixture for ebastine hydroxylation was the same as above. After a ten minute incubation period, the reaction was terminated with 100 µL of ice cold acetonitrile and then spiked with the internal standard terfenadine (100 ng/ml). The reactions were stopped at 10 minutes to minimize secondary metabolite formation Quenched samples were centrifuged at 10,000 rpm for 15 minutes on a desktop mini-centrifuge (Eppendorf AG Hamburg, Germany). A 100 µL sample of supernatant was flash frozen for hydroxyebastine concentration determination via LC/MS/MS analysis. Each construct assay was completed in duplicate or greater. Rates and coupling efficiency (%) are reported as the mean ± SE.

Liquid chromatography- tandem mass spectrometry for quantitation of ebastine and hydroxyebastine. Liquid chromatography-tandem mass spectrometry (LC/MS/MS) was employed for quantitation of ebastine, hydroxyebastine and terfenadine parent ions [M + H]+ and their corresponding fragment ions. The LC/MS/MS system consisted of a Waters Alliance 2795 analytical high performance liquid chromatography separation module (Waters, Milford, MA) coupled with an electrospray ionization mass spectrometer (Waters Quattro Ultima, Waters, Milford, MA) operated in positive mode. Samples were analyzed using a reversed-phase C18, 1.3 Å, 2.1 mm x 20 mm and 2.5 µm pore size column (Waters, Milford, MA). The solvent system was composed of two solutions: solvent A (95% H_2O, 5% acetonitrile (ACN) and 0.1% formic acid (FA)) and solvent B (5% H_2O and 95% ACN, and 0.1% FA). The 10 min gradient LC separation included 8 steps: (1) 90–80% solvent A in 0–1 min (linear); (2) 80–65% solvent A for 1–4 min (linear); (3) 65% solvent A for 4-5 min (isocratic); (5) 65-50% solvent A for 5-7 min (linear); (6) 50% solvent A for 7-8 min (isocratic); (7) 50-90% solvent A for 8-9 min (linear); and (8) 90% solvent A for 9-10 min (isocratic).

The MRM data acquisition consisted of monitoring the following analytes in positive mode using these transitions (parent ion → fragment ion, cone voltage, collision voltage) ebastine (470.4 → 167.0, 30 eV, 30 eV and 470.4 → 203.1, 30 eV, 30 eV), terfenadine (472.4 → 57.2, 30 eV, 35 eV and 472.4 → 436.3, 30 eV, 25 eV) and hydroxyl-ebastine (486.4 → 167.0, 30 eV, 30 eV and 486.4 → 219.1, 30 eV, 30 eV) all with 100 ms dwell time. Quantitation of ebastine and hydroxyebastine was determined using the peak areas normalized to the internal standard (terfenadine 100 ng/ml) from a previously calculated standard curve. Analytical data was processed using Waters Mass Lynx software (version 4.1).

Modeling of CYP2J2. The primary amino acid sequence of M2D34G was used as input to generate a 3-dimensional model of CYP2J2 created using the Phyre Web server (*60*). The resulting pdb file was used as input for the Orientations of Proteins in Membranes (OPM) database (*61*) to generate a model of M2D34 binding with a membrane (Figure 3.4B).

3.4 RESULTS AND DISCUSSION

Construction of CYP2J2 N-deletion mutants. The native human CYP2J2 gene was obtained from Origene. The Kyte-Doolittle hydropathy plot for CYP2J2 (Figure 3.6) shows that approximately the first 33 amino acids form the hydrophobic membrane-spanning domain. From literature, it is known that removal of hydrophobic regions from the N-terminus increases the yields of expression of cytochrome P450s (*26, 49*). Therefore we prepared five different CYP2J2 constructs with varying N-terminal modifications for the purpose of increasing the yield of expression without eliminating their ability to associate with the lipid bilayers. The different N-terminally modified CYP2J2 constructs are listed in Figure 3.1A and the list of primers used for each respective construct are represented in the supplementary data (Table 3.2). The N-terminal modifications made to the CYP2J2 constructs are the following. [1] Replaced the second codon in the gene sequence with Ala (GCT), as many E. coli genes controlled by the lacZ operator have been found to contain this codon (*62, 63*). [2] Incorporated silent mutations in the first 5 to 7 codons to render them both AT rich and to minimize the free energy of mRNA secondary structure (*47, 48, 63, 64*). [3] Truncated part or all of the hydrophobic (membrane spanning) region of the N-terminus as done previously (*22*). [4] Incorporated hydrophilic sequence AKKTSS into the N-terminus (*65, 66*).

One complication in the molecular cloning of CYP2J2 was the presence of an internal NdeI site in the gene (*67*). We circumvented this problem by using an easy and elegant method of digesting the CYP2J2 gene with a different enzyme, AseI, which produced an overhang compatible with the NdeI digested fragment and enabled ligation producing the desired constructs.

Heterologous expression of CYP2J2 in E. coli. All the constructs of CYP2J2 were transformed into DH5alpha cells along with the pTGro7 plasmid encoding for the expression of the GroEL-GroES chaperonin system (*68*). The average yields obtained after Ni-NTA column purification from each of the constructs are shown in Figure 3.1B. The overall protein expression yields corresponded to the size of the N-terminal deletion with yields following: M2D34G>M2D19HG>M2D5HG~M2SMG. The protein expression yields of the full-length

CYP2J2 significantly varied for constructs M2G and M2SMG with yields of 1-2 nmol/L and 27 nmol/L of purified protein, respectively. Interestingly, both M2G and M2SMG are full-length proteins similar to wild type CYP2J2 with a single substitution (Leu2Ala) at the 2nd amino acid in the N-terminal domain (Figure 3.1A). The difference between these two constructs was the introduction of silent mutations at the 3rd, 4th and 6th codons of M2SMG that increased expression 20-fold as represented in Figure 3.1B. Thus, we were able to greatly enhance the expression of full length CYP2J2 (M2SMG) with the introduction of silent mutations at the N-terminus thereby minimizing the free energy of the mRNA secondary structure formation (ΔG of M2G = -3.94; ΔG of M2SMG = -1.69) as calculated in the methods section. The expression of full length CYP2J2 in high yields was essential to fully elucidate the role of the N-terminus of CYP2J2 in membrane binding and association with its redox partner cytochrome P450 reductase.

The complete truncation of the N-terminal hydrophobic region in the M2D34G construct resulted in the protein being located in the soluble fraction at a much higher percentage (~40%) than the proteins expressed from other constructs (Figure 3.1B). M2D19HG, which was modified by truncating 19 N-terminal amino acids, was primarily purified from the *E. coli* membrane fraction (~85%). This indicated that the additional 14 hydrophobic amino acids of D19HG provided a much stronger membrane anchor for association during purification when compared to M2D34G.

Oligomerization Studies. The oligomerization states of the different constructs were estimated by size exclusion chromatography. In Figure 3.2C, we see that the N-terminal hydrophobic regions of M2SMG and M2D5HG induce significantly greater oligomeric states with predominant retention times at 22 min and a much smaller peak at 30 min. The N-terminal truncations of M2D19HG exhibited a different elution profile with two predominant oligomeric states at 22 min and 31 min. Most dramatically, the N-terminal deletions of M2D34G produced a large monomeric state at 31 min with a smaller aggregated peak at 19 min. The overall quantity and stokes radius for the larger oligomeric states corresponded closely with the size of the N-terminus, thus following the pattern M2SMG~M2D5HG>M2D19HG>M2D34G.

Spectrophotometric characterization of CYP2J2 N-terminus mutants and substrate binding assay. The purified oxidized CYP2J2 constructs were analyzed using UV-visible spectra. All the constructs had typical peaks at 417 nm and the α and β bands (Q-bands) at 536 nm and 570 nm respectively. The proteins were reduced and the Fe(II) CO spectra was measured for each of the

constructs (*55*). Figure 3.2B shows the Fe(II)-CO spectra of all the different constructs. They all exhibited prominent peak at 450 nm with little to no presence of a peak at 420 nm. This confirmed that the axial-thiolate ligand was retained and suggested maintenance of a typical P450 fold for this motif in the active site.

***Spectroscopic substrate binding assay*.** Typically for drug metabolizing and steroid synthesizing human cytochrome P450s, binding substrate produces a spin state shift accompanied by the shift of Soret from 417 nm to 393 nm (*40, 56, 69*). To probe the active site of a full-length versus truncated CYP2J2, we studied the substrate binding in Nanodiscs. CYP2J2 is primarily expressed in the human heart where its main function is the conversion of arachidonic acid (AA) into EETs by epoxidation. Using this assay, we did not detect an observable spectral spin state change for AA binding. However, we did measure a modest increase in NADPH consumption rates (data not shown) that indicated binding of the substrate. Additionally, Zeldin and colleagues previously determined the *in vitro* metabolism rate of AA (*70*). In contrast, the other epoxygenases (CYP2C8 and CYP2C9) directly interact with AA, as evidenced by a 27% spin state change for CYP2C8 (*71, 72*). However, this is not unprecedented as there are several examples where substrate binding does not substantially change the spin state for substrates capable of being metabolized. For instance, CYP3A4 metabolizes erythromycin despite a minor spin state shift (5-10%) upon binding (*40*).

CYP2J2 is also involved in the metabolization of certain drugs including ebastine, astemiozole and terfenadine (*73, 74*). We measured the UV-Vis spectra of ebastine binding to CYP2J2. As shown in Figure 3.3A, type I substrate-binding spectra is obtained upon titration with ebastine. This is also true for binding of terfenadine to CYP2J2 (data not shown). The spectral dissociation constant of ebastine binding to the two constructs of CYP2J2 were calculated to be 7.3 ± 1.9 μM for M2SMG and 6.8 ± 0.7 μM for M2D19HG. This reveals that the spectral dissociation constant is likely to be independent of the N-terminus composition of CYP2J2 in Nanodiscs. Unlike other drug metabolizing P450s, the binding of ebastine fits to a single substrate binding equation and does not exhibit cooperativity.

***Association of CYP2J2 with lipid bilayers*.** Nanodiscs are native-like lipid bilayer membranes that have been used to stabilize membrane proteins in solution. We assembled the different N-terminal variants of CYP2J2 into Nanodiscs in order to: (a) functionally stabilize the cytochrome

P450s, (b) study the stability of the association of different CYP2J2 constructs with the lipid bilayers over time, (c) and assess the role of lipid bilayers in controlling the function of P450s.

The N-terminus of membrane-bound native CYP2J2 is hydrophobic and is thought to be involved in association with the membranes. We analyzed the P450 content of the different N-terminally modified CYP2J2 constructs in both the soluble and membrane fractions of *E.coli* cells (Figure 3.1B). We found that M2D34G CYP2J2 (complete N-terminus truncation) was purified from both soluble (40%) and membrane fraction (60%) while M2SMG CYP2J2 (full length) was primarily obtained from the membrane fraction (96%) as seen in Figure 3.1B. The membrane fraction of M2D34G still contained the majority of protein indicating the intrinsic membrane binding affinity was not completely abolished. These results suggested the solubility of the protein was increasing due to the truncation of N-terminal hydrophobic residues similar to other membrane bound CYPs (*25*).

To evaluate if the N-terminus modifications conferred stable association with lipid bilayers, we measured the stability of the CYP2J2-Nanodisc complex over a period of seven days at 4ºC using size exclusion chromatography. The CYP2J2-Nanodiscs peak eluted at 26 minutes (flow rate is 0.5 mL/min) and was measured by monitoring the absorbance at 417 nm. The area under the peak was integrated and used to quantitate percent loss of the CYP2J2-Nanodisc complex. Over 7 days at 4ºC there was loss of ~10-25% of the starting amount of CYP2J2-Nanodiscs (Figure 3.4D). We did not observe the formation of an empty Nanodisc peak or free CYP2J2 in solution indicating the macromolecular complex was likely precipitating upon dissociation and lost in the pre-filtration step of this assay.

Interestingly, despite the truncation of 34 amino acid residues in the M2D34G construct we obtained stable Nanodiscs comparable to that of the full length M2SMG. Surprisingly, M2D19HG demonstrated the greatest stability over the same time course. Thus, the trends observed when purifying proteins from cell lysates do not directly translate to *in vitro* protein-membrane associated systems in standard conditions. These observations indicated that additional residues separate from the N-terminus were also responsible for membrane association. To explore this further, we modeled CYP2J2 in membranes using Phyre and OPM software (*60, 61*). We found that similar to other membrane binding CYPs, the A helix, F-G loop and F′-G′ helices contain hydrophobic groups that likely aid in the association of this protein with the membrane (Figure 3.4B). These residues provide interesting targets for additional mutations to further explore the

membrane binding properties of CYP2J2 and engineer a soluble and monomeric CYP2J2 construct.

Additionally, we measured the P450 content by CO binding at the beginning and end of 7 days to gauge CYP2J2 functionality. The Fe(II)-CO P450 formation at the beginning (day one) and end (day seven) of the time course produced 100% P450 (data not shown), indicating that all the proteins in Nanodiscs retained the typical P450 protein fold with the heme-thiolate motif intact when stored at 4ºC.

CYP2J2 activity and role of membranes. We further studied the role of the N-terminus of CYP2J2 in modulating the activity of the protein with respect to the rate of NADPH oxidation and ebastine hydroxylation. The rate of steady-state NADPH consumption was measured for the four constructs in the presence/absence of ebastine in a three different systems - detergent solubilized system, phospholipid reconstituted system and incorporated into Nanodiscs.

Additionally, the enzymatic activities of CYP2J2 constructs were determined in the three systems by measuring the rate of ebastine hydroxylation (*59, 75*). We measured the ebastine hydroxylation activity of the protein to determine whether the protein is using the transferred electrons from NADPH for a productive pathway to generate desired products or using them unproductively in generating unwanted reactive oxygen species (*76*). We measured the coupling efficiency, which is defined as the ratio of rate of product formation to the rate of NADPH oxidation (Figure 3.5). These experiments provided insight of the role of N-terminus and that of membranes in controlling the NADPH oxidation and ebastine hydroxylation in CYP2J2-CPR system.

NADPH oxidation, product formation and coupling efficiency in CYP2J2:CPR-Nanodiscs. The Nanodisc rates reported here are for a co-incorporated 1:1 homogeneous complex of CYP2J2:CPR (*56*). On average, for the CYP2J2:CPR-Nanodiscs substrate free form the rate of NADPH consumption was ~10 nmol/min/nmol for the four constructs. When a saturating concentration of ebastine was added, a doubling of the NADPH oxidation rate was observed, in the range of 20.3-27.1 nmol/min/mol. Notably, in this defined lipid membrane system we observed similar NADPH oxidation rates for all the constructs; with M2D19HG:CPR-ND exhibiting a slightly higher consumption rate. Taken together, when the ratio of CYP2J2:CPR was equal and incorporated into membrane bilayers we do not detect a significant difference in the NADPH turnover rates for the constructs.

To gauge functionality, we measured the ebastine hydroxylation activity of this system as given in table 1 for M2SMG, M2D5HG, M2D19HG and M2D34G. Due to the narrow range of product formation it was necessary to calculate the coupling efficiencies in order to directly compare the four constructs in this system. The coupling efficiencies in Nanodiscs for M2SMG: CPR, M2D5HG:CPR, M2D19HG:CPR and M2D34G:CPR were determined to be 17.0 ± 0.8, 17.1 ± 0.7, 16.5 ± 0.9 and 13.6 ± 1.3 %, respectively. We considered each of these efficiencies to be very similar, with a slight reduction in the efficiency of M2D34G. Overall, these coupling efficiencies were approximately 6-fold greater than the detergent solubilized system and 3-fold greater than the phospholipid reconstituted system (Table 3.1). This shows that interaction of CYP2J2 and CPR in a membrane environment plays a more important role in controlling the coupling efficiency as compared to the N-terminus hydrophobic domain of CYP2J2.

NADPH oxidation, product formation and coupling efficiency in a phospholipid reconstituted system. In the absence of substrate the phospholipid reconstituted system provided a range of NADPH consumption rates (31.8-65.1 nmol/min/nmol) that followed the extent of the N-terminal truncation. Likewise, in the presence of excess substrate a similar trend in NADPH oxidation was observed (69-121 nmol/min/nmol). However, the ebastine hydroxylation rates for all the constructs were similar (Table 3.1). Interestingly, the NADPH oxidation rates and ebastine hydroxylation rates for the M2SMG and M2D5HG constructs with the majority of the N-terminus intact were nearly identical indicating a similar association with CPR within the reconstituted system. The M2D19HG construct consumed a marginally higher amount of NADPH yet produced the highest amount of product when compared to the other constructs. Strikingly, M2D34G while consuming a relatively high level of NADPH produced the lowest level of product. The coupling efficiencies of this lipid reconstituted system for M2SMG, M2D5HG, M2D19HG and M2D34G were calculated to be 6.1 ± 0.2, 6.1 ± 0.7, 6.2 ± 0.4 and 2.5 ± 0.3 %, respectively. Thus, within this reconstituted system the presence of the full or partially truncated N-terminal domain exhibited similar utilization of NADPH for ebastine hydroxylation. Moreover, it would indicate that despite the different oligomerization states of the different N-terminus constructs, the three constructs' orientation with the exogenous CPR lead to the formation of a productive complex. However, the fully truncated M2D34G construct exhibited a more than a two-fold decrease in efficiency suggesting that the formation of a productive complex between the two proteins is significantly reduced in the absence of the N-terminus. The extent of the analysis is hindered without a

comprehensive understanding of the complexes formed within the POPC reconstituted system. However, sufficient evidence is present to suggest that in absence of a uniform membrane bilayer environment, the N-terminus is important for productive interaction with CPR.

NADPH consumption, product formation and coupling efficiency in a CYP2J2-detergent solubilized system. For detergent solubilized CYP2J2, there was a dramatic increase of NADPH consumption when ebastine was added and like the phospholipid reconstituted system the rates ranged from 44.9 nmol/min/nmol of protein for M2D5HG to 142.5 nmol/min/nmol for the M2D34G mutant. Interestingly, the differences in the NADPH consumption rates in this system followed the order of the N-terminal truncations M2D34G>M2D19HG>M2SMG~M2D5HG.

The functional activity of the constructs was measured in the detergent solubilized system (Table 3.1). We found that the rate of product formation correlated with the rate of NADPH consumption observed. This observation was reinforced upon calculation of the coupling efficiencies for the different constructs. Notably, the coupling efficiencies containing all or part of the N-terminus used NADPH with the same efficiency whereas the fully truncated construct exhibited ~50% reduction.

***NADPH consumption using arachidonic acid as a substrate*.** We also determined that the rate of NADPH oxidation in the presence of excess AA increases marginally (~1.5 fold) above the substrate-free system (data not shown). Overall, the NADPH oxidation rate with AA and ebastine bound to CYP2J2 was slower as compared to other CYPs bound to substrate.(*77*) In CYP3A4, the presence of a spin state changing substrate can significantly affect NADPH oxidation rates, for instance the rate in the absence of the substrate is 25 nmol/min/nmol whereas in the presence of the substrate and a spin state change it can reach 272 nmol/min/nmol. Thus, the modest 1.5-fold increase in NADPH consumption during AA metabolism by CYP2J2 in detergents and Nanodiscs affirms the previous observation that AA does not produce a spin state change. Previously Guengerich and co-workers have shown a strong correlation between the steady-state NADPH oxidation rate and the first electron transfer which can be related to the degree of spin state change (*78*) (*79*).

Comparison of ebastine hydroxylation rate of CYP2J2 isolated from different systems. We compared the ebastine hydroxylation rates of the *E.coli* expressed protein to previous recombinant human CYP2J2 expressed in mammalian, yeast and insect cells. The values obtained had a range of ebastine hydroxylation rates in the different microsomal preparations (*73,74,80*). Previous

studies using mammalian COS-1 and insect baculovirus cells yielded rates (Vmax) of 5.5 and 8.1 nmol/min/nmol, respectively (*73*, *80*). The ebastine hydroxylation rates using yeast microsomes exhibited a relatively high Vmax of 40.1 nmol/min/nmol possibly due to different post-translational modifications in these systems (*74*). In this work, the *E. coli* expressed CYP2J2 constructs in Nanodiscs exhibited similar catalytic rates to what was reported for microsomal preparations of CYP2J2 from insect and mammalian expression systems. Specifically, the turnover numbers of CYP2J2-CPR-Nanodisc systems were the most similar when compared to the aforementioned systems.

Within the Nanodisc system we were able to control the oligomerization state of CYP2J2:CPR and incorporate these proteins in a 1:1 ratio in a defined lipid membrane environment. This model system enabled us to deconstruct the complex interactions of the N-terminally modified CYPs, which revealed in the membrane lipid bilayer of Nanodiscs, the NADPH consumption rates and coupling ratio were quite similar for the different constructs. This suggests that when the different N-terminal constructs of CYP2J2 are incorporated into lipid bilayers they adopt orientations and conformations that enable similar interactions with CPR. Alternatively, in the detergent and phospholipid reconstituted system, the truncation of the N-terminus leads to the increased NADPH oxidation rates and reduced coupling efficiency. It is difficult to delineate the exact factors affecting these rates in detergents and phospholipid reconstituted systems in absence of detailed knowledge of the macromolecular protein complex in these systems.

In Nanodiscs, the dual incorporation of CPR and CYP favors a more productive alignment of the two proteins' redox centers via electrostatic interactions as found in other P450 systems (*81-83*). Additionally, it is possible that the complementary charge interactions of the incorporated CPR with CYP2J2 could be prompting a more productive orientation in membrane, especially for fully N-terminus truncated M2D34G. Our data show strong evidence that the presence of membrane environment is more critical than the presence of N-terminus for efficient electron transfer from NADPH to CYP2J2 orchestrated by CPR. This suggests the adoption of the native-like conformation in lipid bilayers is essential for effective use of reducing equivalents from NADPH.

3.5 CONCLUSIONS

In this work, we significantly enhanced the expression of full length CYP2J2 in *E. coli* with the introduction of silent mutations at the N-terminus of the protein. The expression of full length

CYP2J2 in high yields was essential to elucidate the role of the N-terminus of CYP2J2 in substrate binding, electron transfer and association with its redox partner cytochrome P450 reductase. We demonstrated that with the successful use of hydrophilic motifs and truncations of the N-terminal domain dramatically increases CYP2J2 expression in *E.coli*. All of the constructs expressed exhibited close to 100% P450 content indicating the maintenance of a typical P450 protein fold. Binding assays revealed that the K_d of binding of ebastine to M2D20HG and M2SMG was similar thus showing that the N-terminus does not affect the binding of this substrate to the protein.

We further studied the association of CYP2J2 with lipid bilayers. During purification we observed 40% of the fully truncated M2D34G construct was found in the soluble fraction. However, when the four constructs were incorporated into Nanodiscs, we observed sufficient incorporation and stability over a week at 4ºC and found that the N-terminus is not a key determinant of membrane association in CYP2J2. Therefore we concluded that the association of CYP2J2 with lipid bilayers is mediated by other residues besides the N-terminus.

The NADPH consumption and ebastine hydroxylation functionality of each construct was investigated in a detergent solubilized system, phospholipid reconstituted system and CYP2J2-CPR-Nanodiscs. The coupling efficiencies were calculated to compare enzyme productivity and it was found that the CYP2J2-CPR Nanodisc system was approximately six-fold more efficient than the detergent solubilized system and three-fold more efficient than the phospholipid reconstituted system.

We concluded that the N-terminus does not interfere with effective coupling of NADPH oxidation with ebastine hydroxylation when the protein is in the membrane environment. However in a detergent solubilized system or phospholipid-reconstituted system, an intact N-terminus is required for effective coupling. This suggests that in Nanodiscs, the protein is in a more native-like membrane environment. Additionally, the proteins are monomeric and are effectively interacting with their redox partner CPR. Thus the membrane environment likely facilitates the proper docking of CPR to CYP2J2.

This present study incorporates novel findings with respect to comparing the effects of N-terminal modifications on the properties of CYP2J2 and its ability to interact with its redox partner CPR in the lipid bilayers of Nanodiscs.

3.6 ACKNOWLEDGEMENTS

We thank Ms. Snehita Sri Varma, Dr. Mary Schuler, Dr. Ilia Denisov and Yelena Grinkova at the University of Illinois for helpful discussions. LC/MS/MS analyses were performed at the University Of Illinois - School of Chemical Sciences Mass Spectrometry Laboratory and we thank Dr. Kevin Tucker and Dr. Furong Sun for help with the optimization of the LC/MS/MS method and analysis of the samples. We thank Dr. Ferguson, Dr. Bagchi and Dr. Bunick for allowing us to use their equipment.

3.7 FIGURES AND TABLES

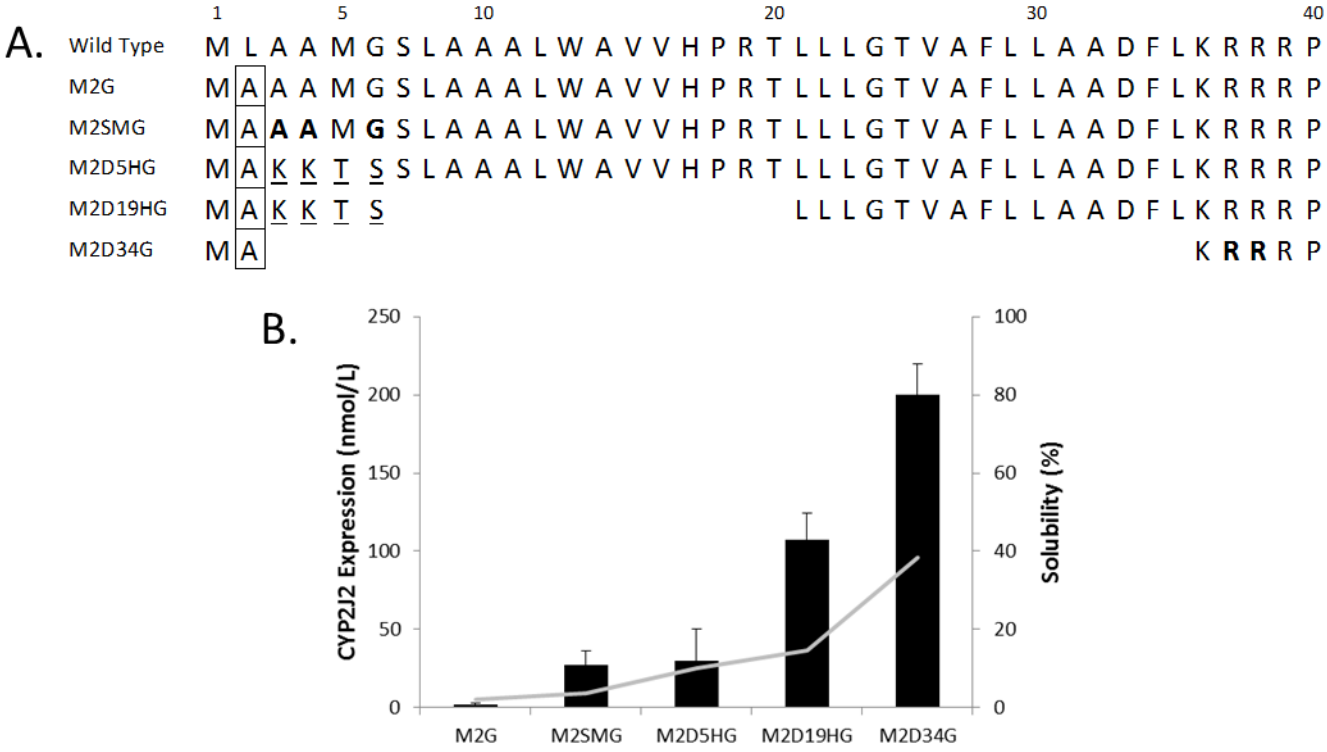

Figure 3.1. Design and Expression of CYP2J2 Mutants. (A) CYP2J2 wild type and design of N-terminal mutant constructs. Boxed residues denote substitution of native Leu with Ala (GCT). Bolded residues represent introduction of AT rich silent mutations. Underlined residues signify introduction of a hydrophillic motif. Gaps represent deletion of N-terminal amino acids. **(B)** CYP2J2 N-terminal mutant expression and solubility in DH5alpha cells. The bar graph denotes expression yields which were highly dependent on N-terminal modifications. The line plot signifies percentage of protein found in the soluble fraction during purification which largely corresponded to N-terminal truncations.

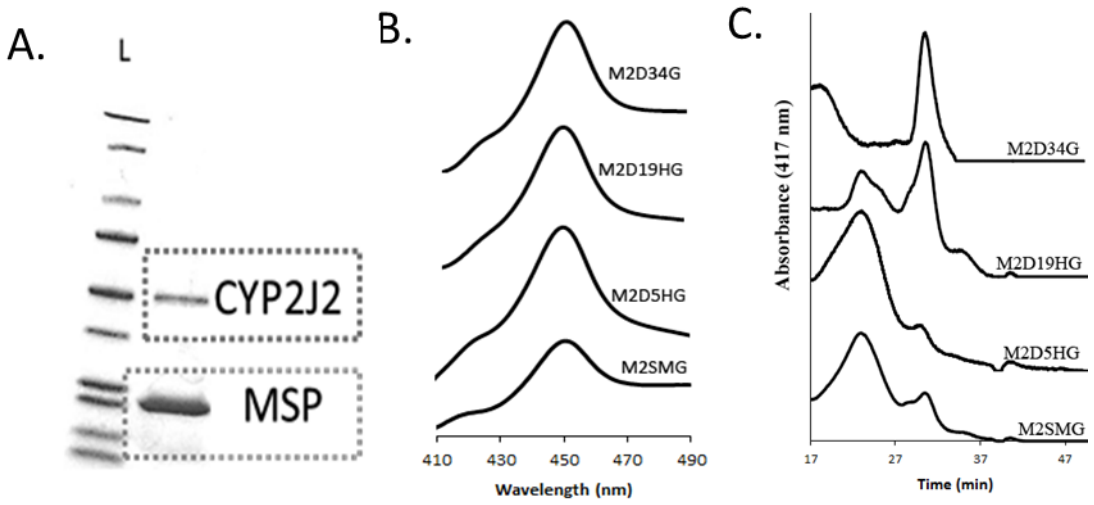

Figure 3.2. Characterization of CYP2J2 constructs. (A) CYP2J2 mutants were incorporated into Nanodiscs and purified using size exclusion chromatography-HPLC. SDS-PAGE was used to verify successful isolation of each respective CYP2J2-ND. The first column contains a protein ladder standard showing that the molecular weight of M2D19HG is close to the ~50-60 kDa standard and the scaffolding protein MSP1T2 has molecular weight close to ~24 kDa. The exact molecular weights were confirmed using ESI-MS. **(B)** CO binding spectra were used to characterize each construct and gauge the protein folding after expression and purification. Each construct exhibited ~100% P450 content which is indicative of a well-folded and functional CYP. **(C)** SEC-HPLC was applied to characterize CYP2J2 mutant oligomerization states in phosphate buffer (0.1 M). The CYP2J2 elution profile was produced by monitoring the heme absorbance at 417 nm. Using water soluble protein standards, we observed that the constructs monomeric state corresponded closely with N-terminal truncations and to followed M2SMG>M2D5HG>M2D19HG>M2D34G.

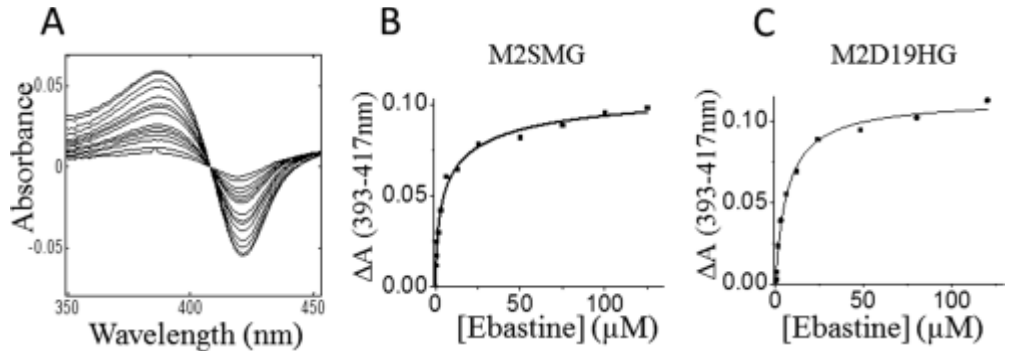

Figure 3.3. Ebastine-binding spectra were fitted to a single binding isotherm. (A) Difference spectra of D19HGND ebastine titration. Ebastine was added incrementally from 0 to 120 mM. **(B, C)** The change of absorbance (DA) from 393 to 417 nm was calculated for each titration and plotted against the corresponding ebastine concentration (mM). Data were fitted with Origin Lab to the single binding isotherm. A single binding isotherm was applied to calculate the Kd of M2SMG and M2D19HG, which were determined to be 7.3 ± 1.9 and 6.8 ± 0.7 mM, respectively

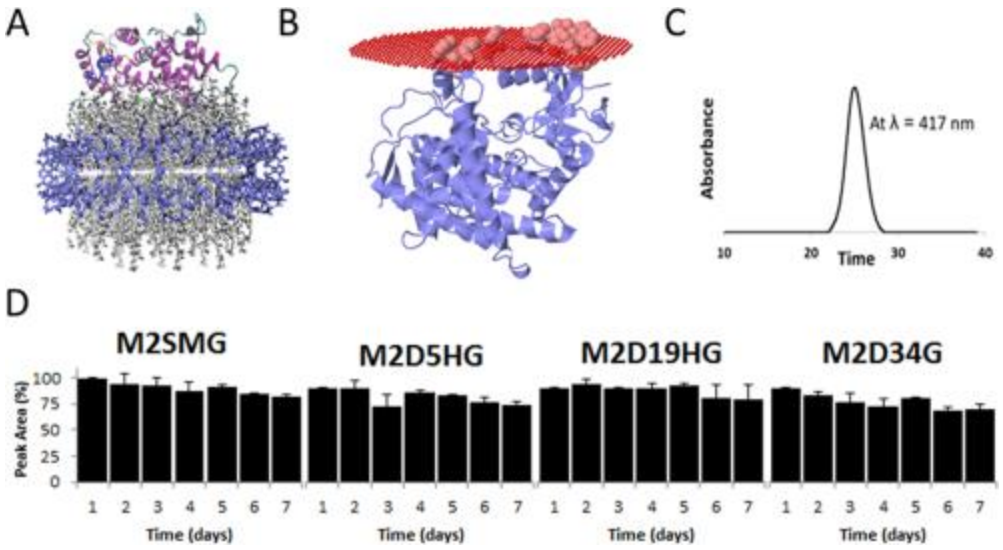

Figure 3.4. Incorporation of CYP2J2 constructs in Nanodiscs and stability assay. (A) Visual molecular dynamics (VMD) was used to construct a representative model of CYP2J2 incorporated into Nanodiscs (CYP2J2 model was obtained using Phyre). In the model, blue represents the membrane scaffolding protein (MSP1D1), the gray are the phospholipids, and the protein ribbon model is the CYP2J2 enzyme. **(B)** Membrane association of M2D34HG model. Highlighted residues in the A helical region (Trp48, Arg49, Leu50, Pro51, Phe52, Leu53, Phe57, Leu58, and Phe61), Lys122 in B′ helix and in the FG loop region (Trp235, Phe239, and Leu240) are predicted by OMP software to be associated with the lipid membrane. Predicted Gibbs free energy for this interaction is 13.8 kcal mol^{-1}. **(C)** CYP2J2 constructs were incorporated into Nanodiscs and monitored at 417 nm SEC-HPLC. The single peak corresponds to homogeneous CYP2J2-Nanodiscs. **(D)** The relative stability of each CYP2J2 construct incorporated into Nanodiscs was monitored using SEC-HPLC over a 7-day period at 4°C. The percent area of the 417-nm peak corresponding to heme absorption was monitored at the established CYP2J2-Nanodisc elution time (∼26 min). We observed a similar relative stability for each of the constructs with an approximate 10–20% degradation over the time course.

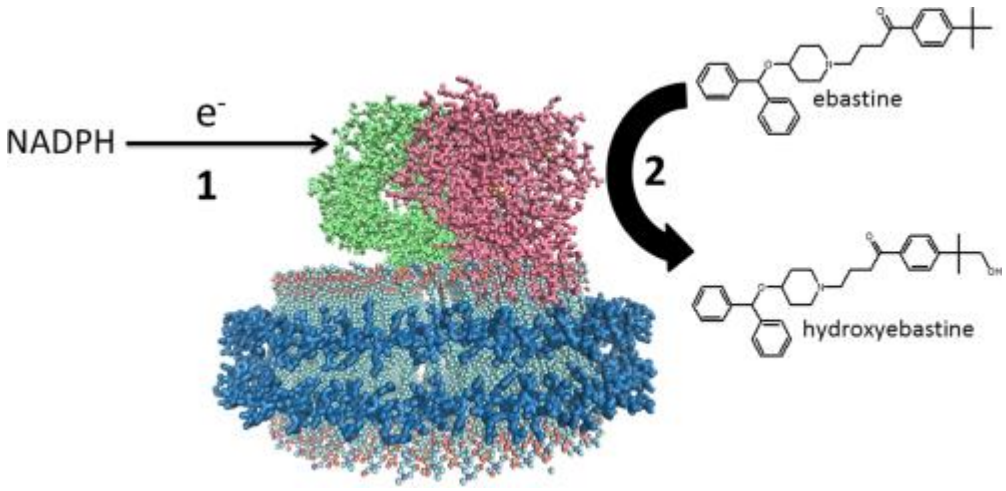

Figure 3.5. Schematic of NADPH oxidation and ebastine hydroxylation by a CPR-CYP2J2 Nanodisc complex. Electrons are shuttled from NADPH to CYP2J2 via cytochrome P450 reductase redox centers (step 1). These electrons subsequently drive CYP2J2 P450 catalysis of ebastine to hydroxyebastine (step 2). Coupling efficiency is measured as the ratio of ebastine hydroxylation (step 2) over NADPH oxidation (step 1).

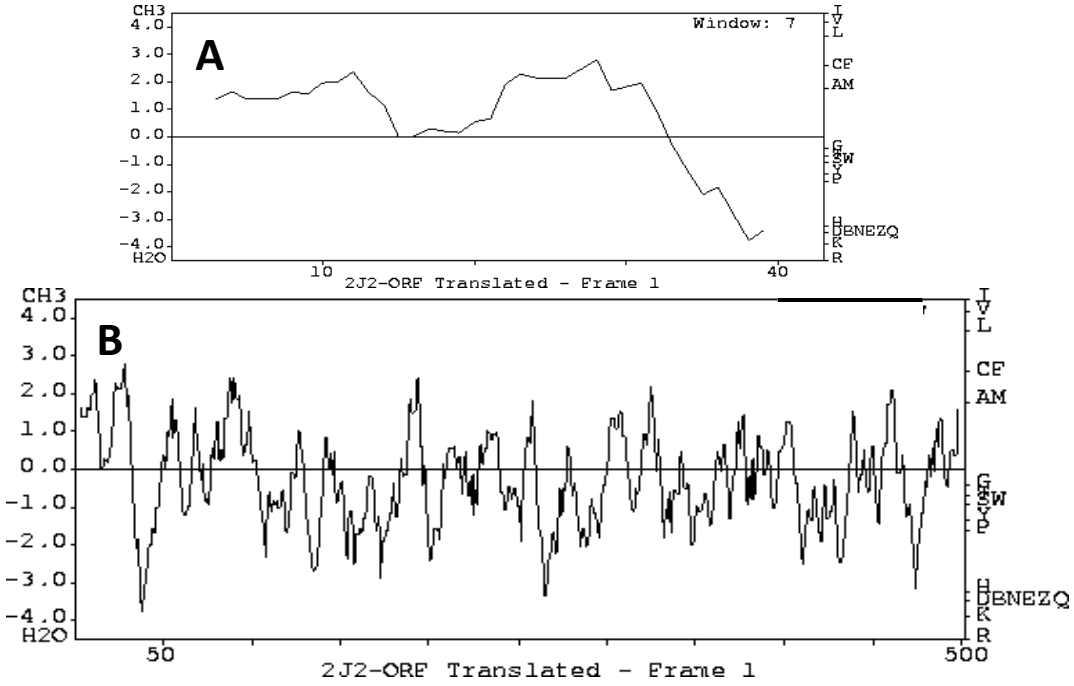

Figure 3.6. Hydropathy plots of CYP2J2. (A) CYP2J2 N-terminus (1-43 amino acids) and (B) Full-length CYP2J2 hydrophobicity.

CYP2J2 Constructs	Substrate-Free NADPH Rate (nmol/min/nmol)	Ebastine NADPH Rate (nmol/min/nmol)	Ebastine Hydroxylation Rate (nmol/min/nmol)	Coupling Efficiency (%)
CYP2J2-CPR Nanodiscs				
M2SMG	9.2 ± 1.5	20.3 ± 0.9	3.8 ± 0.7	17.0 ± 0.8
M2D5HG	7.8 ± 0.8	21.3 ± 0.4	3.7 ± 0.6	17.1 ± 0.7
M2D19HG	12.9 ± 0.7	27.1 ± 1.6	4.5 ± 0.4	16.5 ± 0.9
M2D34G	12.2 ± 0.3	21.2 ± 1.3	2.9 ± 0.1	13.6 ± 1.3
CYP2J2-POPC Reconstituted				
M2SMG	34.0 ± 1.7	69 ± 2.0	4.3 ± 0.2	6.1 ± 0.2
M2D5HG	31.8 ± 2.8	72 ± 6.4	4.4 ± 0.3	6.1 ± 0.7
M2D19HG	38.9 ± 3.3	88 ± 6.3	5.4 ± 0.1	6.2 ± 0.4
M2D34G	65.1 ± 1.3	121 ± 8.5	3.1 ± 0.7	2.5 ± 0.3
CYP2J2-Detergent				
M2SMG	21.5 ± 1.7	50.6 ± 3.7	1.6 ± 0.2	3.2 ± 0.1
M2D5HG	23.2 ± 1.0	44.9 ± 6.1	1.4 ± 0.3	3.1 ± 0.2
M2D19HG	27.3 ± 1.5	72.2 ± 7.3	2.6 ± 0.9	3.5 ± 0.9
M2D34G	28.0 ± 1.4	142.5 ± 18.6	2.4 ± 0.5	1.7 ± 0.1

Table 3.1. NADPH oxidation and ebastine hydroxylation rates of CYP2J2 constructs in detergent solubilized and membrane bound systems. Each of the four constructs were incorporated into Nanodiscs, reconstituted with lipids or solubilized in 0.1% CHAPS and used to measure NADPH consumption and hydroxyebastine product formation. The coupling efficiency was calculated by taking the ratio of ebastine hydroxylation measured using LC-MS/MS versus the NADPH Oxidation monitored via UV-Vis spectroscopy at 340 nm.

Construct	Description	Forward primer 5’ to 3’
M2G	ΔN1 and insertion of Ala	gcaattaatggctgcggcgatgggctctctg
M2SMG	ΔN1, insertion of Ala and silent mutations	gcgattaatggctgcagcaatgggatctctggcggctgccc
M2D5HG	ΔN5 and insertion of AKKTS	gcgattaatggctaaaaaaacttcttctctggcggctgccc
M2D19HG	ΔN19 and insertion of AKKTSS	gcgattaatggctaaaaaaacgtcatcactcctactgggcactgtcgc
M2D34G	ΔN34, insertion of Ala and silent mutations	gcaattaatggctaaacgtcgtcgccaaagaactacccg

Table 3.2 List of all the primers used to perform PCR to generate the required modifications of the 2J2 gene. The reverse primer was common for all the constructs.

3.8 REFERENCES

1. Samuelsson, B. (2012) *J Biol Chem 287*, 10070-80.
2. Hannemann, F., Bichet, A., Ewen, K. M., and Bernhardt, R. (2007) *Biochim Biophys Acta 1770*, 330-44.
3. Bernhardt, R. (2006) *J Biotechnol 124*, 128-45.
4. Delozier TC, Kissling GE, Coulter SJ, Dai D, Foley JF, Bradbury JA, Murphy E, Steenbergen C, Zeldin DC, and Goldstein, J. (2007) *Drug Metab Dispos. 35*, 682-8.
5. Westphal, C., Konkel, A., and Schunck, W. H. (2011) *Prostaglandins Other Lipid Mediat. 96*, 99-108.
6. Wang, H., Jiang, Y., Liu, Y., Lin, C., Cheng, G., Chen, X., Hao, B., Tan, W., Lin, D., and He, F. (2006) *Clin Chim Acta 365*, 125-8.
7. Xiao, B., Li, X., Yan, J., Yu, X., Yang, G., Xiao, X., Voltz, J. W., Zeldin, D. C., and Wang, D. W. (2010) *J Pharmacol Exp Ther 334*, 784-94.
8. Imig, J. D. (2012) *Physiol Rev 92*, 101-30.
9. Imig, J. D., and Hammock, B. D. (2009) *Nat Rev Drug Discov 8*, 794-805.
10. Zhang, Y., El-Sikhry, H., Chaudhary, K. R., Batchu, S. N., Shayeganpour, A., Jukar, T. O., Bradbury, J. A., Graves, J. P., DeGraff, L. M., Myers, P., Rouse, D. C., Foley, J., Nyska, A., Zeldin, D. C., and Seubert, J. M. (2009) *Am J Physiol Heart Circ Physiol 297*, H37-46.
11. Herse, F., Lamarca, B., Hubel, C. A., Kaartokallio, T., Lokki, A. I., Ekholm, E., Laivuori, H., Gauster, M., Huppertz, B., Sugulle, M., Ryan, M. J., Novotny, S., Brewer, J., Park, J. K., Kacik, M., Hoyer, J., Verlohren, S., Wallukat, G., Rothe, M., Luft, F. C., Muller, D. N., Schunck, W. H., Staff, A. C., and Dechend, R. (2012) *Circulation 126*, 2990-9.
12. Panigrahy, D., Edin, M. L., Lee, C. R., Huang, S., Bielenberg, D. R., Butterfield, C. E., Barnes, C. M., Mammoto, A., Mammoto, T., Luria, A., Benny, O., Chaponis, D. M., Dudley, A. C., Greene, E. R., Vergilio, J. A., Pietramaggiori, G., Scherer-Pietramaggiori, S. S., Short, S. M., Seth, M., Lih, F. B., Tomer, K. B., Yang, J., Schwendener, R. A., Hammock, B. D., Falck, J. R., Manthati, V. L., Ingber, D. E., Kaipainen, A., D'Amore, P. A., Kieran, M. W., and Zeldin, D. C. (2012) *J Clin Invest 122*, 178-91.
13. Panigrahy, D., Greene, E. R., Pozzi, A., Wang, D. W., and Zeldin, D. C. (2011) *Cancer Metastasis Rev 30*, 525-40.
14. Panigrahy, D., Kaipainen, A., Greene, E. R., and Huang, S. (2010) *Cancer Metastasis Rev 29*, 723-35.
15. Jiang, J. G., Chen, C. L., Card, J. W., Yang, S., Chen, J. X., Fu, X. N., Ning, Y. G., Xiao, X., Zeldin, D. C., and Wang, D. W. (2005) *Cancer Res 65*, 4707-15.
16. Jiang, J. G., Ning, Y. G., Chen, C., Ma, D., Liu, Z. J., Yang, S., Zhou, J., Xiao, X., Zhang, X. A., Edin, M. L., Card, J. W., Wang, J., Zeldin, D. C., and Wang, D. W. (2007) *Cancer Res 67*, 6665-74.
17. Lee, C. A., Jones, J. P., 3rd, Katayama, J., Kaspera, R., Jiang, Y., Freiwald, S., Smith, E., Walker, G. S., and Totah, R. A. (2012) *Drug Metab Dispos 40*, 943-51.
18. Chen, C., Li, G., Liao, W., Wu, J., Liu, L., Ma, D., Zhou, J., Elbekai, R. H., Edin, M. L., Zeldin, D. C., and Wang, D. W. (2009) *J Pharmacol Exp Ther 329*, 908-18.
19. Lee CA, Jones JP 3rd, Katayama J, Kaspera R, Jiang Y, Freiwald S, Smith E, Walker GS, and Totah, R. (2012) *Drug Metab Dispos. 40*, 943-51.
20. Matsumoto S, Hirama T, Matsubara T, Nagata K, and Yamazoe, Y. (2002) *Drug Metab Dispos. 30*, 1240-5.

21. Skorupa, E., and Kemper, B. (1998) *Methods Mol Biol 107*, 251-66.
22. Cosme, J., and Johnson, E. F. (2002) *Methods Enzymol 357*, 116-20.
23. Williams, P. A., Cosme, J., Sridhar, V., Johnson, E. F., and McRee, D. E. (2000) *J Inorg Biochem 81*, 183-90.
24. Hsu, P. Y., and Wang, L. H. (2003) *Archives of Biochemistry and Biophysics 416*, 38-46.
25. Cosme, J., and Johnson, E. F. (2000) *J Biol Chem 275*, 2545-53.
26. von Wachenfeldt, C., Richardson, T. H., Cosme, J., and Johnson, E. F. (1997) *Archives of Biochemistry and Biophysics 339*, 107-14.
27. Kim, H. J., Lee, S. B., Guengerich, F. P., Park, Y. I., and Dong, M. S. (2007) *Xenobiotica 37*, 356-65.
28. Ahn, T., Guengerich, F. P., and Yun, C. H. (1998) *Biochemistry 37*, 12860-6.
29. Davydov, D. R. (2011) *Expert Opin Drug Metab Toxicol 7*, 543-58.
30. Praporski, S., Ng, S. M., Nguyen, A. D., Corbin, C. J., Mechler, A., Zheng, J., Conley, A. J., and Martin, L. L. (2009) *J Biol Chem 284*, 33224-32.
31. Pernecky, S. J., Larson, J. R., Philpot, R. M., and Coon, M. J. (1993) *Proc Natl Acad Sci U S A 90*, 2651-5.
32. Berka K, Hendrychová T, Anzenbacher P, and Otyepka, M. (2011) *J Phys Chem A. 115*, 11248-55.
33. Conner KP, W. C., Atkins WM. (2011) *Arch Biochem Biophys. 50*, 56-65.
34. Denisov, I. G., and Sligar, S. G. (2011) *Biochim Biophys Acta 1814*, 223-9.
35. Bayburt, T. H., and Sligar, S. G. (2010) *FEBS Lett 584*, 1721-7.
36. Ritchie, T. K., Grinkova, Y. V., Bayburt, T. H., Denisov, I. G., Zolnerciks, J. K., Atkins, W. M., and Sligar, S. G. (2009) *Methods Enzymol 464*, 211-31.
37. Leitz, A. J., Bayburt, T. H., Barnakov, A. N., Springer, B. A., and Sligar, S. G. (2006) *Biotechniques 40*, 601-612.
38. Boldog, T., Grimme, S., Li, M., Sligar, S. G., and Hazelbauer, G. L. (2006) *Proc Natl Acad Sci U S A 103*, 11509-14.
39. Nath, A., Atkins, W. M., and Sligar, S. G. (2007) *Biochemistry 46*, 2059-69.
40. Das, A., Grinkova, Y. V., and Sligar, S. G. (2007) *J Am Chem Soc 129*, 13778-9.
41. Das, A., and Sligar, S. G. (2009) *Biochemistry 48*, 12104-12.
42. Tark, S. H., Das, A., Sligar, S., and Dravid, V. P. (2010) *Nanotechnology 21*, 435502.
43. Marty, M. T., Das, A., and Sligar, S. G. (2012) *Anal Bioanal Chem 402*, 721-9.
44. Das, A., Zhao, J., Schatz, G. C., Sligar, S. G., and Van Duyne, R. P. (2009) *Anal Chem 81*, 3754-9.
45. Zhao, J., Das, A., Zhang, X., Schatz, G. C., Sligar, S. G., and Van Duyne, R. P. (2006) *J Am Chem Soc 128*, 11004-5.
46. Kim, D. H., Kim, K. H., Isin, E. M., Guengerich, F. P., Chae, H. Z., Ahn, T., and Yun, C. H. (2008) *Protein Expr Purif 57*, 188-200.
47. Schauder, B., and McCarthy, J. E. (1989) *Gene 78*, 59-72.
48. Stormo, G. D., Schneider, T. D., and Gold, L. M. (1982) *Nucleic Acids Res 10*, 2971-96.
49. Richardson, T. H., Jung, F., Griffin, K. J., Wester, M., Raucy, J. L., Kemper, B., Bornheim, L. M., Hassett, C., Omiecinski, C. J., and Johnson, E. F. (1995) *Archives of Biochemistry and Biophysics 323*, 87-96.
50. Poulos, T. L. (1996) *Methods Enzymol 272*, 358-68.
51. Poulos, T. L. (1995) *Curr Opin Struct Biol 5*, 767-74.

52. Aiba, I., Yamasaki, T., Shinki, T., Izumi, S., Yamamoto, K., Yamada, S., Terato, H., Ide, H., and Ohyama, Y. (2006) *Steroids 71*, 849-56.
53. Kagawa N, and Cao, Q. (2001) *Arch Biochem Biophys. 393*, 290-6.
54. Joseph, R. E., and Andreotti, A. H. (2008) *Protein Expr Purif 60*, 194-7.
55. Omura, T., and Sato, R. (1964) *J Biol Chem 239*, 2379-85.
56. Denisov, I. G., Baas, B. J., Grinkova, Y. V., and Sligar, S. G. (2007) *J Biol Chem 282*, 7066-76.
57. Causey, K. M., Eyer, C. S., and Backes, W. L. (1990) *Mol Pharmacol 38*, 134-42.
58. Kapust RB, Tözsér J, Fox JD, Anderson DE, Cherry S, Copeland TD, and Waugh, D. (2001) *Protein Eng. 14*, 993-1000.
59. Kang W, Liu KH, Ryu JY, and Shin, J. (2004) *J Chromatogr B Analyt Technol Biomed Life Sci. 813*, 75-80.
60. Kelley LA, and Sternberg, M. (2009) *Nat Protoc. 4*, 363-71.
61. Lomize MA, Lomize AL, Pogozheva ID, and Mosberg, H. (2006) *Bioinformatics. 22*, 623-5.
62. Looman, A. C., Bodlaender, J., Comstock, L. J., Eaton, D., Jhurani, P., Deboer, H. A., and Vanknippenberg, P. H. (1987) *Embo Journal 6*, 2489-2492.
63. Barnes, H. J., Arlotto, M. P., and Waterman, M. R. (1991) *Proc Natl Acad Sci U S A 88*, 5597-601.
64. Yamasaki, T., Izumi, S., Ide, H., and Ohyama, Y. (2004) *J Biol Chem 279*, 22848-56.
65. DeVore NM, and Scott, E. (2012) *Nature 482*, 116-9.
66. Fisher CW, Caudle DL, Martin-Wixtrom C, Quattrochi LC, Tukey RH, Waterman MR, and Estabrook, R. (1992) *FASEB J. 6*, 759-64.
67. Messina, A., Nencioni, S., Gervasi, P. G., Gotlinger, K. H., Schwartzman, M. L., and Longo, V. (2010) *Xenobiotica 40*, 109-18.
68. Xu Z, and Sigler, P. (1998) *J Struct Biol. 124*, 129-41.
69. Sligar, S. G. (1976) *Biochemistry 15*, 5399-406.
70. Wu, S., Chen, W., Murphy, E., Gabel, S., Tomer, K. B., Foley, J., Steenbergen, C., Falck, J. R., Moomaw, C. R., and Zeldin, D. C. (1997) *J Biol Chem 272*, 12551-9.
71. Schoch, G. A., Yano, J. K., Sansen, S., Dansette, P. M., Stout, C. D., and Johnson, E. F. (2008) *J Biol Chem 283*, 17227-37.
72. Schoch, G. A., Yano, J. K., Wester, M. R., Griffin, K. J., Stout, C. D., and Johnson, E. F. (2004) *J Biol Chem 279*, 9497-503.
73. Matsumoto, S., Hirama, T., Matsubara, T., Nagata, K., and Yamazoe, Y. (2002) *Drug Metab Dispos 30*, 1240-5.
74. Hashizume, T., Imaoka, S., Mise, M., Terauchi, Y., Fujii, T., Miyazaki, H., Kamataki, T., and Funae, Y. (2002) *J Pharmacol Exp Ther 300*, 298-304.
75. Liu KH, Kim MG, Lee DJ, Yoon YJ, Kim MJ, Shon JH, Choi CS, Choi YK, Desta Z, and Shin, J. (2006) *Drug Metab Dispos. 34*, 1793-7.
76. Denisov, I. G., Makris, T. M., Sligar, S. G., and Schlichting, I. (2005) *Chem Rev 105*, 2253-77.
77. Sulistyaningdyah WT, Ogawa J, Li QS, Maeda C, Yano Y, Schmid RD, and Shimizu, S. (2005) *Appl Microbiol Biotechnol. 67*, 556-62.
78. Isin, E. M., and Guengerich, F. P. (2008) *Anal Bioanal Chem 392*, 1019-30.
79. Fisher, M. T., and Sligar, S. G. (1985) *Journal of the American Chemical Society 107*, 5018-5019.

80. Liu, K. H., Kim, M. G., Lee, D. J., Yoon, Y. J., Kim, M. J., Shon, J. H., Choi, C. S., Choi, Y. K., Desta, Z., and Shin, J. G. (2006) *Drug Metab Dispos 34*, 1793-7.
81. Bridges, A., Gruenke, L., Chang, Y. T., Vakser, I. A., Loew, G., and Waskell, L. (1998) *J Biol Chem 273*, 17036-49.
82. Shen, S., and Strobel, H. W. (1993) *Archives of Biochemistry and Biophysics 304*, 257-65.
83. Shimizu, T., Tateishi, T., Hatano, M., and Fujii-Kuriyama, Y. (1991) *J Biol Chem 266*, 3372-5.

CHAPTER IV: INCORPORATION OF CHARGED RESIDUES IN THE CYP2J2 F-G LOOP DISRUPTS CYP2J2-LIPID BILAYER INTERACTION

4.1 ABSTRACT

CYP2J2 epoxygenase is an extrahepatic, membrane bound cytochrome P450 (CYP) that is primarily found in the heart and mediates endogenous fatty acid metabolism. CYP2J2 interacts with membranes through an N-terminal anchor and various non-contiguous hydrophobic residues. The molecular details of the motifs that mediate membrane interactions are complex and not fully understood. To gain better insights of these complex protein-lipid interactions, we employed molecular dynamics (MD) simulations using a highly mobile membrane mimetic (HMMM) model that enabled multiple independent spontaneous membrane binding events to be captured. Simulations revealed that CYP2J2 engages with the membrane at the F-G loop through hydrophobic residues Trp-235, Ille-236, and Phe-239. To explore the role of these residues, three F-G loop mutants were modeled from the truncated CYP2J2 construct (Δ34) which included Δ34-I236D, Δ34-F239H and Δ34-I236D/F239H. Using the HMMM coordinates of CYP2J2 the simulations were extended to a full POPC membrane which showed a significant decrease in the depth of insertion for each of the F-G loop mutants. The CYP2J2 F-G loop mutants were expressed in *E. coli* and were shown to be localized to the cytosolic fraction at a greater percentage relative to construct Δ34. Notably, the functional data demonstrated that the double mutant, Δ34-I236D/F239H, maintained native-like enzymatic activity. The membrane insertion characteristics were examined by monitoring CYP2J2 Trp-quenching fluorescence spectroscopy upon binding pyrene phospholipids containing nanodiscs. Relative to the Δ34 construct, the F-G loop mutants exhibited lower Trp quenching and membrane insertion. Taken together, the results suggest that the mutants exhibit a different membrane topology in agreement with the MD simulations and provide important evidence towards the involvement of key residues in the F-G loop of CYP2J2.

[2]Reprinted, with permission, from McDougle DR[§], Baylon JL[§], Meling DD, Kambalyal A, Grinkova YV, Hammernik J, Tajkhorshid E, Das A*. Incorporation of Charged Residues in the CYP2J2 F-G Loop Disrupts CYP2J2-Lipid Bilayer Interaction. BBA Biomembranes. 2015 Oct;1848(10):2460-70. PMID: 26232558

4.2 INTRODUCTION

The cytochrome P450 (CYP) superfamily is a class of heme-containing enzymes that are widespread throughout all kingdoms of life (*1*). In humans, CYPs mediate the biotransformation of both xenobiotics and endogenous substrates for homeostasis (*2*). Eukaryotic CYPs interact with membrane bilayers through an N-terminal anchor as well as various non-contiguous hydrophobic residues that constitute the monofacial membrane-binding domain (*3, 4*).

The CYP interaction with the membrane bilayer is a complex phenomenon that is an active area of both experimental and computational research. While seminal studies correctly identified the general nature of the protein-membrane binding and topology (*5*), more recent examples have elucidated the interactions at the molecular and atomistic levels (*6-8*). Notably, P450 interactions with membranes have been shown to regulate ligand binding mechanisms (*9*), membrane depth of insertion (*10*), redox potentials (*11*), enzyme stability (*12*), structure and orientation (*6*). Additionally, advanced computational approaches have revealed the dynamic nature of CYPs and how their hydrophobic motifs interact with the membrane bilayer (*6, 8*). Both experimental and computational approaches have revealed that CYPs are inserted within the membrane, with a partially imbedded active site and deeply immersed N-terminus and F-G loop (*13, 14*).

CYP2J2 is an extrahepatic human CYP that catalyzes the epoxidation of both omega-3 and omega-6 polyunsaturated fatty acids into a number of biologically active metabolites (*15*). Importantly, CYP2J2 is highly expressed in the myocardium and surrounding aortic epithelium where it has been shown to be a key regulator of cardiovascular homeostasis (*16*). The metabolism of arachidonic acid, an omega-6 polyunsaturated fatty acid, by CYP2J2 produces 8 unique regio- and stereoisomers known as epoxyeicostrienoic acids (EETs) that are collectively characterized as anti-inflammatory and vasodilatory lipid mediators (*17*).

CYP2J2 is anchored within the endoplasmic reticulum (*2*). The presence of the hydrophobic membrane binding domains of CYP2J2 complicates its use in many biochemical assays due to its inherent tendency to aggregate outside of the membrane environment. The disruption of the protein-membrane interactions affords solubility and enables structural elucidation through methods such as nuclear magnetic resonance (NMR) and high resolution x-ray crystallography. Currently, there are no reports of the successful solubilization and subsequent crystallization of any member of the CYP2J subfamily. However, this was achieved for other CYP2 family members including CYP2C5, CYP2A6, CYP2C8, CYP2C9 and CYP2D6 (*4, 18-21*). Specifically, soluble

isozymes were engineered through a combination of deletions and hydrophilic substitutions of targeted membrane binding regions that resulted in increased expression yields and protein homogeneity. For example, the solubility of CYP2C5 was increased by substituting the N-terminus (Δ28) with MAKKTSSKG, adding a four-residue histidine tag at the C-terminus and incorporating five substitutions at the membrane binding interface with the mutations N202H, R206E, I207L, S209G, and S210T (*4*). Similarly, CYP2C9 N-terminal (Δ29) residues were replaced by MAKKTSSKGR, a four-histidine carboxy-tag and the seven amino acid mutations (K206E, I215V, C216Y, S220P, P221A, I222L and I223L) in the F-G loop (*18*). Soon after, CYP2D6 was successfully crystallized by truncating the N-terminus, adding a four-histidine tag at the C-terminus and mutating the F-G loop Leu-230 and Lue-231 with a combination of hydrophilic residues (Asn, Lys, His, Gln, Arg, and Ser) (*21*). Importantly, these changes afforded some of the first structural insights of mammalian P450s through high resolution x-ray crystallography. However, membrane dissociation while maintaining the native functional characteristics is an essential, yet difficult step, in the field of CYP protein engineering.

The truncation of the membrane-spanning CYP N-terminus is the most widely used strategy to disrupt protein-membrane interactions (*19-23*). Indeed, we previously demonstrated that the complete truncation of the CYP2J2 N-terminus results in a construct with significantly increased solubility. Importantly, this truncated construct (Δ34-CYP2J2) exhibited similar substrate turnover rates as the full length CYP2J2 construct in model membranes (*24*). Notably, Δ34 maintained its membrane insertion despite the N-terminal truncation (*24*). Accumulating evidence suggests that the F-G loop of CYPs (Figure 4.1A and 4.3A) is an essential mediator of membrane binding (*25*). Additionally, the F-G loop is positioned at the mouth of the substrate access tunnels and is thought to control the rate of substrate access to the buried active site (*26*). Unlike the N-terminal motif, the non-conservative mutations within the F-G loop region often results in significantly altered enzymatic activity (*27*). Thus far, strategies have typically included random mutagenesis and substitution of alternative CYP chimeras which are typically an exercise of trial-and-error (*28*).

In this study, we used molecular dynamics (MD) simulations in conjunction with experimental studies to evaluate the role of the F-G loop of CYP2J2 in membrane binding and insertion. Previously, MD simulations have been used to study protein-membrane interactions of membrane-bound CYPs (*6-8, 13, 29, 30*). Herein, we first employ a highly mobile membrane-mimetic (HMMM) model (*31*) to capture spontaneous binding of CYP2J2 to the membrane. The HMMM

model employs short-tailed lipids while an organic solvent replaces the hydrophobic core of the membrane, resulting in increased lipid mobility. Due to the enhanced lipid mobility, the model accelerates the association of proteins with the lipid bilayer, and has been successfully employed to capture membrane binding of a variety of peripheral and membrane proteins including the GLA domain (*31*), cytochrome P450 3A4 (*6*), talin (*32*), α-synuclein (*33*), synaptotagmin (*34*), and synaptobrevin (*35*). This approach enabled us to capture atomic level interactions between CYP2J2 and the membrane. Importantly, these interactions were preserved when the short-tailed lipids were extended to a full POPC membrane. Secondly, after a membrane-bound model of CYP2J2 was obtained, we studied the effect of F-G loop mutations on membrane-binding and insertion depth, by taking advantage of the enhanced lipid dynamics of the HMMM model.

To experimentally support the MD findings, hydrophilic residues were engineered in the CYP2J2 F-G loop. Subsequent studies revealed the effects of the mutations on enzyme functionality, subcellular distribution and membrane binding characteristics. The details of the relative depth of insertion were explored by measuring the mutants' intrinsic tryptophan fluorescence and energy transfer to pyrene phospholipids incorporated in lipid bilayers.

Determining the degree of the Trp-pyrene fluorescence resonance energy transfer (FRET) is a widely used method to probe the interaction of both peripheral and membrane proteins with membrane bilayers. Previously, liposomal systems were used to measure the Trp insertion of membrane proteins such as CYP3A4 (*10*) and CYP1A2 (*36*) as well as peripherally binding proteins such as cytochrome C (*37*) and 14-3-3γ (*38*). The use of nanodiscs in this application offers several advantages over traditional liposomal systems. Specifically, nanodiscs are nanoscale discoidal lipid bilayers that exhibit significantly enhanced stability and homogeneity relative to liposomal systems. Additionally, nanodiscs are more easily concentrated without aggregation and lack the typical scattering effects observed with liposomal systems (*14, 24, 39*).

Overall this work provides novel insights on the role of key residues in the CYP2J2 F-G loop and their effects on membrane binding and functional metabolism. The use of MD simulations provides high resolution interactions between the membrane and CYP2J2 F-G loop. Experimentally, the introduction of hydrophilic residues in the F-G loop provides essential functional data as well as an assay for membrane depth of insertion. Understanding the nuances of these interactions will enable new applications with other membrane bound CYPs.

4.3 MATERIALS AND METHODS

Materials. Ampicillin, arabinose, chloroamphenicol and IPTG were from Gold Biotechnology. NADPH and NADP were obtained from P212121.com. Protein standards—thyroglobulin, ferritin, bovine serum albumin, and cytochrome *c*, were purchased from Sigma. Phospholipids 1-palmitoyl-2-oleoyl-sn-glycero-3-phosphocholine (POPC) and 1-hexadecanoyl-2-(9Z-octadecenoyl)-sn-glycero-3-phospho-L serine (POPS) were purchased from Avanti Polar Lipids. The phospholipid 1-hexadecanoyl-2-(1-pyrenedecanoyl)-*sn*-glycero-3-phosphocholine (PYR-PC) was obtained from Life Technologies. Amberlite XAD 2 was procured from Supelco. Nanosep MF (0.2 µ*M*) and Amicon Ultra (10,000 MWCO) centrifugal filters were bought from Millipore. AA and ebastine were purchased from Cayman Chemical. All other materials and reagents used were purchased from Sigma-Aldrich and Fisher Scientific.

Molecular Dynamical Simulations: Preparation of HMMM membrane. The HMMM membrane was constructed starting from a solvated POPC membrane by shortening the lipid tails to only 5 carbons (*31*), while the remaining carbon atoms were converted to 1,1-dichloroethane (DCLE). This resulted in an HMMM membrane patch with two leaflets of short-tailed PC lipids at the interface of water and DCLE, as described in detail elsewhere (*31*). The solvated HMMM membrane contained 137 short-tailed PC lipids in each leaflet and 1,268 DCLE molecules, yielding a system with ~41,000 atoms. The solvated membrane mimetic system was energy minimized for 2,000 steps and simulated for 1 ns using an NP_nAT ensemble with constant area, and with a target normal pressure and temperature of 1.0 atm and 310 K, respectively. A constant area of 10, 281 $Å^2$ (101.4 × 101.4 $Å^2$) was employed, yielding an area of 75 $Å^2$ per lipid (A_L), about 8% higher than the experimental A_L for POPC membranes (*40*). Based on our experience with other peripheral proteins, a mild increase in A_L (5-8%) can significantly accelerate membrane binding (*31, 33*). The resulting membrane was employed in all subsequent binding simulations of wild-type CYP2J2 and its mutants. To mimic the atomic distributions of a full lipid bilayer in the HMMM simulations more closely, a harmonic constraint along the *z*-axis (membrane normal) with a force constant k = 0.05 kcal·mol^{-1}·Å^{-2} was applied to the carbonyl carbon atoms of the short-tailed PC lipids .

CYP2J2 model and initial configurations. A homology model of the catalytic domain of CYP2J2, generously provided by Dr. D. Mansuy (Université René Descartes, Paris France), was employed as the starting structure of CYP2J2 for this study. The homology model was derived

using the available crystal structures of CYP2A6 (PDB: 1Z11), CYP2B4 (PDB: 2BDM), CYP2C5 (PDB: 1NR6), CYP2C8 (PDB: 1PQ2), and CYP2D6 (PDB: 2F9Q) as templates, as previously described (*41*). The sequence identity of the template structures with CYP2J2 ranged from 41% to 45%. The individual sequence identity of each template with CYP2J2 is as follows: CYP2A6: 42%; CYP2B4: 45%; CYP2C5: 41%; CYP2C8: 42%; CYP2D6: 42%. Initially, the CYP2J2 structure was relaxed by placing the enzyme in a water box with dimensions of 90 × 90 × 90 $Å^3$, containing ~20,000 water molecules, generated with the SOLVATE plugin of VMD (*42*), and neutralized with 100 mM NaCl ions using the AUTOIONIZE plugin. The system was then energy minimized for 2,000 steps and simulated for 100 ps with the Cα atoms of the protein harmonically restrained (k = 1 kcal·mol^{-1}·$Å^{-2}$), and followed by 100 ns run with no constraints. The resulting structure of CYP2J2 was used as the initial structure for simulations.

For the membrane-binding simulations, wild-type CYP2J2 was placed ~10 Å above the surface of the HMMM membrane with different initial orientations (50° and 80° with respect to the z-axis). Three initial systems were prepared for simulation, two of which started from the same initial orientation (80°). The resulting structure was further solvated using the SOLVATE plugin, and neutralized with 100 mM NaCl using the AUTOIONIZE plugin of VMD (*42*). Each of the three resulting initial systems consisted of a box with dimensions of 101.4 × 101.4 × 122.0 $Å^3$ and containing ~120,000 atoms. The systems were energy minimized for 2,000 steps and relaxed further for 100 ps with the C□ atoms of the protein harmonically restrained (k = 1 kcal·mol^{-1}·$Å^{-2}$), followed by 40 to 60 ns of production simulation.

To study the effect of F-G loop mutations on membrane binding of CYP2J2, the mutations I236D, F239H, and I236D/F239H were introduced in the last frame of each membrane-binding simulation of the wild-type CYP2J2. This approach allowed us to take advantage of the accelerated lipid dynamics to monitor changes in the membrane insertion of CYP2J2 induced by the mutations. The Asp residue in the mutants was modeled in its deprotonated (charged) form, while the His residue was modeled in its neutral form, to match the expected charge of these side chains at pH 7.4. The resulting systems were energy minimized for 1,000 steps and relaxed further for 100 ps with the C□ atoms of the protein, except for the mutated residues, harmonically restrained (k = 1 kcal·mol^{-1}·$Å^{-2}$), followed by 40 to 50 ns of production simulation.

The resulting models of membrane-bound CYP2J2 and its mutants in the HMMM membrane were extended to a full POPC membrane, to perform additional simulations. A membrane-bound

model of the CYP2J2 for each case (wild-type and mutants) was adopted from the last frames of one of the HMMM membrane-binding simulations described above. The short-tailed lipid bilayer was transformed into a POPC bilayer by removing the DCLE molecules and adding the missing carbons of the lipid tails. The positions of the added lipid tail atoms were refined based on the coordinates of randomly selected lipid molecules obtained from a POPC bilayer equilibrated separately. During these steps, the positions of the lipid atoms already present in the HMMM membrane (headgroups and the initial five carbons of the lipid tails) were preserved, maintaining the original contacts established between the lipids and CYP2J2 during the HMMM simulations. The resulting POPC-bound CYP2J2 systems were then minimized for 2,000 steps and equilibrated for 100 ps while restraining all the protein and short-tailed lipids atoms with a force constant k = 1 kcal·mol^{-1}·Å^{-2} to allow relaxation of the the newly added lipid tail atoms. Following this step, the resulting wild-type and mutants systems were simulated without restraints for 70 to 100 ns.

Pyrene phospholipid partitioning in the membrane. In order to gain a more detailed description of the partitioning and orientation of pyrene molecules in a lipid bilayer, we performed another set of MD simulations. A solvated POPC membrane containing one pyrene phospholipid in each leaflet was constructed to study the dynamics of pyrene in the membrane. A POPC molecule was employed as a template to generate the pyrene-attached phospholipid, by removing carbons from the acyl tail and replacing them by a pyrene moiety. The resulting system was then minimized for 1,000 step and simulated for 1 ns with the heavy atoms of the lipid head groups harmonically restrained (k = 1 kcal·mol^{-1}·Å^{-2}), except for the pyrene phospholipids. The step was then followed by a 50 ns production simulation.

Simulation conditions and protocols. All simulations were performed with NAMD2 (*43*) using the CHARMM27 (*44*) force field with cMAP corrections for the protein and CHARMM36 (*45*) for lipids. Parameters of the pyrene-attached phospholipid were derived by analogy from the CHARMM General Force Field (*46, 47*). The TIP3P model was used for water (*48*). The NP$_n$AT ensemble at 1.0 atm and 310 K, with a constant area of 10,281 Å^2 (101.4 × 101.4 Å^2), was employed for all HMMM simulations. The POPC systems were simulated as an NPT ensemble at the same pressure and temperature. All simulations were performed with a time step of 2 fs. Constant pressure was maintained by the Nosé−Hoover Langevin piston method (*49, 50*) and constant temperature was maintained by Langevin dynamics with a damping coefficient γ of 0.5 ps^{-1} applied to all atoms. A cutoff of 12 Å was used for nonbonded interactions, with a smoothing

function applied after 10 Å. The particle mesh Ewald (PME) method (*51*) was used for long-range electrostatic calculations with a grid density greater than 1 $Å^{-3}$.

Heterologous expression and purification the CYP2J2 F-G loop constructs. The N-terminally truncated CYP2J2 construct (Δ34) was heterologously expressed and purified as described previously (*24, 52*). The mutations for the F-G loop plasmids were prepared using the reverse primers listed in Figure 4.7 and amplified by polymerase chain reaction (PCR) on the pCWori Δ34 plasmid in conjunction with the Δ34 forward primers. Each F-G loop mutant plasmid was co-transformed with the GroEL plasmid and grown in an overnight culture and used for inoculation of 1 L of terrific broth (TB) media supplemented with ampicillin (100 μg/mL) and chloramphenicol (20 μg/mL). The culture was grown at 37˚C and 220 rpm for 2.5 hours and then supplemented with δ-aminolevulinic acid (0.5 mM) and maintained at 26˚C and 160 rpm for 2 hours. Next the culture was induced with 1 mM of Isopropyl β-D-1-thiogalactopyranoside (IPTG) and 2g of arabinose and grown for an additional 44 hours. The cells were isolated via centrifugation for 10 min (2800 g) using a JA-10 rotor (Beckman Coulter, Brea CA) and sonicated in lysis buffer containing dithiothreitol (DTT), 0.2 mM phenylmethanesulfonylfluoride (PMSF), 5 mg DNase, and RNase. The membrane fraction was isolated via ultracentrifugation at 35,000 rpm from 30 min Ti-45 rotor (Beckman) and the soluble fraction was collected for analysis of the CYP content. Protein was extracted using 1% cholate (w/v) and the supernatant layer containing CYP2J2 was obtained by ultracentrifugation 35,000 rpm from 30 min Ti-45 rotor (Beckman). The histidine tagged protein was further purified by running the supernatant through a Ni-NTA column and eluted with 0.1mM DTT, 0.1% (w/v) cholate, 100 mM KPi, 200 mM imidazole and 20% glycerol. CYP2J2 concentration was measured by carbon monoxide difference spectra as described below.

Purification of oligomeric CYP2J2 by size-exclusion chromatography. For the membrane binding studies, the resulting Ni-NTA eluent was further purified using size exclusion - high performance liquid chromatography (SEC-HPLC) on a semi-preparative Superdex 200 10/300 column (GE Life Sciences, Piscataway, NJ) with a mobile phase consisting of 100 mM phosphate buffer (pH 7.4), 1 mM EDTA, 0.5 M NaCl, 2% glycerol and 0.1% cholate at a 0.5 ml/min flow rate. The predominant peak of each construct was collected and adjusted to contain 20% glycerol and concentrated using Amicon Ultra (10,000 MWCO) centrifugal filters (Millipore). The resulting protein concentration was quantified using a Micro BCA protein assay kit (Thermo Sci #23235). Next, the concentrated protein was examined for homogeneity (Figure 4.3C) by injecting

20 µL on a high resolution Superdex 75 10/30 SEC column (GE Life Sciences, Piscataway, NJ) with a mobile phase consisting of 100 mM phosphate buffer (pH 7.4), 1 mM EDTA, 0.5 M NaCl, 2% glycerol and 0.1% cholate at a 0.5 ml/min flow rate. The oligomeric state of the CYP2J2 constructs was estimated using the same mobile phase and Superdex 75 10/30 column and a standard curve plotted using thyroglobulin (669 kDa), ferritin (440 kDa), BSA (67 kDa), and cytochrome *c* (14 kDa) as protein standards (Figure 4.9).

Expression and purification of cytochrome P450 reductase. Cytochrome P450 reductase (CPR) from *Ratticus norvegicus* was expressed and purified as previously described (*24*).

Construction of ΔTrp-MSP1D1. In order to obtain ΔTrp-MSP1D1, the EcoR1-Sac1 gene fragment of MSP1D1 was replaced by the synthetic gene fragment in which two tryptophan codons (TGG) were substituted by phenylalanine codons (TTC). An additional silent mutation was added to create new restriction site (Xba1) in order to facilitate the screening. Briefly, the 300 bp G-block fragment (synthesized by IDT DNA, Inc.) and MSP1D1 plasmid were digested with Eco R1 and Sac1 restriction endonucleases. After separation on agarose gel, the 5.7 kBp fragment of MSP1D1 plasmid was ligated to synthetic insert using T4 ligase. After initial identification of the mutant clones by digestion mapping, the presence of the desired mutations and the absence of the unwanted ones were confirmed by DNA sequencing. MSP expression and purification was performed as described earlier (*53*).

Carbon monoxide binding assay. The carbon monoxide binding characteristics of the constructs were measured after Ni-NTA purification using a modified version of Omura and Sato's method (*54*) as described previously (*24*, *39*, *55*).

Guanidine hydrochloride induced denaturation of CYP2J2. The denaturation of CYP2J2 protein was studied by measuring the change in Soret at 417 nm as a function of increasing concentration of Gd-HCl (0 to 6 M) as previously described (*56*). Solutions containing varying concentrations of guanidinium hydrochloride were incubated with ~2 µM of CYP2J2 for 5 minutes before measuring their UV-vis spectra (800 – 300 nm). The resulting spectra were then processed using a MATLAB subroutine for determination of Soret absorbance changes.

Arachidonic acid metabolism assay for measurement of EETs. Incubations containing empty POPC-nanodiscs (10 µM), CYP2J2 (0.2 µM), CPR (0.6 µM) in 100 mM phosphate buffer (pH 7.4) were incubated with concentrations of arachidonic acid (40 µM) near the critical micelle concentration. The mixture was equilibrated at 37°C for 10 min before reaction initiation with 200

μ*M* NADPH (total volume 500 μL) and was allowed to react for 30 min. CYP2J2-Δ34 AA metabolism linearity over a one hour time course was previously confirmed (*39*). Samples were quenched upon extraction with an equal volume of ethyl acetate (3 times), dried under a steady stream of nitrogen and reconstituted in ethanol. Samples were analyzed using a 1200 series HPLC (Agilent Technologies, Santa Clara, CA) coupled to a 5500 QTRAP LC-MS/MS system (AB Sciex, Foster City, CA) for EET quantification using LC-MS/MS as previously described (*39*).

Assembly of POPC nanodiscs. POPC was solubilized with cholate (50 mM) and mixed with the membrane scaffold protein ΔTrp-MSP1D1 (devoid of Trp ε_{280} = 10,040 mM^{-1} cm^{-1}) in a 65:1 ratio before rocking the mixture at 4°C for one hour. Nanodisc assembly was initiated upon removal of detergents using of Amberlite Biobeads (Supelco). The homogenous nanodisc assembly was isolated using SEC-HPLC with a Superdex 200 10/300 column (GE Life Sciences, Piscataway, NJ) and a mobile phase consisting of 100 mM phosphate buffer (pH 7.4) and a 0.5 ml/min flow rate. The isolated nanodiscs were then concentrated with Amicon Ultra (10,000 MWCO) centrifugal filters (Millipore) to a final concentration of 500 μM.

Assembly of POPC-PYR nanodiscs. Nanodiscs containing PYR-PC were prepared with the same methodology as the POPC nanodiscs with a minor adaptation. Specifically, the PYR-PC was added to the POPC mixture in a 1.5:98.5 molar ratio. The phospholipids were then mixed with MSP1D1 in a 65:1 ratio and allowed to equilibrate for 1 hour at 4°C before detergent removal with Amberlite Biobeads. The assembled nanodiscs were isolated using SEC-HPLC on a Superdex 200 10/300 column (GE Life Sciences, Piscataway, NJ) with a mobile phase consisting of 100 mM phosphate buffer (pH 7.4) and a 0.5 ml/min flow rate (Figure 4.4B). Desired concentration of the incorporated PYR-PC was confirmed in solution spectrophotometrically at 342 nm using the molar extinction coefficient 42 mM^{-1} cm^{-1} (Figure 4.4B inset).

Assembly of POPC-PYR-POPS nanodiscs. Nanodiscs containing PYR-PC were prepared as described for the POPC-PYR nanodiscs, albeit with the addition of differing ratios of anionic phospholipids (POPS). Nanodiscs containing 30% and 60% POPS were prepared by mixing POPC/PYR/POPS in a molar ratio of 68.5:1.5:30 and 38.5:1.5:60, respectively. Each POPC/PYR/POPS mixture was added to MSP1D1 in a 65:1 ratio and allowed to equilibrate for 1 hour at 4°C before detergent removal with Amberlite Biobeads. The assembled nanodiscs were isolated using SEC-HPLC on a Superdex 200 10/300 column (GE Life Sciences, Piscataway, NJ) with a mobile phase consisting of 100 mM phosphate buffer (pH 7.4) and a 0.5 ml/min flow rate

Steady state fluorescence titration experiments. Steady state fluorescence measurements were performed using a K2 multi-frequency phase and modulation fluorometer (ISS, Urbana, IL, USA). Fluorescence experiments utilized purified monomeric CYP (1 μM), nanodiscs (50 μM), 100 mM phosphate buffer (pH 7.4) and 1 mM Na-EDTA maintained at 25°C with a circulating water bath. Emission spectra of the intrinsic fluorescence of the CYP interacting with nanodiscs were recorded from 300-400 nm with an excitation of 295 nm and bandwidths of 8 nm for both excitation and emission measurements. The maximal initial fluorescence (F_o) was measured by preparing samples containing CYP and ΔTrp-MSP1D1 POPC nanodiscs (50 μM), incubating for 10 min and recording the emission spectra. The quenched fluorescence measurement (F) was recorded after an incubation (10 min) of individually preparing samples containing CYP with pyrene nanodiscs (50 μM) comprised of ΔTrp-MSP1D1 POPC, ΔTrp-MSP1D1 POPC/POPS (70:30), or ΔTrp-MSP1D1 POPC/POPS (40:60). A parallel sample devoid of CYP was recorded after each measurement and subsequently subtracted from the main spectra using Vinci 2 software (Urbana, IL, USA). Samples were analyzed for changes in the Trp fluorescent maxima (λ_{max}) as well as for the ratio of changes in the initial fluorescent intensity (F_o) and final fluorescence (F).

Data analysis Data were analyzed and presented as means ± standard error. Data were collected multiple times and were analyzed for statistical significance using a Student's paired *t* test where $*p < 0.05$, $**p < 0.01$, and $***p < 0.001$.

4.4 RESULTS AND DISCUSSION

Molecular dynamics simulations - membrane-bound form of CYP2J2. In order to generate a membrane-bound model of CYP2J2 which would allow us to better understand the key lipid-protein interactions involved in membrane binding of the protein, we performed three independent MD simulations between 40 and 60 ns, starting with the □34-CYP2J2 placed above a phosphatidyl choline (PC) HMMM lipid bilayer. The aim was to capture the spontaneous membrane binding and insertion of the protein into lipid bilayer in unbiased simulations. Owing to the enhanced lipid dynamics of the membrane model, spontaneous membrane binding of the catalytic domain of CYP2J2 was consistently observed during these simulations (Figure 4.1). The analysis of the three resulting simulations reveals a similar behavior in terms of depth of insertion and orientation in the membrane of CYP2J2 (Figure 4.1B and Figure 4.5). The resulting binding pose of CYP2J2 suggests that the enzyme can interact with the membrane through hydrophobic residues located in the F-G loop region, in particular residues Trp-235, Ille-236 and Phe-239. During the simulations,

these side chains were observed to insert in the membrane (i.e., positioning below the reference plane defined by the PO_4 level) (Figure 4.1B). The N-terminal loop formed containing residue Trp-48 is also observed to insert into the membrane after binding (Figure 4.1B).

Starting from the HMMM membrane-bound models of CYP2J2, the short-tailed lipids (with five carbons in each tail) were extended to full POPC lipids (see Methods), resulting in a model of CYP2J2 bound to a POPC membrane as shown in Figure 4.1A. The extended model simulation shows that the main interactions observed in the HMMM model are preserved, and Trp-48, as well as residues Trp-235, Ile-236 and Phe-239 located in the F-G loop remain inserted in the membrane (inserted below the PO_4 level) (Figure 4.1B and Figure 4.5). In order to test the convergence of the membrane-bound models of CYP2J2, we characterized the orientation that the enzyme with respect to the lipid bilayer by calculating the heme tilt angle, defined as the angle between the heme plane (defined as the plane containing the four porphyrin nitrogen atoms) and membrane normal (z-axis). In the three extended POPC simulations, the heme tilt angle converges to values ~50°, suggesting a convergent membrane-bound pose for CYP2J2 (Figure 4.6). The orientation that CYP2J2 adopts in the membrane is similar to that reported for other membrane-bound CYPs, measured both from experiments and from simulations, which are reported to be around 60 to 70° (*6*, *57*).

Simulation of pyrene partitioning in the membrane. We performed experiments to evaluate the interaction of the mutated CYP2J2 proteins with membranes by measuring the Trp quenching by pyrene phospholipids inserted into the homogeneous lipid bilayer. Therefore, in order to identify potential interactions between a pyrene molecule attached to a phospholipid and the membrane-bound CYP2J2, we performed a separate simulation of a POPC membrane containing a single pyrene phospholipid in each leaflet for 50 ns in the absence of CYP2J2. The goal was to characterize the distribution of the pyrene molecules within the lipid bilayer and use it to infer information on the potential interaction of the side chains of CYP2J2 with pyrene upon membrane binding based on the location of this moiety in the membrane. The distribution of the z-position for each molecule revealed that the pyrene moiety is located mainly in the hydrophobic core of the membrane, below the phosphate groups (Figure 4.1C). Despite being attached to their respective phospholipid tail, pyrene molecules are able to sample a wide range of insertion depth within the hydrophobic core of the membrane, as indicated by their wide z-position distributions. Interestingly, the insertion depth of CYP2J2 in the POPC membrane would allow for the side

chains of Trp-48 and Trp-235 to interact with the pyrene moiety located in the PYR-ND, as indicated by their z-position distributions (Figure 4.1C). The distribution of the z-position of each side chain shows that they both insert to a similar level around the PO_4 level, with Trp-235 slightly more inserted than Trp-48. Therefore using PYR-ND one can delineate the membrane interactions of the CYP2J2 mutants with the lipid bilayer using experimental approaches as described later.

CYP2J2 construct design. The initial structural analysis and MD simulations suggested two hydrophobic residues in the F-G loop, Ile-236 and Phe-239, as putative membrane anchors (Figure 4.1A and 4.3A). These sites were mutated to hydrophilic residues with the aim of altering membrane-binding characteristics by decreasing the overall hydrophobicity of this region. To this end, two single mutations, I236D (Δ34-I236D) and F239H (Δ34-F239H), as well as a construct containing both I236D and F239H (Δ34-double) were designed. Apart from the N-terminal anchor, the CYP F-G loop has been hypothesized to be the primary membrane-binding motif. This assumption is further supported by the observation that the greatest structural differences between the soluble prokaryotic CYPs and the membrane bound mammalian CYPs are found in the F and G helices and the F-G loop (*58*). Notably, CYP2D6 was successfully solubilized and crystallized by truncating the N-terminus and mutating the F-G loop Leu-230 and Leu-231 with a combination of hydrophilic residues that included I230D and I231R (*21*). Following a similar design strategy we mutated Ile-236 and Phe-239 to hydrophilic residues to examine the effects on solubility and functionality. Additionally, the close proximity of the naturally occurring Trp-235 to the mutated sites enabled membrane-binding studies using fluorescence spectroscopy.

Molecular dynamics simulations of membrane binding modes of the F-G loop mutants. We studied the effect of these specific F-G loop mutations on membrane binding of CYP2J2 by introducing the mutations in the membrane-bound models obtained from MD simulations. To achieve this, we used the final snapshot of each of the three HMMM membrane-binding simulations, introduced the mutations and performed production simulations on the system. This approach allowed us to monitor changes in the membrane insertion depth of the protein due to mutations in the F-G loop. Single mutations Δ34-I236D and Δ34-F239H, as well as double mutation Δ34-double were introduced in the membrane-bound CYP2J2, resulting in 3 models for each mutant, which were simulated individually between 40 and 50 ns.

The results of these simulations show that the mutations affect the insertion of the F-G loop to various degrees (Figure 4.2). The I236D mutation promotes the detachment of Trp-235 from the

membrane. In the cases were this mutation is introduced (I236D and 1236D/F239H), Trp-235 moves from a fully inserted position to an average position that is above the PO_4 and choline levels, with occasional detachment of the residue from the membrane (Figure 4.2A and 4.2B). In both cases, the position of Trp-235 side chain (above the phosphate level) is maintained upon the conversion of the HMMM membrane with short-tail lipids to a full POPC membrane (Figure 4.2A and 4.2B). In the POPC membrane, the average position of Trp-235 resulting from the I236D mutation is between 5 to 10 Å above the reference PO_4 plane, as shown in Figure 4.2D. The F239H mutation, on the other hand, seems to have a smaller effect on Trp-235 insertion, causing only transient detachment of Trp-235 both in the short-tail lipid membrane and in the POPC membrane (Figure 4.2C), resulting on an average relative position that is close to the Trp-235 insertion in the wild type case (Figure 4.2D). Taken together, the simulations indicate that introducing mutations in the F-G loop results in a shallower membrane insertion of Trp-235 in the F-G loop when compared to the wild-type simulations. As discussed later, this was corroborated by an increased percentage of the mutants in the cytosolic fraction and fluorescence experiments where we measured CYP2J2 Trp quenching by membranes containing pyrene lipids.

Expression and purification of CYP2J2 F-G loop mutants. The growths of all constructs were performed in DH5alpha cells due their relatively slow growth and expression characteristics that improve the overall yields of functional P450 (*52*). We previously demonstrated that the N-terminus truncated CYP2J2 construct (Δ34) exhibited greater solubility, yet still maintained its ability to insert in the membrane bilayers of nanodiscs (*24*). Interestingly, the percentage of protein found in the soluble fraction during purification corresponded to the number of F-G loop mutations. Specifically, the percentage of protein in the soluble fraction of Δ34-double, Δ34-I236D, Δ34-F239H and Δ34 were 56.7%, 46.3%, 43.8% and 37.5%, respectively (Figure 4.3B). These results provide the expression and membrane binding characteristics of the CYP constructs in the *E. coli* membrane. The ratio of the membrane to soluble fraction of the protein only provides an indication of enzyme solubility and is not directly applicable to other systems such as model membranes and mammalian cells. Therefore we further explored the membrane insertion of these constructs using a Trp quenching assay in Nanodiscs as described later.

Spectral characterization, denaturation studies, and size-exclusion chromatography of the F-G loop mutants. The F-G loop mutants exhibited typical Soret and Q-bands similar to wild type CYP2J2 (data not shown). To investigate the potential heme-thiolate perturbations the mutants

were reduced (Fe^{II}) and bound with carbon monoxide. All constructs exhibited a prominent 451 nm peak, albeit with some 420 nm peak, indicating that the charged mutations in the F-G loop did not largely perturb the heme-thiolate motif interactions and the common P450 fold (Figure 4.8). Furthermore, the stability of the mutants was assessed by performing guanidine hydrochloride denaturation studies using UV-Vis spectroscopy. The 417 nm Soret absorbance is attributed to the uniquely coordinated ferric (Fe^{III}) heme. In the presence of increasing concentration of guanidine hydrochloride (Gd-HCl), the absorbance of the CYP at 417 nm decreased, indicating heme loss due to protein unfolding (*56*). The three constructs demonstrated comparable stability in Gd-HCl with a decrease in peak intensity of ~45%. The Δ34 construct exhibited less denaturation with an overall 30% decrease in the Soret peak intensity in the presence of 6M Gd-HCl (Figure 4.3D).

The range of oligomers formed from each mutant after Ni-NTA purification was examined using semi-preparative size exclusion chromatography All the constructs produced a predominant peak that eluted with a volume of ~15.5 ml on the Superdex 200 10/300 column (data not shown) using the conditions listed in the materials and methods. The primary oligomer was collected, concentrated and its homogeneity and molecular weight was assessed using a high resolution Superdex 75 10/30 column. As seen in Figure 4.3C, all the constructs show a single oligomer that corresponded to the monomeric form of the protein as measured using protein standards (Figure 4.9). Taken together, the results suggest that the non-conservative mutations did not change the protein in regards to P450 fold, oligomeric state and stability.

Arachidonic acid metabolism. Typically, random introduction of mutations in the F-G loop of CYPs alters their function as compared to the wild type construct (*27*). Therefore we examined the effect of the F-G loop mutation on the CYP2J2 mediated metabolism of arachidonic acid (AA) in the presence of a 50 μM concentration of empty POPC nanodiscs. As discussed in the steady state fluorescence section, a CYP to nanodisc stoichiometric ratio of 1:50 was chosen to ensure that the CYP construct was completely bound to nanodiscs. Under these conditions, the functional differences between CYP2J2 are results of differences in their ability to metabolize AA and not due to discrepancies between the membrane-bound and unbound states. AA is a slowly metabolized endogenous substrate that forms EET metabolites that are potent vasodilators and anti-inflammatory lipids (*17, 59*). The metabolism of AA is complex, as it produces four unique epoxide regio-isomers. Interestingly, the Δ34-I236D metabolism of AA was increased with a ~1.6 greater catalytic efficiency of all regio-isomers when compared to Δ34 (Figure 4.3E). Conversely,

the function of Δ34-F239H was dramatically decreased relative to Δ34, indicating that the mutant's native function has been altered. Notably, the Δ34-double construct produced the EET metabolites with similar catalytic efficiency to Δ34 as shown in Figure 4.3E. Interestingly, none of the mutations altered the ratio of the EET products produced by CYP2J2 (data not shown), which suggests that the active site was not drastically altered.

In both mammalian and bacterial systems, the F-G loop is an important regulator of substrate access channels (*60*). Moreover, this region has been shown to be flexible with open/closed conformations and provides the roof of the internal substrate-binding pocket which mediates substrate recognition (*61*). Recent evidence suggests that the conformation of the F-G loop and ligand type may alter ligand egress routes. Specifically, MD simulations predicted that the non-helical CYP2C9 F-G loop would favor egress pathways through the membrane bilayer (*62*). In this work we demonstrate that single mutations in this region can alter the catalytic turnover characteristics of the epoxidation of arachidonic acid (Figure 4.3E). Interestingly, the enhanced catalytic functionality of Δ34-I236D or decreased activity of Δ34-F239H did not alter the enzyme regioselectivity and therefore cannot simply be rationalized based on their enhanced solubility or active site alteration. Rather these changes suggest that the introduction of the acidic residue either alters the loop conformation dependent egress pathways and/or substrate recognition sites. Notably, these effects are abolished in the Δ34-double construct, which restores wild-type activity.

While only a small amount of histidine is charged at its physiological pH, this may be an important stabilizing residue. The combination of an anionic and cationic residue introduction was selected for the crystallization of CYP2D6 due to its restoration of wild-type like activity (*21*). Importantly, these mutations were chosen as a practice of trial-and-error. The rational introduction of the double mutation in CYP2J2 F-G loop corroborates this strategy. However, MD simulations demonstrated that although there is a close interaction of the side-chains we failed to observe a salt-bridge formation (data not shown).

CYP2J2 construct membrane insertion into pyrene nanodiscs. To investigate the CYP2J2 constructs' insertion in the membrane bilayer, we measured the relative Trp quenching energy transfer between the protein monofacial Trp residues and pyrene phospholipids. To this end, we prepared nanodiscs with pyrene phospholipids (PYR-ND) using the ΔTrp-MSP1D1 construct in which Trp residues were mutated to Phe. As shown in Figure 4.4A, the Trp residues of the CYP2J2 membrane binding region are predicted to interact with pyrene phospholipids incorporated in the

membrane bilayer. Using a POPC/PYR-PC molar ratio of 64:1 the expected PYR-PC was 1 pyrene molecule per nanodisc leaflet. Previously, pyrene-containing liposomes have been successfully employed to characterize membrane insertion properties of peripheral and integral CYP proteins (*10, 63, 64*). Here we demonstrate use of PYR-ND as a new iteration of this method with a few key advantages. Notably, the PYR-ND is a 10 nm discoidal lipid bilayer that is homogeneous (Figure 4.4B) and exhibits superior stability. Additionally, the nanodisc also enables stoichiometric control of the lipid compositions.

As previously discussed, MD simulations revealed that the pyrene moiety can sample a wide range of orientations just under the phospholipid heads in the membrane core. Upon insertion into the membrane bilayer the two residues, Trp48 and Trp235, were shown to interact with pyrene. Thus, in the presence of saturating concentrations of PYR-ND, the experiment is a measure of membrane depth of insertion of these fluorophores.

For the depth of insertion measurements, the CYP to PYR-ND (1:50) ratio was chosen based on fluorescence titrations that revealed that the overall Trp florescence was quenched with excess PYR-ND (data not shown). This has been previously detailed in other cases and is thought to reflect that there are two populations of Trp residues (*65*). Specifically, one population that interacts with the pyrene upon insertion and another population that is buried in the protein and is not substantially quenched (*65*). Therefore the relative extent of non-ideal Trp quenching is represented here by the quenched fluorescence (F) divided by the initial fluorescence (F_o).

The FRET transfer of energy is a dynamic quenching interaction. Evidence of a FRET between the Trp (donor) and pyrene (quencher) was observed upon titration of the CYP to a sample of PYR-ND. Specifically, a decrease in the Trp fluorescence of CYP is accompanied by an increase in the pyrene emission (Figure 4.4C). Using the PYR-ND system we examined the relative quenching of Trp fluorescence (F/F_o) as a function of both the mol% of anionic phospholipids (POPS) and the absence/presence of 0.5 M NaCl. The rationale of these two conditions used is explained below.

In the absence of anionic lipids, the differences among the CYP2J2 mutants F/F_o are subtle (Figure 4.4D). Specifically, Δ34, Δ34-I236D, Δ34-F239H and Δ34-double exhibited average F/F_o ratios of 0.82 ± 0.02, 0.848 ± 0.01, 0.845 ± 0.04 and 0.89 ± 0.01, respectively. These results suggest that the F-G loop mutants are oriented in a way that the Trp residues are not as deeply imbedded. Overall the quenching ratios reflect similar values observed with CYP3A4 binding to liposomes.

Specifically, when the Trp quenching properties of CYP3A4 were examined with in phosphatidylcholine (PC) vesicles containing 1.5 mol% of PYR-PC the initial F/F_o values were ~0.85 (*10*). Conversely, in the case of CYP1A2, a negligible amount of quenching is observed with neutral phospholipid vesicles (*36*).

The presence of anionic lipids is known to induce both CYP conformational shifts as well as increased penetration into membrane bilayers (*10, 36*). Thus, we further examined the membrane insertion properties (relative F/F_o changes) of CYP2J2 when anionic lipids (POPS) were incorporated into the bilayers of nanodiscs (Figure 4.4D). When 30 mol% of POPS was substituted at the expense of POPC, we observed greatly enhanced differences among the F-G loop mutants and the Δ34 construct. Specifically, Δ34, Δ34-I236D, Δ34-F239H and Δ34-double exhibited average F/F_o ratios of 0.65 ± 0.03, 0.82 ± 0.002, 0.81 ± 0.01 and 0.84 ± 0.04, respectively. Interestingly, the differences among the F-G loop mutants and the Δ34 construct were the most pronounced when 60 mol% of POPS was incorporated into nanodiscs. For these experiments, Δ34, Δ34-I236D, Δ34-F239H and Δ34-double exhibited average F/F_o ratios of 0.52 ± 0.005, 0.74 ± 0.02, 0.7 ± 0.03 and 0.82 ± 0.002, respectively. Thus, using a high percentage of anionic lipids we were able to affect the greatest changes between the Δ34 construct and the F-G loop mutants. While these results are only qualitative, the different membrane binding interactions induced by the presence of anionic lipids suggest that the hydrophobicity and charge of the F-G loop is important for POPS mediated depth of insertion. Specifically, these differences support the assumption that the enzyme topology is altered when the F-G loop is mutated with these hydrophilic residues. This conclusion is supported by the MD data that demonstrate these residues are putative membrane anchors and hydrophilic mutations detach this region from the leaflet.

To further explore the nature of the membrane depth of insertion, we examined the effect of a high concentration of NaCl on the F/F_o ratio when the 60 mol% POPS PYR-ND was employed to achieve the maximum membrane interaction of CYP2J2 (Figure 4.4E). Importantly, high salt concentrations effectively solubilize membrane proteins, altering their nature from an irreversibly membrane bound protein to a state of protein that can bind and dissociate in a peripheral manner (*4*). This effect was observed when the Δ34G construct was examined, with a decrease in the Trp quenching (F/F_o) from 0.52 to 0.71, for the no salt buffer to 0.5M NaCl buffer, respectively. Surprisingly, the presence of a high concentration of NaCl had little effect on the extent of Trp quenching for the F-G loop mutants which demonstrates the membrane insertion depth is

maintained despite the high salt concentration. Overall, the MD simulation results and sub-cellular localization in *E. coli* studies suggests that these proteins are peripherally binding in the no salt buffer.

Here we demonstrate that the subtle topology nuances between similar constructs and membrane depth of insertion can be measured using Trp quenching studies. While the fluorescence experiments only provide a relative measure of membrane insertion characteristics, this approach is an effective tool to understand how mutations, lipid composition and NaCl can alter the depth of insertion.

4.5 CONCLUSIONS

In this work, we demonstrate that the CYP2J2 F-G loop region is an important protein-membrane interface that controls membrane insertion and substrate metabolism characteristics. The HMMM model simulations revealed that CYP2J2 interacts at the F-G loop through the Trp-235, Ille-236 and Phe-239 residues. Importantly, these binding interactions and the protein orientation were preserved in the MD simulations when the short-tailed lipids were extended to POPC lipids. The effects of mutating the putative membrane anchors Ile-236 and Phe-239 with hydrophilic residues were also examined. These mutations significantly decrease the F-G loop depth of insertion when used in MD simulations. To experimentally corroborate these findings, four CYP2J2 constructs (Δ34, Δ34-I236D, Δ34-F239H and Δ34-double) were expressed in E. coli. Notably, the F-G loop mutant expression yields derived from the membrane fraction were substantially decreased and the protein was localized to the cytosolic fraction to a greater extent. While all constructs demonstrated sufficient P450 content and stability we observed significant differences in their functional metabolism. Wild-type activity was restored through the introduction of a double mutation F239H and I236D. Thus, we experimentally demonstrate that the insertion of CYP2J2 into the membrane bilayers of PYR-ND is influenced by the overall hydrophobicity of the F-G loop. The relative membrane binding characteristics were experimentally derived by monitoring CYP2J2 Trp quenching after insertion into the membrane bilayers of PYR-ND. The N-terminal truncated construct Δ34-CYP2J2 exhibited membrane binding to a greater extent than the F-G loop mutants (Δ34-I236D and Δ34-F239H) suggesting a different enzyme topology in agreement with the MD simulations.

4.6 ACKNOWLEDGMENTS

We gratefully acknowledge the use of the Sligar lab fluorometer and helpful discussions on fluorescence measurements with Dr. Mark McLean. We want to thank Dr. Ko, Dr. Bagchi and Dr. Ferguson for allowing the use of their equipment. We appreciate the continued support of Dr. Kevin Tucker of the UIUC School of Chemical Sciences and Dr. Zhong Li at the Metabolomics lab of the UIUC Roy J. Carver Biotechnology Center. This work was supported in part through the American Heart Predoctoral Fellowship [14PRE20130015] (DRM), American Heart Association Scientist Development Grant [15SDG25760064] (AD) and in part by the National Institutes of Health (R01-GM101048, U54-GM087519, and P41-GM104601 (ET), and in part by the National Institutes of Health (R01-GM101048, U54-GM087519, and P41-GM104601 to ET). All simulations have been performed using XSEDE resources (grant MCA06N060 to ET). The Roy J. Carver Biotechnology Center's 5500 QTrap MS was funded by the National Institutes of Health National Center for Research Resources [Grant S10-RR024516].

4.7 FIGURES AND TABLES

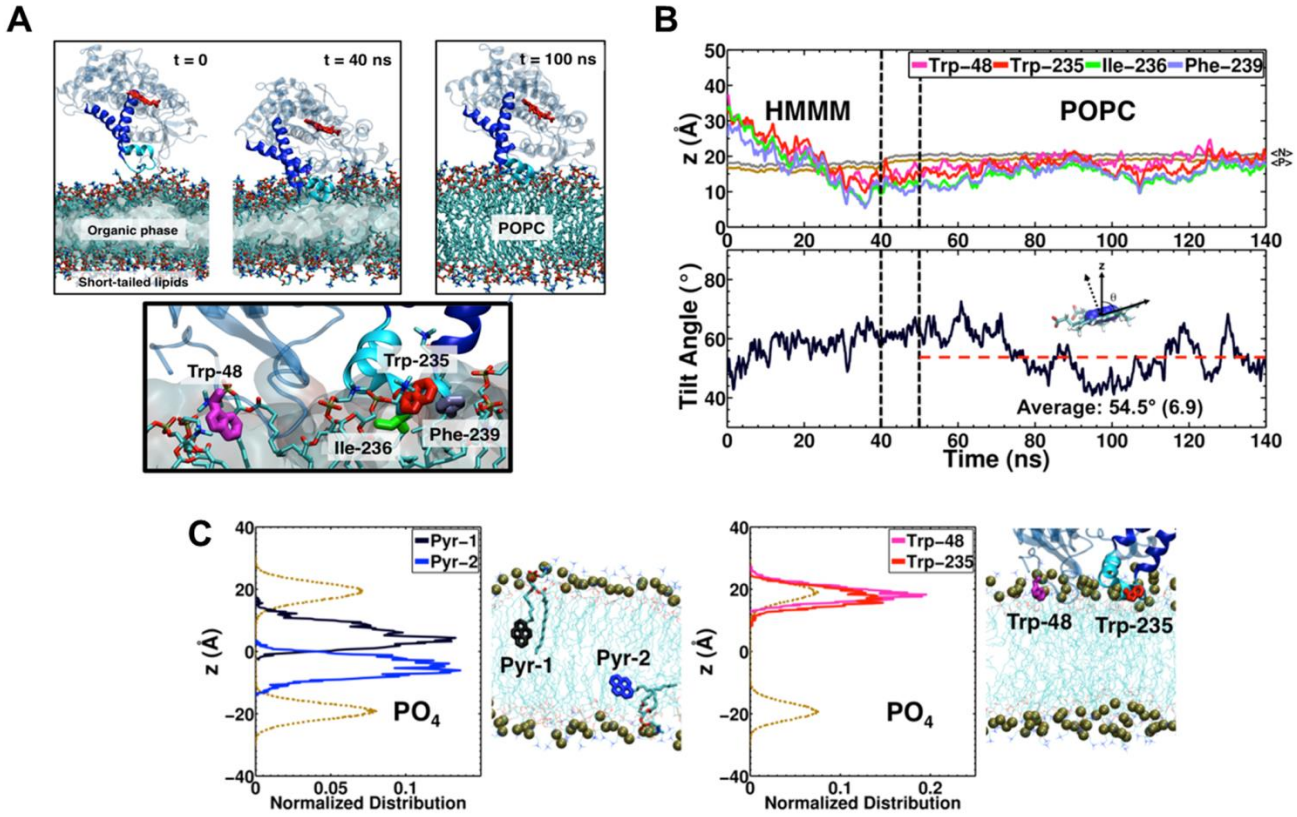

Figure 4.1. Insertion of CYP2J2 into Membrane. (A) (Top) Membrane binding of CYP2J2 captured with the HMMM membrane in 40 ns. The membrane-bound model of CYP2J2 was extended to a POPC membrane and simulated for another 100 ns. The stick backbone of the heme is colored red, the F- and G- helices are blue with the remaining P450 colored light blue. Lipids are shown in stick representation. (Bottom) Residues Trp-48, Trp-235, Ile-236 and Phe-239, identified to interact with the membrane upon binding, are shown in stick representation. **(B)** (Top) Time series of the center of mass (COM) z-coordinate of the side chains Trp-48, Trp-235, Ile-236 and Phe-239 for the HMMM and POPC membranes. A side chain is assumed to insert into the membrane when its COM z-position is below the reference plane defined by the COM z-position of the PO_4. The black dashed lines indicate the time allowed for the grown POPC membrane to relax. The positions of the phosphorous (PO_4) and nitrogen (choline) atoms of the lipids are show in in brown and gray, respectively. (Bottom) Time series of the heme tilt angle of CYP2J2 in the HMMM and POPC membranes. The red dashed line indicates the average for the heme tilt angle in the POPC membrane. **(C)** Distribution of the z-coordinate of pyrene molecules attached to phospholipids and of the Trp-48 and Trp-235 side chains, obtained from separate simulations. The dashed brown lines indicate the distribution of the z-coordinate PO_4 group of each leaflet. The location of pyrene and Trp side chains in the simulation is also shown.

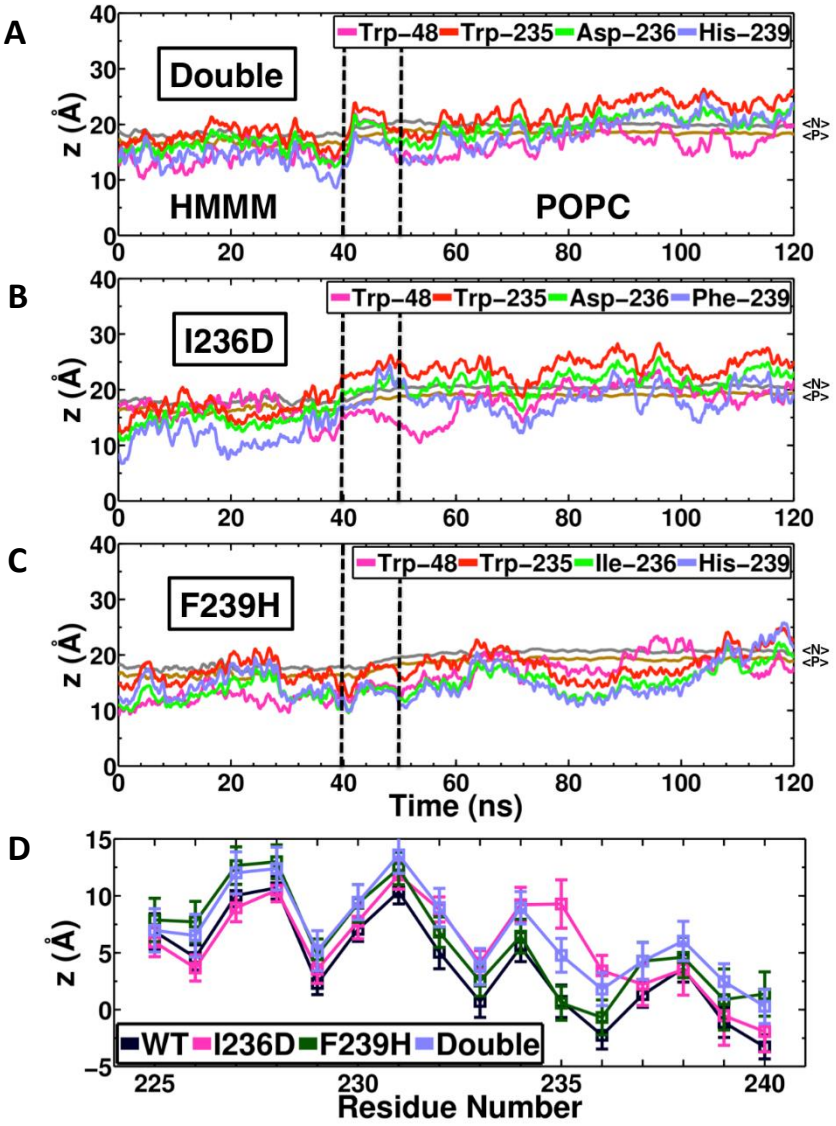

Figure 4.2. Effect of F-G loop mutations in membrane-binding of CYP2J2. Time series of the COM z-position of side chains Trp-48, Trp-235, Ile-236 and Phe-239 for the HMMM and POPC membranes shown for **(A)** I236D/F239H mutant, **(B)** I236D mutant and **(C)** F239H mutant. For each case, the HMMM simulations were extended to a POPC membrane and simulated 80 ns. The black dashed lines indicate the time allowed for the extended POPC membrane to relax after conversion from HMMM. The positions of the phosphorous (PO_4) and nitrogen (choline) atoms of the lipids are show in in brown and gray, respectively. **(D)** Average relative position of the COM z-coordinate of the side chains forming the F-G loop (residues 225 to 240) with respect to the reference plane defined by the COM z-position of the PO_4. The average was taken from the last 20 ns of simulations for each case. The error bars represent one standard deviation.

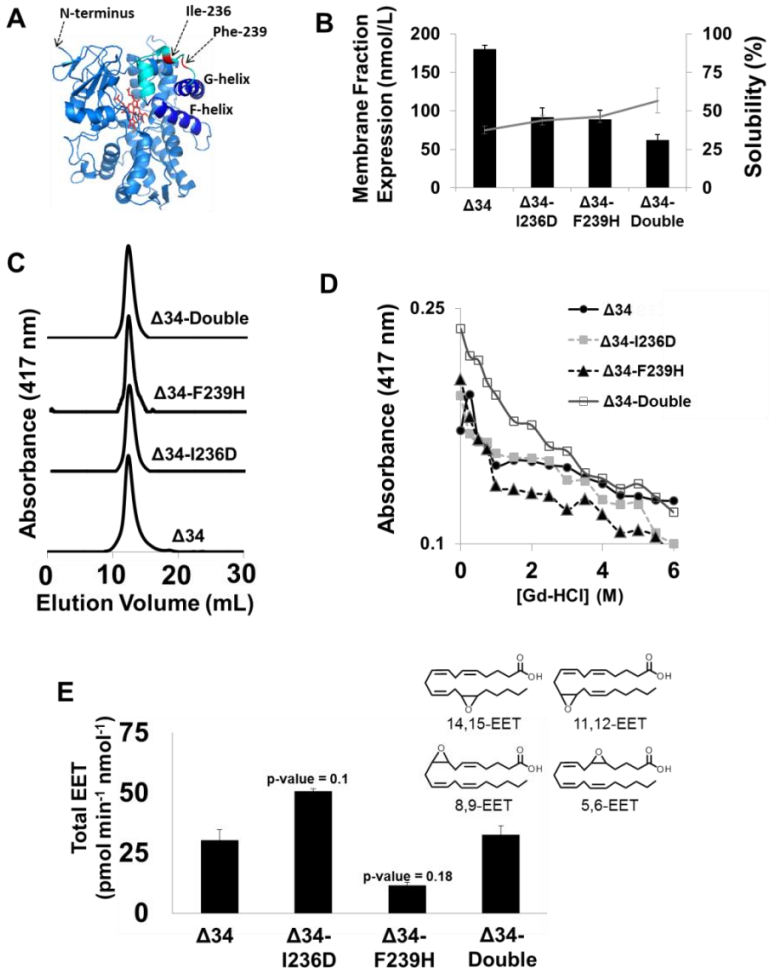

Figure 4.3. Biochemical characterization of the CYP2J2 F-G loop mutants. (A) Representation of the CYP2J2 Δ34 homology model. The stick backbone of the heme is colored red, the F- and G- helices are dark blue with the remaining P450 protein fold and helices colored light blue. The two residues selected for mutation (I236 and F239) are colored red on the F-G loop represented by cyan. **(B)** The three CYP2J2 mutants Δ34-I236D, Δ34-F239H and Δ34-double were recombinantly expressed in E. coli. The bar graph denotes expression yields purified from the membrane fraction whereas the line plot signifies percentage of CYP found in the soluble fraction during purification. **(C)** The size exclusion chromatography purified CYP2J2 protein was examined for homogeneity and elution volume with a high resolution Superdex 75 10/30 column **(D)** Changes to the stability of each CYP2J2 construct was assessed by monitoring the loss of the prosthetic heme monitored at 417 nm using UV-Vis spectroscopy in the presence of increasing concentrations of guanidine hydrochloride. **(E)** F-G loop mutant functionality was gauged by monitoring the metabolism of arachidonic acid (40 μM) using LC/MS/MS in a phospholipid reconstituted system. The rate of the conversion of arachidonic acid to total EET consisting of 14,15-, 11,12-, 8,9- and 5,6-EET were determined for the wild-type construct and each of the three F-G loop mutants. In the arachidonic acid assay we did not observe statistical significance below $p < 0.05$ when using a paired, two-tailed student's t-test but did see a trend towards significance for Δ34-I236D and Δ34-F239H with p-values of 0.1 and 0.18, respectively.

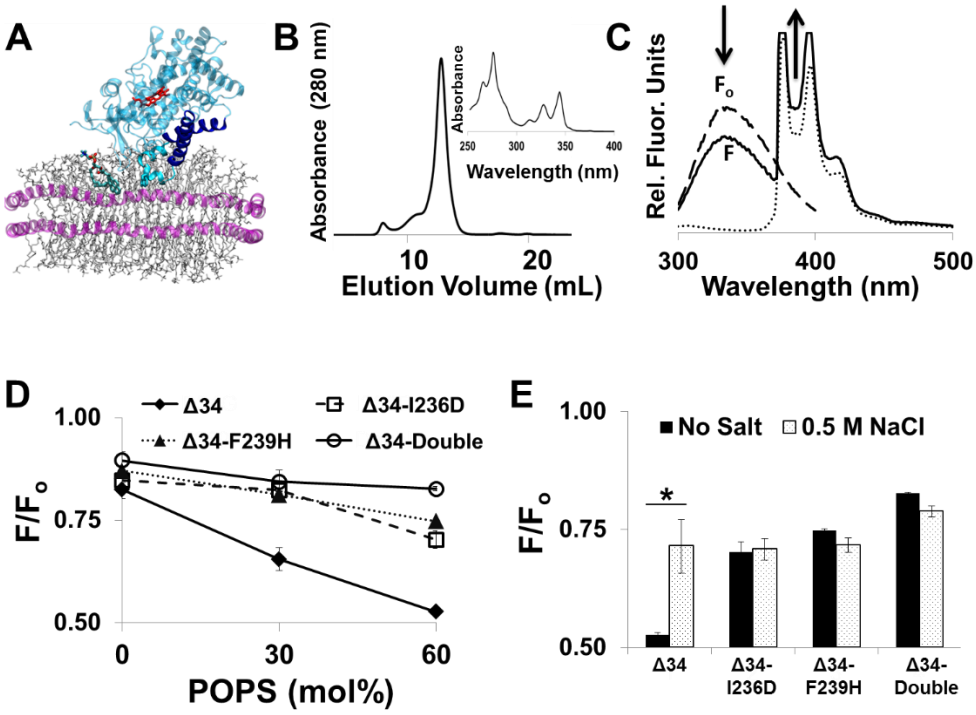

Figure 4.4. Fluorescence studies with CYP2J2 F-G loop constructs. (A) Schematic of CYP2J2 insertion into pyrene nanodiscs (PYR-ND). The F-G loop is located between the CYP2J2 F- and G-helices (represented in blue) and contains the Trp 235 residue, which interacts with the pyrene phospholipids (shown in cyan stick model) incorporated in the membrane bilayer of nanodiscs (phospholipids are grey and membrane scaffold protein is purple). **(B)** Size-exclusion HPLC chromatography of the PYR-ND. (Inset) Spectra demonstrating successful PYR-PC phospholipids incorporation into nanodiscs. **(C)** The relative membrane insertion characteristics of each construct were determined by measuring CYP2J2 Trp quenching. F_o (dashed line) is the Trp-fluorescence maximum CYP2J2 in the presence of POPC nanodiscs (lacking pyrene). F (solid line) is the quenched CYP2J2 Trp fluorescence due to insertion in pyrene nanodiscs. The dotted line represents the pyrene nanodisc fluorescence spectra (excitation 295 nm; emission 300-600 nm) in the absence of protein. **(D)** Trp fluorescence signals of CYP2J2 constructs were monitored in the presence of empty nanodiscs (F_0) and presence of PYR-ND (F) to calculate F/F_o. The F/F_o was measured using PYR-ND containing POPS/POPC molar ratios of 0:100, 30:70 and 60:40. **(E)** The effect of 0.5M NaCl on F/F_o ratio was measured for each CYP2J2 F-G loop mutant using 60 mol% POPS PYR-ND

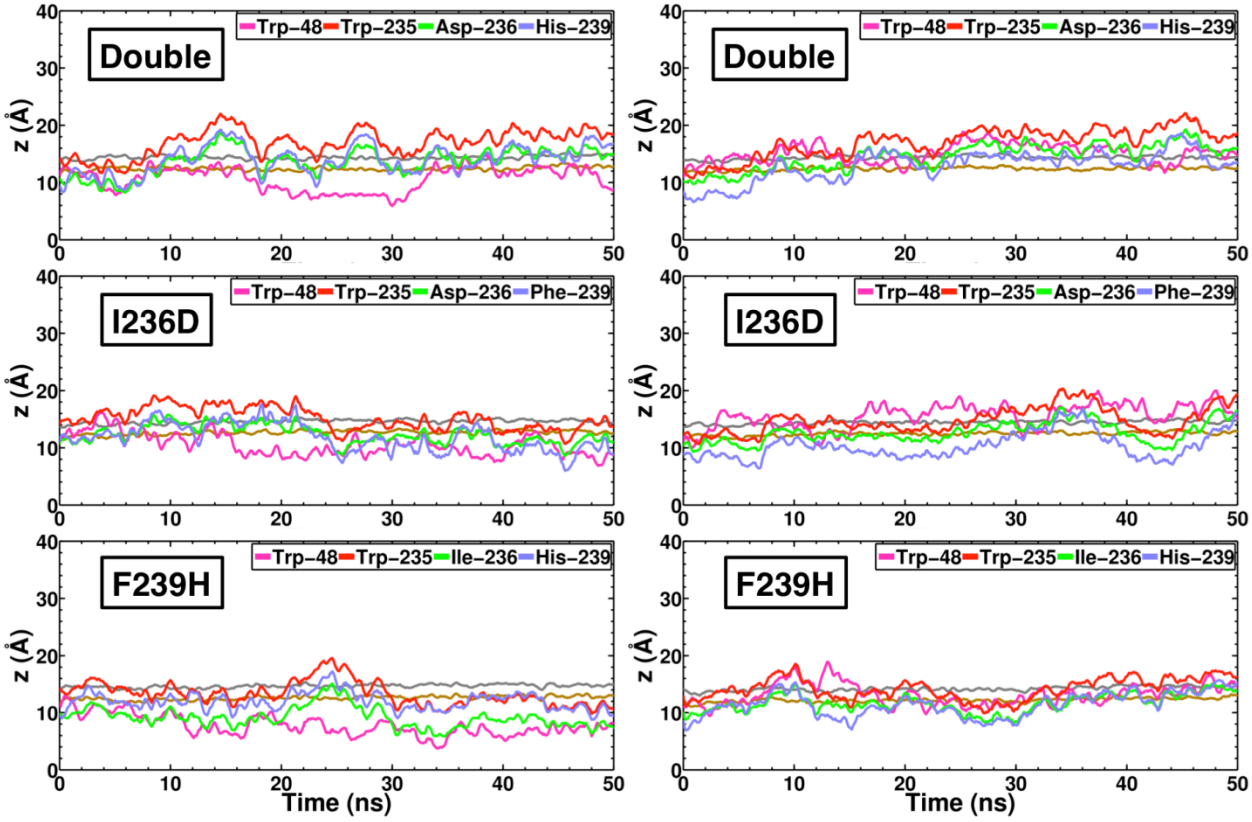

Figure 4.5. Effect of F-G loop mutations in membrane-binding of CYP2J2. Time series of the COM z-position of side chains Trp-48, Trp-235, Ile-236 and Phe-239 for the additional HMMM simulations for **(Top)** Δ34G-double mutant, **(Middle)** Δ34G-I236D mutant and **(Bottom)** Δ34G-F239H mutant. The positions of the phosphorous (PO_4) and nitrogen (choline) atoms of the lipids are show in in brown and gray, respectively.

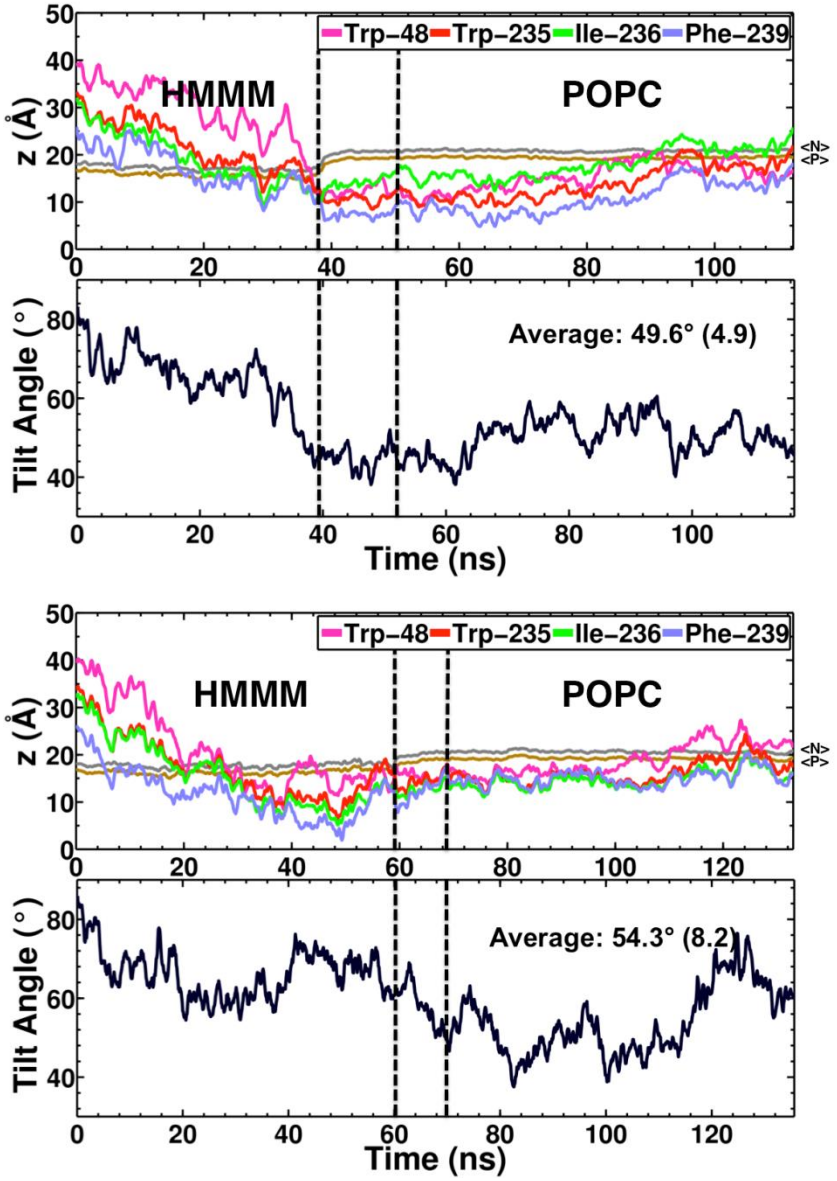

Figure 4.6. Time series of the center of mass (COM) z-coordinate of side chains Trp-48, Trp-235, Ile-236 and Phe-239 and the heme tilt angle for the additional HMMM binding simulations. Each simulation was extended to a POPC membrane. The black dashed lines indicate the time allowed for the grown POPC membrane to relax after conversion from the HMMM. The positions of the phosphorous (PO_4) and nitrogen (choline) atoms of the lipids are show in brown and gray, respectively. (Bottom)

Construct	Primer Nucleotide Sequence
Δ34-I236D	GGG CAG GAA TTT CAT GTC CCA TGG AAA GAC ATT GTA GAG CTG G
Δ34-F239H	GGG CAG GTG TTT CAT TAT CCA TGG AAA GAC ATT GTA GAG CTG G
Δ34-Double	GGG CAG GTG TTT CAT GTC CCA TGG AAA GAC ATT GTA GAG CTG G

Figure 4.7. F-G Loop Mutant Primers. The Δ34 forward primer was used in conjunction with each individual reverse primer listed above (5' to 3') and amplified on the pCWori wild-type CYP2J2 Δ34 plasmid for production of Δ34G-I236D, Δ34G-F239H and Δ34G-double plasmids. Site-directed mutagenesis was used for introduction of residue mutations as denoted by the underlined codons.

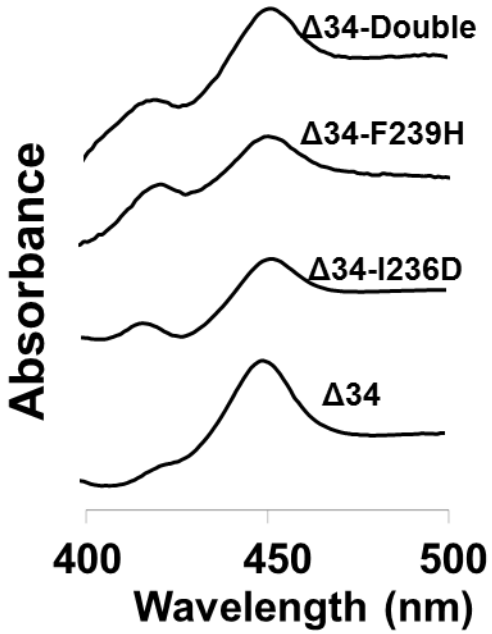

Figure 4.8. F-G Loop Mutant CO-Binding Spectra. Carbon-monoxide binding spectra were measured for each construct to examine perturbations of the heme-thiolate motif and overall maintenance of typical P450 protein folding.

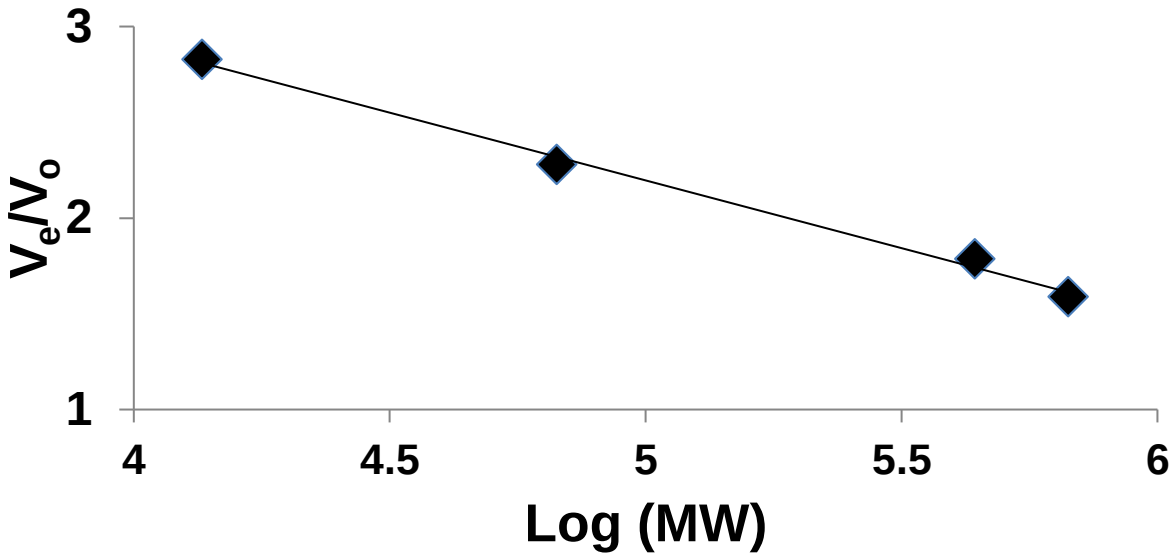

Figure 4.9. Spherical protein mass standard curve. SEC-HPLC using a Superdex 75 10/35 and a mobile phase of 100 mM phosphate buffer (pH 7.4), 1 mM EDTA, 0.5 M NaCl, 2% glycerol and 0.1% cholate at a 0.5 ml/min flow rate. A standard curve was constructed by plotting the ratio of the elution volume (Ve) to void volume (Vo) against the log of the molecular weight of the standard to estimate the oligomerization state of CYP2J2. Protein standards included thyroglobulin (669 kDa), ferritin (440 kDa), BSA (67 kDa), and cytochrome *c* (14 kDa) as standards.

4.8 REFERENCES

1. Nelson, D. R., Koymans, L., Kamataki, T., Stegeman, J. J., Feyereisen, R., Waxman, D. J., Waterman, M. R., Gotoh, O., Coon, M. J., Estabrook, R. W., Gunsalus, I. C., and Nebert, D. W. (1996) P450 superfamily: update on new sequences, gene mapping, accession numbers and nomenclature, *Pharmacogenetics 6*, 1-42.
2. Anzenbacher, P., and Anzenbacherova, E. (2001) Cytochromes P450 and metabolism of xenobiotics, *Cell Mol Life Sci 58*, 737-747.
3. Pernecky, S. J., Larson, J. R., Philpot, R. M., and Coon, M. J. (1993) Expression of truncated forms of liver microsomal P450 cytochromes 2B4 and 2E1 in Escherichia coli: influence of NH2-terminal region on localization in cytosol and membranes, *Proc Natl Acad Sci U S A 90*, 2651-2655.
4. Williams, P. A., Cosme, J., Sridhar, V., Johnson, E. F., and McRee, D. E. (2000) Mammalian microsomal cytochrome P450 monooxygenase: structural adaptations for membrane binding and functional diversity, *Mol Cell 5*, 121-131.
5. Black, S. D. (1992) Membrane topology of the mammalian P450 cytochromes, *FASEB J 6*, 680-685.
6. Baylon, J. L., Lenov, I. L., Sligar, S. G., and Tajkhorshid, E. (2013) Characterizing the membrane-bound state of cytochrome P450 3A4: structure, depth of insertion, and orientation, *J Am Chem Soc 135*, 8542-8551.
7. Denisov, I. G., Shih, A. Y., and Sligar, S. G. (2012) Structural differences between soluble and membrane bound cytochrome P450s, *J Inorg Biochem 108*, 150-158.
8. Berka, K., Paloncyova, M., Anzenbacher, P., and Otyepka, M. (2013) Behavior of human cytochromes P450 on lipid membranes, *Journal of Physical Chemistry B 117*, 11556-11564.
9. Nath, A., Grinkova, Y. V., Sligar, S. G., and Atkins, W. M. (2007) Ligand binding to cytochrome P450 3A4 in phospholipid bilayer nanodiscs: the effect of model membranes, *J Biol Chem 282*, 28309-28320.
10. Kim, K. H., Ahn, T., and Yun, C. H. (2003) Membrane properties induced by anionic phospholipids and phosphatidylethanolamine are critical for the membrane binding and catalytic activity of human cytochrome P450 3A4, *Biochemistry 42*, 15377-15387.
11. Das, A., Varma, S. S., Mularczyk, C., and Meling, D. D. (2014) Functional investigations of thromboxane synthase (CYP5A1) in lipid bilayers of nanodiscs, *Chembiochem 15*, 892-899.
12. Denisov, I. G., Grinkova, Y. V., McLean, M. A., and Sligar, S. G. (2007) The one-electron autoxidation of human cytochrome P450 3A4, *The Journal of Biological Chemistry 282*, 26865-26873.
13. Berka, K., Hendrychova, T., Anzenbacher, P., and Otyepka, M. (2011) Membrane position of ibuprofen agrees with suggested access path entrance to cytochrome P450 2C9 active site, *J Phys Chem A 115*, 11248-11255.
14. Bayburt, T. H., and Sligar, S. G. (2002) Single-molecule height measurements on microsomal cytochrome P450 in nanometer-scale phospholipid bilayer disks, *Proc Natl Acad Sci U S A 99*, 6725-6730.
15. Arnold, C., Markovic, M., Blossey, K., Wallukat, G., Fischer, R., Dechend, R., Konkel, A., von Schacky, C., Luft, F. C., Muller, D. N., Rothe, M., and Schunck, W. H. (2010)

Arachidonic acid-metabolizing cytochrome P450 enzymes are targets of {omega}-3 fatty acids, *J Biol Chem 285*, 32720-32733.
16. Delozier, T. C., Kissling, G. E., Coulter, S. J., Dai, D., Foley, J. F., Bradbury, J. A., Murphy, E., Steenbergen, C., Zeldin, D. C., and Goldstein, J. A. (2007) Detection of human CYP2C8, CYP2C9, and CYP2J2 in cardiovascular tissues, *Drug Metab Dispos 35*, 682-688.
17. Spector, A. A. (2009) Arachidonic acid cytochrome P450 epoxygenase pathway, *J Lipid Res 50 Suppl*, S52-56.
18. Williams, P. A., Cosme, J., Ward, A., Angove, H. C., Matak Vinkovic, D., and Jhoti, H. (2003) Crystal structure of human cytochrome P450 2C9 with bound warfarin, *Nature 424*, 464-468.
19. Yano, J. K., Hsu, M. H., Griffin, K. J., Stout, C. D., and Johnson, E. F. (2005) Structures of human microsomal cytochrome P450 2A6 complexed with coumarin and methoxsalen, *Nat Struct Mol Biol 12*, 822-823.
20. Schoch, G. A., Yano, J. K., Wester, M. R., Griffin, K. J., Stout, C. D., and Johnson, E. F. (2004) Structure of human microsomal cytochrome P450 2C8. Evidence for a peripheral fatty acid binding site, *J Biol Chem 279*, 9497-9503.
21. Rowland, P., Blaney, F. E., Smyth, M. G., Jones, J. J., Leydon, V. R., Oxbrow, A. K., Lewis, C. J., Tennant, M. G., Modi, S., Eggleston, D. S., Chenery, R. J., and Bridges, A. M. (2006) Crystal structure of human cytochrome P450 2D6, *J Biol Chem 281*, 7614-7622.
22. Williams, P. A., Cosme, J., Vinkovic, D. M., Ward, A., Angove, H. C., Day, P. J., Vonrhein, C., Tickle, I. J., and Jhoti, H. (2004) Crystal structures of human cytochrome P450 3A4 bound to metyrapone and progesterone, *Science 305*, 683-686.
23. DeVore, N. M., and Scott, E. E. (2012) Structures of cytochrome P450 17A1 with prostate cancer drugs abiraterone and TOK-001, *Nature 482*, 116-119.
24. McDougle, D. R., Palaria, A., Magnetta, E., Meling, D. D., and Das, A. (2013) Functional studies of N-terminally modified CYP2J2 epoxygenase in model lipid bilayers, *Protein Science 22*, 964-979.
25. Pikuleva, I. A. (2004) Putative F-G loop is involved in association with the membrane in P450scc (P450 11A1), *Mol Cell Endocrinol 215*, 161-164.
26. Kingsley, L. J., and Lill, M. A. (2014) Ensemble generation and the influence of protein flexibility on geometric tunnel prediction in cytochrome P450 enzymes, *PLoS One 9*, e99408.
27. Murtazina, D., Puchkaev, A. V., Schein, C. H., Oezguen, N., Braun, W., Nanavati, A., and Pikuleva, I. A. (2002) Membrane-protein interactions contribute to efficient 27-hydroxylation of cholesterol by mitochondrial cytochrome P450 27A1, *J Biol Chem 277*, 37582-37589.
28. Kang, J. Y., Ryu, S. H., Park, S. H., Cha, G. S., Kim, D. H., Kim, K. H., Hong, A. W., Ahn, T., Pan, J. G., Joung, Y. H., Kang, H. S., and Yun, C. H. (2014) Chimeric cytochromes P450 engineered by domain swapping and random mutagenesis for producing human metabolites of drugs, *Biotechnol Bioeng 111*, 1313-1322.
29. Cojocaru, V., Balali-Mood, K., Sansom, M. S., and Wade, R. C. (2011) Structure and dynamics of the membrane-bound cytochrome P450 2C9, *PLoS Comput Biol 7*, e1002152.
30. Lonsdale, R., Rouse, S. L., Sansom, M. S., and Mulholland, A. J. (2014) A multiscale approach to modelling drug metabolism by membrane-bound cytochrome P450 enzymes, *PLoS Comput Biol 10*, e1003714.

31. Ohkubo, Y. Z., Pogorelov, T. V., Arcario, M. J., Christensen, G. A., and Tajkhorshid, E. (2012) Accelerating membrane insertion of peripheral proteins with a novel membrane mimetic model, *Biophys J 102*, 2130-2139.
32. Arcario, M. J., and Tajkhorshid, E. (2014) Membrane-induced structural rearrangement and identification of a novel membrane anchor in talin F2F3, *Biophys J 107*, 2059-2069.
33. Vermaas, J. V., and Tajkhorshid, E. (2014) Conformational heterogeneity of alpha-synuclein in membrane, *Biochim Biophys Acta 1838*, 3107-3117.
34. Wu, Z., and Schulten, K. (2014) Synaptotagmin's role in neurotransmitter release likely involves Ca(2+)-induced conformational transition, *Biophys J 107*, 1156-1166.
35. Blanchard, A. E., Arcario, M. J., Schulten, K., and Tajkhorshid, E. (2014) A highly tilted membrane configuration for the prefusion state of synaptobrevin, *Biophys J 107*, 2112-2121.
36. Ahn, T., Guengerich, F. P., and Yun, C. H. (1998) Membrane insertion of cytochrome P450 1A2 promoted by anionic phospholipids, *Biochemistry 37*, 12860-12866.
37. Mustonen, P., Virtanen, J. A., Somerharju, P. J., and Kinnunen, P. K. J. (1987) Binding of Cytochrome-C to Liposomes as Revealed by the Quenching of Fluorescence from Pyrene-Labeled Phospholipids, *Biochemistry 26*, 2991-2997.
38. Song, Y., Yang, Z., Ke, Z., Yao, Y., Hu, X., Sun, Y., Li, H., Yin, J., and Zeng, C. (2012) Expression of 14-3-3gamma in patients with breast cancer: correlation with clinicopathological features and prognosis, *Cancer Epidemiol 36*, 533-536.
39. McDougle, D. R., Kambalyal, A., Meling, D. D., and Das, A. (2014) Endocannabinoids Anandamide and 2-Arachidonoylglycerol Are Substrates for Human CYP2J2 Epoxygenase, *J Pharmacol Exp Ther 351*, 616-627.
40. Kucerka, N., Tristram-Nagle, S., and Nagle, J. F. (2005) Structure of fully hydrated fluid phase lipid bilayers with monounsaturated chains, *J Membr Biol 208*, 193-202.
41. Lafite, P., Andre, F., Zeldin, D. C., Dansette, P. M., and Mansuy, D. (2007) Unusual regioselectivity and active site topology of human cytochrome P450 2J2, *Biochemistry 46*, 10237-10247.
42. Humphrey, W., Dalke, A., and Schulten, K. (1996) VMD: visual molecular dynamics, *J Mol Graph 14*, 33-38, 27-38.
43. Phillips, J. C., Braun, R., Wang, W., Gumbart, J., Tajkhorshid, E., Villa, E., Chipot, C., Skeel, R. D., Kale, L., and Schulten, K. (2005) Scalable molecular dynamics with NAMD, *J Comput Chem 26*, 1781-1802.
44. Mackerell, A. D., Jr., Feig, M., and Brooks, C. L., 3rd. (2004) Extending the treatment of backbone energetics in protein force fields: limitations of gas-phase quantum mechanics in reproducing protein conformational distributions in molecular dynamics simulations, *J Comput Chem 25*, 1400-1415.
45. Vanommeslaeghe, K., Hatcher, E., Acharya, C., Kundu, S., Zhong, S., Shim, J., Darian, E., Guvench, O., Lopes, P., Vorobyov, I., and Mackerell, A. D., Jr. (2010) CHARMM general force field: A force field for drug-like molecules compatible with the CHARMM all-atom additive biological force fields, *J Comput Chem 31*, 671-690.
46. Vanommeslaeghe, K., and MacKerell, A. D., Jr. (2012) Automation of the CHARMM General Force Field (CGenFF) I: bond perception and atom typing, *J Chem Inf Model 52*, 3144-3154.

47. Vanommeslaeghe, K., Raman, E. P., and MacKerell, A. D., Jr. (2012) Automation of the CHARMM General Force Field (CGenFF) II: assignment of bonded parameters and partial atomic charges, *J Chem Inf Model 52*, 3155-3168.
48. Jorgensen, W. L., Chandrasekhar, J., Madura, J. D., Impey, R. W., and Klein, M. L. (1983) Comparison of Simple Potential Functions for Simulating Liquid Water, *J Chem Phys 79*, 926-935.
49. Feller, S. E., Zhang, Y. H., Pastor, R. W., and Brooks, B. R. (1995) Constant-Pressure Molecular-Dynamics Simulation - the Langevin Piston Method, *J Chem Phys 103*, 4613-4621.
50. Martyna, G. J., Tobias, D. J., and Klein, M. L. (1994) Constant-Pressure Molecular-Dynamics Algorithms, *J Chem Phys 101*, 4177-4189.
51. Darden, T., York, D., and Pedersen, L. (1993) Particle Mesh Ewald - an N.Log(N) Method for Ewald Sums in Large Systems, *J Chem Phys 98*, 10089-10092.
52. Zelasko, S., Palaria, A., and Das, A. (2013) Optimizations to achieve high-level expression of cytochrome P450 proteins using Escherichia coli expression systems, *Protein Expres Purif 92*, 77-87.
53. Denisov, I. G., Grinkova, Y. V., Lazarides, A. A., and Sligar, S. G. (2004) Directed self-assembly of monodisperse phospholipid bilayer Nanodiscs with controlled size, *J Am Chem Soc 126*, 3477-3487.
54. Omura, T., and Sato, R. (1964) The Carbon Monoxide-Binding Pigment of Liver Microsomes. Ii. Solubilization, Purification, and Properties, *J Biol Chem 239*, 2379-2385.
55. Meling, D. D., McDougle, D. R., and Das, A. (2014) CYP2J2 epoxygenase membrane anchor plays an important role in facilitating electron transfer from CPR, *J Inorg Biochem 142C*, 47-53.
56. Yu, X. C., Shen, S., and Strobel, H. W. (1995) Denaturation of cytochrome P450 2B1 by guanidine hydrochloride and urea: evidence for a metastable intermediate state of the active site, *Biochemistry 34*, 5511-5517.
57. Bonthuis, D. J., and Netz, R. R. (2013) Beyond the Continuum: How Molecular Solvent Structure Affects Electrostatics and Hydrodynamics at Solid-Electrolyte Interfaces, *Journal of Physical Chemistry B 117*, 11397-11413.
58. Otyepka, M., Skopalik, J., Anzenbacherova, E., and Anzenbacher, P. (2007) What common structural features and variations of mammalian P450s are known to date?, *Bba-Gen Subjects 1770*, 376-389.
59. Wu, S., Moomaw, C. R., Tomer, K. B., Falck, J. R., and Zeldin, D. C. (1996) Molecular cloning and expression of CYP2J2, a human cytochrome P450 arachidonic acid epoxygenase highly expressed in heart, *J Biol Chem 271*, 3460-3468.
60. Grahamlorence, S., Amarneh, B., White, R. E., Peterson, J. A., and Simpson, E. R. (1995) A 3-Dimensional Model of Aromatase Cytochrome-P450, *Protein Science 4*, 1065-1080.
61. Poulos, T. L. (2003) Cytochrome P450 flexibility, *Proc Natl Acad Sci U S A 100*, 13121-13122.
62. Cojocaru, V., Winn, P. J., and Wade, R. C. (2012) Multiple, ligand-dependent routes from the active site of cytochrome P450 2C9, *Curr Drug Metab 13*, 143-154.
63. Mustonen, P., Virtanen, J. A., Somerharju, P. J., and Kinnunen, P. K. (1987) Binding of cytochrome c to liposomes as revealed by the quenching of fluorescence from pyrene-labeled phospholipids, *Biochemistry 26*, 2991-2997.

64. Somerharju, P. (2002) Pyrene-labeled lipids as tools in membrane biophysics and cell biology, *Chem Phys Lipids 116*, 57-74.
65. Eftink, M. R., and Selvidge, L. A. (1982) Fluorescence quenching of liver alcohol dehydrogenase by acrylamide, *Biochemistry 21*, 117-125.

CHAPTER V: ANANDAMIDE AND 2-ARACHIDONOYLGLYCEROL ARE SUBSTRATES FOR HUMAN CYTOCHROME P450 2J2 EPOXYGENASE

5.1 ABSTRACT

The endocannabinoids, anandamide (AEA) and 2 -arachidonoylglycerol (2-AG) are arachidonic acid derivatives that are known to regulate human cardiovascular functions. CYP2J2 is the primary cytochrome P450 in the human heart and is most well-known for the metabolism of arachidonic acid (AA) to the biologically active epoxyeicosatrienoic acids (EETs). Herein we demonstrate that both 2-AG and AEA are substrates for metabolism by CYP2J2 epoxygenase in the model membrane bilayers of nanodiscs. Reactions of CYP2J2 with AEA formed four AEA-epoxyeicosatrienoic acids (EET-EA) whereas incubations with 2-AG yielded detectable levels of only two 2-AG epoxides (EET-G). Notably, 2-AG was shown to undergo enzymatic oxidative cleavage to form AA through a NADPH dependent reaction with CYP2J2 and cytochrome P450 reductase (CPR). The formation of the predominant AEA and 2-AG epoxides were confirmed using microsomes prepared from the left myocardium of porcine and bovine heart tissues. The nuances of the ligand-protein interactions were further characterized using spectral titrations, stopped-flow small molecule ligand egress and molecular modeling. The experimental and theoretical data were in agreement which showed that substitution of the AA carboxylic acid with the 2-AG ester-glycerol changes the binding interaction of these lipids within the CYP2J2 active site leading to different product distributions. In summary, we present data for the functional metabolomics of AEA and 2-AG by a membrane bound cardiovascular epoxygenase.

[3]Reprinted, with permission from Daniel R. McDougle, Amogh Kambalyal, Daryl D. Meling and Aditi Das. Endocannabinoids – Anandamide and 2- Arachidonoylglycerol are Substrates for Human Cytochrome P450 2J2 Epoxygenase. J. Pharmacology and Experimental Therapeutics. 2014 Dec; 351(3):616-27. PMID:25277139

5.2 INTRODUCTION

The human body contains endogenous cannabinoids (endocannabinoids) that elicit similar effects as Δ9-tetrahydrocanabinol (THC), the principal component of cannabis. The two most well characterized endocannabinoids are anandamide (AEA) and 2-arachidonylglycerol (2-AG) that primarily exert their effects by activating the cannabinoid receptors - cannabinoid receptor 1 (CB1) and cannabinoid receptor 2 (CB2). Dysregulation of the endocannabinoids have been implicated in a wide range pathologies including anxiety disorders, neurodegenerative diseases, obesity and heart disease (*1*). Therefore, a thorough understanding of all the potential metabolic pathways in the body is necessary to potentially target and alter these pathophysiological conditions.

Endocannabinoids are derivatives of arachidonic acid (AA) that are stored in the plasma membrane (Figure 5.1). AA is the primary substrate for the eicosanoid synthesizing cascade that includes three branches -the cyclooxygenase (COX), lipoxygenase (LOX) and cytochrome P450 epoxygenase (EPOX) pathways (*2*). Endocannabinoids provide substrate for the eicosanoid-synthesizing cascade through both direct and indirect pathways. The indirect route is through the cleavage of either the AEA ethanolamide motif by fatty acid amide hydrolase (FAAH) or the 2-AG glycerol motif by monoacylglycerol lipase (MAGL), which produces AA that can enter one of the three branches (*2*). Alternatively, AEA can directly enter each of the pathways and produce a diverse range of metabolites with different pharmacological properties when compared to the endocannabinoid parent compound. Prior to this work, 2-AG was only shown to be a direct substrate of the COX and LOX pathways, although the 2-AG epoxide metabolites had been extracted from rat kidney, spleen and brain tissues (*3*). Recently it has been shown that endocannabinoids regulate human cardiovascular functions and are important for homeostasis (Pacher et al., 2009). Thus it is of interest to evaluate the metabolism of endocannabinoids by relevant heart enzymes. In this work, we reveal the nuances of the metabolism of 2-AG and AEA by the predominant EPOX enzyme in the heart, CYP2J2 epoxygenase. CYP2J2 is an extrahepatic cytochrome P450 that is highly expressed in the myocardium and surrounding aortic epithelium and has been shown to be an important regulator of cardiovascular function (*4-6*). CYP2J2 produces potent lipid epoxide mediators derived from AA known as epoxyeicosatrienoic acids (EETs), that are involved in pain, inflammation, kidney and cardiovascular disease (*7, 8*). Additionally, the epoxygenases also produce hydroxyeicosatetraeonic acids (HETE) that are hydroxylated at the 19- or 20-Ω position of AA.

Currently, there are no reports of the direct oxygenation of 2-AG by a CYP. Previous studies with several recombinant P450 epoxygenases (CYP2C8, CYP2C11, and CYP2C3) failed to produce 2-AG epoxide metabolites (*3*). In this work, we show that CYP2J2 epoxygenase metabolizes 2-AG to form 11,12-EET-G and 14,15-EET-G. Several reports have demonstrated the CYP mediated metabolism of AEA to 20-HETE-EA, 5(6)-, 8(9)-, 11(12)- and 14(15)-EET-EAs by CYP3A4, CYP4F2, CYP4X1, CYP2B6 and CYP2D6 (*9-12*). Notably, it was demonstrated that these new metabolites provide different pharmacological profiles when compared to the parent endocannabinoid. Herein we characterize the oxidation of 2-AG and AEA with the heart epoxygenase CYP2J2 using both recombinantly expressed CYP2J2 and heart microsomes.

Additionally, the activities of endocannabinoids are regulated through various activation and inactivation pathways. 2-AG is primarily inactivated through hydrolysis by MAGL (*8*). However, inhibition of this enzyme does not completely block the 2-AG conversion to AA (*13*). This indicates the presence of alternative pathways of attenuation. Here we demonstrate another potential pathway where 2-AG is converted to AA by CYP2J2 and other P450s.

In summary, we elucidate the nuances of binding and metabolism of AA and its derivatives, AEA and 2-AG, by CYP2J2 using LC-MS/MS, LC-MS, spectral titrations, small molecule ligand egress studies and molecular modeling. For all studies with recombinant protein we used nanodiscs (nanoscale lipid bilayers) to solubilize and stabilize membrane bound CYP2J2. Nanodiscs have been previously used to functionally stabilize membrane protein in solution and on surfaces (*14-19*). Importantly, the use of these model membranes significantly reduced scattering and enabled spectroscopic characterization by increasing the solubility of the hydrophobic lipid substrates and membrane protein.

5.3 MATERIALS AND METHODS

Materials. NADPH and NADP were obtained from P212121.com. 1-palmitoyl-2-oleoyl-sn-glycero-3-phosphocholine (POPC) and 1-hexadecanoyl-2-(9Z-octadecenoyl)-sn-glycero-3-phospho-L serine (POPS), 1-heptadecanoyl-2-arachidonoyl-sn-glycero-3-[phosphoinositol-4',5'-bisphosphate] (PIP2) were purchased from Avanti Polar Lipids, Inc. AA, 2-AG, AEA, AEA-d4, MS-PPOH, 14,15-EET, 11-12-EET, 8,9-EET, 5,6-EET, 16,17-EpDPE, 2-(14,15-epoxyeicosatrienoyl glycerol), 14,15-EET ethanolamide was obtained from Cayman Chemical. Whole cow and porcine hearts were obtained fresh from the University of Illinois Meat Sciences

Laboratory. Polyclonal CYP2J2 antibody (catalog No. ABIN1529400) and the HRP conjugated donkey anti-rabbit antibody (Catalog No. ABIN101948) were purchased from antibodies-online.com. Recombinant CYP2C8 supersomes were purchased from BD Biosciences Gentest. The anti-oxidant butylated hydroxytoluene (BHT) was obtained from Sigma. All other materials and reagents used were purchased from Sigma-Aldrich and Fisher Scientific.

Recombinant expression of CYP2J2 in *E. coli*. The recombinant CYP2J2 (construct D34G) was expressed and purified as published previously (*20, 21*). Briefly, DH5alpha cells containing the His-tagged and N-terminally truncated CYP2J2 plasmid and pTGro7 chaperonin plasmid were cultured in 30 mL of Luria Bertani (LB) media with chloroamphenicol (20 µg/mL) and ampicillin (100 µg/mL) at 37˚C and 250 rpm overnight. The resulting culture was used to inoculate 500 mL of Terrific Broth (TB) containing ampicillin (100 µg/mL) and chloroamphenicol (20 µg/mL). The culture was grown at 37˚C and 220 rpm until reaching an O.D. = 1.0, then δ-aminolevulinic acid (500 µl of 0.5 mM) was added and then grown for 2h at 26˚C and 160 rpm. 1 mM of Isopropyl β-D-1-thiogalactopyranoside (IPTG) and 2g of arabinose were added to each 500 mL culture for induction and subsequently grown for an additional 44 hours (Kagawa N and Cao, 2001). The cells were harvested via centrifugation (2800 g for 10 min) using a JA-10 rotor (Beckman Coulter, Brea, CA) at 4˚C. The cells were then sonicated in lysis buffer (DTT, and 0.2 mM phenylmethanesulfonylfluoride (PMSF), 5 mg of DNase and RNase) before ultracentrifugation at 140,000 g from 30 min Ti-45 rotor (Beckman) for membrane fraction isolation. Protein was extracted from the membrane fraction using 1.0% (w/v) cholate and stirred at 4˚C for four hours. The membrane fraction was removed by ultracentrifugation (140,000 g) for 30 min with a Ti-45 rotor (Beckman). CYP2J2 was isolated from the supernatant by running the solution through a Ni-NTA column and eluting in 0.1% (w/v) cholate, 100 mM KPi, 200 mM imidazole and 20% glycerol with yields of ~150 nmol/L.

Expression and purification of cytochrome P450 reductase. Expression of the redox partner cytochrome P450 reductase (CPR) from Rattus norvegicus was described previously (*20*). Briefly, CPR starter cultures were used to inoculate 1L of LB supplemented with ampicillin (100 µg/mL) and riboflavin (1 mg/L) and grown for 4 hours at 37˚C and 220 rpm, before induction with IPTG (1 mL of 1 mM) and then grown for 18-20 hours at 33˚C and 220 rpm. Upon harvesting the cells by centrifugation (2800 g for 10 min), the cells were treated with 500 mL of cold lysozyme buffer (75 mM Tris pH 8.0, 0.25 M sucrose, 0.25 mM EDTA and 0.02 mg/mL lysozyme) and allowed to

stir at 4˚C for 30 min. The resulting solution was centrifuged (2800 g for 10 min), and resuspended in 40 mL of lysis buffer (50 mM Tris pH 8.0 and 1mM PMSF) at 4ºC before sonication on ice (5 cycles x 30 seconds) with 1-minute rests. The membrane fraction was isolated via ultracentrifugation and solubilized in column buffer (50 mM Tris pH 7.7, 0.1 mM EDTA 0.1 mM DTT and 20% (v/v) glycerol) containing 0.2% (v/v) Triton x-100 for an hour at 4ºC. The solution was subjected to ultracentrifugation (140,000 g for 30 min) and the resulting supernatant was loaded onto 2'5'ADP Agarose, followed by detergent removal using a DEAE sepharose column.

Incorporation of CYP2J2 into Nanodiscs. Purified CYP2J2 was incorporated into the membrane bilayers of Nanodiscs as previously described with the only modification being the addition of POPS (*20*). POPS and POPC lipid stocks were combined in chloroform in a 20:80 molar ratio and dried down under a steady stream of N_2. The lipid mixture was reconstituted with 200 mM cholate in phosphate buffer (pH 7.4) and added to membrane scaffold protein MSP1D1(-) in a 65:1 molar ratio and mixed at 4˚C for 1 hour. Purified CYP2J2 (100 mM KPi (pH 7.4), 20% (v/v) glycerol, and 0.1% cholate) was added to the solution in a CYP2J2:MSP molar ratio of 1:10 and mixed for several hours before detergent removal with Amberlite beads overnight. The CYP2J2-Nanodiscs were separated from empty Nanodiscs using a Ni-NTA column and eluted with 100 mM phosphate buffer containing 200 mM imidazole. Homogenous CYP2J2-ND populations were further purified using size-exclusion chromatography utilizing an Alliance 2695 analytical separation module (Waters, Milford, MA) coupled to a Waters 996 photodiode diode array detector (Waters) and a semi-preparative Superdex 10/200 column (GE Healthcare) column.

Recombinant CYP2J2 metabolism assays containing arachidonic acid, anandamide and 2-arachidonoyl glycerol. Incubation mixtures containing CYP2J2-ND (0.2 µM) CPR (0.6 µM), 0.1% (w/v) BHT in 100 mM phosphate buffer (pH 7.4) and either AA, AEA or 2-AG (500 µL total volume) were equilibrated at 37ºC for five minutes before the reaction was initiated with the addition of 1 mM of NADPH. Importantly, CPR was added to the CYP-Nanodisc in the optimal 3:1 CPR to CYP ratio. Previous reports demonstrated the incorporation of the same full-length CPR construct into Nanodiscs using the same conditions as verified by size-exclusion chromatography (*17*). Additionally, in a previous work we prepared discs containing both the full length and truncated forms of 2J2 using size exclusion chromatography and showed that the nanodiscs retain both the P450 and the reductase when incorporated into the membrane bilayer (*20*). Incubations for subsequent qualitative LC-MS analysis contained saturating concentrations

of each substrate whereas samples for quantitative kinetic analysis contained either 1, 5, 10, 20, 40 or 60 µM of each respective substrate. Incubations were reacted for 30 minutes, unless otherwise stated in the figure legends. Samples lacking NADPH were performed in parallel as a routine control. For termination of the reaction, samples were quenched with glacial acetic acid to pH of 3-4 and extracted (three times) with an equal volume of ice cold ethyl acetate, vortexed 1 minute and centrifuged at 1590 g for 3 min for phase separation (*12*). The organic layer was removed and dried under a steady stream N_2 and then reconstituted with 100 µL of methanol. AA, AEA and 2-AG incubations were qualitatively analyzed using LC-MS as described below. For quantitative analysis, LC-MS/MS was used to directly quantify 14,15-, 11,12-, 8,9- and 5,6-EET turnover when AA was used as the substrates. For quantitative analysis of EET-G, extracted samples were split into two pools. The first pool was quantified for EET content without further processing and the second pool was saponified to convert EET-G to the corresponding EET regioisomer and then analyzed for 14,15-, 11,12-, 8,9- and 5,6-EET compositions. The quantification of the 14,15-EET-EA metabolite was accomplished using LC-MS/MS as described below.

Preparation of bovine and porcine microsomes and incubations. Fresh heart microsomes were prepared from the left myocardium of female porcine and male bovine hearts using differential centrifugation methods as described previously (*22*). Briefly, tissue from the left myocardium was dissected to remove the endo- and epicardium and minced. Tissue was weighed and diluted to 20% (w/v) using a buffer containing 250 mM sucrose, 10 mM Tris-Cl (pH 7.5), 1 mM PMSF and a protease inhibitor cocktail for mammalian tissue extraction (Nacalai Tesque #25955-11). Next, tissue was homogenized on ice for 1 minute at maximum speed using a metal Bio-homogenizer (Biospec Inc., Bartlesville, OK). A low speed centrifugation step was employed to remove large tissue debris at 3000 g for 20 minutes at 4°C. The supernatant was then centrifuged at 10,000 g for 20 minute at 4°C using a Ti-45 rotor (Beckman) and then repeated once more. The resulting supernatant was centrifuged at 100,000 g for 90 min at 4°C to pellet the sarcoplasmic reticulum containing heart CYPs. The cell pellet was then re-suspended in 50mM Tris (pH 7.5), 1mM DTT, 1mM EDTA and 20% glycerol with a Teflon homogenizer. The resulting microsomal solution was aliquoted and stored at -80°C until future use. Microsomal protein content was calculated using a BCA assay kit from Thermo Fisher Scientific (Product No. 23233). Incubations with both porcine and bovine microsomes were performed with a concentration of 1 mg/ml of

microsomes with saturating concentrations of AA, AEA and 2-AG and then processed as described with recombinant CYP2J2-ND incubations.

Immunoblotting of CYP2J2 located in cow and porcine heart microsomes. Heart microsomes were prepared as described above and used for CYP2J2 immunoblotting following a previously described protocol (*23*). In short, samples were boiled for 10 minutes 5x Laemmli buffer supplemented with 8 M urea and ran on a 12% SDS polyacrylamide gel. Proteins were transferred to the nitrocellulose membrane and blocked with 5% low-fat milk in Tris-buffered saline with tween 20 (TBST) for 1 hour before adding the primary polyclonal antibody raised against the 250-275 segment of human CYP2J2 (antibodies-online.com, catalog No. ABIN1529400). The membrane was washed three times with TBST and the HRP conjugated donkey anti-rabbit antibody (Catalog No. ABIN101948) was used for detection. Blots were visualized using a HRP development solution (Thermo Sci. Catalog No. 34095) and a ChemiDoc XRS+ system (Biorad Inc., Hercules, CA).

Saponification of EET-G regioisomers to EETs and quantification. For the quantification of EET-G in solution, the extracted fatty acids were cleaved from the glycerol backbone using methanolic potassium hydroxide (KOH) hydrolysis as previously described (*24*). Extracted samples were hydrolyzed in 1 mL of methanol containing 0.4 N KOH and incubated at 50ºC for one hour. Next 1.5 mL of Millipore water was added and glacial acetic acid was used to achieve pH 3-4. Samples were extracted with an equal volume of ice cold ethyl acetate (3x), vortexed 1 minute and centrifuged at 1600 g for 3 min for phase separation (*12*). The organic layer was removed and dried under a steady stream of N_2 and then reconstituted with 100 µL of methanol. Thus, the saponified sample contained both free EETs originally present in solution and EETs derived from EET-G hydrolysis. EET-G quantification at the time of reaction quenching was calculated using Equation 1.

(Equation 1) EET-G = EET (saponified) - Free EET

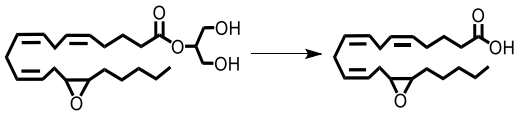

Equation 1. EET-G to EET conversion. Extracted EET-G regioisomers were converted to their corresponding EETs using methanolic KOH (0.4 N) and quantified using LC-MS/MS as described below.

LC-ESI-MS product analysis. AA, AEA and 2-AG regioisomers were resolved using a C18 column 2.1 x 150 mm, 3.5 µM (Waters, XTerra, P/N 186000408) and a Waters Alliance 2695 HPLC coupled to an electrospray ionization (ESI) source. For analysis of AA and AEA metabolites, the mobile phases consisted of mobile phase A (Acetonitrile/H_2O/Formic Acid, 95:5:0.1) and mobile phase B (Acetonitrile/H_2O/Formic Acid, 5:95:0.1) and were ran from 0-1 min, 60% A; 1-41 min, 60-20% A; 41-42 min 0% A and then returned to initial conditions. The same solvent system was used in the analysis of 2-AG metabolites with a gradient of 0-1 min, 70% A; 1-51 min, 70-20% A; 51-52 min 0% A and then returned to initial conditions. For ESI, a Q-TOF Ultima time of flight mass spectrometer was used in positive ion mode for analysis of AEA, with a spray voltage of 4.5 V and capillary temperature of 200ºC. Data were collected and processed using Mass Lynx software (version 4.1), initially scanning from 200 to 800 mass to charge ratio (m/z) and processed for the selected AEA-EET m/z of 364. The mass and elution time of the 14,15-EET-EA moiety was confirmed using the commercially available authentic standard. The detection of AA and 2-AG metabolites were detected with the same system in negative ion mode, with a cone voltage of 35 V and a 200ºC desolvation temperature, scanning from 200 to 800 mass to charge ratio (m/z) and processed for the selected EET m/z of 319 and EET-G m/z of 393-394. The mass and elution times of the EET regio-isomers were confirmed with commercially available authentic standards. For 2-AG analysis, the mass and elution time of the commercially available 14,15-EET-G, EETs and AA lipids were confirmed with authentic standards purchased from Cayman Chemical.

Liquid chromatography- tandem mass spectrometry for quantitation of 14,15-, 11,12-, 8,9-, 5,6-EETs, 14,15-EET-EA and 14,15-EET-G. Quantification EET regioisomers derived from *in vitro* CYP2J2 incubations were analyzed with the 5500 QTRAP LC/MS/MS system (AB Sciex, Foster City, CA) with a 1200 series HPLC system (Agilent Technologies, Santa Clara, CA) including a degasser, an autosampler, and a binary pump. The LC separation was performed on an Agilent Zorbax Eclipse XDB C18 column (4.6 x 150 mm, 5 µm) (Agilent Technologies, Santa Clara, CA) with mobile phase A (0.1% formic acid in water) and mobile phase B (0.1% formic acid in acetonitrile). The flow rate was 0.4 mL/min. The linear gradient was as follows: 0-2 min, 90% A; 8 min, 50% A; 13-25 min, 25% A; 30 min, 20% A; 35 min, 15% A; 36-42 min, 90% A. The autosampler was set at 5ºC. The injection volume was 5 µL. Mass spectra were acquired with negative electrospray ionization (ESI) and the ion spray voltage was -4500 V. The source

temperature was 450 ºC. The curtain gas, ion source gas 1, and ion source gas 2 were 32, 50, and 65, respectively. Multiple reaction monitoring (MRM) was used to quantify EETs: 5(6)-EET m/z 319.2 → m/z 191.0; 8(9)-EET m/z 319.2 → m/z 155.1; 11(12)-EET m/z 319.2 → m/z 167.0; 14(15)-EET m/z 319.2 → m/z 219.1; internal standard 16(17)-EpDPE m/z 343.2 → m/z 274.1.

Quantification of 14,15-EET-EA samples were analyzed using the with the 5500 QTRAP LC/MS/MS system with a LC separation method consisting of 0-1min, 50%A; 5-17min, 0%A; 17.5-23min, 50%A. The autosampler was set at 5ºC. The injection volume was 2 µL. Mass spectra were acquired with positive electrospray ionization (ESI) and the ion spray voltage was 5500 V. The source temperature was 450 ºC. The curtain gas, ion source gas 1, and ion source gas 2 were 32, 50, and 65, respectively. Multiple reaction monitoring (MRM) was used to quantify 14(15)-EET Ethanolamide (m/z 364.3 → m/z 346.3) with spiked d4-Anandamide (m/z 352.3 → m/z 287.2) as the internal standard).

Direct quantification of the 14,15-EET-G regioisomer were analyzed using the 5500 QTRAP LC/MS/MS system with a linear gradient as follows: 0-2 min, 90% A; 8 min, 55% A; 13-25 min, 40% A; 30 min, 30% A; 35 min, 25% A; 40 min, 2% A; 45-47min, 15%A; 48-56min, 0%A; 57-62min, 90%A. Mass spectra were acquired under positive (ion spray voltage at 5500 V) electrospray ionization (ESI). The source temperature was 450 ºC. 14,15-EET-G (m/z 395.3--> m/z 377.3) was measured in positive ESI with arachidonoly-1-thio-glycerol (m/z 395.3--> m/z 287.3) as an internal standard.

Quantification of CYP2J2-ND rate of 2-AG ester cleavage. The rate of 2-AG ester cleavage was quantified using a reversed-phase liquid chromatography (HPLC) system consisting of an Alliance 2695 analytical separation module (Waters, Milford MA) coupled to a Waters 996 photodiode array (PDA) and a C18 column, 1.3 Å, 2.1 mm × 50 mm, 3.5 µm pore size column (Waters, XTerra). The mobile system was composed of two solutions: solvent A (H_2O/ACN/AcOH 95:5:0.1) and solvent B (H_2O/ACN/AcOH 5:95:0.1). The linear gradient was as follows: 0-1 min, 60% A; 30 min, 20% A; 31 min, 0% A; return to initial conditions. Elution times of 12.6 min for 2-AG and 19.7 min for AA were verified with authentic standards. Quantification of free AA was calculated using AA absorbance at 204 nm. For kinetic analysis, samples containing CYP2J2-ND (50 pmol; 0.2 µM), CPR (150 pmol; 0.6 µM), 0.1% BHT in 0.1M phosphate buffer (pH 7.4) were incubated at 37ºC for 5 minutes with 1, 5, 10, 20, 40 and 80 µM

of 2-AG before initiation of reaction with 1 mM NADPH at 37 ºC for 20 minutes. Controls lacking either NADPH or CYP2J2 were run simultaneously with 80 µM of 2-AG.

CYP2J2 MOE Homology Modeling. A multiple sequence alignment was performed using the protein data bank to cross-reference the CYP2J2 sequence against 2A1, 2D6, 2E1, 2R1, 2A6, 2C8, 2B4, 2C5, 2C9, 2A13. For construction of the CYP2J2 homology model, crystal structure PDB coordinates were used for the isozymes' with the closest homology to 2J2 and included CYP2B4 (backbone-42% primary sequence homology), 2C8 (B-region-38% primary sequence homology), 2R1 (FG region-40% primary sequence homology) and 2C9 (β4-region-26% primary sequence homology). An open CYP2J2 conformation was initially used to dock AA, AEA, 2-AG following previously described procedures (*25*). Two apparent CYP2J2 active site cavities, exhibited adjacent/overlapping areas near the heme in agreement with the highest propensity of ligand binding number (PLB) and were both used for docking of each respective substrate. Next, we conducted an energy minimization step for each respective ligand conformation and the induced fitting resulted in the CYP2J2-substrate model used to examine heme and ligand distances as well as the predicted interacting active site residues. Lastly, interaction energies were calculated for each substrate to examine the energetics and feasibility of substrate binding.

Spectral titrations of CYP2J2-ND. Spectral binding studies were performed by titrating AA (both arachidonic acid and sodium arachidonate), AEA, 2-AG, MS-PPOH and ebastine against CYP2J2-Nanodiscs (8 µM) in 100 mM phosphate buffer (pH 7.4). Importantly, substrate stocks were prepared with DMSO (5 mM and 50 mM) after the addition of ethanol and acetonitrile were determined to cause type I binding. CYP2J2-ND were incrementally titrated with increasing concentrations of each putative substrate (either 5 mM or 50 mM stocks) at 22ºC and allowed to equilibrate for 5 minutes before measuring the spectra. The total dilution of the original CYP2J2 concentration was ≤ 1.5%. Absorbance spectra were collected from 800-200 nm using a Cary Bio 300 UV-Vis spectrophotometer (Agilent Technologies, Santa Clara CA). Raw absorbance spectra were processed to the corresponding subtraction spectra using a standard MATLAB subroutine (Mathworks Inc., MI). The absolute absorbance difference of the subtraction spectra (peak and trough) were plotted against the corresponding substrate concentration in Origin Lab (Origin Lab Inc., Northhampton, MA) and fitted using a single binding isotherm (Eq. 2).

(Equation 2) $\Delta A = A_{max}[S] / (Ks + [S])$

Where ΔA is the absorbance difference at each difference spectra peak and trough, A_{max} is the amplitude corresponding to maximal spin shift, K_s is the spectral dissociation constant, S is the substrate concentration. None of the substrates investigated exhibited any homotropic cooperativity and hence the titration data was fitted to a single binding isotherm.

Cyanide binding and equilibrium constant (K_s) determination for CYP2J2-ND. The steady-state cyanide spectral equilibrium constants were determined by titrating cyanide concentrations (800 mM and 4 M stocks) against ~3 μM of CYP2J2-ND in the absence and the presence of 40 μM of AA, AEA, 2-AG and MS-PPOH until saturation was reached (*15*). The CYP2J2 concentration change due to cyanide addition was ≤ 3% and did not affect Soret peak height. The raw data collected was converted into the difference spectra using a MATLAB subroutine (Mathworks Inc., MI). The ΔA ($\Delta A_{444-414nm}$) was plotted against the corresponding cyanide concentration and fitted to a single binding isotherm equation using Origin Pro 8.6 (San Clemente, CA) with equation 1 where $\Delta A = \Delta A_{444-414nm}$.

Transient cyanide binding kinetics to CYP2J2 active site measured using stopped-flow spectroscopy. The cyanide binding kinetics to the CYP2J2 active site in the absence and presence of varying concentrations of AA, AEA, 2-AG and MS-PPOH was determined using stopped-flow spectroscopy. Raw data was collected using an Applied Photophysics SX.18MV (Leatherhead, UK) spectrophotometer to monitor the rate of cyanide binding. A dual syringe system was prepared, with syringe I containing CYP2J2-ND in the absence or presence of varying concentrations (10, 20 and 40 μM) of substrate and syringe 2 containing 80 mM cyanide in the absence or presence of varying concentrations (10, 20 and 40 μM) of substrate. The relatively high cyanide concentration was selected based on steady state cyanide binding measurements and was necessary to ensure pseudo first-order binding kinetics (*26*). The parameters for rapid mixing and data collection were as follows: 1.5 msec of dead time, external triggering mechanism, photodiode array detection and collection obtained on a logarithmic scale over 20 seconds. The raw data was converted to the difference spectra by subtracting each successive scan from the time = 0 scan using a MATLAB subroutine (Mathworks Inc., MI) that produced the typical 446 and 415 nm cyanide binding peaks. The difference of absorbance was plotted against time and analyzed with a double exponential equation using Origin Pro 8.6.

(Equation 3) $\Delta A_{444-414nm} = A_0 + A_1 e^{xk_1} + A_2 e^{xk_2}$

Where A_1 and A_2 are the amplitudes of the fast and slow phases of the reaction respectively and k_1 and k_2 are the rates of fast and slow phases of substrate binding to the protein, determined from fitting data obtained to equation 3.

Data Analysis. Data were analyzed and presented as means ± standard error. For all experiments, data were collected in triplicate (n = 3) or greater. Stopped flow data were analyzed for statistical significance using a student's t-test where $p < 0.05$, $p < 0.01$ and $p < 0.001$ were denoted by *, **, and ***, respectively

5.4 RESULTS

CYP2J2 mediated metabolism of AA and AEA determined using LC-ESI-MS. We first investigated the metabolism of AA and AEA by CYP2J2. CYP2J2 was recombinantly expressed in *E.coli*, purified and assembled into nanodiscs as described in the materials and methods. Due to increased functional stability of the CYP2J2-CPR-nanodisc system, all the studies reported here were done with the proteins incorporated into nanodiscs. To examine the metabolism of AA and AEA, a LC-ESI-MS method was developed to qualitatively assess the product formation. Importantly, the use of a slow linear gradient was necessary for separation of the regioisomers and structural identification by mass and elution time. Product analysis of CYP2J2-ND-CPR incubations with AA produced four regioisomers (m/z = 319.5) corresponding to the mass and elution times of 14,15-, 11,12-, 8,9- and 5,6-EET (Figure 5.2A). The additional peaks (m/z 319), 19-HETE, was confirmed at earlier elution times (11 min). Similarly, analysis of CYP2J2 and AEA incubations produced the same olefin oxygenation pattern as AA, with a regioisomer corresponding to the elution times of 14,15-EET-EA as confirmed using the authentic standard (Figure 5.2B). The identity of the 11,12-, 8,9-, and 5,6-EET-EA were extrapolated based on literature describing the elution profile and peak mass confirmation. Similar to AA, the presence of two additional metabolites corresponding to 19- and 20-HETE-EAs were observed. These results show that both AA and AEA are substrates of CYP2J2 and form four epoxide products similar to previous reports with other P450s (Snider et al., 2010).

CYP2J2 mediated metabolism of 2-AG determined using LC-ESI-MS. The in vitro incubations containing CYP2J2-ND-CPR and 2-AG produced the following products - two detectable 2-AG epoxide metabolites (m/z 393.3), arachidonic acid (m/z 303.3) and EETs (m/z 319.5) as shown in Figure 5.3. Authentic standards were used to confirm the 14,15-EET-G, EETs (14,15-, 11,12-, 8,9-, 5,6-EET) and AA metabolites. While the 11,12-EET-G was not

commercially available, the results from EET-G saponification confirmed the production of the 11,12-regioisomer.

In contrast to AA and AEA, only two olefin sites of 2-AG were epoxidized to form 2-AG-EETs (m/z 393.3). Thus, the functional data suggests that the interaction of 2-AG within the CYP2J2 binding pocket is influenced by the presence of the bulky glycerol group of 2-AG (Figure 5.1). Previous incubations with other P450s have failed to produce the EET-G regioisomers (*3*). Here we report that CYP2J2 is identified as an isoform of P450 that produces epoxide 2-AG metabolites. As a control we analyzed CYP2C8 (supersomes) with 2-AG following the same methodology and failed to observe any detectable EET-G formation (Figure 5.8). This suggests that CYP2J2 may be unique in the epoxidation of 2-AG as compared to other family 2 P450s.

Quantitative analysis of CYP2J2 mediated epoxidation of 2-AG and AEA using LC-ESI-MS/MS. The detection and quantification of fatty acids and their metabolites have been most commonly examined using radio flow HPLC due to the high sensitivity and ease of use (*27*). Alternatively, detection by mass spectrometry after derivatization, coupled with gas chromatography or liquid chromatography has also been widely used for EET analysis (*28*). Here we successfully used HPLC coupled to a triple quadrupole detector utilizing one of the most sensitive commercially available ion trap (QTRAP 5500) which enabled a highly sensitive, accurate and reproducible method for detection of all the EET regioisomers in multiple reaction monitoring (MRM) mode. The limit of quantitation (LOQ) with a 10:1 signal to noise ratio for 5(6)-EET was 5.0 ng/mL, whereas 8,9-, 11,12-, 14,15-EET were calculated at 2.5 ng/mL. Prior to each run a six point standard curve was generated for each set of samples using authentic standards. Extraction efficiency was calculated for each of the EET regioisomers using the acidification and the three step ethyl acetate extraction. 14,15-, 11,12-, and 8,9-, and 5,6-EETs were extracted from the reaction mixture with a 95% or greater efficiency. Reaction linearity was demonstrated for each of the substrates at 15, 30 and 60 minutes with R^2 values of 0.98 or greater. The advantages of a LC-MS/MS method are that it provides structural elucidation, quantification and efficiency with excellent sensitivity without the need of derivatization. This method should be widely applicable for complex biological samples with low levels of EETs. The identification of the metabolites of 2-AG and AEA were followed by quantification and measurement of the rate of formation using a LC-MS-MS method as described in the materials and method section (Figure 5.4).

The rates of formation of the two EET-G regioisomers were determined by saponification of the EET-G to the corresponding EET regioisomers. The final value of EETs arising from EET-G was obtained by subtracting the free EETs as determined in the materials and methods. The kinetics of EET-G formation were as follows: 14,15-EET-G Vmax = 265.4 ± 12.3 pmol/min/nmol and Km = 32.6 ± 1.7 μM; 11,12-EET-G Vmax = 125.5 ± 5.2 pmol/min/nmol and Km = 13.6 ± 1.3 μM.

In a separate experiment, the rate of metabolism of arachidonic acid to form the four EET regio-isomers was measured in the presence of saturating concentrations of AA. Catalytic rates were calculated at 103 ± 4.6, 61.5 ± 5.6, 18.4 ± 1.7 and 8.9 ± 0.1 pmol/min/nmol of CYP2J2 for 14,15-, 11,12-, 8,9- and 5,6-EET, respectively.

Additionally, we examined the CYP2J2 mediated epoxidation of saturating amounts of AEA (60 μM) towards the production of 14,15-EET-EA which was calculated to be 391 ± 12 pmol/min/nmol of CYP2J2. Thus, the production of the 14,15-EET-EA appears to proceed at a significantly faster rate when compared to the production 14,15-EET from AA despite sharing a similar qualitative product profile and binding characteristics as discussed later.

CYP2J2 mediated 2-AG ester cleavage and production of free AA. The ESI-LC-MS product analysis of 2-AG incubations revealed significant amounts of free AA in solution (Figure 5.3). Control experiments showed that the conversion of 2-AG to AA required the presence of both NADPH and CPR for catalytic turnover indicating that the reaction proceeded through an oxidative mechanism (controls not shown). As seen in Figure 5.4D, analysis of 2-AG incubations followed Michaelis-Menten kinetics, indicating that the reaction was dependent on substrate binding. The Km of the ester cleavage reaction was calculated at 3.25 μM with a V_{max} of 2.2 ± 0.2 nmol/min/nmol of CYP2J2. Samples lacking NADPH and CYP2J2 were ran in parallel as controls. Arachidonic acid was not detected in the NADPH-free sample. Additionally, 2-AG was stable in buffer at 37ºC with negligible hydrolysis. The ability of CYP to mediate ester cleavage reactions has long been reported and rates determined in this work show similar catalytic properties of other CYP isozymes (*29, 30*). However, this is the first account of the P450 mediated cleavage of a fatty acid ester of an endogenous substrate. The same reactions were run with CYP2C8 (supersomes) which also produced AA in a NADPH dependent reaction (Figure 5.8). However, CYP2C8 epoxygenase did not demonstrate the ability to oxygenate the 2-AG olefin bonds.

Bovine and porcine heart microsomes metabolism of AA and 2-AG. To examine whether the novel endocannabinoid epoxygenation reactions would occur within a complex environment in the

presence of other proteins, we prepared heart microsomes from the tissue of bovine and porcine left ventricular myocardium. The rate of metabolism of AA, AEA and 2-AG are summarized in Table 5.2. We chose bovine and porcine species because they both contain CYP2J2 with high sequence homology to humans (Figure 5.10). CYP2J2 immunoblotting of the bovine and porcine microsomes were performed using a polyclonal rabbit IgG antibody for human CYP2J2. The microsomal preparations cross-reacted with the CYP2J2 antibody demonstrating the presence of CYP2J2 cross-reactivity in bovine and porcine hearts (Figure 5.11). First, the functionality was assessed by measuring AA metabolism of bovine and porcine microsomes which produced 1.8 ± 0.3 and 2.08 ± 0.02 pmol min^{-1} mg^{-1} microsomal protein of EETs (all regio-isomers), respectively. Next we quantified 2-AG metabolism by directly measuring the production of the 14,15-EET-G regioisomer by bovine and porcine microsomes that was calculated at 1.17 ± 0.57 and 1.1 ± 0.55 pmol min^{-1} mg^{-1} microsomal protein, respectively. The 14,15-EET-EA isomer was produced with a higher turnover in both bovine and porcine microsomes with values of 1.96 ± 0.05 and 2.25 ± 0.07 pmol min^{-1} mg^{-1} microsomal protein, respectively.

CYP2J2 mediated lipase activity. CYP2J2 mediated oxidative cleavage of 2-AG into arachidonic acid raised questions whether this enzyme could act as a lipase and use AA containing phospholipids as direct substrates. PIP2 (phosphatidylinositol 4,5-bisphospate) is present in the plasma membrane where it is cleaved by phospholipase C to produce AA for subsequent entry into the eicosanoid cascade (*8*). Thus, we incubated PIP2 with CYP2J2-ND-CPR-NADPH system utilizing PIP2 concentrations below its critical micelle formation (CMC). In these experiments we did not to observe formation of AA or diacylglycerol (*31*).

Spectral binding studies of CYP2J2 with AA, AEA and 2-AG. In an effort to understand the binding interactions of AA and its derivatives (AEA and 2-AG) with the active site of CYP2J2, we performed spectroscopic binding studies. First, the interactions of AA, AEA, 2-AG, ebastine and MS-PPOH with the CYP2J2-ND active site were investigated using UV-Vis spectral binding titrations (Figure 5.5). As controls, the spectral binding properties of the potent epoxygenase inhibitor N-methylsulfonyl-6-(2-propargyloxyphenyl) hexanamide (MS-PPOH) (*32*) and ebastine were investigated and both induced type-I shifts with apparent spectral binding constants (K_s) of 10.8 ± 1.5 μM and 5.6 ± 0.7, respectively.

The fatty acids presented with smaller changes in spin-state and minor shifts in Soret band. Specifically, the Soret band at 417 nm red-shifted by 0.5 nm with a slight decrease in amplitude

for both AA and AEA. The difference spectra revealed prominent troughs for both ligands at 414 nm and broad peaks at 434 and 435 nm for AA and AEA, respectively (Figure 5.5A). Both substrates were fitted to single binding isotherm with apparent K_s of 11.3 ± 1.3 μM for AA and 13.1 ± 1.4 μM for AEA (Figure 5.5D). The similarities between AA and AEA spectral shifts and binding equilibrium suggest that the presence of the ethanolamide (AEA) motif does not significantly alter substrate distances and positioning in relation to the heme when compared with AA. Conversely, 2-AG spectral titrations resulted in a blue-shift while slightly decreasing the Soret. The apparent K_s of binding for 2-AG was calculated at 18 ± 2.7 μM. Taken together, these data demonstrate that the modification of the carboxylic acid of the arachidonic acid with the glycerol moiety affects binding in CYP2J2's large yet narrow binding cavity (*33*). Note that the observed Soret shifts are not as prominent as xenobiotic P450 substrates, yet are consistent with the few published spectra of other fatty acids binding to membrane bound CYPs (*34*). Moreover, the lack of significant Soret perturbations corresponds to the relatively low turnover rates of the AA metabolizing epoxygenases such as CYP2J2 (*35*). Additionally, these experiments were further validated using steady state cyanide binding experiments in the presence of AA, AEA and 2-AG to probe the access and binding of cyanide to the heme (Figure 5.9).

Kinetics of cyanide binding to CYP2J2-ND in the presence of substrates. The cyanide binding kinetics of CYP2J2 was investigated in the absence or presence of hydrophobic substrates using stopped-flow spectroscopy. For each substrate tested, rapid mixing and formation of the heme-cyanide complex red-shifted the Soret (Figure 5.6A). As shown in Figure 5.6B, the difference spectra Δ ($A_{444-414\ nm}$) were analyzed as a function of time and yielded an exponential biphasic curve that were comprised of a fast and slow phase (*36*). The "fast phase" corresponds to the rate of cyanide binding to the ferric heme active site. Specifically, it can be used as a direct measure of substrate egress from the immediate vicinity of the heme active site to accommodate formation of the cyanide complex. In the fast phase the presence of increasing concentrations ebastine significantly decreased cyanide-binding rates in a concentration-dependent manner. Conversely, the fatty acid ligands only slightly decreased cyanide binding (Figure 5.6C). The ratio of the fast-and slow-phase amplitudes were compared to determine how ligand concentrations affect the presence of the ratios. As seen in Figure 5.6D-G, saturating concentrations of ebastine significantly increases the ratio of the slow-phase (17.4% to 66.4%) whereas the arachidonate containing ligands only slightly increased the slow-phase ~10%. To rule out non-specific fatty acid

binding we examined the rates of cyanide binding in the presence of saturating concentrations of palmitate. As shown in Figure 5.6H the presence of palmitate does not noticeably alter the ratio of the two phases. While not dramatic, the reported results provide important characterization of the nature of fatty acid binding.

CYP2J2 Homology Modeling with AA, AEA and 2-AG. Molecular Operating Environment (MOE, Chemical Computing Group) software was used to identify substrate-binding characteristics within the active site of a CYP2J2 homology model. A hybrid structure model was constructed from the crystal PDB coordinates of similar CYP isozymes (class dependent sequence alignment strategy) as described in the materials and methods section (*37*). This approach takes advantage of the conserved sequences that maintain the secondary and tertiary P450 folds to generate the core structures surrounding the buried catalytic sites. Given the fatty acids relatively low turnover there are likely many 'unproductive' conformations within the active site. As shown in Figure 5.7A, AA was docked in the most preferred configuration for epoxidation of the 14,15-olefin when closest to the heme (5.1 Å), followed by the 11,12-, 8,9-, and 5,6-olefins with calculated heme distances of 8.6, 11.3 and 12.9 Å, respectively. As shown in Figure 5.7B, the distances of the AEA 14,15-, 11,12-, 8,9- and 5,6-olefins were calculated at 6, 8.5, 12.1 and 13.5 Å, respectively. Interestingly, 2-AG (Figure 5.7C) yielded significantly different active site interactions albeit with similar heme distances of the 14,15-, 11,12-, 8,9- and 5,6-olefin estimated at 5.9, 7.6, 9 and 11.5 Å, respectively. The interaction potential energies predict feasibility of binding and were similar for each polyunsaturated fatty acid with calculations of -68.3 kcal/mol, -69.4 kcal/mol, and -73.4 kcal/mol for AA, 2-AG and AEA, respectively. Thus, the olefin distances of the MOE model were in agreement experimental differences observed in AA, AEA and 2-AG metabolism. Additionally, the model predicted significantly different binding characteristics based on the presence of the carboxylate/ethanolamide or glycerol moiety. For example, a patch of hydrophobic residues appeared to mediate AA and AEA positioning within the CYP2J2 active site with Pro 112, Ile 487 and Ile 376 common for both substrates. Interactions of polar residues were fewer with only Gln 228 interacting with the polar carboxylate/ethanolamide groups. Conversely, positioning of the 2-AG utilized both hydrophobic residues (Ile127, Val 380 and Ile 487) as well as interactions of the hydrophilic glycerol moiety with polar CYP2J2 residues (Asn 231, Ser 224, Gln 228 and Ser 64). The relatively fewer polar interactions of AA and AEA might enable sampling of different conformations of these substrates in the active site leading to the epoxidation

of the 8,9- and 5,6-olefin groups. Conversely, the glycerol group appears tethered and cannot sample orientations for epoxidation of the 8,9- and 5,6-olefins. In absence of a high resolution CYP2J2 crystal structure, this model provides a useful tool to predict the interactions of AA, AEA and 2-AG within the active that provide CYP2J2's regioselectivity.

5.5 DISCUSSION

Extrahepatic CYP2J2 epoxygenase metabolizes AA to form EETs that are essential for regulation of blood pressure and cardiovascular function (*38*). As previously mentioned, AA derived endocannabinoids play an important role in the cardiovascular system. Therefore we explored the metabolism of functionalized arachidonate containing lipids such as the endocannabionids with the cytochrome P450 most highly expressed in the human heart. The two most well characterized, arachidonic acid derived endocannabinoids are AEA and 2-AG whose dysregulation have been implicated in a wide range of pathophysiological states (*1, 39, 40*). Herein, we demonstrate CYP2J2 mediated metabolism of AEA and 2-AG using recombinant human CYP2J2 and heart microsomes derived from bovine and porcine tissues. The results provided here show the endocannanbinoids 2-AG and AEA are both substrates of human CYP2J2 and that the predominant products, 14,15-EET-EA and 14,15-EET-G, are produced in heart microsomal systems of two different mammalian species, lending credibility to the proposed pathway in tissues.

The qualitative product analysis of CYP2J2-AEA incubations by LC-MS revealed four epoxide regio-isomers at the 5,6-, 8,9-, 11,12- and 14,15-olefin positions. The quantitative analysis of 14,15-EET-EA exhibited 4-fold more product when compared to the rate of formation of 14,15-EET regioisomer from AA. Previously, the oxygenation of AEA into a single hydroxy-product, 20-HETE ethanolamide, as well as four epoxide regio-isomers 5,6-, 8,9-, 11,12- and 14,15-EET-EA were demonstrated by several hepatic P450s including CYP2D6, CYP3A4 and CYP4F2 (*41*). However, this is the first report of the AEA metabolism by a CYP epoxygenase that is highly expressed in the myocardium and endocardium. Given the increasing reports of an endocannabinoid mediated regulation of blood pressure and the cardiovascular system, the role of the oxygenated AEA metabolites may provide an interesting avenue for future studies. For instance, AEA is a partial agonist of both CB1 and CB2 receptors whereas the 5,6-EET-EA metabolite selectively binds CB2 with much greater affinity (*42*). Additionally there is mounting evidence of CB2-cardioprotection versus CB1-cardiotoxicity and the ability to selectively target these pathways may provide a useful therapeutic target for the treatment of heart disease (*40, 43*).

Moreover, less is known about the physiological effects of the other EET-EA metabolites and whether they also exhibit differential receptor binding profiles and in vivo effects.

Previously, the epoxide metabolites of 2-AG, 14,15- and 11,12-EET-G were found endogenously in rat kidney and spleen tissues. These metabolites bound both CB1 and CB2 with greater affinity than 2-AG (*3*). Incubations with family 2 CYPs - CYP2C8, CYP2C11, and CYP2C3 failed to produce these metabolites (*3*). Therefore it was concluded that these epoxide metabolites do not arise from epoxidation of 2-AG through the CYP pathway. Our modeling studies show that CYP2J2 contains a relatively large active site that can accommodate 2-AG as compared to other family 2 CYPs. Moreover, we show it is possible to directly oxygenate 2-AG by CYP2J2 to produce relatively high levels of both 14,15- and 11,12-EET-G. Additionally our results show that CYP2J2 produces only two epoxide metabolites - 14,15-EET-G and 11,12-EET-G similar to the 2-AG epoxide metabolites identified *in vivo*. Thus, these results provide an alternative pathway for the biosynthesis of 2-AG epoxides through the direct enzymatic oxygenation by CYP2J2.

Due to the demonstrated beneficial functions of the endocannabinoids, there are several drugs in the market that target the enzymes that attenuate the *in vivo* levels of these substrates (*44*). Previous inhibition of enzymes that inactivate AEA and 2-AG have shown that the inhibition is incomplete (*13*) indicating that there may be alternative pathways of attenuation of these endocannabinoids. We demonstrate here that 2-AG is converted to AA by CYP2J2 and CYP2C8 using an oxidative ester cleavage mechanism. Subsequent control experiments confirmed that the cleavage proceeded via an oxidative NADPH-dependent CYP2J2-CPR mechanism. To our knowledge, these results provide the first evidence of a P450 mediated endocannabinoid attenuation pathway for production of free arachidonic acid for subsequent metabolism in the classical eicosanoid pathways (COX, LOX and EPOX). Thus far, there have been no reports of an oxidative ester cleavage mechanism of endogenous 2-AG. However, other P450 isozymes have long been recognized as important sources of carbonyl products through non-hydrolytic ester cleavage reactions (*29*, *30*).

The potential of CYP2J2 to produce its own substrate through the cleavage of arachidonic acid from PIP2 was also explored. Several different conditions were examined and it was concluded the PIP2 is not a CYP2J2 substrate. Considering the tissue distribution of cytochrome P450s, the role of a CYP mediated attenuation of 2-AG may constitute further examination *in vivo*.

The binding interactions of arachidonic acid and its derivatives with the active site of CYP2J2 revealed relatively low spin state changes. Thus, the uses of the nanoscale lipid bilayers of nanodiscs were essential for the characterization of AA, AEA and 2-AG binding in spectroscopic studies with minimal spectral scattering. In general, there are very few examples of human CYP titrations in the literature, likely due to issues with solubility, scattering and low spin state changes. Interestingly, the few that have been published typically present with a similar spectra to what is presented in this work (*34*). The ebastine, MS-PPOH and 2-AG Soret shifts present with classical type I binding modes (Figure 5.5). The binding of AA and AEA was less clear and difficult to conclusively assign the classical type I and type II shifts due to the low signal to noise ratio. However, all the binding shifts were concentration dependent and reach saturation and are present with clear peaks/troughs lending credibility to the calculated binding constants. While the spin-state changes of the arachidonic acid and the derivatives are minor when compared with ebastine they do correspond to the relatively low catalytic turnover of these substrates. Importantly, the relatively slow turnover rates of CYP2J2 resemble the functions of the steroid synthesizing P450's that regulate complex homeostatic processes rather than the very fast detoxification functions of liver CYPs.

The results for the CYP2J2-ND substrate-free and substrate-bound stopped-flow cyanide binding experiments are summarized in Figure 5.6 and Table 5.3. For cyanide binding studies we employed ebastine and showed that the rates of the fast phase were significantly decreased with increasing ebastine concentrations similar to other P450-substrate systems (*26*). Conversely, AA, AEA and 2-AG only showed modest inhibition of cyanide binding as shown in Figure 5.6C and indicated that they either more easily egress from the active site or are bound as to not block cyanide binding. Similarly, the ratio of the fast- to slow-phase was significantly decreased in the presence of increasing concentrations of ebastine and only modestly decreased in the presence of increasing concentrations of AA, AEA and 2-AG (Figure 5.6E – G). This effect was consistent and repeatable and not due to non-specific fatty acid binding as evidenced by the lack of change induced by palmitate (Figure 5.6H).

The enzymatic turnover of CYP2J2 is several orders of magnitude lower than xenobiotic metabolizing hepatic P450s and it might be tempting to disregard the potential biological significance of the CYP2J2 pathway based solely on these low enzymatic turnover rates. However, the extrahepatic epoxygenases, including CYP2J2, function to regulate complex homeostatic

functions within the body and exhibit significantly lower turnover of the endogenous fatty acids (*35*) in a highly regulated manner. Thus, the formation of these metabolites likely represents a far more elegant mechanism for control of the many delicate homeostatic processes within organs such as the heart and kidneys. Therefore, similar to the steroid synthesizing CYPs, the enzymatic expression levels rather than the catalytic turnover are likely the prominent mechanism for metabolic control in each respective organ.

In summary, we have demonstrated the ability of CYP2J2 to metabolize a diverse range of AA-containing substrates into a number of unique metabolites that have previously been shown to contain important physiological effects *in vivo*. Additionally, we provide important evidence that CYP2J2 can directly attenuate 2-AG levels through a NADPH-dependent oxidative cleavage mechanism, thereby producing free arachidonic acid for subsequent metabolism within the classical eicosanoid cascade. We further show that the formation of the metabolites of 2-AG and AEA are in agreement with the spectral binding studies and modeling.

5.6 ACKNOWLEDGMENTS

We thank Dr. Ilia Denisov and Dr. Matthew Edin for helpful discussions. We thank Mr. William Arnold for editing the work. We greatly appreciate the contributions of Dr. Zhong Li at the Metabolomics Lab of Roy J. Carver Biotechnology Center, University of Illinois at Urbana-Champaign. We want to thank Furong Sun and Dr. Kevin Tucker for their continued support at the School of Chemical Sciences mass spectrometry facility, University of Illinois at Urbana-Champaign. We thank Prof. Stephen Sligar for providing the gene encoding MSP1D1 and MSP1E3D1 and Prof. Robert Gennis for the use of stopped flow equipment, and Dr. Hanlin Ouyang for technical assistance. We thank Prof. Mary Schuler, Brendon Colón, and Eryk Radziszewski for training and assistance with the MOE modeling software. We thank Dr. Fan and Holly Pondenis for assistance with CYP2J2 immunoblotting. We want to thanks Dr. Bunick for providing us with the homogenizer. This work was funded in part through the American Heart Predoctoral Fellowship [14PRE20130015] (D.R.M). The Roy J. Carver Biotechnology Center's 5500 QTrap MS was funded by NIH National Center for Research Resources [S10RR024516]. The School of Chemical Sciences Q-TOF Ultima mass spectrometer was purchased in part with a grant from the National Science Foundation, Division of Biological Infrastructure [DBI-0100085].

5.7 FIGURES AND TABLES

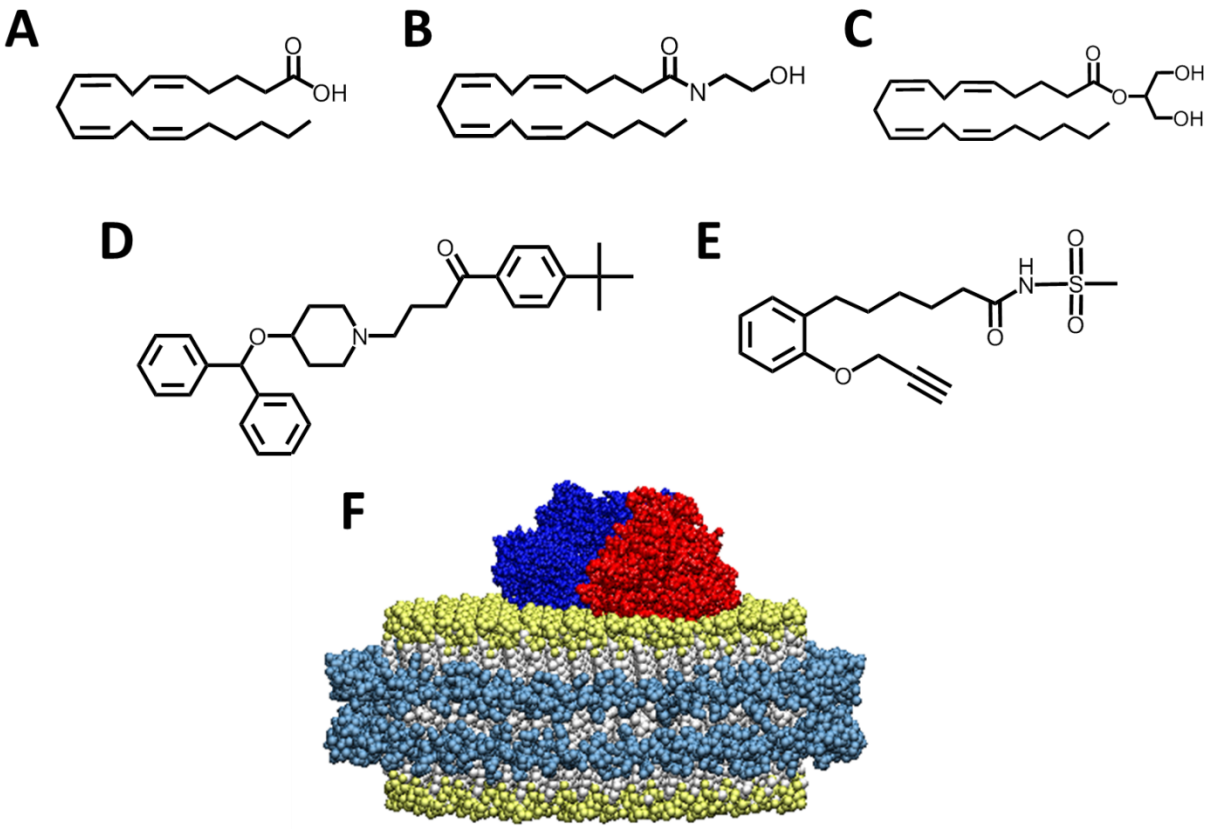

FIGURE 5.1. Chemical structures of substrates that bind to CYP2J2-nanodiscs. Endogenous CYP2J2 ligands include **(A)** arachidonic acid, **(B)** anandamide and **(C)** 2-arachidonoyl glycerol. **(D)** The xenobiotic, ebastine, is a cardiotoxic 2J2 substrate. **(E)** MS-PPOH (N-(methylsulfonyl)-2-(2-propynyloxy)-benzenehexanamide) is a non-specific CYP inhibitor. **(F)** Schematic of CYP2J2 and CPR incorporated into the membrane bilayers of nanodiscs. The membrane scaffold protein (MSP) is represented in cyan surrounding a bilayer of phospholipids colored white with gold phosphate head groups. CYP2J2 is red and its obligate redox partner cytochrome P450 reductase is colored blue.

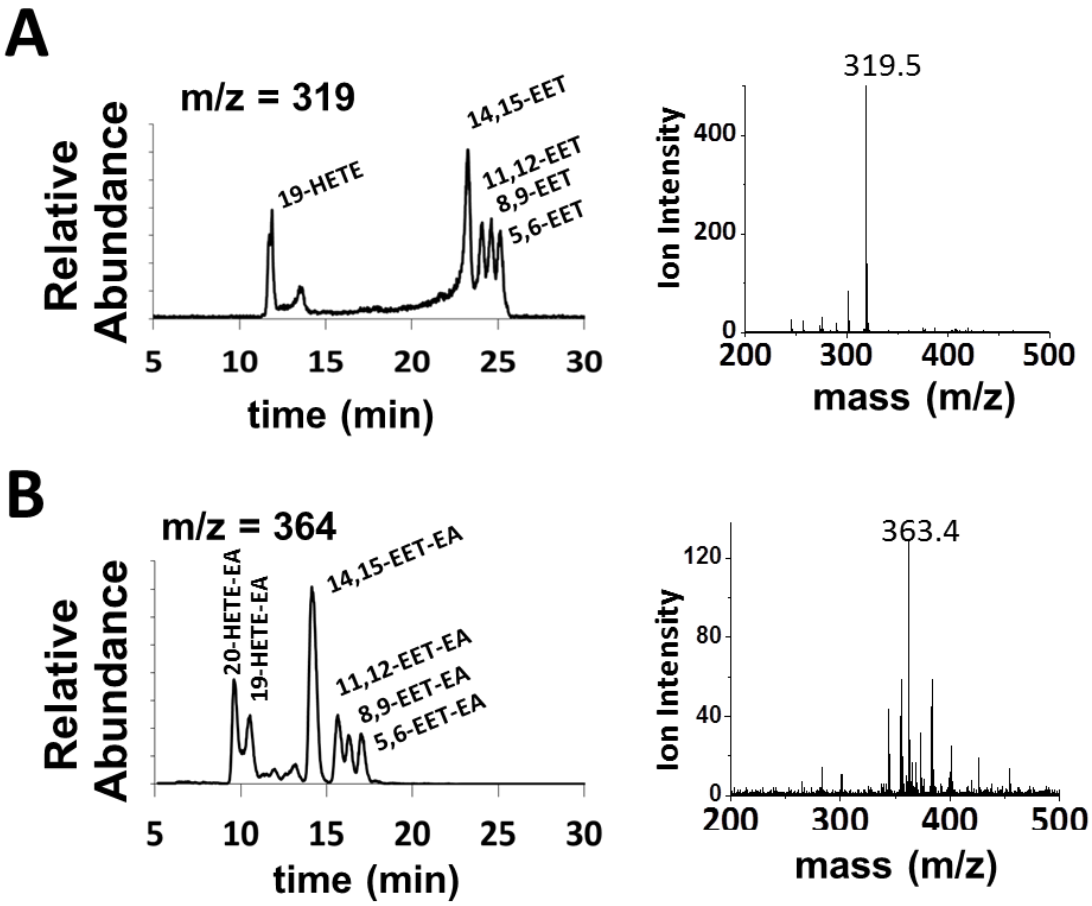

FIGURE 5.2. Metabolism of AA and AEA by human CYP2J2-ND-CPR identified qualitatively using LC-ESI-MS. CYP2J2-ND incubations with substrates were analyzed as described in the materials and methods. The different regio-isomers of **(A)** AA (m/z = 319.5 of 14,15-EET at 22.5 min) and **(B)** AEA (m/z = 363.4 of 14,15-EET-EA at 14 min) produced six different products including four epoxide regio-isomers at the 5,6-, 8,9-, 11,12- and 14,15-olefin positions and two HETEs.

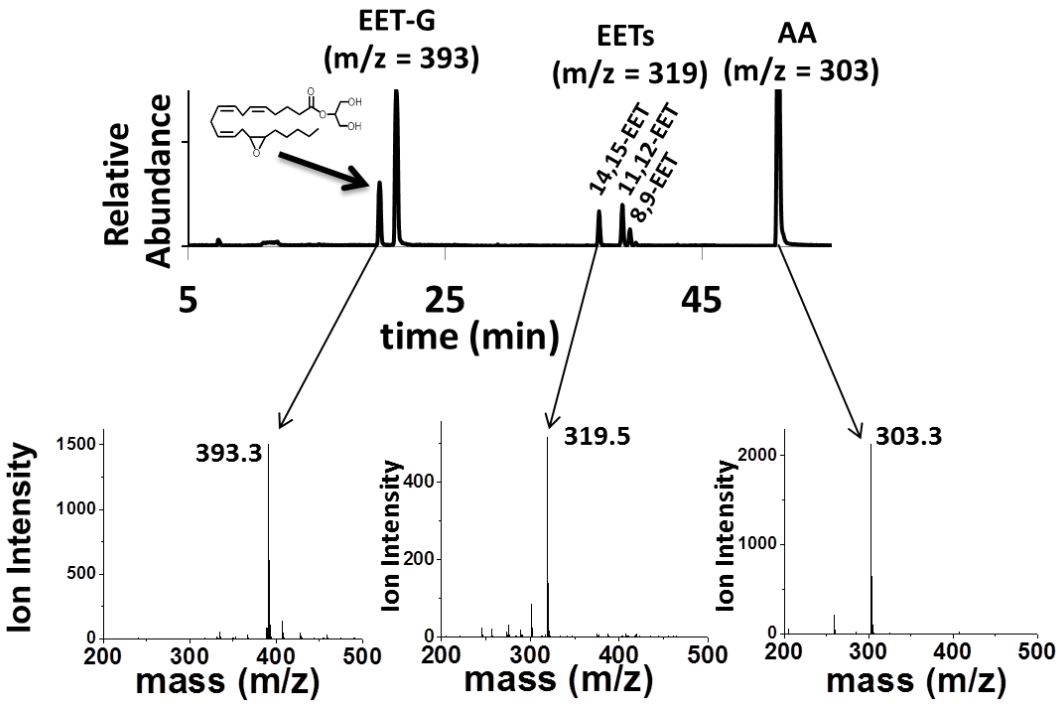

FIGURE 5.3. Metabolism of 2-AG by CYP2J2-ND-CPR identified qualitatively using LC-ESI-MS. Metabolism of 2-AG by incubations with CYP2J2-ND-CPR revealed the following metabolic profile as represented in the chromatogram that consists of an overlay of two EET-G regio-isomers, 14,15-EET-G and 11,12-EET-G (m/z 393), three detectable EET regio-isomers, 14,15-EET, 11,12-EET and 8,9-EET (m/z = 319) and arachidonic acid (m/z = 303).

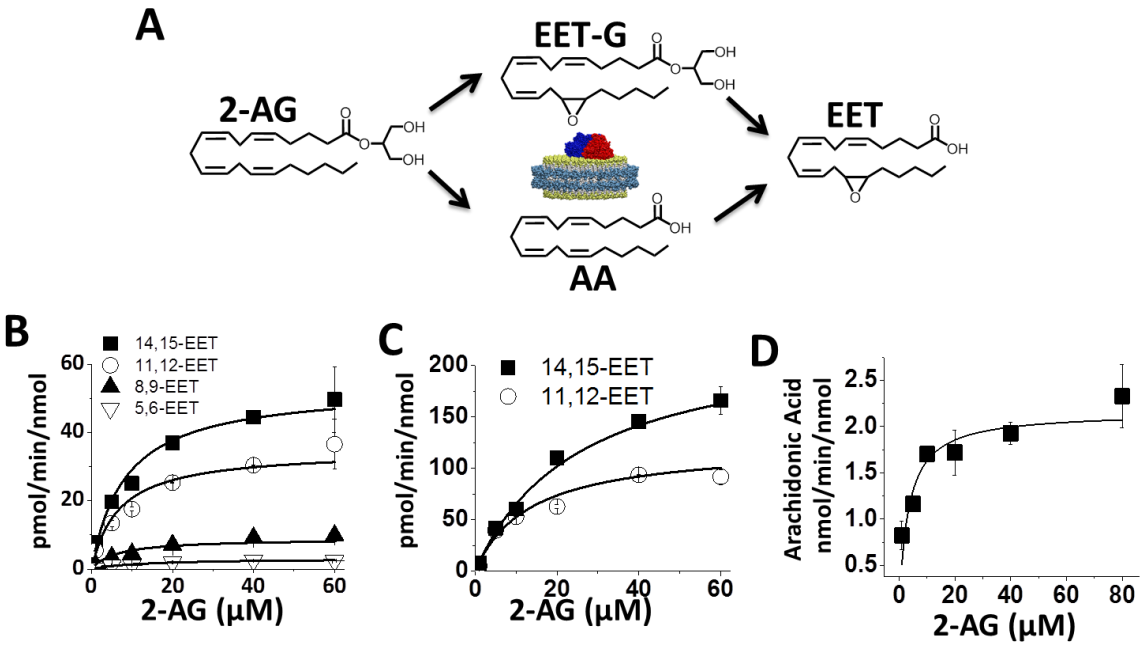

FIGURE 5.4. Kinetics of CYP2J2 mediated metabolism of 2-AG. (A) Schematic of the proposed routes of 2-AG metabolism by CYP2J2 that produces AA, EET-G and EET. The kinetic rates of the three products were quantified as described in the materials and methods. **(B)** Kinetics of the formation of the four regio-isomers, 14,15-, 11,12-, 8,9- and 5,6-EET were detected by LC-MS-MS. These correspond to the free EETs in solution that were generated either from epoxidation of AA or oxidative ester cleavage of EET-G. **(C)** Kinetics of the formation of the two EET-G regioisomers, 14,15-EET-G and 11,12-EET-G analyzed as described in the materials and methods section. **(D)** The kinetics of CYP2J2-ND mediated 2-AG ester cleavage and arachidonic acid production were determined by monitoring AA formation. The data were fitted to Michaelis-Menten kinetics in Origin Pro 8.6 for calculation of V_{max} and K_m. The kinetic rates of the epoxidation reactions and side reactions are summarized in Table 5.1.

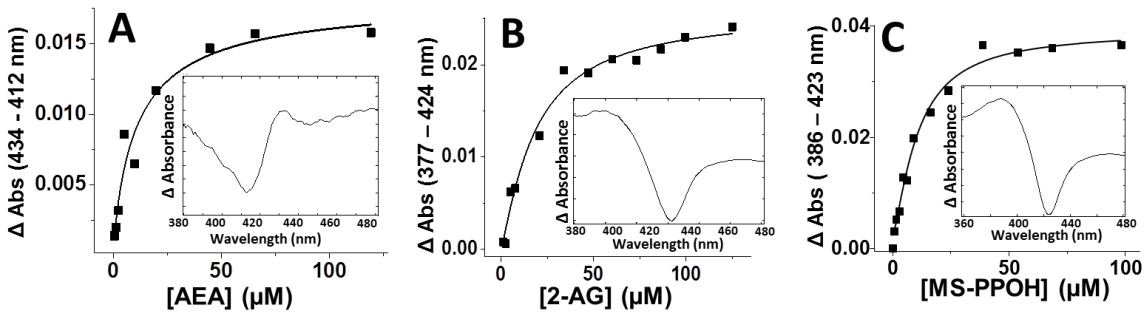

D

	Difference Spectrum			
CYP2J2 + Ligand	**Peak λ_{max} (nm)**	**Trough λ_{max} (nm)**	**K_s (μM)**	**ΔA_{max} (peak - trough)**
Arachidonic Acid[a]	434	414	11.3 ± 1.3	0.028
Anandamide	435	414	13.1 ± 1.4	0.016
2-Arachidonoyl glycerol	393	417	18 ± 2.7	0.024
MS-PPOH	386	423	10.8 ± 1.5	0.036
Ebastine	387	422	5.6 ± 0.7	0.11

[a] λ_{max} was determined at lower concentrations of ligand due to scattering.

FIGURE 5.5. Equilibrium binding using absorption spectra for interactions of substrate with CYP2J2-Nanodiscs. (A) AEA titration K_s was determined to be 13.1 ± 1.4 μM (inset: difference spectrum of AEA bound CYP2J2-Nanodiscs). **(B)** 2-AG titration K_s was determined to be 18 ± 2.7 μM (inset: difference spectrum of 2-AG bound CYP2J2-Nanodiscs) **(C)** MS-PPOH titration K_s was determined to be 10.8 ± 1.5 μM (inset: difference spectrum of MS-PPOH bound CYP2J2-Nanodiscs showing a type I binding mode) **(D)** Summary of the λ_{max} (nm) of peak/trough, K_s and Δ_{max} for binding of arachidonic acid, anandamide, 2-arachidonoyl glycerol, ebastine and MS-PPOH to CYP2J2-Nanodiscs.

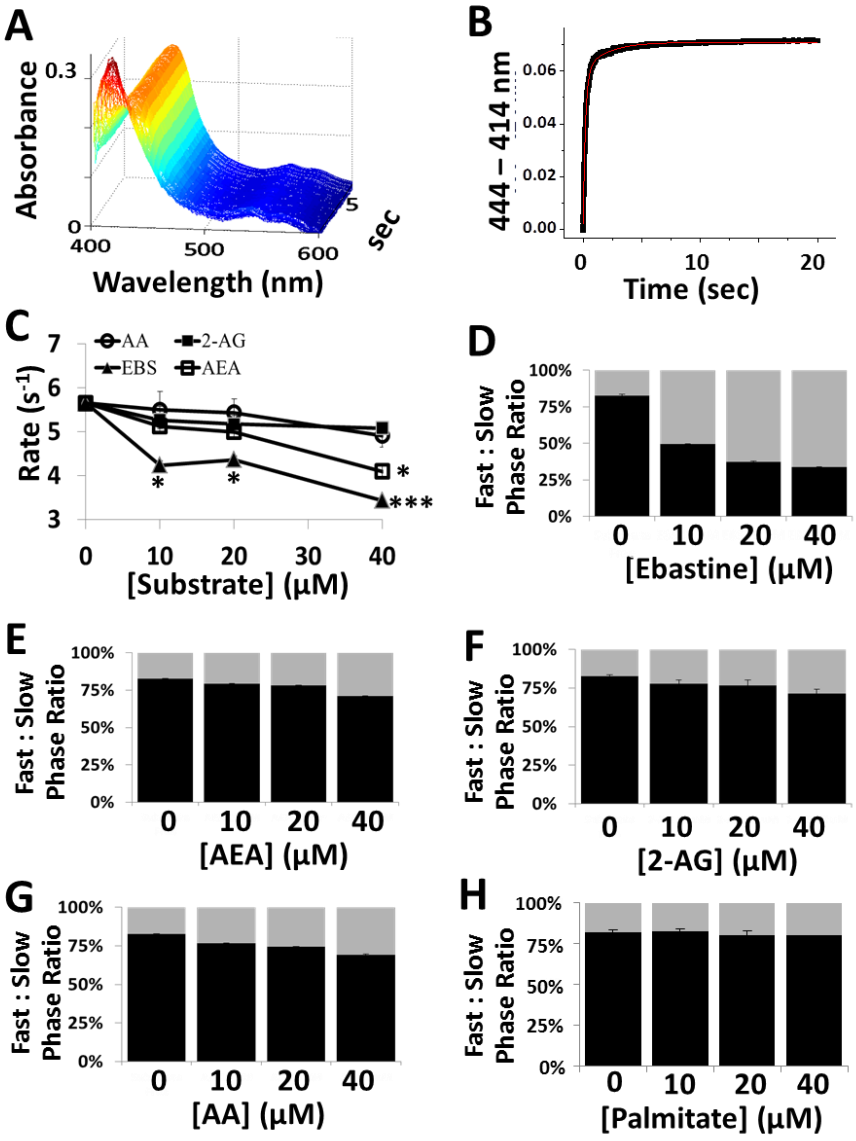

FIGURE 5.6. Stopped-flow cyanide binding spectroscopy with CYP2J2-ND and AA, 2-AG, AEA and ebastine. (A) Stopped-flow spectroscopy was used to monitor kinetics of cyanide binding to CYP2J2-ND by recording the formation of the cyanide-heme complex at 444 nm as a function of time in the presence of saturating [CN-]. **(B)** The difference spectra (ΔAbs 444-414 nm) was plotted against time and fitted to a double exponential equation for determination of the rate of the **(C)** fast-phase for each substrate concentration tested and determination of statistical significance relative to the substrate free condition when $p < 0.05$, $p < 0.01$ and $p < 0.001$ which are denoted by *, **, and ***, respectively. The ratio of the amplitudes of the fast-phase (black) to slow-phase (gray) were dramatically altered in the presence of **(D)** ebastine whereas the presence of the polyunsaturated fatty acids such as **(E)** AEA **(F)** 2-AG and **(G)** AA were modestly changed. **(H)** The saturated fatty acid palmitate did not alter cyanide binding characteristics.

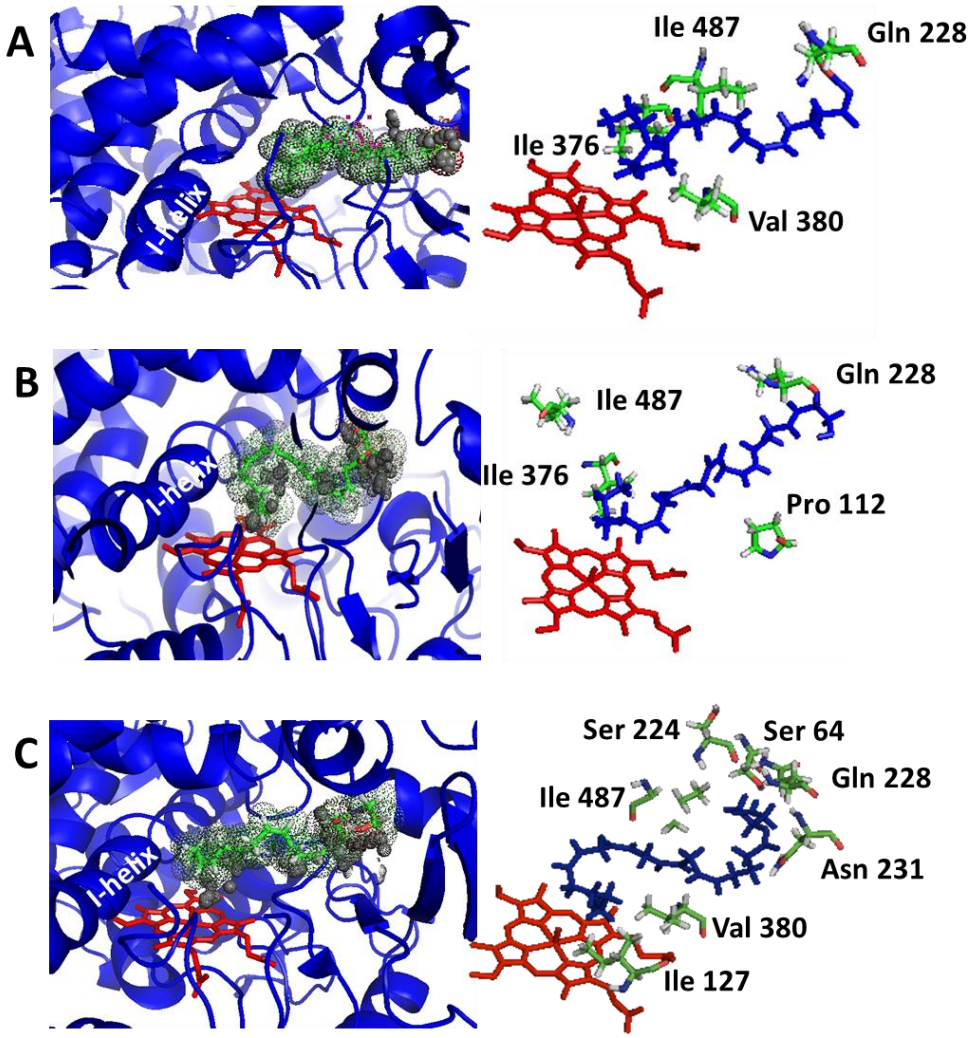

FIGURE 5.7. Substrate bound CYP2J2 Homology model with arachidonic acid, anandamide and 2-arachidonoyl glycerol. Proposed docking of the polyunsaturated fatty acids into the active site of CYP2J2. (Left) the substrate **(A)** AA **(B)** AEA and **(C)** 2-AG are represented as stick figures (green) surrounded by space-filling dots. The CYP2J2 ribbon structure is colored blue and the heme-oxygen motif is in red. The interaction potential energies predict feasibility of binding and were similar for each polyunsaturated fatty acid with calculations of -69.4 kcal/mol, and -73.4 kcal/mol for 2-AG and AEA, respectively. (Right) predicted ligand-residue interactions within the CYP2J2 active site for **(A)** AA **(B)** AEA and **(C)** 2-AG.

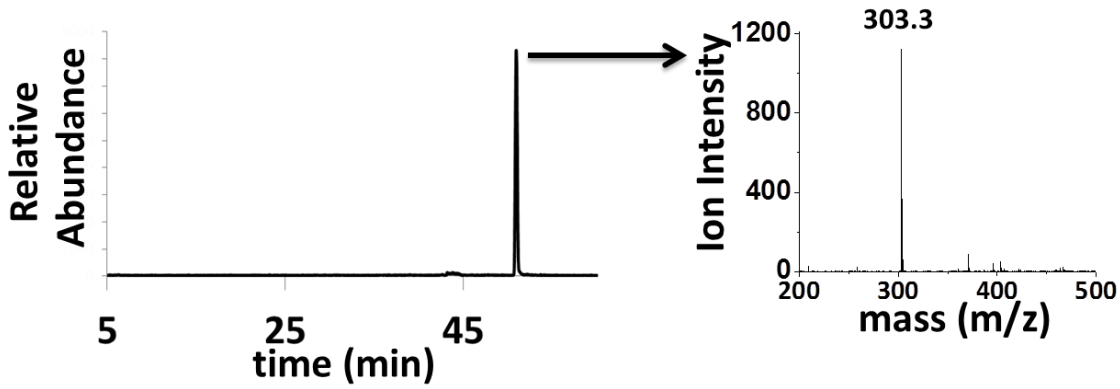

Figure 5.8. Incubations of CYP2C8 supersomes with 2-AG. Incubations containing CYP2C8 and 2-AG were performed as described in the materials and methods. Product analysis revealed the presence of arachidonic acid in the reaction but did not produce detectable levels of EET-G or EETs.

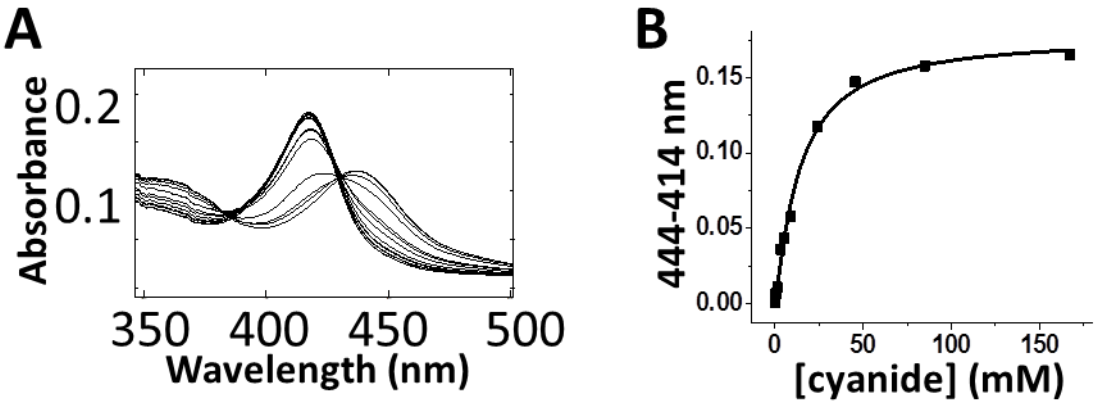

Figure 5.9. Steady-state cyanide binding to substrate-free and substrate bound CYP2J2-ND. **(A)** The UV-Vis spectra of an equilibrium binding titration of cyanide to CYP2J2-ND. The binding of cyanide red shifted the Soret band. **(B)** The change in absorbance (ΔAbs) from 444 nm to 414 nm was calculated for each titration and plotted against the corresponding cyanide concentration. Data were fit to the single binding isotherm by using Origin Pro 8.6. The cyanide K_s (μM) of substrate-free and 40 μM substrate bound were calculated for each substrate. The apparent binding constant (K_s) of the steady state cyanide binding to the active site of substrate free CYP2J2-ND was calculated at 3.1 ± 0.2 mM. The presence of 40 μM of either AA or AEA modestly increased the Ks of cyanide binding to 7.7 ± 1.1 mM and 5.2 ± 1.4 mM, respectively. The presence of 2-AG only slightly shifted the K_s of cyanide binding to 4.3 ± 0.2 mM. When the system was incubated with 40 μM of ebastine, the K_s of cyanide binding more than tripled with values of 13.3 ± 0.2 mM (Table 5.3). Notably, these results were inversely proportional to the equilibrium binding constants calculated from spectral binding assays. This suggests that a tighter substrate binding blocks cyanide access to the active site.

```
Porcine_CYP2J2      MPLALGSLAEALWTALRPSTILLGAVAFLFFADFLKKRRPKNYPPGPPRLPFIGNLFHLD
Bovine_CYP2J2       MLEALSSLATALWAALRPDTVLLGTLAFLLFVDFLKRRHPKNYPPGPPGLPFVGNLFQLD
Human_CYP2J2        MLAAMGSLAAALWAVVHPRTLLLGTVAFLLAADFLKRRRPKNYPPGPWRLPFLGNFFLVD
                    *  *:.*** ***:.::* *:***::***: .****:*:********  ***:**:* :*

Porcine_CYP2J2      LDKGHLSLQRFVKKYGNVFSLDFGALSSVVITGLPFIKEAFVHQDKNFSNRPIVPIQQRV
Bovine_CYP2J2       PEKVPLVLHQFVKKYGNVFSLDFGTVPSVLITGLPLIKEVLVHQGQIFSNRPIVPLQEHI
Human_CYP2J2        FEQSHLEVQLFVKKYGNLFSLELGDISAVLITGLPLIKEALIHMDQNFGNRPVTPMREHI
                     ::  * :: *******:***::* :.:*:*****:***.::* .: *.***:.*:::::

Porcine_CYP2J2      FKDKGVVMSNGQVWKEQRRFALTTLRNFGLGKKSLEERIQEEAQYLIQAIGEENGQPFNP
Bovine_CYP2J2       INNKGLIMSSGQLWKEQRRFALTTLRNFGLGKKSLEERIQEEASYLIQTIREENGQPFDP
Human_CYP2J2        FKKNGLIMSSGQAWKEQRRFTLTALRNFGLGKKSLEERIQEEAQHLTEAIKEENGQPFDP
                    ::.:*::**.** *******:**:********************.:* ::* *******:*

Porcine_CYP2J2      HFKINNAVSNIICSITFGERFDYQDNQFQELLKLLDEVMCLQTSVWCQIYNIIPWIMKFL
Bovine_CYP2J2       HLTINNAVSNIICSITFGERFDYQDDQFQELLRMLDEILNLQTSMCCQLYNVFPRIMNFL
Human_CYP2J2        HFKINNAVSNIICSITFGERFEYQDSWFQQLLKLLDEVTYLEASKTCQLYNVFPWIMKFL
                    *:.******************:***. **:**::***:  *::*  **:**::* **:**

Porcine_CYP2J2      PGPHQTLFSNWEKLKMFVAHVIENHRRDWNPAEARDFIEAYLQEIEKHKGDATSSFQEEN
Bovine_CYP2J2       PGPHQALFSNMEKMKMFVARMIENHKRDWNPAEARDFIDAYLQEIEKHKGDATSSFQEEN
Human_CYP2J2        PGPHQTLFSNWKKLKLFVSHMIDKHRKDWNPAETRDFIDAYLKEMSKHTGNPTSSFHEEN
                    *****:**** :*:*:**:::*::*::******:****:***:*:.**.*:.****:***

Porcine_CYP2J2      LICSTLDLFVAGTETTSTTLRWGLLYMALYPEIQEKVQAEIDRVLGQLQQPSTAARESMP
Bovine_CYP2J2       LIYNTLDLFLAGTETTSTSLRWGLLFMALNPEIQEKVQAEIDRVLGQSQQPSMAARESMP
Human_CYP2J2        LICSTLDLFFAGTETTSTTLRWALLYMALYPEIQEKVQAEIDRVIGQGQQPSTAARESMP
                    ** .*****.********:***.**:*** **************:** **** *******


Porcine_CYP2J2      YTNAVIHEVQRMGNIIPLNVPREVAEDTTLAGYHLPKGTMVIANLTALHSDPTEWATPDT
Bovine_CYP2J2       YTNAVIHEVLRMGNIIPLNVPREVAVDTTLAGYHLPKGTMVMTNLTALHRDPTEWATPDT
Human_CYP2J2        YTNAVIHEVQRMGNIIPLNVPREVTVDTTLAGYHLPKGTMILTNLTALHRDPTEWATPDT
                    ********* **************: **************:::****** **********

Porcine_CYP2J2      FNPEHFLENGKFKKREAFLPFSVGKRACLGEQLARTELFVFFTSLLQKFSFRPPDNEKLS
Bovine_CYP2J2       FNPEHFLENGQFKKRESFLPFSIGKRMCLGEQLARTELFIFFTSLLQKFTFRPPENEQLS
Human_CYP2J2        FNPDHFLENGQFKKREAFMPFSIGKRACLGEQLARTELFIFFTSLMQKFTFRPPNNEKLS
                    ***:******:*****:*:***:*** ************:*****:***:****:**:**

Porcine_CYP2J2      LKFRMGLTLSPVTYRICAVPRA
Bovine_CYP2J2       LKFRVSLTLAPVSHRLCAVPRG
Human_CYP2J2        LKFRMGITISPVSHRLCAVPQV
                    ****:.:*::**::*:****:
```

Figure 5.10. Multiple sequence alignment of human, bovine and porcine CYP2J2 sequences. Inter-species alignments of CYP2J2 from porcine, bovine and calculated an 80% homology for comparison of porcine to bovine, 77% homology for porcine to human and a 75% homology for bovine to human. The single fully conserved residue for each of all of the species is denoted by (*). The majority of other residues polarity was maintained as represented by (:) for the conservation of strong groups and (.) for conservation of weak groups.

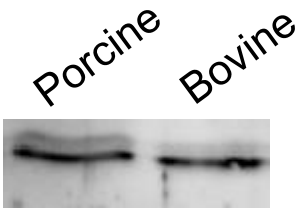

Figure 5.11. CYP2J2 immunoblotting in bovine and porcine microsomes using a polyclonal rabbit IgG antibody for human CYP2J2. The inter-species cross-reactivity with the anti-body raised against the human CYP2J2 was examined. From left to right, lane 1 contains 100 ug of pig heart microsomes, lane 2 contains 100 ug of cow heart microsomes and lane 3 contains 100 pmol of recombinant CYP2J2 used in these studies.

	Km (μM)	V_{max} (pmol/min/nmol)	V_{max} / K_m
14,15-EET-G	32.6 ± 1.7	265.4 ± 12.3	8.1 ± 0.3
11,12-EET-G	13.6 ± 1.3	125.5 ± 5.2	9.2 ± 0.2
14,15-EET	8.3 ± 2.0	53.3 ± 2.9	6.4 ± 1.25
11,12-EET	6.7 ± 1.3	34.8 ± 1.5	5.1 ± 0.4
8,9-EET	6.2 ± 1.8	8.9 ± 1.1	1.4 ± 0.3
5,6-EET	12.7 ± 3.8	3.1 ± 0.3	0.2 ± .05

Table 5.1. The product formation kinetics for CYP2J2 nanodisc incubations with 2-arachidonoyl glycerol (2-AG).

Substrate	Metabolite(s) Detected	Bovine Microsomes pmol min^{-1} mg^{-1}	Porcine Microsomes pmol min^{-1} mg^{-1}
AA	**Total EET (all regio-isomers)**	1.8 ± 0.3	2.08 ± 0.02
2-AG	**14,15-EET-G**	1.1 ± 0.57	1.18 ± 0.55
AEA	**14,15-EET-EA**	1.96 ± 0.05	2.25 ± 0.07

Table 5.2. Metabolism of AA, 2-AG and AEA by bovine and porcine heart microsomes.

	Steady State Cyanide Binding	Stopped Flow Cyanide Binding Kinetics		
	Cyanide (K_s)	**Fast-Phase Rate (s^{-1})**	**Slow Phase Rate (s^{-1})**	**Fast-Phase (%)**
Substrate Free	3.1 ± 0.2	5.6 ± 0.1	0.6 ± .06	82.6 ± 2.08
AA (10 μM)	NT	5.5 ± 0.4	0.8 ± 0.2	76.6 ± 2.0
AA (20 μM)	NT	5.4 ± 0.3	1.1 ± 0.1*	74.2 ± 2.7
AA (40 μM)	7.7 ± 1.1	4.9 ± 0.2	1.19 ± 0.1**	69.3 ± 3.4
AEA (10 μM)	NT	5.1 ± 0.1	0.7 ± .04	79.3 ± 1.6
AEA (20 μM)	NT	5.0 ± 0.1	0.9 ± 0.01*	78 ± 0.3
AEA (40 μM)	5.2 ± 1.4	4.1 ± 0.1*	1.1 ± 0.02**	71 ± 0.3
2-AG (10 μM)	NT	5.2 ± 0.3	0.8 ± 0.1	77.6 ± 4.1
2-AG (20 μM)	NT	5.1 ± 0.1	0.9 ± 0.07*	76.8 ± 1.6
2-AG (40 μM)	4.3 ± 0.2	5.1 ± 0.01	1.0 ± .01**	71.5 ± 0.4
Ebastine (10 μM)	NT	4.2 ± 0.1*	0.46 ± 0.01*	49.5 ± 0.1
Ebastine (20 μM)	NT	4.3 ± 0.08*	0.46 ± .01*	37.4 ± 0.29
Ebastine (40 μM)	13.3 ± 0.2	3.4 ± 0.04***	0.41 ± .001**	33.6 ± 0.42
Palmitate (40 μM)	NT	5.5 ± 0.04	0.6 ± .02	80 ± 0.1
MSPPOH (10 μM)	16.1 ± 0.51	4.1 ± .04	0.49 ± .016	64.6 ± 1.82

N.D. = not detected

Table 5.3. Summary of cyanide binding in the presence of fatty acids and ebastine. Substrate concentrations were compared to the substrate free sample and significance was attained when $p < 0.05$, $p < 0.01$ and $p < 0.001$ and were denoted by *, **, and ***, respectively.

5.8 REFERENCES

1. Kogan, N. M., and Mechoulam, R. (2007) Cannabinoids in health and disease, *Dialogues Clin Neurosci 9*, 413-430.
2. Yang, J., Dong, H., and Hammock, B. D. (2011) Profiling the regulatory lipids: another systemic way to unveil the biological mystery, *Curr Opin Lipidol 22*, 197-203.
3. Chen, J. K., Chen, J., Imig, J. D., Wei, S., Hachey, D. L., Guthi, J. S., Falck, J. R., Capdevila, J. H., and Harris, R. C. (2008) Identification of novel endogenous cytochrome p450 arachidonate metabolites with high affinity for cannabinoid receptors, *J Biol Chem 283*, 24514-24524.
4. Alghasham, A., Ali, A., Ismail, H., Dowaidar, M., and Settin, A. A. (2012) CYP2J2 -50 G/T and ADRB2 G46A gene polymorphisms in Saudi subjects with hypertension., *Genet Test Mol Biomarkers 16*, 1027-1031.
5. Delozier, T. C., Kissling, G. E., Coulter, S. J., Dai, D., Foley, J. F., Bradbury, J. A., Murphy, E., Steenbergen, C., Zeldin, D. C., and Goldstein, J. A. (2007) Detection of human CYP2C8, CYP2C9, and CYP2J2 in cardiovascular tissues, *Drug Metab Dispos 35*, 682-688.
6. Panigrahy, D., Edin, M. L., Lee, C. R., Huang, S., Bielenberg, D. R., Butterfield, C. E., Barnes, C. M., Mammoto, A., Mammoto, T., Luria, A., Benny, O., Chaponis, D. M., Dudley, A. C., Greene, E. R., Vergilio, J. A., Pietramaggiori, G., Scherer-Pietramaggiori, S. S., Short, S. M., Seth, M., Lih, F. B., Tomer, K. B., Yang, J., Schwendener, R. A., Hammock, B. D., Falck, J. R., Manthati, V. L., Ingber, D. E., Kaipainen, A., D'Amore, P. A., Kieran, M. W., and Zeldin, D. C. (2012) Epoxyeicosanoids stimulate multiorgan metastasis and tumor dormancy escape in mice, *J Clin Invest 122*, 178-191.
7. Imig, J. D., and Hammock, B. D. (2009) Soluble epoxide hydrolase as a therapeutic target for cardiovascular diseases, *Nat Rev Drug Discov 8*, 794-805.
8. Rouzer, C. A., and Marnett, L. J. (2011) Endocannabinoid Oxygenation by Cyclooxygenases, Lipoxygenases, and Cytochromes P450: Cross-Talk between the Eicosanoid and Endocannabinoid Signaling Pathways, *Chem Rev 111*, 5899-5921.
9. Snider, N. T., Kornilov, A. M., Kent, U. M., and Hollenberg, P. F. (2007) Anandamide metabolism by human liver and kidney microsomal cytochrome p450 enzymes to form hydroxyeicosatetraenoic and epoxyeicosatrienoic acid ethanolamides, *J Pharmacol Exp Ther 321*, 590-597.
10. Snider, N. T., Sikora, M. J., Sridar, C., Feuerstein, T. J., Rae, J. M., and Hollenberg, P. F. (2008) The Endocannabinoid Anandamide Is a Substrate for the Human Polymorphic Cytochrome P450 2D6, *Journal of Pharmacology and Experimental Therapeutics 327*, 538-545.
11. Sridar, C., Snider, N. T., and Hollenberg, P. F. (2011) Anandamide Oxidation by Wild-Type and Polymorphically Expressed CYP2B6 and CYP2D6, *Drug Metabolism and Disposition 39*, 782-788.
12. Stark, K., Dostalek, M., and Guengerich, F. P. (2008) Expression and purification of orphan cytochrome P450 4X1 and oxidation of anandamide, *Febs J 275*, 3706-3717.
13. Blankman, J. L., Simon, G. M., and Cravatt, B. F. (2007) A comprehensive profile of brain enzymes that hydrolyze the endocannabinoid 2-arachidonoylglycerol, *Chem Biol 14*, 1347-1356.

14. Bayburt, T. H., and Sligar, S. G. (2010) Membrane protein assembly into Nanodiscs, *FEBS Lett 584*, 1721-1727.
15. Das, A., Varma, S. S., Mularczyk, C., and Meling, D. D. (2014) Functional investigations of thromboxane synthase (CYP5A1) in lipid bilayers of nanodiscs, *Chembiochem 15*, 892-899.
16. Denisov, I. G., and Sligar, S. G. (2011) Cytochromes P450 in nanodiscs, *Biochim Biophys Acta 1814*, 223-229.
17. Grinkova, Y. V., Denisov, I. G., and Sligar, S. G. (2010) Functional reconstitution of monomeric CYP3A4 with multiple cytochrome P450 reductase molecules in Nanodiscs, *Biochem Biophys Res Commun 398*, 194-198.
18. Nath, A., Grinkova, Y. V., Sligar, S. G., and Atkins, W. M. (2007) Ligand binding to cytochrome P450 3A4 in phospholipid bilayer nanodiscs: the effect of model membranes, *J Biol Chem 282*, 28309-28320.
19. Orlando, B. J., McDougle, D. R., Lucido, M. J., Eng, E. T., Graham, L. A., Schneider, C., Stokes, D. L., Das, A., and Malkowski, M. G. (2014) Cyclooxygenase-2 catalysis and inhibition in lipid bilayer nanodiscs, *Arch Biochem Biophys 546*, 33-40.
20. McDougle, D. R., Palaria, A., Magnetta, E., Meling, D. D., and Das, A. (2013) Functional studies of N-terminally modified CYP2J2 epoxygenase in model lipid bilayers, *Protein Sci 22*, 964-979.
21. Zelasko, S., Palaria, A., and Das, A. (2013) Optimizations to achieve high-level expression of cytochrome P450 proteins using Escherichia coli expression systems, *Protein Expres Purif 92*, 77-87.
22. Pretorius, P. J., Pohl, W. G., Smithen, C. S., and Inesi, G. (1969) Structural and functional characterization of dog heart microsomes, *Circ Res 25*, 487-499.
23. Zeldin, D. C., Foley, J., Goldsworthy, S. M., Cook, M. E., Boyle, J. E., Ma, J., Moomaw, C. R., Tomer, K. B., Steenbergen, C., and Wu, S. (1997) CYP2J subfamily cytochrome P450s in the gastrointestinal tract: expression, localization, and potential functional significance, *Mol Pharmacol 51*, 931-943.
24. Capdevila, J. H., Dishman, E., Karara, A., and Falck, J. R. (1991) Cytochrome P450 arachidonic acid epoxygenase: stereochemical characterization of epoxyeicosatrienoic acids, *Methods Enzymol 206*, 441-453.
25. Baudry, J., Li, W., Pan, L., Berenbaum, M. R., and Schuler, M. A. (2003) Molecular docking of substrates and inhibitors in the catalytic site of CYP6B1, an insect cytochrome p450 monooxygenase, *Protein Eng 16*, 577-587.
26. Denisov, I. G., Grinkova, Y. V., McLean, M. A., and Sligar, S. G. (2007) The one-electron autoxidation of human cytochrome P450 3A4, *The Journal of Biological Chemistry 282*, 26865-26873.
27. Wu, S., Moomaw, C. R., Tomer, K. B., Falck, J. R., and Zeldin, D. C. (1996) Molecular cloning and expression of CYP2J2, a human cytochrome P450 arachidonic acid epoxygenase highly expressed in heart, *J Biol Chem 271*, 3460-3468.
28. Zhu, Y., Schieber, E. B., McGiff, J. C., and Balazy, M. (1995) Identification of arachidonate P-450 metabolites in human platelet phospholipids, *Hypertension 25*, 854-859.
29. Guengerich, F. P. (1987) Oxidative cleavage of carboxylic esters by cytochrome P-450, *J Biol Chem 262*, 8459-8462.

30. Peng, H. M., Raner, G. M., Vaz, A. D., and Coon, M. J. (1995) Oxidative cleavage of esters and amides to carbonyl products by cytochrome P450, *Arch Biochem Biophys 318*, 333-339.
31. Huang, W., Jiang, D., Wang, X., Wang, K., Sims, C. E., Allbritton, N. L., and Zhang, Q. (2011) Kinetic analysis of PI3K reactions with fluorescent PIP2 derivatives, *Anal Bioanal Chem 401*, 1881-1888.
32. Falck, J. R., Belosludtsev, Y. Y., Reddy, K. K., Reddy, K. M., Shortt, M. F., Chauhan, K., Capdevila, J. H., and Wei, S. Z. (1997) Eicosanoid biosynthesis: Differential inhibition of cytochrome P450 epoxygenase and omega-hydroxylase, *Bioorg Med Chem Lett 7*, 3053-3056.
33. Lafite, P., Andre, F., Zeldin, D. C., Dansette, P. M., and Mansuy, D. (2007) Unusual regioselectivity and active site topology of human cytochrome P450 2J2, *Biochemistry 46*, 10237-10247.
34. Loughran, P. A., Roman, L. J., Miller, R. T., and Masters, B. S. (2001) The kinetic and spectral characterization of the E. coli-expressed mammalian CYP4A7: cytochrome b5 effects vary with substrate, *Arch Biochem Biophys 385*, 311-321.
35. Westphal C, Konkel A, and WH., S. (2011) CYP-eicosanoids--a new link between omega-3 fatty acids and cardiac disease?, *Prostaglandins Other Lipid Mediat. 96*, 99-108.
36. Bidwai, A. K., Meyen, C., Kilheeney, H., Wroblewski, D., Vitello, L. B., and Erman, J. E. (2013) Apolar distal pocket mutants of yeast cytochrome c peroxidase: Hydrogen peroxide reactivity and cyanide binding of the TriAla, TriVal, and TriLeu variants, *Bba-Proteins Proteom 1834*, 137-148.
37. Baudry, J., Rupasinghe, S., and Schuler, M. A. (2006) Class-dependent sequence alignment strategy improves the structural and functional modeling of P450s, *Protein Eng Des Sel 19*, 345-353.
38. Spector, A. A. (2009) Arachidonic acid cytochrome P450 epoxygenase pathway, *J Lipid Res 50 Suppl*, S52-56.
39. Pacher, P., Batkai, S., and Kunos, G. (2006) The endocannabinoid system as an emerging target of pharmacotherapy, *Pharmacol Rev 58*, 389-462.
40. Pacher, P., and Steffens, S. (2009) The emerging role of the endocannabinoid system in cardiovascular disease, *Semin Immunopathol 31*, 63-77.
41. Snider, N. T., Walker, V. J., and Hollenberg, P. F. (2010) Oxidation of the endogenous cannabinoid arachidonoyl ethanolamide by the cytochrome P450 monooxygenases: physiological and pharmacological implications, *Pharmacol Rev 62*, 136-154.
42. Snider, N. T., Nast, J. A., Tesmer, L. A., and Hollenberg, P. F. (2009) A cytochrome P450-derived epoxygenated metabolite of anandamide is a potent cannabinoid receptor 2-selective agonist, *Mol Pharmacol 75*, 965-972.
43. Mukhopadhyay, P., Mohanraj, R., Batkai, S., and Pacher, P. (2008) CB1 cannabinoid receptor inhibition: promising approach for heart failure?, *Congest Heart Fail 14*, 330-334.
44. Cravatt, B. F., and Lichtman, A. H. (2003) Fatty acid amide hydrolase: an emerging therapeutic target in the endocannabinoid system, *Curr Opin Chem Biol 7*, 469-475.

CHAPTER VI: CYP2J2 AND ENDOCANNABINOID PATHWAY CROSSTALK PRODUCES OMEGA-3 ENDOCANNABINOID EPOXIDES

6.1 ABSTRACT

Numerous clinical studies suggest that diets rich in omega-3 (ω-3) fatty acids provide beneficial anti-inflammatory effects, in part, through their conversion to bioactive metabolites. In the following study, we report on a new class of ω-3 derived metabolites originating from the cross-talk between endocannabinoid and cytochrome P450 (CYP) epoxygenase metabolic pathways. These metabolites share structural similarity to both their endocannabinoid and epoxide parent compounds, with potential to exert similar physiological effects. The direct biosynthesis of these metabolites was mediated by enzymes of the CYP epoxygenase pathway while their degradation was facilitated by soluble epoxide hydrolase (sEH) and fatty acid amide hydrolase (FAAH). The presence of these metabolites in rat brain prompted neuroinflammation studies using BV-2 microglia cells, which showed that the predominant metabolites dose-dependently ameliorated pro-inflammatory IL-6 cytokines whilst increasing anti-inflammatory IL-10 cytokines, in part, through cannabinoid receptor-2 (CB2) receptor activation. Additional studies revealed that these metabolites exerted anti-angiogenic effects in human microvascular endothelial cells (HMVECs), vasodilatory properties in bovine coronary arteries and reciprocally regulated platelet aggregation in washed human platelets. Taken together, these bifunctional ligands exhibited enhanced endocannabinoid properties while retaining their epoxide-like bioactivity.

[4]Submitted for publication as Daniel R. McDougle, Amr A. Abdeen, Josephine E. Watson, Reheman Adili, Megan Caputo, John Krapf, Rodney Johnson, Kristopher Kilian, Michael Holinstat and Aditi Das[*]. Anti-inflammatory Omega-3 Endocannabinoid Epoxides.

6.2 INTRODUCTION

Epidemiological evidence suggests that a diet rich in omega-3 fatty acids (ω-3 FAs) promotes beneficial cardiovascular (*1*) neurological (*2*), and anti-inflammatory (*3*) health effects. However, the biochemical mechanism(s) facilitating these effects has yet to be fully elucidated. There is mounting evidence to suggest that these actions are mediated through the oxidative and non-oxidative metabolism of ω-3 FAs into bioactive metabolites.

One of the non-oxidative pathways involves the conversion of ω-3 FAs into endocannabinoids. Endocannabinoids elicit similar effects as Δ9-tetrahydrocannabinol (THC), the active ingredient of *Cannabis sativa*. They play important physiological roles that are primarily exerted through activation of the cannabinoid receptors – cannabinoid receptor 1 (CB1) and 2 (CB2) (*4, 5*). One of the well-studied endocannabinoids is an arachidonate (ω-6 FA) derivative known as anandamide (AEA) (Figure 6.1). AEA is involved in regulating physiological processes in both the central nervous system (CNS) and peripheral tissues (*6-8*). It was recently reported that the ω-3 FA, docosahexaenoic acid (DHA), can be converted to docosahexaenoic ethanolamide (DHEA) which acts as a weak cannabinoid receptor agonist (Figure 6.1) (*7, 8*). DHEA exhibits anti-cancer (*7, 8*), anti-inflammatory (*9*) and synaptogenic (*10*) properties and has been detected in both the brain and retina at concentrations comparable to those for AEA (*11-13*). Another ω-3 FA, eicosapentanoic acid (EPA), is similarly converted to eicosapentanoic ethanolamide (EPEA) (Figure 6.1) (*14*). Notably, dietary supplementation with EPA and DHA resulted in increased levels of EPEA and DHEA at the expense of AEA, thereby providing a mechanism for modulation of the ω-6 and ω-3 lipidome (*15*). Overall, the *in vivo* formation of ω-3 endocannabinoids – DHEA and EPEA motivates a careful characterization of their metabolism in order to better understand the complex interrelationships that exist among these lipid metabolism pathways.

Endocannabinoids are metabolized by eicosanoid synthesizing enzymes to generate complex lipid metabolites with multiple functional groups that tend to exhibit unique biological functions (*16*). There are three broad classes of eicosanoid synthesizing enzymes - the cyclooxygenases (COX), lipoxygenases (LOX) and cytochrome P450 epoxygenases (CYP). The CYP epoxygenase branch typically generate epoxide lipid metabolites that are anti-inflammatory, anti-nociceptive, and anti-hypertensive (*17*). Previously, we detailed how a specific epoxygenase, CYP2J2, converted AEA into AEA epoxides (EET-EAs) (*18*) (Figure 6.1). Notably, Hollenberg and

coworkers demonstrated that the 5,6-EET-EA metabolite selectively binds cannabinoid receptor 2 (CB2) with 1000-fold greater affinity than cannabinoid receptor 1 (CB1) (*19*). Recently it was shown that DHEA can be converted by enzymes of the LOX pathway to form novel oxygenated metabolites with CB2-preferring agonist activity (*20*). However, there have yet to be any studies examining EPEA or DHEA metabolism by the CYP epoxygenases.

In general, CYP epoxygenases functionalize polyunsaturated FAs olefins with molecular oxygen to form an epoxide motif that imparts bioactivity. A physiologically important pathway includes the epoxygenation of arachidonic acid (AA), DHA, and EPA into epoxyeicosatrienoic acids (EETs), epoxydocosapentaenoic acids (EDPs), and epoxyeicosatetraenoic acids (EEQs), respectively (*21, 22*). Thus we hypothesized that some of the CYP epoxygenases could directly utilize DHEA and EPEA as substrates to form novel bioactive oxygenated metabolites with potential to modulate the inflammatory response. Moreover, this unexplored pathway would provide new insights towards understanding the beneficial health benefits of ω-3 FAs.

The present report tests the hypothesis that CYP epoxygenases metabolize DHEA and EPEA to form novel ω-3 endocannabinoids epoxides - EDP-EA and EEQ-EA (Figure 6.1). These metabolites are produced as a result of the cross-talk between enzymes in the CYP epoxygenase and endocannabinoid metabolic pathways. Herein, we employed a newly developed mass spectrometry method to determine the levels of the ω-3 endocannabinoid epoxides endogenously present in various rat tissues. Furthermore we demonstrate that they are naturally produced in lipopolysaccharide (LPS) stimulated BV2 microglial cells (resident macrophages in brain). One of the primary epoxygenases of the brain and heart, CYP2J2, was expressed, purified and incorporated into nanodisc bilayers for metabolism studies. This CYP epoxygenase found to directly convert DHEA and EPEA substrates to a diverse range of epoxides. We also explored common degradation pathways of these endocannabinoid epoxides by soluble epoxide hydrolase (sEH) and fatty acid amide hydrolase (FAAH).

Besides unraveling the pathway for the formation and degradation of EEQ-EA and EDP-EA, we also report the potential biological functions of the ω-3 endocannabinoid epoxides. These metabolites have two functional motifs – "N-acyl ethanolamide of endocannabinoids" and "epoxide" that typically function through divergent signaling pathways with many similar functional outcomes. Anti-inflammatory effects are common to both motifs and given the presence

of these metabolites in the brain we explored their potential role in a model of neuro-inflammation using BV2 microglial cells. Additionally, as these epoxides were widely distributed in the periphery and because ω-3 FA epoxides are known to be vasoactive, we also studied the "epoxide-like" property of these molecules by measuring vasodilation in bovine coronary artery, angiogenesis in human microvascular endothelial cells (HMVECs) and platelet aggregation in washed human platelets.

Taken together, this is the first report of a new class of ω-3 endocannabinoid epoxides – EDP-EA and EEQ-EA in the brain and periphery that are produced through direct epoxygenation by CYP epoxygenases that exert both 'endocannabinoid-like" and "epoxide-like" biological activities. Overall, the complete understanding of the biosynthetic pathways and evaluation of some key biological activities will provide new insights into disease pathologies linked to the dietary consumption of ω-3 and ω-6 fatty acids.

6.3 MATERIALS AND METHODS

Tissue Cell Culture Materials. Dr. Robert H. McCusker Jr. (University of Illinois at Urbana-Champaign) generously provided the BV-2 cell line originally created by Blasi et. al.(*23*). Primary human microvascular endothelial cells (HMVEC) were purchased from cell systems (Certificate #CSC 2M1). Complete serum containing medium kit was purchased from cell systems (Cat. #4Z0-500). Fetal bovine serum (cat. #16140-071) and DMEM (cat. 10-013-CV) were obtained from Gibco. Pertussis toxin (cat. #181) was purchased from List Bio Labs. AM630 (cat. #10006974), rimonabant (cat. #9000484), GW9962 (cat. #70785), LY294002 (cat. #70920), HA-100 (cat. #14955), AMG9810 (cat. #14715), ruthenium red (cat. #14339), wortmannin (cat. #10010591) were procured from Cayman Chemical.

Animal Materials. Fresh bovine hearts were obtained on ice from the local slaughterhouse at time of slaughter. Fresh whole female porcine brains and hearts were obtained from the UIUC meat sciences laboratory. At the time of sacrifice, male Sprague-Dawley (250-300 gm) rat carcasses were obtained from the Division of Animal Resource facility (University of Illinois at Urbana-Champaign) and immediately dissected for brain, heart, kidneys, spleen and livers organs.

Other Chemical and Reagents Materials. Technical grade meta-chloroperoxybenzoic acid (Cat #273031) and dichloromethane was obtained from Sigma-Aldrich. Eicosapentaenoic acid (EPA) and docosahexaenoic acid (DHA) used for synthesis were purchased from Nu-Chek Prep Inc (Elysian, MN). 1-ethyl-3-(3-dimethylaminopropyl) carbodiimide (EDC) HCl was purchased from

Thermo Scientific (catalog #22980). N-hydroxysuccinimide (NHS) was purchase from Acros Organics (catalog #157270250). NADPH was obtained from P212121 (Ann Arbor, MI). POPC [1-hexadecanoyl-2-(9*Z*-octadecenoyl)-sn-glycero-3-phosphocholine],1-palmitoyl-2-oleoyl-sn-glycero-3-phosphocholine], POPS [1-hexadecanoyl-2-(9*Z*-octadecenoyl)-sn-glycero-3-phospho-l serine] were purchased from Avanti Polar Lipids (Alabaster, AL). 19,20-EDP, 16,17-EDP, 17,18-EEQ, 14,15-EEQ, 11,12-EEQ, 8,9-EEQ, 5,6-EEQ and 14,15-EET were obtained from Cayman Chemical (Ann Arbor, MI). The antioxidant butylated hydroxytoluene (BHT) and was obtained from Sigma-Aldrich (St. Louis, MO). PAR4-AP (AYPGKF) was purchased from GL Biochem (Shanghai, China). Thrombin was purchased from Enzyme Research Laboratories (South Bend, IN), Collagen, ristocetin was purchased from Chorono LOG. ADP was purchased from Sigma. All other materials and reagents used were purchased from Sigma-Aldrich and Fisher Scientific.

Chemical synthesis of EEQ-EA and EDP-EA regioisomers. EEQ-EA and EDP-EA chemical synthesis was performed using a two-step synthesis. For non-specific epoxygenation reaction, 10 mg of either EPA or DHA was dissolved in 2 mL of dichloromethane (DCM) with 2 molar equivalents of mCPBA and reacted for 1 hour. The reaction was stopped with an equal volume of 10% aqueous $NaHCO_3$ for removal of mCPBA from the organic layer and the aqueous layer was re-extracted with equal volumes of DCM (3x) and dried under vacuum. Purification was achieved using normal phase high-performance liquid chromatography (NP-HPLC) using a Zorbax-NH_2 5 µm 9.4 x 250 mm semi-preparative column (Agilent, PN880952-208) with an isocratic gradient (hexane/methanol/acetic acid; 90:10:0.1) coupled to a high-performance liquid chromatography (HPLC) system (Figure 6.13A-B). In the instances of co-eluting regioisomers of DHA epoxides (19,20-EDP and 13,14-EDP) and EPA epoxides (17,18-EEQ and 11,12-EEQ), the mixtures were further purified on the same system using a reversed phase high-performance liquid chromatography (RP-HPLC), Sun Fire Prep C18 5 µm 19 x 50 mm (Waters, PN 186002566) and a mobile system composed of solvent A (H_20/acetonitrile/acetic acid 95:5:0.1) and solvent B (H_20/acetonitrile/acetic acid 5:95:0.1) and a linear gradient from 50% A to 0% A in 50 minutes (Figure 6.13C-D). The synthesis of 17,18-EEQ, 14,15-EEQ, 11,12-EEQ, 8,9-EEQ, 5,6-EEQ, 19,20-EDP and 16,17-EDP was confirmed by comparing retention times relative to authentic standards purchased from Cayman Chemical and high resolution mass spectrometry.

In the second step, the coupling of each respective EEQ or EDP regioisomer to ethanolamine was achieved by dissolving the epoxide/EDC/NHS/ethanolamine in acetonitrile in 1:10:10:10 ratio and

rocking at room temperature for 16 hours. Lastly, the resulting EEQ-EA and EDP-EA regioisomers were purified by RP-HPLC using a Sun Fire Prep C18 5 μm 19 x 50 mm column (Waters, PN 186002566). Purity and retention times were assessed using bioanalytical RP-HPLC and successful synthesis was confirmed by high resolution mass spectroscopy and proton nuclear magnetic resonance (Figure 6.14).

Synthesis of 17,18-DiHETE-EA and 19,20-DiHDPA-EA authentic standards. The EPA and DHA terminal epoxides, 17,18-EEQ and 19,20-EDP, were synthesized and purified as described above. The conversion of 17,18-EEQ and 19,20-EDP (100 ug) to the corresponding diol was accomplished by first solubilizing the standard in 100 uL acetonitrile and adding 1 mL of glacial acetic acid and water (1:1). The hydration of the epoxide to the diol moiety was accomplished by purging the reaction with N_2 and incubating the reaction at 45°C for 12 hours. The resulting diols were extracted with ethyl acetate and purified by RP-HPLC. The ethanolamide coupling was performed with the same conditions as the epoxides as listed above. Successful synthesis of the standards was confirmed by high resolution mass spectrometry and RP-HPLC elution times.

Expression and purification of cytochrome P450 reductase. Cytochrome P450 reductase (CPR) from *Ratticus norvegicus* was expressed and purified as previously described (*24*).

Liquid chromatography mass spectrometry analysis. Samples were analyzed with the 5500 QTRAP LC/MS/MS system (AB Sciex, Foster City, CA) in Metabolomics Lab of Roy J. Carver Biotechnology Center, University of Illinois at Urbana-Champaign. Software Analyst 1.6.2 was used for data acquisition and analysis. The 1200 series HPLC system (Agilent Technologies, Santa Clara, CA) includes a degasser, an autosampler, and a binary pump. The LC separation was performed on an Agilent Eclipse XDB-C18 (4.6 x 150mm, 5μm) with mobile phase A (0.1% formic acid in water) and mobile phase B (0.1% formic acid in acetontrile). The flow rate was 0.4 mL/min. The linear gradient was as follows: 0-2min, 90%A; 8min, 55%A; 13-25min, 40%A; 30min, 30%A; 35min, 25%A; 40-47min, 20%A; 47.5-54min, 90%A. The autosampler was set at 5°C. The injection volume was 10 μL. Positive mass spectra were acquired with the ion spray voltage of 5500 V under electrospray ionization (ESI). The source temperature was 450°C. The curtain gas, ion source gas 1, and ion source gas 2 were 32 psi, 60 psi, and 60 psi, respectively. Multiple reaction monitoring (MRM) was used for quantitation: 19,20-EDP-EA and 7,8-EDP-EA m/z 388.1 → m/z 62.1; 16,17-EDP-EA, 13,14-EDP-EA, and 10,11-EDP-EA m/z 388.1 → m/z 370.1; 17/18-EEQ-EA, 14/15-EEQ-EA, and 11/12-EEQ-EA m/z 362.1 → m/z 344.1;

8/9-EEQ-EA m/z 362.1 → m/z 62.0; 5/6-EEQ-EA m/z 362.1 → m/z 91.0; EPEA 346.3 → m/z 62.1; DHEA 372.4 → m/z 62.1; Anandamide m/z 348.3 → m/z 62.1. Internal standards were monitored at: m/z 350.3 → m/z 66.1 for EPEA-d4, m/z 376.4 → m/z 66.1 for DHEA-d4; m/z 352.3 → m/z 66.1 for anadamide-d4, m/z 372.1 → m/z 354.1 for 14/15-EET-EA-d8.

LC-MS/MS method for quantitation of 17,18-DiHETE-EA and 19,20-DiHDPA-EA. Samples were analyzed with the 5500 QTRAP LC/MS/MS system (AB Sciex, Foster City, CA) in Metabolomics Lab of Roy J. Carver Biotechnology Center, University of Illinois at Urbana-Champaign. Software Analyst 1.6.2 was used for data acquisition and analysis. The 1200 series HPLC system (Agilent Technologies, Santa Clara, CA) includes a degasser, an autosampler, and a binary pump. The LC separation was performed on an Agilent Eclipse XDB-C18 (4.6 x 150mm, 5μm) with mobile phase A (0.1% formic acid in water) and mobile phase B (0.1% formic acid in acetontrile). The flow rate was 0.4 mL/min. The linear gradient was as follows: 0-2min, 90%A; 8min, 60%A; 15-22min, 40%A; 23-29min, 90%A. The autosampler was set at 10°C. The injection volume was 1 μL. Positive mass spectra were acquired with the ion spray voltage of 5000 V under electrospray ionization (ESI). The source temperature was 450 °C. The curtain gas, ion source gas 1, and ion source gas 2 were 32 psi, 60 psi, and 55 psi, respectively. Multiple reaction monitoring (MRM) was used for quantitation: 19,20-DHDPA-EA m/z 406.3→m/z 370.3; 17,18-DHETE-EA m/z 380.3→m/z 344.3. Internal standard 14,15-DHET-EA was monitored at m/z 382.3→ m/z 346.3.

Extraction of AEA, EPEA, DHEA, EEQ-EA and EDP-EAs from rat tissue. The tissue extractions of AEA, DHEA, EPEA, EEQ-EAs and EDP-EAs were performed similarly as previously reported for the quantitative analysis of the EDCs (*25, 26*). Following Sprague-Dawley euthanasia, whole organs were immediately dissected, pooled (n = 3/pool), weighed and mechanically homogenized on ice with a Bio-homogenizer (Biospec, Bartlesville, OK) in a 1:1 ratio with PBS supplemented with AUDA (30 μm) and PMSF (1 mM) until a homogenous slurry was formed. The equivalent of 1 gram of each tissue was homogenized in 40 mL of ethyl acetate/hexane (9:1) with a Bio-homogenizer (Biospec, Bartlesville, OK) at room temperature and then sonicated for 1 min. The resulting solution was washed with a 30% volume of water and centrifuged for layer separation. The organic layer was removed and the aqueous layer was extracted twice with an equal volume of ethyl acetate/hexane (9:1). The pooled organic supernatant was removed using a Buchi 120 rotary evaporator (New Castle, DE), reconstituted in 1 mL of

chloroform and the metabolites of interest were isolated by solid-phase extraction (SPE) using a 1 mL silica gel column (Sigma # 214477). The reconstituted samples were added to the pre-conditioned silica column, washed 3 column volumes of chloroform and then eluted with 4 column volumes of methanol/chloroform (1:9). The eluent was dried and samples were reconstituted in ethanol for analysis via LC-MS-MS.

To validate the method, the metabolite extraction linearity was examined for each class of lipids from homogenized rat brain tissue. The metabolites 17,18-EEQ-EA, 19,20-EDP-EA, DHEA, EPEA and AEA were spiked at 20, 60 and 300 ng into homogenized rat brain tissue and extracted as described above. The average percent recovery was calculated by subtracting a non-spiked sample of each metabolite for comparison to authentic standards at low, middle and high levels on the standard curve. Extraction linearity for 20, 60 and 300 ng of all metabolites (17,18-EEQ-EA, 19,20-EDP-EA, DHEA, EPEA and AEA) were similar among lipids with average percent recoveries of 89.1 ± 3.1, 84.8 ± 2.8, and 71.5 ± 4.5 %, respectively.

Whole-cell metabolism assays. BV-2 microglial cells were seeded in 6-well dishes (5 x 10^5/well) and grown to 90% confluence in DMEM (Gibco, USA), 10% fetal bovine serum (Gibco, USA), penicillin (100 U/mL) and streptomycin (0.1 mg/mL) at 37°C and 5% CO_2. At the time of the experiment the supernatant was replaced with serum free media and cells were activated with 100 ng/mL of LPS for 12 hrs. In one set of experiments the supernatant and cells were collected at 1, 2, 4, 8, and 12 hours post-LPS stimulation and examined for the natural production of target lipid mediators. Alternatively, after the 12 hour LPS activation, cells were incubated with either EPEA (20 µM) or DHEA (20 µM) in serum free media for 30 minutes. The general P450 inhibitor, ketoconazole (0.5 µM) was added in some experiments for CYP inhibition of the CYP3A, CYP2C and CYP2J families. Controls lacking LPS stimulation were run in parallel with the experiment. After the appropriate time-period, cells were scraped and the supernatant was collected and subjected to three rapid freeze-thaw cycles using liquid N_2 and a warm water bath (37°C) for cell lysis. The supernatant and cells were extracted three-times with 4 volumes of ethyl acetate/hexane (9:1).

Incubations of EPEA and DHEA with brain microsomes. The preparation of microsomes derived from mouse tissues was achieved using previously described differential centrifugation methods(*18*). Tissues were dissected from Sprague-Dawley rats, weighed, homogenized and diluted to 20% (w/v) using a buffer containing 250 mM sucrose, 10 mM Tris-Cl (pH 7.5), 1 mM

PMSF and a protease inhibitor cocktail for mammalian tissue extraction (Nacalai Tesque #25955-11). A series of low (3000g) and medium speed (10,000g) centrifugation speeds were employed to remove cellular debris, nuclear and mitochondrial fractions. The resulting supernatant is centrifuged at 100,000 g for 90 min at 4°C to pellet the endoplasmic reticulum containing CYPs. The cell pellet was re-suspended in 50mM Tris (pH 7.5), 1mM DTT, 1mM EDTA and 20% glycerol with a Teflon homogenizer. Microsomal protein content was measured using a BCA assay kit (Thermo Fisher Scientific, Product No. 23233). Incubations with microsomes were performed at a concentration of 1 mg/ml of microsomes with high concentrations of DHEA and EPEA and then extracted using three volumes of ethyl acetate/hexane (9:1) three times. The organic layer was dried under vacuum and reconstituted in ice cold ethanol for LC-MS/MS analysis.

CYP2J2-ND kinetic metabolism of EPEA and DHEA. Human CYP2J2 was heterologously expressed and incorporated into the lipid bilayers of nanodiscs as previously described (*24*). Incubation mixtures contained CYP2J2-ND (0.2 μM), CPR (0.6 μM), BHT (0.1%) and incremental increases of either EPEA or DHEA (500 μl total volume) in 100 mM phosphate buffer (pH 7.4). Samples were equilibrated at 37°C for 5 minutes before the reaction was initiated with the addition of 0.5 mM NADPH. Reactions were stopped after 15 minutes, extracted three times with 1 mL of ethyl acetate and the organic layer was dried and reconstituted in ice cold ethanol for LC-MS/MS analysis.

Kinetic analysis of 17,18-EEQ-EA and 19,20-EDP-EA hydrolysis by soluble epoxide hydrolase. LC-MS/MS was performed to quantitate the conversion of the terminal epoxide to their vicinal diols using LC-MS/MS. Enzymatic linearity over a 10 min period was confirmed. Enzyme kinetics were estimated using incremental increases of substrate for the generation of kinetic curves that were fit to the Michaelis-Menten equation for calculation of V_{max} and K_m. Incubations were performed with recombinant sEH ($[E]_{final}$ = 6 nM) in $NaPO_4$ (100 mM, pH 7.4), bovine serum albumin (0.1 mg/ml) and substrate (17,18-EEQ-EA or 19,20-EDP-EA) at 37°C. After 5 minutes the reaction was stopped with methanol supplemented with AUDA (0.5 µM) and the solution was centrifuged to pellet protein (10,000 g x 10 min). The supernatant was collected and analyzed via LC-MS/MS.

PRESTO-Tango β-arrestin recruitment assay. Functional CB1 and CB2 assays were performed by the NIMH PDSP as previously described (*27*). In short, each metabolite was screened in triplicate at 10 µM in transiently transfected CB1/CB2 HEK293 cells for their ability

to functionally activate each respective receptor. Results reflect the percent receptor activation relative to CP55940 EC90.

Microglial neuroinflammation studies. BV2 microglial cells were plated in 24-well dishes (2 x 10^5/well) and grown to 80-90% confluence in DMEM (Gibco, USA), 10% fetal bovine serum (Gibco, USA) penicillin (100 U/mL) and streptomycin (0.1 mg/mL) at 37°C and 5% CO_2. At the time of the experiment, media was replaced with serum-free media and the cells were pre-treated with 19,20-EDP-EA for 4 hours prior to stimulation with 25 ng/mL LPS (Sigma-Aldrich, USA). Media was collected at 24 hours and the production of nitric oxide (NO) was determined by evaluating the media nitrite (NO_2^-) content using the Griess method. Collected media (80 µL) was mixed with Griess reagent A (Cayman Chem, #780018) and Griess reagent B (Cayman Chem, #780020) and the absorbance at 490 nm was used to quantify NO_2^- production using a standard curve. Media supernatant was also examined for the production of IL-6 (Cayman, #583371) and IL-10 (affymetrix eBioscience, #88-7105-22) cytokines. Compound cytotoxicity was assessed by measuring lactate dehydrogenase (LDH) release in the media using a commercially available kit (Cayman Chem, #601170).

Platelet aggregation studies. University of Michigan Review Board approved studies and written informed consent was obtained from all participants prior to blood collection. Human whole blood was drawn from the antecubital vein of healthy donors. Platelet- rich-plasma (PRP) was obtained from whole blood by centrifugation at 200g for 10 minutes. Platelets were pelleted from PRP in the presence of ACD (2.5%) and apyrase (0.02 U/mL) by centrifugation at 2000g for 10 minutes then resuspended in Tyrodes buffer (12 mM $NaHCO_3$, 127 mM NaCl, 5 mM KCl, 0.5 mM NaH_2PO_4, 1 mM $MgCl_2$, 5 mM glucose, 10 mM HEPES) to a final concentration of 3.0 x 10^8 platelets/mL. Change in light transmission was recorded by eight channel platelet aggregometer (Chronolog) under stirring at 1200 rpm at 37°C.

Washed human platelets were incubated with 12.5 µM, 25 µM, and 50 µM 17,18-EEQ-EA for 5 min and platelet aggregation was induced by 5 µM AA, Thrombin (1 nM), PAR4-AP (50µM), collagen (2mg/mL) U46619 (1 µM). DMSO and 14,15 EET were used as controls. No platelet agonists were added for the tests of 19, 20-EDP-EA in washed platelets. Experiments with platelet rich plasma (PRP) were adjusted to 3.0 x 10^8 platelets/mL using PPP from same donor. PRP was incubated with 12.5 µM, 25 µM, and 50 µM 17,18-EEQ EA for 5 min and platelet aggregation was induced by ADP (1 µM), collagen (2 µg/mL) or ristocetin (1 mg/mL).

Bovine coronary artery vasodilation assay. Fresh bovine hearts were procured on ice from the local butcher. The left anterior coronary artery was dissected from the adjacent connective tissue and cut into 2 mm ring sections. The artery lumen was then mounted on two parallel pins attached to a piezoelectric transducer for isometric tension measurements using a Myograph Tissue Bath System (DMT, Ann Arbor, MI) as previously described(*28*). Basal tension (100% relaxation) was set at 30 mN and tissues were equilibrated in Krebs Buffer (130 mM NaCl, 4.7 mM KCl, 1.18 mM KH_2PO_4, 1.17 mM $MgSO_4$, 14.9 mM $NaHCO_3$, 5.5 mM dextrose, 0.026 mM EDTA, 1.6 mM $CaCl_2$) for 1 hr. Maximal contractions were determined by washing with Krebs buffer supplemented with 60 mM KCl for 3 min, and then washed with Krebs Buffer to return to basal tension. This step was repeated until consistent contractile measurements were achieved. The thromboxane receptor agonist U46619 (20-40 nM) was used to constrict the rings to approximately 40-80% of maximal contraction (0% relaxation). Cumulative additions of either EEQ, EDP, EEQ-EA and EDP-EA (1 nM, 10 nM, 100 nM, 1 µM, 10 µM) were added to each chamber and the resulting % relaxation was plotted against the corresponding substrate dose.

Inhibition of human microvascular cell tube formation. The EEQ, EEQ-EA, EDP, and EDP-EA inhibition of vascular endothelial cell growth factor (VEGF) promoted tube formation was assessed in human microvascular endothelial cells (HMVEC, Cell Systems) as previously described(*29*). Briefly, 35 µl of matrigel are plated on the bottom of a 48 well plate and allowed to gel for 30 minutes at 37ºC. ~15,000 HMVECs are then seeded per well in EBM-2 media (Lonza) Supplemented with VEGF at 50% of the concentration used in EGM-2. After adding the compounds at the desired concentration, tube formation by HMVECs was quantified after 8 hours. Cells were imaged using a Cannon Rebel DSLR camera and tube area was quantified using ImageJ.

LC-ESI-MS for global analysis of CYP2J2-ND incubations with EPEA and DHEA. The reactions containing CYP2J2, CPR and NADPH with either EPEA or DHEA were resolved using a XTerra C18 column 2.1 × 150 mm, 3.5 μM (Waters), and a Waters Alliance 2695 reversed-phase high performance liquid chromatography (HPLC) coupled to an electrospray ionization (ESI) source. The different regioisomers were separated with mobile phase A (acetonitrile/H_2O/formic acid, 95:5:0.1) and mobile phase B (acetonitrile/H_2O/formic acid, 5:95:0.1) over a linear gradient as follows: 0–1 minute, 40% B; 41 minutes, 80% A; 42 minutes, 100% B; and then returned to initial conditions. For ESI, a Q-TOF Ultima time-of-flight mass spectrometer was used in positive

ion mode, with a spray voltage of 4.5 V and capillary temperature of 200°C. The mass and elution times of the metabolites were confirmed using authentic standards synthesized in-house.

17,18-EEQ-EA and 19,20-EDP-EA hydrolysis by rat forebrain membranes containing FAAH. The preparation of rat forebrain membranes were achieved using dounce homogenization in buffer (50 mM Tris pH 7.4, 1 mM EDTA and 3 mM $MgCl_2$) and membrane pelleting as previously described (*30*). Incubations contained 100 µg forebrain protein in a 0.5 mL reaction containing 50 mM Tris (pH 7.4), 1 mM EDTA, 3 mM $MgCl_2$, and 17,18-EEQ-EA or 19,20-EDP-EA at 50 µM. Linearity of the reactions were confirmed at 5, 20 and 40 minutes. Reactions were quenched with methanol containing 1 mM PMSF and centrifuged to pellet protein (10,000 g x 10 min). The supernatant was collected and analyzed via LC-MS/MS as outlined below.

LC-MS/MS method for quantitation of 17,18-EEQ and 19,20-EDP. Analyses were performed using the 5500 QTRAP LC/MS/MS system (AB Sciex, Foster City, CA) in Metabolomics Lab of Roy J. Carver Biotechnology Center, University of Illinois at Urbana-Champaign. The 1200 series HPLC system (Agilent Technologies, Santa Clara, CA) includes a degasser, an autosampler, and a binary pump, and this system was used to separate the metabolites. LC separation was performed on an Agilent Eclipse XDB-C18 (4.6 x 150mm, 5µm) with mobile phase A (0.1% formic acid in water) and mobile phase B (0.1% formic acid in acetonitrile) at a flow rate was 0.4 mL/min. The linear gradient was as follows: 0-2min, 90%A; 8min, 55%A; 13-25min, 40%A; 30min, 30%A; 35min, 25%A; 40min, 20%A; 45-47min, 15%A; 48-54min, 90%A. The autosampler was set at 5°C. The injection volume was 10 µL. Negative mass spectra were acquired with the ion spray voltage of -4500 V under electrospray ionization (ESI). The source temperature was 450 °C. The curtain gas, ion source gas 1, and ion source gas 2 were 32 psi, 50 psi, and 55 psi, respectively. Multiple reaction monitoring (MRM) was used for quantitation: 17,18-EEQ m/z 317.0 → m/z 299.0 and 19,20-EDP m/z 343.0 → m/z 299.0 using 14,15-EET as the internal standard.

Primary microglia neuroinflammation studies. Primary microglia cultures were isolated from freshly euthanized piglets following previously described methods (*31*). Isolated microglia cells were plated at 2 x 10^6 in 24-well plates and allowed to adhere for 3 hrs before a 1 hour compound pre-incubation step followed by stimulation with LPS (10 ng/mL) for 12 hours in presence or absence of compound. Supernatant was analyzed for IL-6 content using a porcine specific ELISA

(R&D Systems Inc., Minneapolis, USA cat #P6000B). The final vehicle (DMSO) concentration was 0.04% (n = 3 or greater).

Statistics. Results are presented as average ± standard error unless noted otherwise. Kinetic parameters were determined by nonlinear regression of the Michaelis-Menten equation using Origin Pro 8.6. Data were analyzed for statistical significance using a two-sided student's *t*-test where $*P < 0.05$, $**P < 0.01$, and $***P < 0.001$.

6.4 RESULTS

The ω-3 endocannabinoid epoxides are endogenous lipids in the brain and peripheral tissues. Previously, a wide range of N-acyl amide lipids have been successfully quantified using HPLC coupled with fluorescence detection (*32*), GC-MS (*33*), LC-MS (*34*), and Ag^+ coordination LC-MS/MS in selected reaction monitoring (SRM) mode (*35*). As shown in Figure 6.2A, a new LC-MS/MS in multiple reaction monitoring mode (MRM) was developed to structurally identify and quantitate EDP-EA regioisomers (19,20-, 16,17-, 13,14-, 10,11-, and 7,8-), EEQ-EA regioisomers (17,18-, 14,15-, 11,12-, 8,9-, and 5,6-), EPEA, DHEA, and AEA. The authentic standards of EEQ-EA and EDP-EA regioisomers were prepared in a two-step synthesis and purified using HPLC as reported in the methods section.

The target endocannabinoid metabolites were extracted from the tissues using a two-step extraction method followed by LC-MS/MS (*25*). To estimate the basal levels of the endogenous EEQ-EA and EDP-EA regioisomers, three sets of pooled (n = 3) Sprague-Dawley rat brain, spleen, heart, liver, and kidneys were extracted and analyzed. As shown in Figure 6.2B, both classes of EEQ-EA and EDP-EA metabolites were measured in rat brain, with the two terminal epoxides, 17,18-EEQ-EA and 19,20-EDP-EA being the predominant metabolites. A similar trend was also observed in peripheral organs with both classes of metabolites being found in all the tissues (Figure 6.2C; Table 6.1). Specifically, the values of 17,18-EEQ-EA were relatively consistent among tissues from brain, spleen, heart, liver, and kidney with levels varying from 60-90 pmol $gram^{-1}$, whereas the values of 19,20-EDP-EA were more variable with brain, spleen, heart, liver, and kidney levels measured at 70-400 pmol $gram^{-1}$ (Figure 6.2C and Table 6.1).

Notably, similar levels of DHEA were extracted from tissues, which were generally comparable to the levels of 19,20-EDP-EA and AEA. Conversely, relatively low levels of EPEA parent compound were detected, with levels significantly lower than the corresponding 17,18-EEQ-EA. Importantly, the relatively higher levels of DHEA and lower EPEA levels are consistent with what

is reported in the literature lending credibility to the quantitative values (*9*). Some of the metabolites were also detected at lower levels in porcine brains and pooled human plasma (Table 6.1). The detection of the ω-3 endocannabinoid epoxides warranted further investigation with regards to their production in live cells.

EEQ-EA and EDP-EA are naturally produced by LPS stimulated BV-2 microglial cells. Microglial cells are metabolically active brain macrophages that continuously survey the brain parenchyma and maintain homeostasis. If microglia encounter harmful endogenous ligands and microbes, they display pro-inflammatory activity followed by anti-inflammatory activity to promote defense and healing, respectively. Previously, it was demonstrated that activation of BV-2 microglia resulted in upregulation of AEA metabolizing CYPs which produced EET-EA regioisomers when supplemented with AEA (*19*). Given the endogenous presence of EPEA and DHEA in the brain (Figure 6.2B), we explored metabolite production by quiescent and activated BV-2 microglial cells in a post-LPS stimulated time-course. As shown in Table 6.2, both EEQ-EA and EDP-EA metabolites are naturally produced at 1 hour after LPS stimulation and persist throughout a 12 hour period. Similar results were observed for EPEA and AEA at 4 hours, with levels more than an order of magnitude greater than the epoxides at 12 hours. While DHEA levels time-dependently increased from 1-4 hours, they diminished at 12 hours.

To test whether activated BV-2 microglial cells could directly convert the EPEA and DHEA parent compounds into EEQ-EA and EDP-EA metabolites, we used cell media supplemented with either EPEA or DHEA for 30 min and analyzed for metabolite production. As shown in Figures 6.2D and 6.2E, EPEA and DHEA were rapidly converted to all EEQ-EA and EDP-EA regioisomers, respectively. Total levels of EEQ-EAs were approximately one order of magnitude greater than EDP-EAs. Importantly, the production of both the EEQ-EA and EDP-EA metabolites was reduced when cells were pre-incubated with the CYP inhibitor ketoconazole (0.5 μM), thus showing that the ω-3 endocannabinoid epoxides are produced enzymatically via involvement of CYP epoxygenase enzymes.

Epoxygenation of EPEA and DHEA by rat brain microsomes. To evaluate the ability of the rat brain CYPs to directly epoxygenate EPEA and DHEA, we performed metabolism studies where we incubated rat brain microsomes with substrate in the presence of the CYP redox partner, cytochrome P450 reductase (CPR), and NADPH. As shown in Figure 6.3A, when EPEA was utilized as substrate, the microsomal CYP epoxygenases produced all EEQ-EA regioisomers, with

catalytic preference for the terminal olefin (17,18-EEQ-EA) which accounted for 46% of the total epoxide product. Similarly, when DHEA was used in the reactions, epoxygenases produced all the EDP-EA regioisomers, with preference for the terminal olefin (19,20-EDP-EA), which accounted for 48% of total epoxide formed (Figure 6.3B). In an effort to understand the substrate specificity and regioselectivity when both substrates are present, we performed rat brain microsomal incubations in the presence of equimolar amounts of EPEA and DHEA (Figure 6.3C). Notably, there was some evidence of competition between EPEA and DHEA as the total EEQ-EA and EDP-EA products were reduced in this reaction. Similar results were obtained when pig brain microsomes were used to study metabolism of DHEA and EPEA (Figure 6.6). Taken together, this suggests that similar CYP epoxygenases are implicated in the metabolism of both DHEA and EPEA and there is competition for the substrates among the various CYP isoforms in rat brain microsomes. Microsomes contain various CYP epoxygenase enzymes; therefore it is important to identify which isoform is responsible for the formation of these metabolites in human.

Recombinant human CYP2J2 incorporated into nanodiscs directly epoxygenates EPEA and DHEA to form EEQ-EA and EDP-EA metabolites. In humans, the epoxygenase pathway is predominantly mediated by CYP2C8, CYP2C9, and CYP2J2. Notably, these isozymes were previously shown to convert both EPA and DHA into EEQ and EDP monoepoxides, respectively (*36*). Previously we showed that the ω-6 endocannabinoids, AEA and 2-arachidonoylglycerol, are converted into their corresponding epoxides by CYP2J2 epoxygenase, the most highly expressed CYP epoxygenase in brain and cardiovascular system (*18, 37*).

CYP2J2 was recombinantly expressed and incorporated with its redox partner into nanodiscs (*18*). CYP2J2-CPR-nanodisc incubations with EPEA or DHEA linearly produced EEQ-EA and EDP-EA regioisomers for 30 minutes (data not shown). Kinetic curves of metabolism were generated for both EPEA and DHEA and were fit to Michaelis-Menten kinetics. As shown in Figure 6.3D, CYP2J2-ND metabolism of EPEA into EEQ-EA regioisomers followed Michaelis-Menten kinetics with Vmax, Km and Vmax/Km values listed in the top right table. Notably, CYP2J2 demonstrated a preference for the EPEA (80 μM) terminal olefin with the average regioselectivity of the different regioisomers reported in figure 6.3D; top middle. CYP2J2-ND metabolism of DHEA produced EDP-EA regioisomers following Michaelis-Menten kinetics with Vmax, Km and Vmax/Km listed in the adjacent table (Figure 6.3D; bottom right). The CYP2J2 enzyme demonstrated a dramatic preference for the DHEA (80 μM) terminal olefin with the

average regioselectivity the regioisomers reported in Figure 6.3D; bottom middle. Therefore we demonstrate that CYP2J2 can metabolize EPEA and DHEA with substantially higher efficiency than the reported rates for EPA or DHA (*36*). As the terminal epoxides 17,18-EEQ-EA and 19,20-EDP-EA were predominantly produced by the CYP enzymes, further characterization and biological activity was measured using these epoxides.

Hydrolysis of 17,18-EEQ-EA and 19,20-EDP-EA by soluble epoxide hydrolase and fatty acid amide hydrolase (FAAH). The EEQ-EA and EDP-EA metabolites are unique in that they contain both epoxide and ethanolamide motifs (Figure 6.1). Therefore we next evaluated if these metabolites are targets for both soluble epoxide hydrolase (sEH) and fatty acid amide hydrolase (FAAH). Bioactive fatty acid epoxides are short-lived lipid mediators due to their rapid inactivation by soluble epoxide hydrolase (sEH) *in vivo*. Previous studies have shown that EEQ and EDP are hydrolyzed to their less active di-hydroxy metabolites by sEH (*38*). To determine if sEH hydrolyzes 17,18-EEQ-EA and 19,20-EDP-EA into their corresponding vicinal diols 17,18-DiHETE-EA and 19,20-DiHDPA-EA (Figure 6.3E), we developed a new LC-MS/MS method for quantitation of the diols. Incubations containing 17,18-EEQ-EA or 19,20-EDP-EA with sEH were performed. Enzyme kinetics were estimated and fitted to the Michaelis-Menten equation. As shown in Figure 6.3F, 17,18-EEQ-EA was rapidly hydrolyzed with V_{max}/K_m value of 77.7 ± 1.9 nmol min^{-1} mg^{-1} of sEH (Figure 6.3F). Interestingly, the metabolism of 19,20-EDP-EA was substantially slower with V_{max}/K_m value of 12.3 ± 0.2 nmol min^{-1} mg^{-1} of sEH (Figure 6.3G).

In separate studies, 17,18-EEQ-EA hydrolysis to 17,18-EEQ by rat forebrains containing FAAH was measured approximately three-fold faster than 19,20-EDP-EA conversion to 19,20-EDP (Figure 6.8). Taken together, we show that both 17,18-EEQ-EA and 19,20-EDP-EA are efficiently hydrolyzed by human sEH and FAAH with preference for 17,18-EEQ-EA metabolite.

Anti-inflammatory signaling actions of 17,18-EEQ-EA and 19,20-EDP-EA. One of the striking hallmarks of ongoing inflammation in neurodegenerative diseases is chronic microglial activation (macrophages in the CNS) (*39*). There is a wide interest in unearthing lipid metabolites that can reduce microglial activation and thereby combat neuroinflammation. Several studies indicate that the endocannabinoids reduce microglial-promoted neuroinflammation through activation of the CB2 receptor. Consequently, there is a strong interest in search for the discovery of endocannabinoid derivatives that are CB2 selective agonists as means to mitigate inflammatory pathologies (*40-42*). The 17,18-EEQ-EA and 19,20-EDP-EA metabolites have "N-acyl

ethanolamide endocannabinoid" functional motif and are also produced endogenously by activated BV-2 microglia cells (Figure 6.2D-E; Table 6.2). Hence we examined the anti-inflammatory effects of these molecules using LPS stimulated microglial cells.

As shown in Figure 6.4A, 17,18-EEQ-EA dose-dependently decreased LPS-induced production of IL-6 and nitrite, whilst decreasing LPS-induced cytotoxicity in BV-2 cells, further demonstrating nullification of the pro-inflammatory effects (*43*). We also observed significant production of the anti-inflammatory cytokine IL-10 (Figure 6.4A). More potent dose-dependent inhibition was measured when 19,20-EDP-EA was employed, as evidenced by significant inhibition of IL-6 and nitrite production at concentrations equal or greater than 2.5 μM (Figure 6.4B). Moreover, the LPS-induced cytotoxicity was significantly decreased at doses equal or greater than 5 μM. Similar to 17,18-EEQ-EA, the 19,20-EDP-EA metabolite also promoted the production of IL-10 in the presence of LPS.

It is known that both fatty acid epoxides and endocannabinoids function through multiple receptors (*6, 44*). Therefore, we performed mechanistic studies with selected inhibitors to delineate the mechanism of the anti-inflammatory action (Figure 6.4C-D and Figure 6.9). Using CB2 selective antagonist (AM630) or PPAR-γ selective antagonist (GW9662), we consistently observed a partial reversal of the anti-inflammatory effects of both metabolites indicating that CB2 and PPARγ are involved in mediating the anti-inflammatory action of 17,18-EEQ-EA (Figure 6.4C) and 19,20-EDP-EA (Figure 6.4D). Lastly, the anti-inflammatory effects of the compounds was confirmed at 5 μM using freshly isolated piglet microglia cells stimulated with LPS which diminished IL-6 production thereby confirming their activity in primary cells (Figure 6.10). As previously noted, the anti-inflammatory response of both 17,18-EEQ-EA and 19,20-EDP-EA were more pronounced in the BV-2 cell line,.

Determination of the activation of cannabinoid receptor-2 by 17,18-EEQ-EA and 19,20-EDP-EA using β-arrestin-recruitment PRESTO-Tango assay. Previously it was shown that CYP-mediated epoxidation of both AEA and 2-AG resulted in increased CB2 binding and activation (*35, 45*). Additionally, as shown in Figure 6.4C-D, it was determined that the anti-inflammatory action of endocannabinoid epoxides is partly mediated by CB2. In literature, EPEA and DHEA are reported as weak agonists of the cannabinoid receptors (*9*). To explore if oxygenation of EPEA or DHEA by CYPs alters the activity at these receptors, functional assays were performed utilizing

a β-arrestin-recruitment PRESTO-Tango assay for comparison to full CB1 and CB2 agonists as previously described (*27*).

As shown in Figure 6.4E, the DHEA parent compound was a weak agonist of CB2 with little activation of CB1, as determined previously. However, the DHEA monoepoxides, 19,20-EDP-EA and 16,17-EDP-EA, were more potent functional activators of both cannabinoid receptors with greater preference for the CB2 receptor. Similarly, the EPEA parent compound was a weak agonist of CB1 with negligible activation of CB2 but the conversion to the EPEA monoepoxides, 17,18-EEQ-EA and 14,15-EEQ-EA, also demonstrated significant CB2 activation of CB2 relative to EPEA. Thus, the CYP-mediated epoxygenation of EPEA and DHEA resulted in formation of their corresponding epoxides that are CB2 preferring partial agonists. Qualitatively, these findings generally support the hypothesis that the CYP mediated epoxygenation of ω-6 and ω-3 endocannabinoids produces CB2 preferring metabolites and are consistent with what is reported in the literature for both AEA and 2-AG (*19, 35*). As the PUFA epoxides are also documented hemodynamic regulators, efforts were undertaken to determine a potential role for the omega-3 endocannabinoid epoxides in regulating aspects of the clotting cascade.

The endocannabinoid epoxides 17,18-EEQ-EA and 19,20-EDP-EA are regulators of platelet function. The CYP-mediated epoxygenation of AA produces EETs that are endothelial derived hyperpolarizing factors (EDHF) that inhibit platelet aggregation and adhesion to endothelial cells (*46*). Correspondingly, 17,18-EEQ and 19,20-EDP metabolites also inhibit platelet aggregation with comparable IC_{50} values relative to 14,15-EET (*47*). Thus, the EEQ-EA and EDP-EA metabolites were hypothesized to modulate platelet function. Using washed human platelets we show that 17,18-EEQ-EA inhibited AA-induced platelet aggregation in a dose-dependent manner (*48*) (Figure 6.5A). These inhibitory effects were not observed in thrombin, PAR4-AP, collagen and U46619 induced platelet aggregation (Figure 6.11). Additionally, no significant inhibition of platelet aggregation in platelet rich plasma was observed when ADP, collagen, or ristocetin was used to induce aggregation (Figure 6.12). Thus, the anti-platelet aggregatory properties of 17,18-EEQ-EA appear to specifically inhibit the AA-induced platelet aggregation.

Conversely, 19,20-EDP-EA did not inhibit AA-induced platelet aggregation. Rather a dose-dependent increase of aggregation under stirring conditions, in the absence of any agonist, was consistently observed (Figure 6.5B). As the 19,20-EDP metabolite mediates anti-platelet aggregatory properties, there was a deviation in the behavior of 19,20-EDP-EA, suggesting that

the addition of the ethanolamide motif to 19,20-EDP is responsible for the observed pro-aggregatory effects.

17,18-EEQ-EA and 19,20-EDP-EA mediate coronary artery vasodilation. CYP epoxygenases convert ω-3 fatty acids EPA and DHA into their corresponding epoxides EEQ and EDP that are vasodilatory in nature (*49*). These epoxide metabolites are thought to be largely responsible for the observed anti-hypertensive effects of ω-3 fatty acids (*50*). Therefore, we compared the vasodilatory effects of 17,18-EEQ-EA and 19,20-EDP-EA relative to the 17, 18- EEQ and 19, 20-EDP parent compounds by monitoring their ability to relax bovine coronary arteries pre-constricted with U-44619 using isometric tension measurements. As shown in Figures 6.5C and 6.5D, both 17,18-EEQ-EA and 19,20-EDP-EA dose-dependently relaxed constricted bovine coronary arteries. However, the ED_{50} values were approximately two-fold greater than 17,18-EEQ and 19,20-EDP. Thus, the endocannabinoid epoxides were vasodilatory in nature, albeit with reduced potency relative to their epoxide parent compounds.

17,18-EEQ-EA and 19,20-EDP-EA inhibit angiogenesis in human dermal microvascular endothelial cells (HMVEC). Angiogenesis plays many roles in both normal homeostatic functions as well as many pathological disease states. Accumulating evidence suggests that consumption of ω-3 fatty acids inhibit angiogenesis in cancer (*49*). Similarly, endocannabinoids are recognized for their ability to inhibit cancer, in part through their anti-angiogenic properties (*51*, *52*). To determine if the EEQ-EAs and EDP-EAs demonstrate a greater, similar, or diminished ability to inhibit angiogenesis, a matrigel tubulogenesis assay was performed utilizing HMVEC and pro-angiogenic VEGF, as previously described (*29*). As represented in Figure 6.5E, 17,18-EEQ-EA at 1 and 3 μM dose-dependently inhibited VEGF-mediated tubulogenesis with a decrease of tubulogenesis surface area of 18% and 46%, respectively. Parallel studies were used for 17,18-EEQ, which produced similar, albeit slightly less potent results with 1 and 3 μM average decreases of 9% and 28%, respectively. Identical conditions were used to screen 19,20-EDP-EA at 1 and 3 μM with tubulogenesis surface area decreased by 31% and 75%, respectively. Following a similar albeit less potent trend, 19,20-EDP at 1 and 3 μM decreased tubulogenesis by 25% and 61%, respectively. Previously, the anti-angiogenic actions of the EDP metabolites were shown to be mediated through potent inhibition of VEGF-stimulated cell migration through a yet to be identified ω-3 epoxyeicosanoid pathway (*53*).

6.5 DISCUSSION

In this work, we demonstrate that the ω-3 endocannabinoids, EPEA and DHEA, are oxygenated by enzymes of the CYP epoxygenase pathway to generate a novel class of bioactive lipids that we termed as ω-3 endocannabinoid epoxides - EEQ-EAs and EDP-EAs. These molecules share structural similarity to both their endocannabinoid and epoxide parent compounds, with potential to exert physiological effects that are mediated through the cross talk of the endocannabinoid and epoxide signaling pathways. To gain improved understanding of the formation, degradation and biological function of these metabolites, we performed several studies.

First, a targeted lipidomics LC-MS/MS method was developed which revealed a wide distribution of EEQ-EAs and EDP-EAs in both the brain and peripheral organs. Notably, the detection of relatively high endogenous levels of the terminal epoxides, 17,18-EEQ-EA and 19,20-EDP-EA regioisomers, in the rat brain and peripheral tissues are close to the levels of AEA and DHEA. This suggested that they are produced enzymatically and implicated the involvement of the CYP epoxygenases in their biosynthesis comes as the terminal ω-3 double bond is the preferred site of the CYP mediated catalysis of ω-3 FAs (*22*).

As the microglial cytochrome P450 (CYP) epoxygenase pathway is upregulated under inflammatory conditions (*54*), there is a strong possibility of CYP mediated metabolism of these endocannabinoids. We demonstrated that BV-2 microglia CYPs are involved in EPEA/DHEA metabolism as the epoxygenation of both substrates was significantly diminished by pre-incubating microglia cells with ketoconazole (0.5 μM). Ketoconazole is involved in CYP inhibition of the CYP2, CYP3 and CYP4 families (Figure 6.2D-E).

The discovery of the metabolites in the different tissues prompted us to investigate the specific CYP enzymes that synthesize these metabolites. We performed *in vitro* incubations of DHEA and EPEA with the rat brain microsomes and quantified the epoxide products by LC-MS/MS. While the metabolism of DHEA and EPEA by microsomes informs us about metabolism in milieu of other proteins, it is important to identify specific CYPs that give rise to these epoxides in humans. In humans, the main epoxygenases are CYP2C8, CYP2C9 and CYP2J2. Consequently, we did further metabolism studies with CYP2J2 (the major epoxygenase in the brain and heart of human) and brain microsomes to directly epoxygenate EPEA and DHEA (Figure 6.3A-D). As shown in Figure 6.3A and 6.3B, rat brain microsomes epoxygenated both EPEA and DHEA with similar

preference for both ligands. When equimolar amounts of EPEA and DHEA were added to the incubation, we observed a comparable decrease of EEQ-EA and EDP-EA total products relative to incubations when only one ligand was employed (Figure 6.3C). This implied that DHEA and EPEA are in competition for some of the same CYPs with neither substrate showing clear preference for these enzymes. Because the rat CYP epoxygenases are enzymatically different from human CYP epoxygenases, we also performed incubations with porcine brain microsomes which contain a CYP2J isozyme with similar homology as human CYP2J2 (*18*). Importantly, the pig brain microsomes exhibited similar trends as the rat brain microsomes that supported the hypothesis that some of the same CYPs oxygenate both EPEA and DHEA (Figure 6.6). We further demonstrated using recombinant human CYP2J2 incorporated into nanodiscs, which revealed an epoxygenation of both substrates at comparable rates, albeit with a different regioselectivity (Figure 6.3D).

As discussed above, we confirmed the direct epoxygenation of EPEA/DHEA by recombinant protein, brain microsomes, and microglial cells. Thus, when adequate EPEA/DHEA and specific CYP epoxygenases are present, these metabolites will be spontaneously generated *in vivo*. However, there is the possibility of an indirect biosynthetic route that involves the CYP-mediated epoxygenation of ω-3 FAs into EEQ or EDP, followed by their re-esterification and storage into the plasma membrane. These epoxides are then cleaved by phospholipases and converted to EEQ-EA or EDP-EA metabolites, presumably through the same biosynthetic pathway as EPEA or DHEA.

The EEQ-EA and EDP-EA metabolites are unique in that they contain both epoxide and ethanolamide motifs that are specific functional targets for both soluble epoxide hydrolase (sEH) and fatty acid amide hydrolase (FAAH). Therefore in order to estimate if the *in vivo* half-life of the metabolites might differ among classes we examined the degradation of 17,18-EEQ-EA and 19,20-EDP-EA metabolism by soluble epoxide hydrolase (sEH) and fatty acid amide hydrolase (FAAH). In mammals, these serine hydrolases are found in the brain as well as the peripheral organs where they rapidly inactivate bioactive lipids via hydrolysis (*55, 56*). Previous reports demonstrated that both EEQ and EDP regioisomers are efficiently hydrolyzed by sEH to their corresponding diols and are preferred substrates relative to the ω-6 EETs (*38*). Herein, we show the sEH conversion of 17,18-EEQ-EA into 17,18-DiHETE-EA is more than 7-fold more efficient than the 19,20-EDP-EA hydrolysis to 19,20-EDP (Figure 6.3F-G). Additionally, the 17,18-EEQ-

EA hydrolysis to 17,18-EEQ by rat forebrains containing FAAH was measured approximately three-fold faster than 19,20-EDP-EA conversion to 19,20-EDP (Figure 6.8). Thus, the relatively faster turnover of EEQ-EA was of interest since its endogenous levels were comparable to EDP-EA, which might suggest that EEQ-EA is being produced at a faster rate. Consistent with this idea, it is known that EPA and DHA are absorbed at similar rates in the brain, but EPA levels are ~300 fold lower than DHA due to rapid oxygenation through different pathways (*57*). Thus, it is logical to surmise that EEQ-EA levels might be increased at the expense of EPA through metabolism in CYP epoxygenase and EDC pathways in the brain.

The similar endogenous brain levels of these metabolites prompted examination of both their bioactive signaling properties in the context of the CNS. Both the epoxide and ethanolamide functional motifs separately exert anti-inflammatory effects in a wide range of tissues including the brain (*41, 58*). As discussed above, the production of EEQ-EA and EDP-EA regioisomers by LPS-stimulated BV-2 cells suggested a role for these metabolites in microglia inflammation (Table 6.2). As shown in Figure 6.4A-B, both 17,18-EEQ-EA and 19,20-EDP-EA dose-dependently inhibited the production of two prototypic pro-inflammatory biomarkers, IL-6 and NO, whilst increasing the production of the anti-inflammatory cytokine, IL-10. Additionally, the reduction of lactate dehydrogenase (LDH) release associated with LPS stimulation provided further confirmation of the nullification of toll-like receptor-4 signaling. The decrease of IL-6 and increase of IL-10 cytokines raises questions whether these metabolites can influence microglia states from the pro-inflammatory M1 phenotype to the repair M2 phenotype that produces anti-inflammatory cytokines. This notion is consistent with recent reports that detail a role for CB2 ligands and epoxide lipids (EETs) in the promotion of the M2 macrophage phenotype (*59, 60*). Notably, the anti-inflammatory effects were blocked, in part, with AM630 (CB2 inhibitor), GW99662 (PPARγ inhibitor) (Figure 6.4C-D) and pertussis toxin (PTX) (Figure 6.9C-D). Importantly, PTX acts to ribosylate the α_i subunit thereby attenuating CB1/CB2 intracellular signaling through its typical pathway. However, the inhibitors/toxins that were tested only partially blocked the anti-inflammatory effects of the endocannabinoid epoxides suggesting alternative pathways.

To validate the CB2 mediated anti-inflammatory pathway we employed a β-arrestin recruitment assay for both CB1 and CB2 receptors (Figure 6.4E). The functional assay demonstrated that the epoxygenation of the EPEA and DHEA converted weak CB1/CB2 agonists to partial CB2 agonists. Interestingly, the 19, 20-, and 16,17-EDP-EA were shown to be the most potent and

preferential CB2 agonists with the CB2:CB1 activation ratio of three- and four-fold, respectively. These findings were consistent with previous studies that demonstrated that the CYP-mediated epoxygenation of the ω-6 endocannabinoids, AEA and 2-AG, produced novel endocannabinoid epoxides with increased potency and preferential targeting of CB2 (*19, 35*). Collectively these separate studies establish that the CYP mediated epoxidation of endocannabinoids such as AEA, 2-AG, DHEA and EPEA enhances the activation of the CB2 receptor and possibly provides a CYP mediated mechanism to regulate inflammatory pathologies by producing anti-inflammatory metabolites.

EETs play an important role in neuroglio-vascular coupling and there is potential interaction between EETs and neuroactive endocannabinoid signaling pathways (*58*). Relative to EETs the effects of EEQs and EDPs share many of the same physiological effects, such as vasodilation and inhibition of platelet aggregation, while exerting opposite effects in the inhibition of angiogenesis. We therefore focused on the potential biological actions of 17,18-EEQ-EA and 19,20-EDP-EA in the blood and vasculature.

The inhibition of platelet aggregation by 17,18-EEQ-EA (Figure 6.5A) is consistent with what is known about the 17,18-EEQ parent compound and other related epoxides. Specifically, the CYP metabolism of AA, EPA, and DHA produces bioactive epoxides such as 14,15-EET that are recognized for their ability to inhibit platelet aggregation and reduce thrombocyte adhesion (*61*). Conversely, early reports demonstrated that 2-AG and AEA induce platelet aggregation only after hydrolysis by fatty acid amide hydrolase (FAAH) through a pro-clotting arachidonic acid mediated mechanism (*62, 63*). Surprisingly, 19,20-EDP-EA failed to inhibit platelet aggregation and rather promoted platelet clotting under stirring conditions (Figure 6.5B). When it is considered that 19,20-EDP, 19,20-DHETE, and DHA are anti-aggregatory mediators, our finding reveal a potentially important structure activity relationship among these lipids. Moreover, this affords the first evidence of a pro-platelet aggregatory mechanism of an ω-3 derived metabolite which should be taken into consideration when weighing the potential benefits of DHA supplementation. Moreover, when targeting these pathways it is critical to understand how each metabolite will affect the wide range of physiological functions in order to maintain lipid concentrations within a therapeutic window.

Considering that lipid mediators such as thromboxane promote platelet aggregation while simultaneously constricting vessels, we examined the effects of the EEQ-EAs and EDP-EAs on

vascular tone. The pro-vasodilatory effects of 17,18-EEQ and 19,20-EDP parent compounds are well documented and are thought to be associated with the anti-hypertensive effects associated with ω-3 supplementation (*22, 64*). The administration of both 17,18-EEQ-EA and 19,20-EDP-EA provided less potent dose-dependent relaxation of pre-constricted bovine arteries, which suggested a mechanistic function similar to that of the parent epoxide mediators (Figure 6.5C-D).

The anti-angiogenic effects of the EDPs are opposite to the pro-angiogenic effects of the EETs and identifying the roles of eicosanoids in these functions constitutes an active area of research (*49*). As shown in Figure 6.5E, the anti-angiogenic effects of 17,18-EEQ-EA and 19,20-EDP-EA were more potent when compared to their epoxide parent compounds in VEGF promoted angiogenesis of HMVEC cells. This additive effect is possibly mediated through the endocannabinoid moiety that also provides anti-cancer activity (*7, 8*).

Overall, we report on a new class of metabolites that are naturally produced from endogenous ω-3 endocannabinoids via cross talk of the enzymes in the endocannabinoid and cytochrome P450 pathways. These dual functional lipid-signaling molecules show diverse bioactivity with respect to their inflammatory action, vasodilation, platelet aggregation and angiogenesis. Taken together, these separate studies establish that the CYP mediated epoxidation of ω-3 endocannabinoids DHEA and EPEA leads to the formation of CB2-preferring agonist activity when compared to the parent compounds.

When considered in the larger context of ω-3 FA dietary supplementation and the current development of sEH and FAAH inhibitors as therapeutics, it is critically important to first understand what lipids comprise the lipidome and what their biological actions are in order to fully understand the mechanisms of these drugs and avoid any untoward effects. In summary, this is the first step to evaluate CYP epoxygenase derived ω-3 endocannabinoid epoxides that in the future by virtue of their biological properties will serve as potential therapeutic targets for diseases such as neuroinflammation and cerebrovascular disorders.

6.6 ACKNOWLEDGMENTS

The authors greatly appreciate the contributions of Dr. Zhong Li at the Metabolomics Laboratory of Roy J. Carver Biotechnology Center, University of Illinois at Urbana-Champaign. The authors thank Furong Sun and the School of Chemical Sciences mass spectrometry facility, University of Illinois at Urbana-Champaign. The authors thank Prof. Stephen Sligar for providing the gene encoding MSP1D1. The genes encoding CB1 and CB2 were generous gifts from Professor Ken

Mackie. HEK293T cells was provided by the Prof. Jing Yang lab. We gratefully acknowledge Dr. Shah and the Prof. William Campbell lab for the hands-on training in the bovine coronary artery vasodilation assay. We sincerely thank Dan Gilman for the generous gifts of fresh bovine hearts. We greatly appreciate the procurement of freshly isolated Sprague-Dawley rat tissues by Holly Fairfield. This work was supported in part by the National Institutes of Health (NIH) Office of Dietary Supplement (ODS), GM105671 (M.H.) and HL114405 (M.H.) and AHA SDG grant (A.D) and AHA predoctoral fellowship (D.R.M). The study was partially funded by HD069899 (RWJ).

6.7 FIGURES AND TABLES

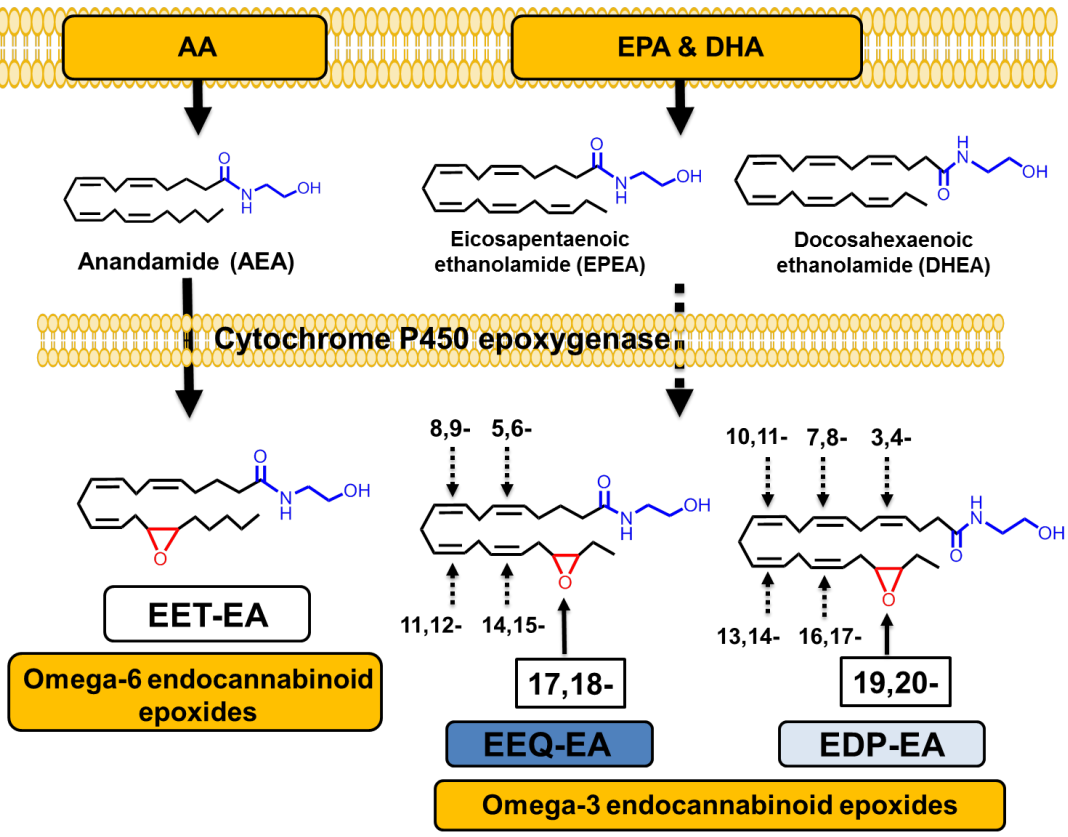

Figure 6.1. Overview of the CYP epoxygenase mediated metabolism of endocannabinoids. Both ω-6 and ω-3 dietary fatty acids are stored in plasma membrane and can be converted to ω-6 and ω-3 endocannabinoids - AEA, DHEA and EPEA. AEA is a substrate for enzymes of the cytochrome P450 (CYP) epoxygenase pathway that produces EET-EA metabolites (14,15-EET-EA regioisomer shown). Another possible pathway includes the metabolism of EPEA and DHEA by CYP epoxygenases to form EEQ-EA and EDP-EA regioisomers, respectively. The terminal endocannabinoid epoxide regioisomer is shown and other possible epoxides at each double bond are denoted by the numbering system.

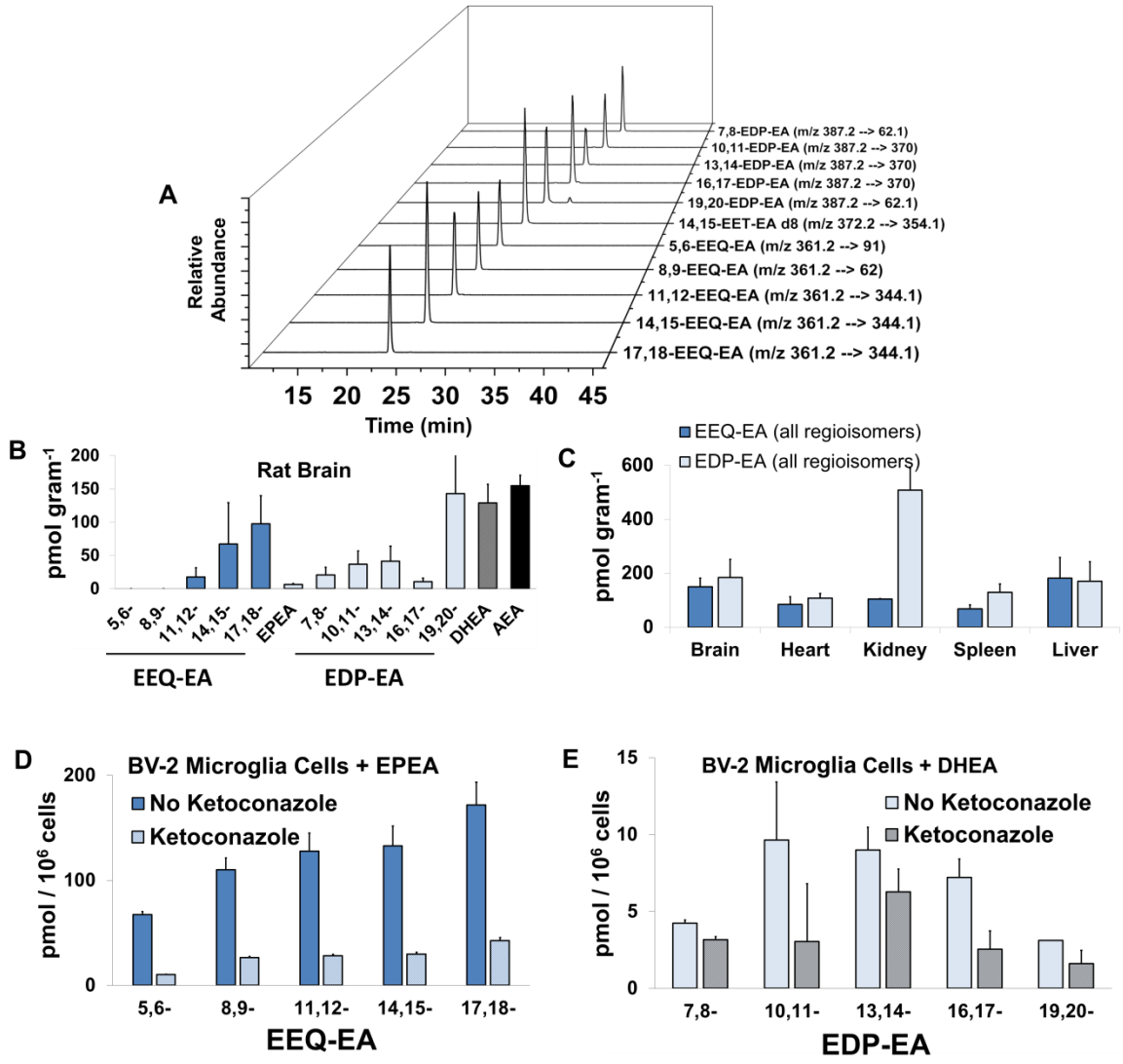

Figure 6.2. Endogenous levels of EEQ-EA and EDP-EA regioisomers in rat tissues and their production in BV-2 microglia. (A) Authentic standards were used for the development of a LC-MS/MS method in the separation and quantitation of EEQ-EA, EDP-EA, AEA, EPEA, and DHEA lipid mediators using MS/MS fragments and retention times unique to each lipid class. (B) Lipid metabolites were extracted and analyzed from pooled Sprague-Dawley rat (n = 3) brain and (C) peripheral organs as described in the materials and methods. (D) & (E) LPS-activated BV-2 microglia cells directly convert EPEA to EEQ-EA regioisomers and DHEA into EDP-EA regioisomers was examined in the absence and presence of the CYP inhibitor ketoconazole (0.5 μM).

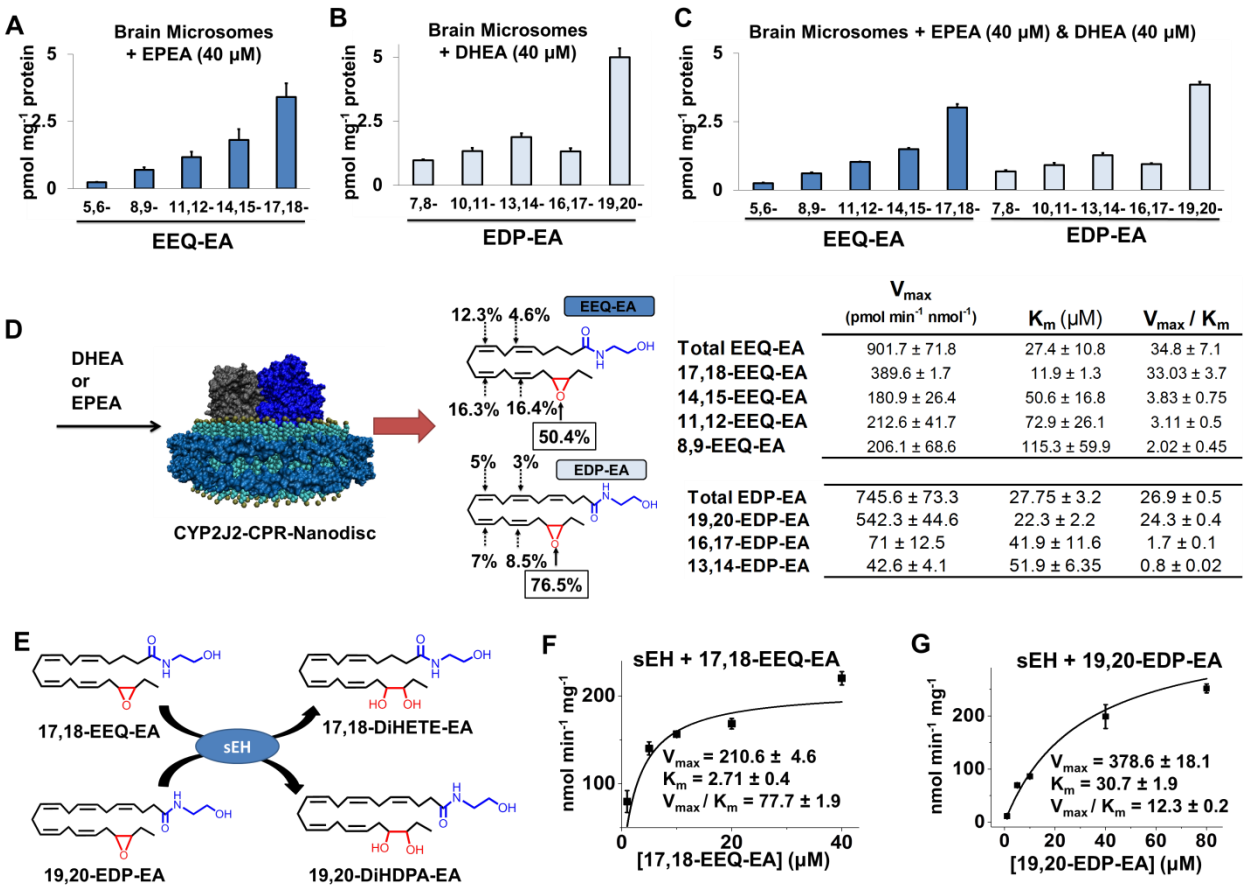

	V_{max} (pmol min^{-1} nmol^{-1})	K_m (µM)	V_{max} / K_m
Total EEQ-EA	901.7 ± 71.8	27.4 ± 10.8	34.8 ± 7.1
17,18-EEQ-EA	389.6 ± 1.7	11.9 ± 1.3	33.03 ± 3.7
14,15-EEQ-EA	180.9 ± 26.4	50.6 ± 16.8	3.83 ± 0.75
11,12-EEQ-EA	212.6 ± 41.7	72.9 ± 26.1	3.11 ± 0.5
8,9-EEQ-EA	206.1 ± 68.6	115.3 ± 59.9	2.02 ± 0.45
Total EDP-EA	745.6 ± 73.3	27.75 ± 3.2	26.9 ± 0.5
19,20-EDP-EA	542.3 ± 44.6	22.3 ± 2.2	24.3 ± 0.4
16,17-EDP-EA	71 ± 12.5	41.9 ± 11.6	1.7 ± 0.1
13,14-EDP-EA	42.6 ± 4.1	51.9 ± 6.35	0.8 ± 0.02

Figure 6.3. Direct enzymatic production of EEQ-EA and EDP-EA regioisomers and hydrolysis by soluble epoxide hydrolase. Brain microsomes were incubated with substrate in the presence of CPR and NADPH to measure the capacity of endoplasmic reticulum epoxygenases to directly epoxygenate either (A) EPEA (40 µM), (B) DHEA (40 µM) or (C) EPEA (40 µM) + DHEA (40 µM). (D) CYP2J2-CPR was incorporated into nanodiscs. The membrane scaffold protein (cyan) surrounds a lipid bilayer (aqua marine with gold phospholipid head groups) in which both CYP2J2 (dark blue) and CPR (grey) are incorporated. The regioselectivity and kinetics of EPEA and DHEA metabolism by human CYP2J2-CPR-Nanodiscs was performed leading to the epoxidation of EPEA to EEQ-EA or DHEA to EDP-EA. The production of the total product and each specific EEQ-EA and EDP-EA regioisomers were fit to Michaelis-Menten kinetics with the calculated K_m, V_{max} and V_{max}/K_m values listed in the adjacent table. (E) Incubations containing sEH ($[E]_{final}$ = 6 nM) in sodium phosphate (100 mM, pH 7.4), bovine serum albumin (0.1 mg/ml) and (F) 17,18-EEQ-EA or (G) 19,20-EDP-EA were performed at 37°C to measure conversion of epoxides to the corresponding vicinal diols using LC-MS/MS. Enzyme kinetics were estimated using incremental increases of substrate for the generation of kinetic curves that were fitted to the Michaelis-Menten equation for calculation of V_{max} and K_m. Incubations were performed in triplicate or greater and kinetic parameters were calculated using Origin Pro.

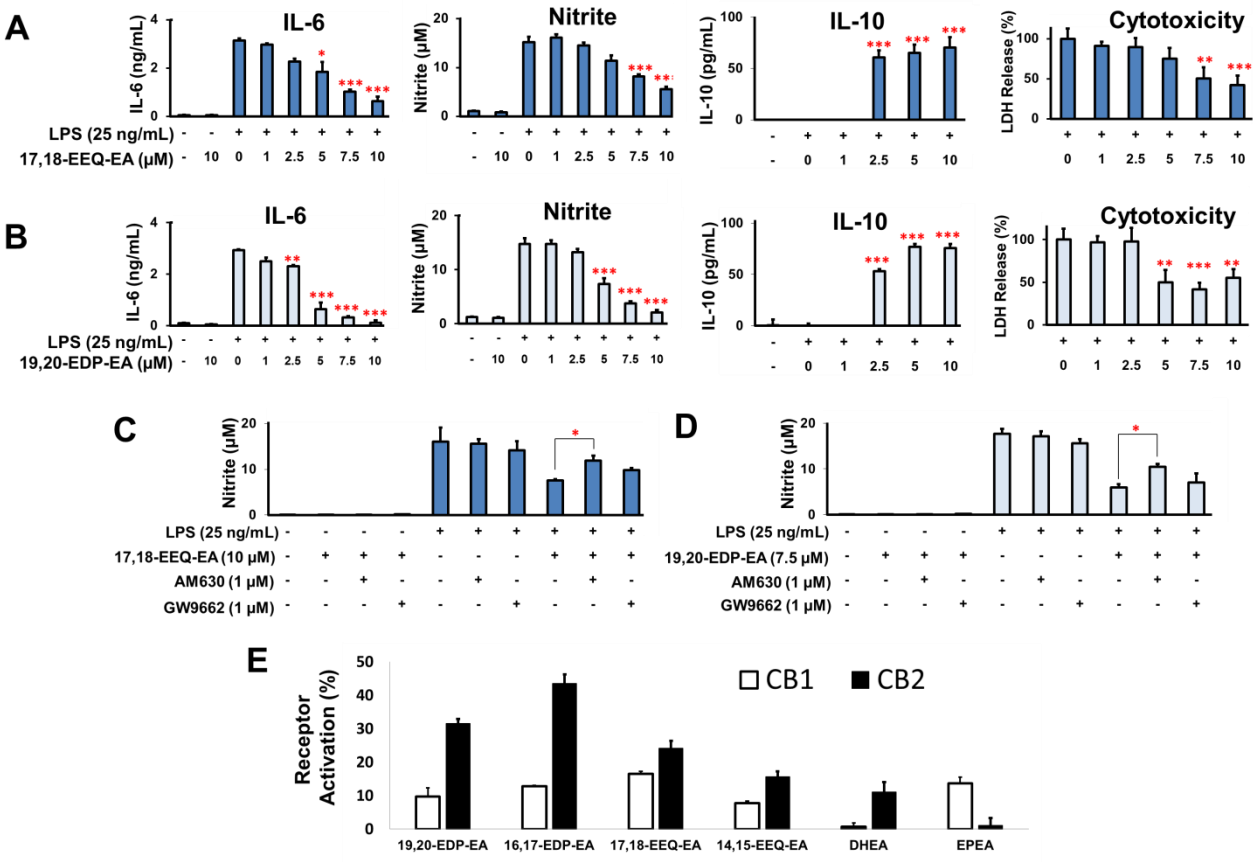

Figure 6.4. 17,18-EEQ-EA, 19,20-EDP-EA effects on LPS stimulated BV2 microglial cells and signaling properties. BV2 microglial cells were pretreated with a dose response of either (A) 17,18-EEQ-EA or (B) 19,20-EDP-EA for 4 hours followed by LPS (25 ng/mL) stimulation. Culture medium was collected after 24 hours and analyzed for pro-inflammatory cytokines (Nitric oxide, IL-6) and anti-inflammatory cytokines (IL-10). Production of lactate dehydrogenase (LDH) was measured to assess cell toxicity relative to LPS in stimulated BV-2 microglia (n = 6). (C) The potential targets of 17,18-EEQ-EA and 19,20-EDP-EA were studied using AM630 (CB2 specific inhibitor) and GW9662 (PPARγ specific inhibitor) to gauge reversal of the anti-inflammatory effects by monitoring nitrite production (n = 6) (D) 17,18-EEQ-EA and 19,20-EDP-EA binding mediated activation of CB1 and CB2 receptors was measured using β-arrestin recruitment luciferase reporter assay in transiently transfected HEK293 cells. Values represent the percent activation of each ligand (10 μM) relative to a full CB1 and CB2 agonist (CP55940) at its EC90 (n = 3).

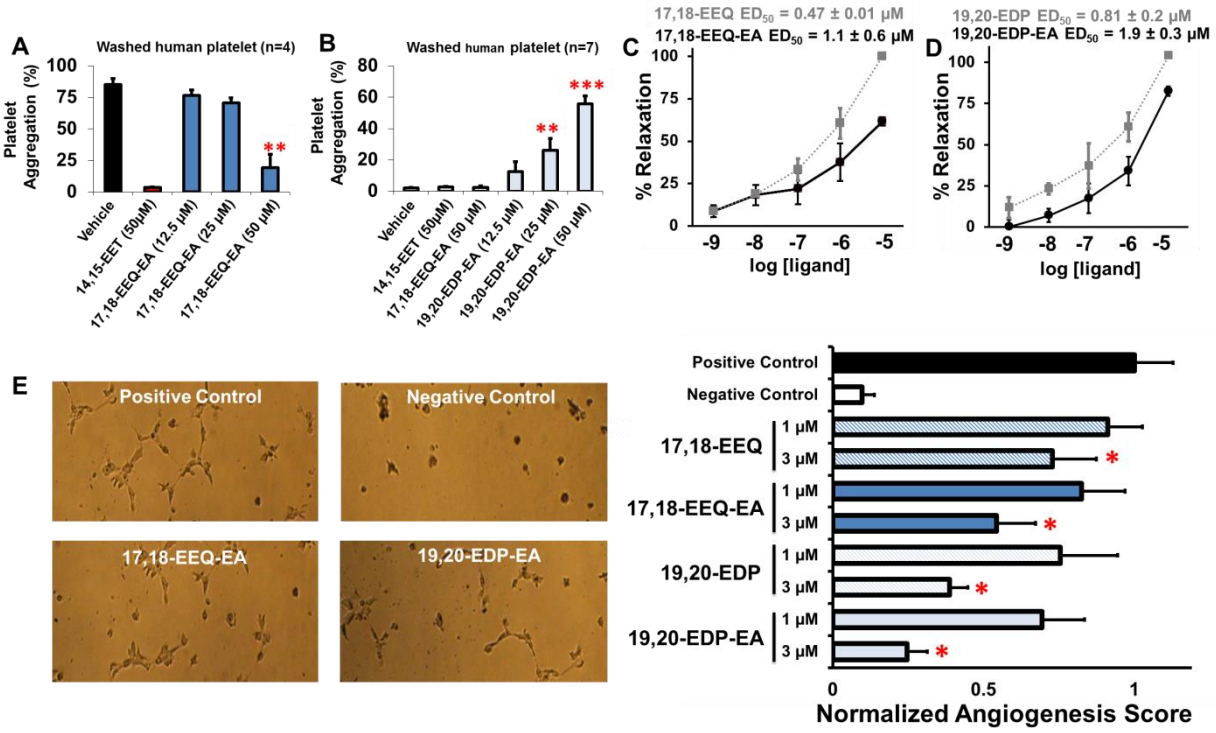

Figure 6.5. Biological effects of 17,18-EEQ-EA and 19,20-EDP-EA on platelet aggregation, vasculature tension and angiogensis. The physiological functions of 17,18-EEQ-EA and 19.20-EDP-EA regioisomers were examined in biological assays to characterize their effects on platelet aggregation, vasodilation and angiogenesis. In whole human blood, **(A)** 17,18 EEQ EA dose-dependently inhibited AA-induced platelet aggregation (n = 4) whereas **(B)** 19, 20 EDP EA - induced platelet aggregation under stirring conditions in the absence of a platelet agonist (n = 7). Dose-dependent relaxation of bovine coronary arteries pre-constricted with U-46619 (40 nM) was measured for **(C)** 17,18-EEQ-EA and 17,18-EEQ **(D)** 19,20-EDP for and 19,20-EDP for the calculation of the ED50. **(E)** 17,18-EEQ-EA and 19,20-EDP-EA were assessed for their ability to inhibit VEG-F promoted angiogenesis in HMVEC plated on Matrigel (n =7). Compounds were studied in parallel to each of their epoxide and ethanolamide parent compounds. All values are means ± SE.

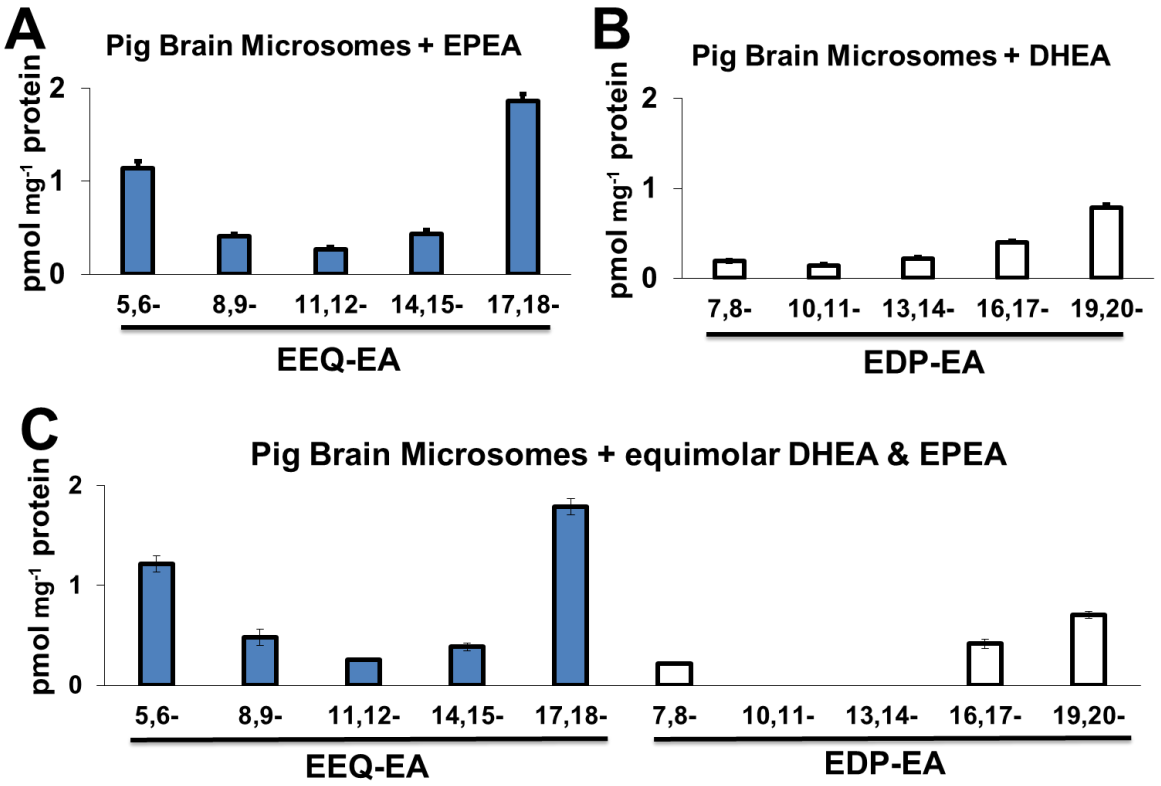

Figure 6.6. Incubations of EPEA and DHEA with pig brain microsomes. Microsomes were prepared from pooled (n=2) homogenized whole porcine brain to measure the capacity of endoplasmic reticulum epoxygenases to directly epoxygenate **(A)** EPEA (40 µM), **(B)** DHEA (40 µM) and **(C)** Equimolar mixture of EPEA (40 µM) and DHEA (40 µM).

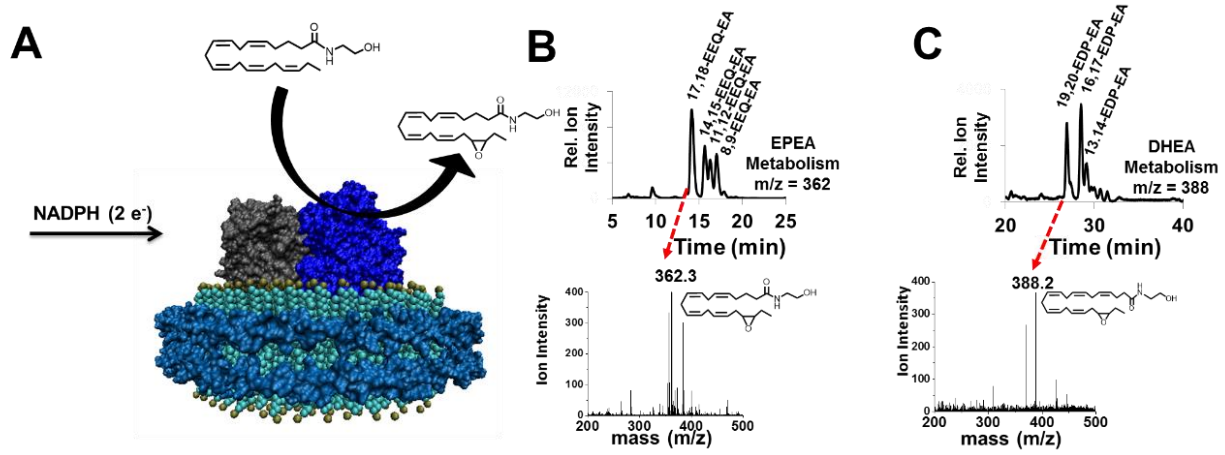

Figure 6.7. LC-ESI-MS global analysis of the CYP2J2-ND mediated metabolism of EPEA and DHEA. LC-ESI-MS was employed to qualitatively characterize CYP2J2 nanodisc metabolism of EPEA and DHEA. **(A)** Schematic of the CYP2J2-ND reactions. In the diagram the membrane scaffold protein (cyan) surrounds a lipid bilayer (light grey) in which both CYP2J2 (red) and CPR (grey) are incorporated. The addition NADPH provides the electron source that drives the P450 cycle resulting in the olefin epoxidation of EPEA to EEQ-EA. The CYP2J2-ND metabolism of **(B)** EPEA produced the four detectable epoxide products 17,18-, 14,15-, 11,12-, and 8,9-EEQ-EA whereas **(C)** DHEA produced the three detectable epoxide products 19,20-, 16,17-, and 13,14-EDP-EA.

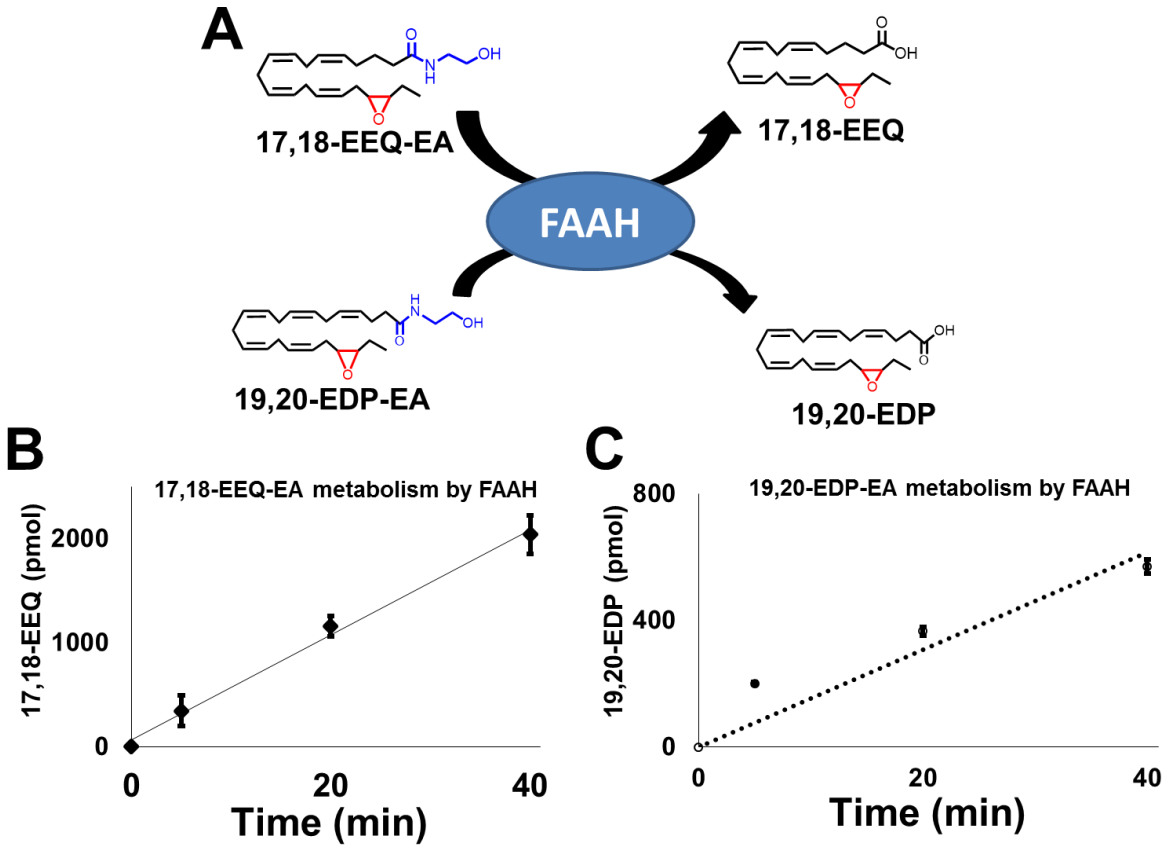

Figure 6.8. Time-dependent hydrolysis of 17,18-EEQ-EA and 19,20-EDP-EA hydrolysis by rat forebrain membranes. Rat forebrain membranes containing fatty acid amide hydrolysis (FAAH) were isolated and protein content was determined using a BCA assay as described in the supplemental methods. Incubations were performed with 100 µg of forebrain protein, 50 µM of substrate (17,18-EEQ-EA or 19,20-EDP-EA) in the presence of 50 mM Tris (pH 7.4), 1 mM EDTA, 3 mM $MgCl_2$ at 37°C as previously described. Samples were quenched with methanol containing 1 mM PMSF at 5, 20 and 40 minutes and analyzed via LC-MS/MS.

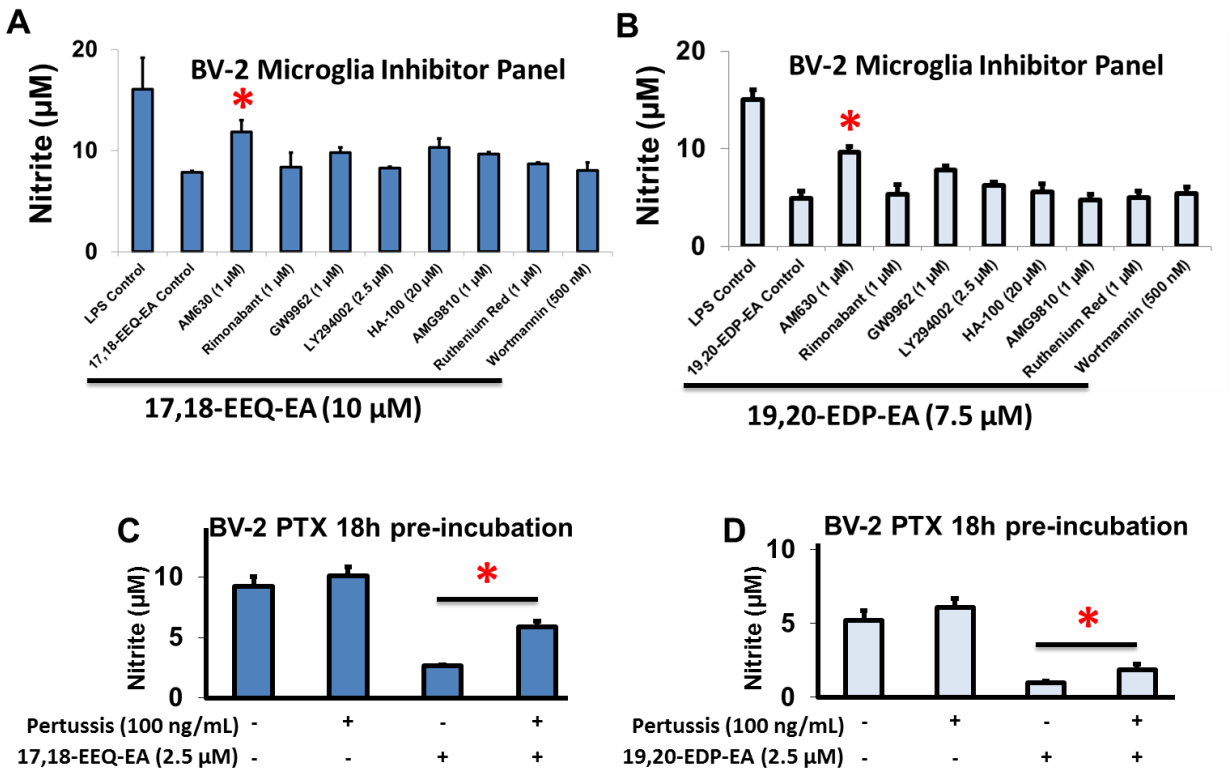

Figure 6.9. Effects of inhibitors on 17,18-EEQ-EA and 19,20-EDP-EA mediated anti-inflammatory effects in BV-2 microglia cells. A panel of inhibitors were screened for their ability to reverse **(A)** 17,18-EEQ-EA and **(B)** 19,20-EDP-EA mediated anti-inflammatory effects in BV-2 microglia cells. Inhibitor concentrations were chosen based on reported EC50 values and lack of inhibitor effect in the assay. **(C-D)** BV-2 cells were pre-incubated with vehicle or pertussis toxin (100 ng/mL) in serum free-media for 18 hours prior to LPS stimulation in the absence or presence of **(C)** 17,18-EEQ-EA and **(D)** 19,20-EDP-EA.

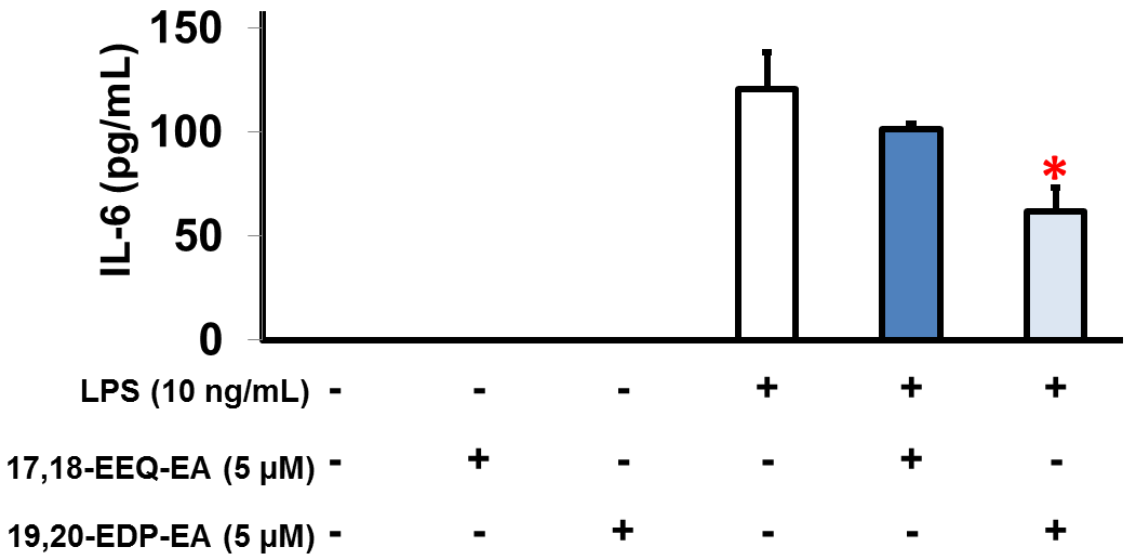

Figure 6.10. In vitro primary piglet microglial neuroinflammation model. Isolated piglet microglia cells were pre-treated with either 17,18-EEQ-EA (5 µM) or 19,20-EDP-EA (5 µM) for 1 hour before stimulation with LPS (10 ng/mL). After 12 hours the supernatant was collected and IL-6 content was measured via ELISA. The final vehicle (DMSO) concentration was 0.04% and each group represents an n = 3 or greater.

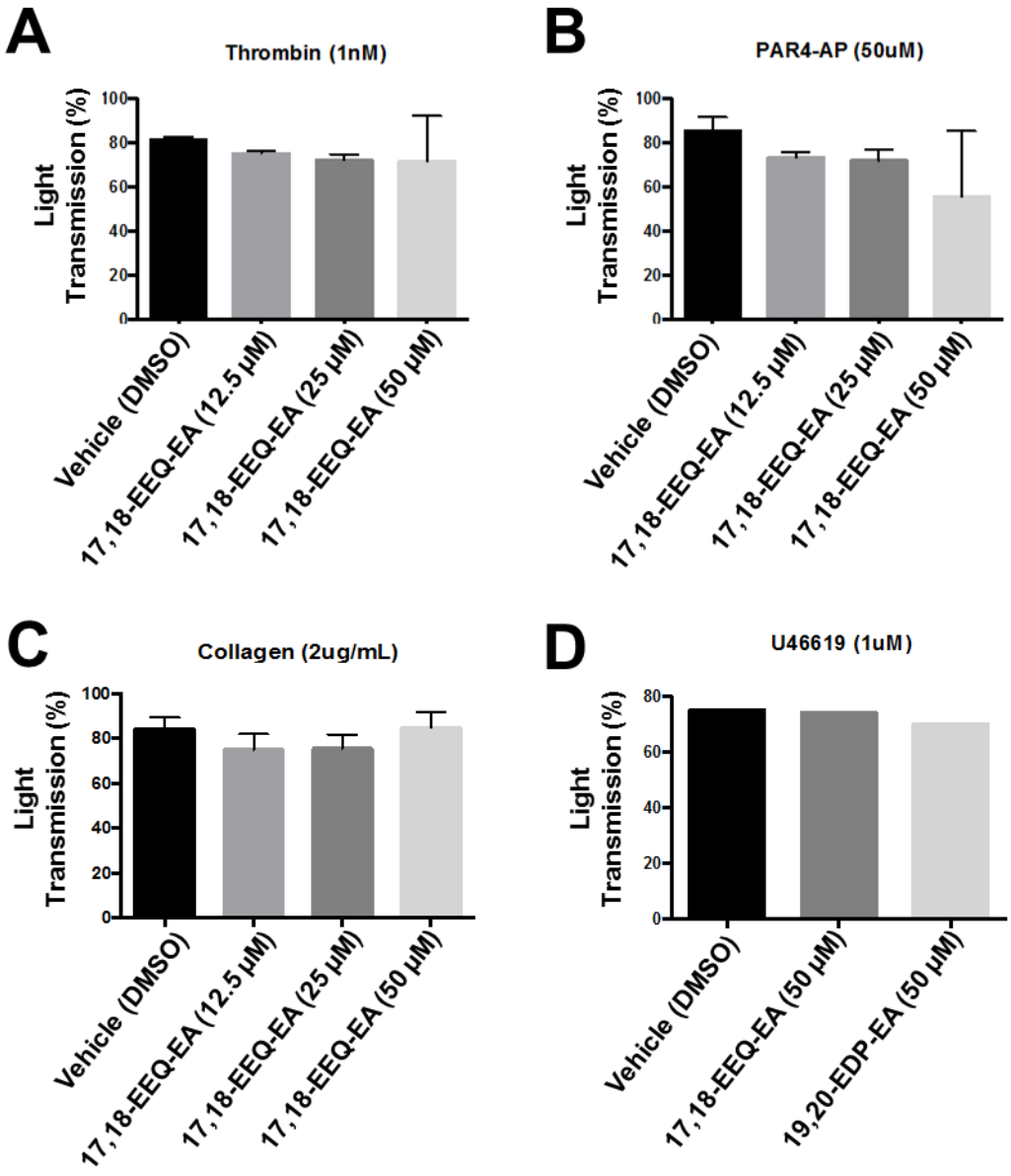

Figure 6.11. Effects of 17,18-EEQ-EA on thrombin, PAR4-AP, collagen or U44619-induced aggregation in washed human platelets. Washed human platelets were activated with either **(A)** 1 nM thrombin **(B)** 50 µM PAR-AP **(C)** 2 µg/mL collagen in the presence of 12.5, 25 and 50 µM 17,18-EEQ-EA (n = 3) which had no significant effect on platelet aggregation as determined by light transmission (%). **(D)** Similarly, washed human platelets activated with 1 µM U46619 (n = 1) did not exhibit any change in the presence of either 50 µM 17,18-EEQ-EA or 19,20-EDP-EA as estimated by light transmission (%).

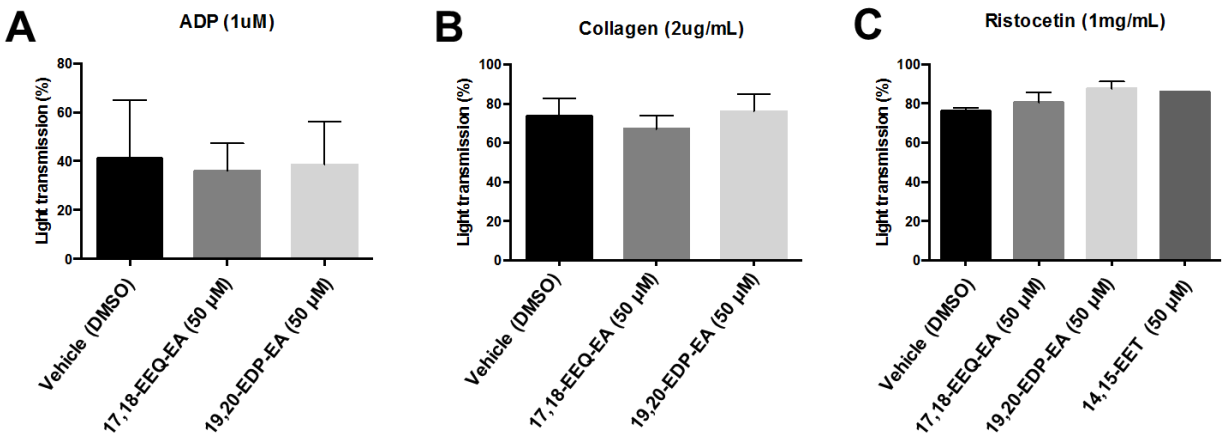

Figure 6.12. 17,18-EEQ-EA and 19,20-EDP-EA effects on ADP, collagen or ristocetin-induced platelet aggregation in platelet rich plasma. The effects of 17,18-EEQ-EA, 19,20-EDP-EA at 50 µM relative to vehicle (DMSO) in were investigated in platelet rich plasma clotting via **(A)** ADP (1 µM), **(B)** collagen (2 µg/mL) and **(C)** ristocetin (1 mg/mL).

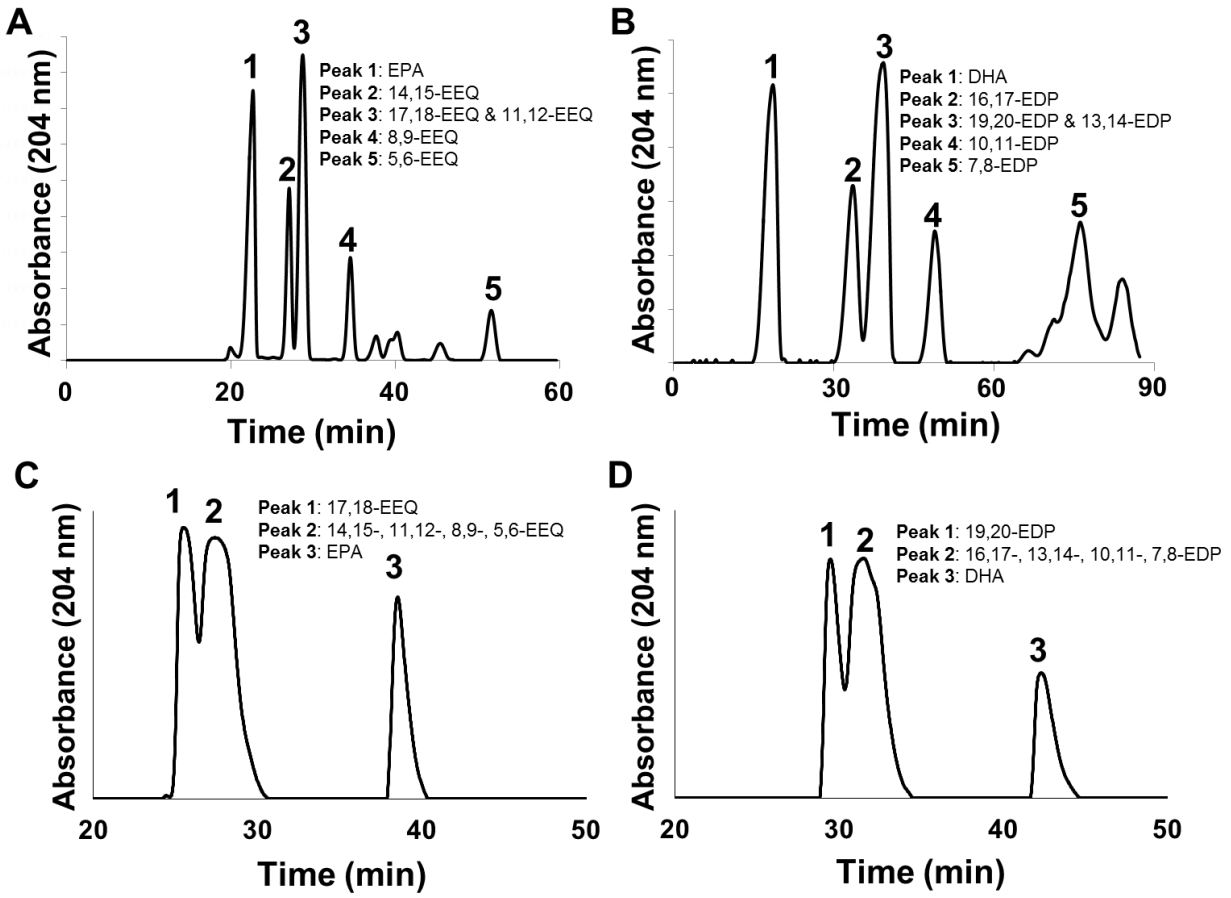

Figure 6.13. Purification of EDP and EEQ regio-isomers from crude reaction mixture by normal- and reversed-phase HPLC. Synthesis reactions detailing the non-specific olefin epoxidation of EPA or DHA are detailed in the materials and methods. A combination of both normal phase-high performance liquid chromatographay (NP-HPLC) and reversed phase-high performance chromatography (RP-HPLC) were necessary for isolation epoxides. NP-HPLC was employed for separation of (A) EEQ and (B) EDP regioisomers from the crude reaction mixture. RP-HPLC was employed due to the alternative elution profile of (C) EEQ and (D) EDP regioisomers which elutes with the terminal epoxide first (17,18-EEQ or 19,20-EDP-EA) followed by the sequential elution of the other metabolites. The isolation of specific EEQ (17,18-, 14,15-, 11,12-, 8,9-, and 5-6-EEQ) and EDP (19,20-, 16,17-, 13,14-, 10,11-, and 7,8-EDP) regioisomers were confirmed using high resolution mass spectrometry and commercially available authentic standards for use in analytical RP-HPLC.

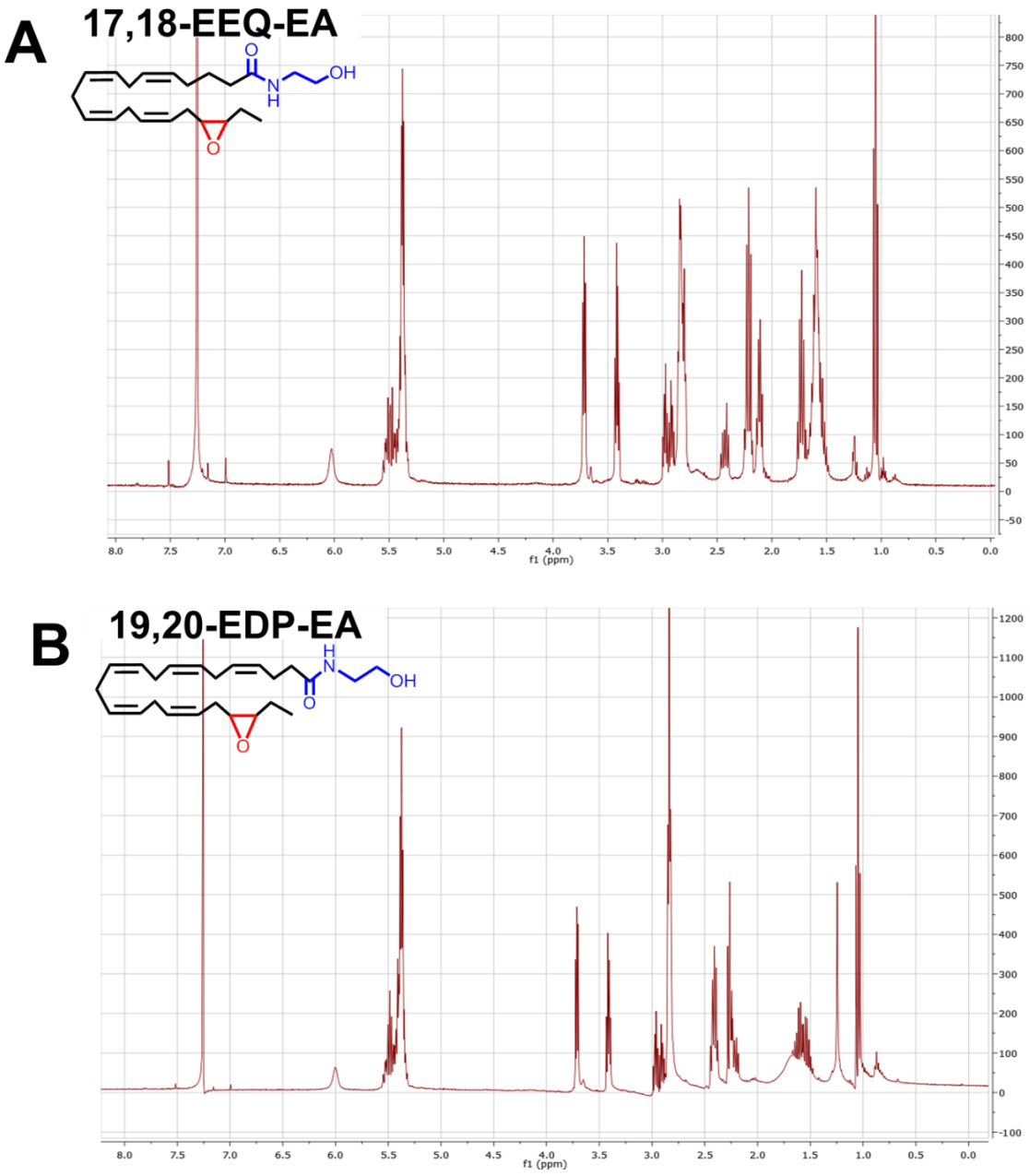

Figure 6.14. Spectral Data of purified 17,18-EEQ-EA and 19,20-EDP-EA. (A) ^{1}H NMR (400 MHz, $CDCl_3$) δ6.03 (s, 1H), 5.55 to 5.33 (m, 10H), 3.72 (t, 2H, J = 4Hz), 3.42 (quartet, 2H, J= 4 Hz), 3.03 to 2.79 (m, 6H), 2.43 (dt, 1H, J = 2Hz), 2.25 to 2.05 (m, 4H), 1.73 (apparent quintet, 2H, J = 8Hz), 1.67 to 1.48 (m, 6H), 1.05 (t, 3H, J = 8Hz). HRMS (m/z) calc. mass = 362.2695; HRMS measured mass = 362.2693; atomic form = $C_{22}H_{36}NO_3$; UV-Vis λ_{max} = 191 nm; Purity > 98% **(B)** ^{1}H NMR (400 MHz, $CDCl_3$) δ6.03 (s, 1H), 5.55 to 5.33 (m, 8H), 3.72 (t, 2H, J = 4Hz), 3.42 (quartet, 2H, J= 4 Hz), 3.00 to 2.79 (m, 8H), 2.43 (apparent quintet, 1H, J = 2Hz), 2.25 to 2.05 (m, 4H), 1.73 (apparent quintet, 2H, J = 8Hz), 1.67 to 1.48 (m, 6H), 1.05 (t, 3H, 8Hz). HRMS calc. mass = 388.2828 ; HRMS (m/z) measured mass = 388.2852; atomic form = $C_{24}H_{38}NO_3$; UV-Vis λ_{max} = 191 nm; Purity > 98%.

	Rat Brain (pmol/gm)	Rat Heart (pmol/gm)	Rat Kidney (pmol/gm)	Rat Spleen (pmol/gm)	Rat Liver (pmol/gm)	Pig Brain (pmol/gm)	Human Plasma (pg/mL)
17,18-EEQ-EA	97.4 ± 42.2	50.2 ± 14.9	93.2 ± 90.4	65.3 ± 42.7	60.6 ± 24.7	105.7 ± 99.1	N.D.
14,15-EEQ-EA	67 ± 62	52.1 ± 33.1	12.8 ± 12.2	10.8 ± 6.5	161.2 ± 65.7	42.4 ± 41.4	N.D.
11,12-EEQ-EA	17.3 ± 14	10.5 ± 7.8	N.D.	3.8 ± 2.2	36.6 ± 14.9	31 ± 29.9	N.D.
8,9-EEQ-EA	N.D.	N.D.	N.D.	2.6 ± 1.7	N.D.	1.3 ± 0.6	N.D.
5,6-EEQ-EA	N.D.	N.D.	N.D.	0.1 ± 0.05	N.D.	N.D.	N.D.
EPEA	6.2 ± 1.6	9.4 ± 6.0	37.1 ± 21	9.2 ± 4.1	80.8 ± 20.1	2.2 ± 0.4	N.D.
19,20-EDP-EA	142.7 ± 58.7	87.3 ± 62.1	420.7 ± 265	72.4 ± 43.9	148 ± 60.4	136.9 ± 110.7	167.3 ± 11.8
16,17-EDP-EA	10.4 ± 5.2	4.2 ± 2.8	15.7 ± 9.5	N.D.	N.D.	2.2 ± 1.1	N.D.
13,14-EDP-EA	41.1 ± 22.7	13 ± 9.7	61.7 ± 55	35.4 ± 22	37 ± 15.1	0.5 ± 0.5	N.D.
10,11-EDP-EA	36.5 ± 20.1	10.2 ± 8.3	56.7 ± 54.9	31.6 ± 19.2	33.5 ± 13.6	N.D.	N.D.
7,8-EDP-EA	20.5 ± 11.4	10.2 ± 8.3	34.4 ± 42.1	20.5 ± 12.7	24.3 ± 9.9	N.D.	N.D.
DHEA	128.9 ± 27.9	57.7 ± 24.4	49.6 ± 22.2	22.9 ± 1.3	195.1 ± 48.7	265.5 ± 100	13.3 ± 0.4
Anandamide	154.5 ± 15.8	65.6 ± 25.0	565.2 ± 306	162.4 ± 87.1	567.7 ± 141.9	2825 ± 975	20.6 ± 2.6

Table 6.1. Summary of the average levels of detected EEQ-EA, EDP-EA, EPEA, DHEA and AEA levels in rat brain, rat heart, rat kidney, rat spleen, rat liver, porcine brain and human plasma. Sprague-Dawley rat tissues, pig brain and human pooled plasma were analyzed for EEQ-EA, EDP-EA, EPEA, DHEA and AEA metabolites as described in the materials and methods (main text).

	BV-2 Microglia post-LPS stimulation		
	1 hr	4 hr	12 hr
Total EEQ-EA (pmol / 10^6 cells)	1.8 ± 0.1	4.1 ± 0.5	30.1 ± 8.4
Total EDP-EA (pmol / 10^6 cells)	5.9 ± 0.5	182.5 ± 15.9	172.8 ± 70.3
Total EPEA (pmol / 10^6 cells)	17.3 ± 2	483.4 ± 8.7	2042 ± 939.2
Total DHEA (pmol / 10^6 cells)	30.3 ± 8.4	324.3 ± 20.2	6.7 ± 4.6
Total AEA (pmol / 10^6 cells)	7.4 ± 1.1	215.6 ± 33.1	4895 ± 540.9

Table 6.2. Time course of EEQ-EA, EDP-EA, EPEA, DHEA and AEA production by LPS stimulated BV-2 cells. 6-well plates were seeded with 500,000 BV-2 cells and grown to 80-90% confluence. Microglia were stimulated with LPS (100 ng/mL) and placed back in the incubator (37°C and 5% CO2) for each specified period of time. At each time point, cells were scraped in the supernatant, lysed and extracted three times with ethyl acetate/hexane (9:1). The organic layer was dried down and re-suspended in ethanol for targeted lipidomic analysis using LC-MS/MS as described in the main text.

6.8 REFERENCES

1. Kris-Etherton, P. M., Harris, W. S., and Appel, L. J. (2002) Fish consumption, fish oil, omega-3 fatty acids, and cardiovascular disease, *Circulation 106*, 2747-2757.
2. Morris, M. C., Evans, D. A., Tangney, C. C., Bienias, J. L., and Wilson, R. S. (2005) Fish consumption and cognitive decline with age in a large community study, *Arch Neurol 62*, 1849-1853.
3. Duda, M. K., Tintinu, A. J., O'shea, K. M., Chess, D. J., and Stanley, W. C. (2008) Dietary supplementation with fish oil, but not with flaxseed oil, reduces plasma free fatty acids and prevents pressure overload induced left ventricular dysfunction, *Eur Heart J 29*, 225-225.
4. Skaper, S. D., and Di Marzo, V. (2012) Endocannabinoids in nervous system health and disease: the big picture in a nutshell, *Philos Trans R Soc Lond B Biol Sci 367*, 3193-3200.
5. Fonseca, B. M., Costa, M. A., Almada, M., Correia-da-Silva, G., and Teixeira, N. A. (2013) Endogenous cannabinoids revisited: a biochemistry perspective, *Prostaglandins Other Lipid Mediat 102-103*, 13-30.
6. Pacher, P., Batkai, S., and Kunos, G. (2006) The endocannabinoid system as an emerging target of pharmacotherapy, *Pharmacol Rev 58*, 389-462.
7. Brown, I., Cascio, M. G., Rotondo, D., Pertwee, R. G., Heys, S. D., and Wahle, K. W. (2013) Cannabinoids and omega-3/6 endocannabinoids as cell death and anticancer modulators, *Prog Lipid Res 52*, 80-109.
8. Brown, I., Cascio, M. G., Wahle, K. W., Smoum, R., Mechoulam, R., Ross, R. A., Pertwee, R. G., and Heys, S. D. (2010) Cannabinoid receptor-dependent and -independent anti-proliferative effects of omega-3 ethanolamides in androgen receptor-positive and -negative prostate cancer cell lines, *Carcinogenesis 31*, 1584-1591.
9. Meijerink, J., Balvers, M., and Witkamp, R. (2013) N-Acyl amines of docosahexaenoic acid and other n-3 polyunsatured fatty acids - from fishy endocannabinoids to potential leads, *Br J Pharmacol 169*, 772-783.
10. Kim, H. Y., and Spector, A. A. (2013) Synaptamide, endocannabinoid-like derivative of docosahexaenoic acid with cannabinoid-independent function, *Prostag Leukotr Ess 88*, 121-125.
11. Sugiura, T., Kondo, S., Sukagawa, A., Tonegawa, T., Nakane, S., Yamashita, A., Ishima, Y., and Waku, K. (1996) Transacylase-mediated and phosphodiesterase-mediated synthesis of N-arachidonoylethanolamine, an endogenous cannabinoid-receptor ligand, in rat brain microsomes - Comparison with synthesis from free arachidonic acid and ethanolamine, *Eur J Biochem 240*, 53-62.
12. Bisogno, T., Delton-Vandenbroucke, I., Milone, A., Lagarde, M., and Di Marzo, V. (1999) Biosynthesis and inactivation of N-arachidonoylethanolamine (anandamide) and N-docosahexaenoylethanolamine in bovine retina, *Arch Biochem Biophys 370*, 300-307.
13. Sheskin, T., Hanus, L., Slager, J., Vogel, Z., and Mechoulam, R. (1997) Structural requirements for binding of anandamide-type compounds to the brain cannabinoid receptor, *J Med Chem 40*, 659-667.
14. Artmann, A., Petersen, G., Hellgren, L. I., Boberg, J., Skonberg, C., Nellemann, C., Hansen, S. H., and Hansen, H. S. (2008) Influence of dietary fatty acids on endocannabinoid and N-acylethanolamine levels in rat brain, liver and small intestine, *Biochim Biophys Acta 1781*, 200-212.

15. Rossmeisl, M., Jilkova, Z. M., Kuda, O., Jelenik, T., Medrikova, D., Stankova, B., Kristinsson, B., Haraldsson, G. G., Svensen, H., Stoknes, I., Sjovall, P., Magnusson, Y., Balvers, M. G. J., Verhoeckx, K. C. M., Tvrzicka, E., Bryhn, M., and Kopecky, J. (2012) Metabolic Effects of n-3 PUFA as Phospholipids Are Superior to Triglycerides in Mice Fed a High-Fat Diet: Possible Role of Endocannabinoids, *Plos One 7*.
16. Rouzer, C. A., and Marnett, L. J. (2011) Endocannabinoid Oxygenation by Cyclooxygenases, Lipoxygenases, and Cytochromes P450: Cross-Talk between the Eicosanoid and Endocannabinoid Signaling Pathways, *Chem Rev 111*, 5899-5921.
17. Spector, A. A. (2009) Arachidonic acid cytochrome P450 epoxygenase pathway, *J Lipid Res 50 Suppl*, S52-56.
18. McDougle, D. R., Kambalyal, A., Meling, D. D., and Das, A. (2014) Endocannabinoids - Anandamide and 2- Arachidonoylglycerol are Substrates for Human Cytochrome P450 2J2 Epoxygenase, *J Pharmacol Exp Ther*.
19. Snider, N. T., Nast, J. A., Tesmer, L. A., and Hollenberg, P. F. (2009) A cytochrome P450-derived epoxygenated metabolite of anandamide is a potent cannabinoid receptor 2-selective agonist, *Mol Pharmacol 75*, 965-972.
20. Yang, R., Fredman, G., Krishnamoorthy, S., Agrawal, N., Irimia, D., Piomelli, D., and Serhan, C. N. (2011) Decoding functional metabolomics with docosahexaenoyl ethanolamide (DHEA) identifies novel bioactive signals, *J Biol Chem 286*, 31532-31541.
21. Barbosa-Sicard, E., Markovic, M., Honeck, H., Christ, B., Muller, D. N., and Schunck, W. H. (2005) Eicosapentaenoic acid metabolism by cytochrome P450 enzymes of the CYP2C subfamily, *Biochem Biophys Res Commun 329*, 1275-1281.
22. Arnold, C., Markovic, M., Blossey, K., Wallukat, G., Fischer, R., Dechend, R., Konkel, A., von Schacky, C., Luft, F. C., Muller, D. N., Rothe, M., and Schunck, W. H. (2010) Arachidonic acid-metabolizing cytochrome P450 enzymes are targets of {omega}-3 fatty acids, *J Biol Chem 285*, 32720-32733.
23. Blasi, E., Barluzzi, R., Bocchini, V., Mazzolla, R., and Bistoni, F. (1990) Immortalization of murine microglial cells by a v-raf/v-myc carrying retrovirus, *J Neuroimmunol 27*, 229-237.
24. McDougle, D. R., Palaria, A., Magnetta, E., Meling, D. D., and Das, A. (2013) Functional studies of N-terminally modified CYP2J2 epoxygenase in model lipid bilayers, *Protein Science 22*, 964-979.
25. Kingsley, P. J., and Marnett, L. J. (2003) Analysis of endocannabinoids by Ag+ coordination tandem mass spectrometry, *Anal Biochem 314*, 8-15.
26. Richardson, D., Ortori, C. A., Chapman, V., Kendall, D. A., and Barrett, D. A. (2007) Quantitative profiling of endocannabinoids and related compounds in rat brain using liquid chromatography-tandem electrospray ionization mass spectrometry, *Anal Biochem 360*, 216-226.
27. Kroeze, W. K., Sassano, M. F., Huang, X. P., Lansu, K., McCorvy, J. D., Giguere, P. M., Sciaky, N., and Roth, B. L. (2015) PRESTO-Tango as an open-source resource for interrogation of the druggable human GPCRome, *Nat Struct Mol Biol 22*, 362-U328.
28. Hedegaard, E. R., Nielsen, B. D., Kun, A., Hughes, A. D., Kroigaard, C., Mogensen, S., Matchkov, V. V., Frobert, O., and Simonsen, U. (2014) KV 7 channels are involved in hypoxia-induced vasodilatation of porcine coronary arteries, *Br J Pharmacol 171*, 69-82.

29. Abdeen, A. A., Weiss, J. B., Lee, J., and Kilian, K. A. (2014) Matrix composition and mechanics direct proangiogenic signaling from mesenchymal stem cells, *Tissue engineering. Part A 20*, 2737-2745.
30. Hillard, C. J., Wilkison, D. M., Edgemond, W. S., and Campbell, W. B. (1995) Characterization of the Kinetics and Distribution of N-Arachidonylethanolamine (Anandamide) Hydrolysis by Rat-Brain, *Bba-Lipid Lipid Met 1257*, 249-256.
31. Ji, P., Schachtschneider, K. M., Schook, L. B., Walker, F. R., and Johnson, R. W. (2016) Peripheral viral infection induced microglial sensome genes and enhanced microglial cell activity in the hippocampus of neonatal piglets, *Brain Behav Immun 54*, 243-251.
32. Schmidt, A., Brune, K., and Hinz, B. (2006) Determination of the endocannabinoid anandamide in human plasma by high-performance liquid chromatography, *Biomed Chromatogr 20*, 336-342.
33. Muccio, G. G., and Stella, N. (2008) An optimized GC-MS method detects nanomolar amounts of anandamide in mouse brain, *Anal Biochem 373*, 220-228.
34. Chen, J., Paudel, K. S., Derbenev, A. V., Smith, B. N., and Stinchcomb, A. L. (2009) Simultaneous Quantification of Anandamide and Other Endocannabinoids in Dorsal Vagal Complex of Rat Brainstem by LC-MS, *Chromatographia 69*, 1-7.
35. Chen, J. K., Chen, J., Imig, J. D., Wei, S., Hachey, D. L., Guthi, J. S., Falck, J. R., Capdevila, J. H., and Harris, R. C. (2008) Identification of novel endogenous cytochrome p450 arachidonate metabolites with high affinity for cannabinoid receptors, *J Biol Chem 283*, 24514-24524.
36. Westphal, C., Konkel, A., and Schunck, W. H. (2011) CYP-eicosanoids-A new link between omega-3 fatty acids and cardiac disease?, *Prostag Oth Lipid M 96*, 99-108.
37. Dutheil, F., Dauchy, S., Diry, M., Sazdovitch, V., Cloarec, O., Mellottee, L., Bieche, I., Ingelman-Sundberg, M., Flinois, J. P., de Waziers, I., Beaune, P., Decleves, X., Duyckaerts, C., and Loriot, M. A. (2009) Xenobiotic-Metabolizing Enzymes and Transporters in the Normal Human Brain: Regional and Cellular Mapping as a Basis for Putative Roles in Cerebral Function, *Drug Metab Dispos 37*, 1528-1538.
38. Morisseau, C., Inceoglu, B., Schmelzer, K., Tsai, H. J., Jinks, S. L., Hegedus, C. M., and Hammock, B. D. (2010) Naturally occurring monoepoxides of eicosapentaenoic acid and docosahexaenoic acid are bioactive antihyperalgesic lipids, *J Lipid Res 51*, 3481-3490.
39. Amor, S., Puentes, F., Baker, D., and van der Valk, P. (2010) Inflammation in neurodegenerative diseases, *Immunology 129*, 154-169.
40. Benito, C., Tolon, R. M., Pazos, M. R., Nunez, E., Castillo, A. I., and Romero, J. (2008) Cannabinoid CB2 receptors in human brain inflammation, *Br J Pharmacol 153*, 277-285.
41. Ashton, J. C., and Glass, M. (2007) The cannabinoid CB2 receptor as a target for inflammation-dependent neurodegeneration, *Curr Neuropharmacol 5*, 73-80.
42. Nagarkatti, P., Pandey, R., Rieder, S. A., Hegde, V. L., and Nagarkatti, M. (2009) Cannabinoids as novel anti-inflammatory drugs, *Future Med Chem 1*, 1333-1349.
43. Nishio, K., Horie, M., Akazawa, Y., Shichiri, M., Iwahashi, H., Hagihara, Y., Yoshida, Y., and Niki, E. (2013) Attenuation of lipopolysaccharide (LPS)-induced cytotoxicity by tocopherols and tocotrienols, *Redox Biol 1*, 97-103.
44. Spector, A. A. (2009) Arachidonic acid cytochrome P450 epoxygenase pathway, *J Lipid Res 50 Suppl*, S52-56.

45. Snider, N. T., Nast, J. A., Tesmer, L. A., and Hollenberg, P. F. (2009) A Cytochrome P450-Derived Epoxygenated Metabolite of Anandamide Is a Potent Cannabinoid Receptor 2-Selective Agonist, *Molecular Pharmacology 75*, 965-972.
46. Krotz, F., Riexinger, T., Buerkle, M. A., Nithipatikom, K., Gloe, T., Sohn, H. Y., Campbell, W. B., and Pohl, U. (2004) Membrane potential-dependent inhibition of platelet adhesion to endothelial cells by epoxyeicosatrienoic acids, *Arterioscl Throm Vas 24*, 595-600.
47. Vanrollins, M. (1995) Epoxygenase Metabolites of Docosahexaenoic and Eicosapentaenoic Acids Inhibit Platelet-Aggregation at Concentrations Below Those Affecting Thromboxane Synthesis, *Journal of Pharmacology and Experimental Therapeutics 274*, 798-804.
48. Ikei, K. N., Yeung, J., Apopa, P. L., Ceja, J., Vesci, J., Holman, T. R., and Holinstat, M. (2012) Investigations of human platelet-type 12-lipoxygenase: role of lipoxygenase products in platelet activation, *J Lipid Res 53*, 2546-2559.
49. Zhang, G., Panigrahy, D., Mahakian, L. M., Yang, J., Liu, J. Y., Stephen Lee, K. S., Wettersten, H. I., Ulu, A., Hu, X., Tam, S., Hwang, S. H., Ingham, E. S., Kieran, M. W., Weiss, R. H., Ferrara, K. W., and Hammock, B. D. (2013) Epoxy metabolites of docosahexaenoic acid (DHA) inhibit angiogenesis, tumor growth, and metastasis, *Proc Natl Acad Sci U S A 110*, 6530-6535.
50. Fischer, R., Konkel, A., Mehling, H., Blossey, K., Gapelyuk, A., Wessel, N., von Schacky, C., Dechend, R., Muller, D. N., Rothe, M., Luft, F. C., Weylandt, K., and Schunck, W. H. (2014) Dietary omega-3 fatty acids modulate the eicosanoid profile in man primarily via the CYP-epoxygenase pathway, *J Lipid Res 55*, 1150-1164.
51. De Petrocellis, L., Melck, D., Palmisano, A., Bisogno, T., Laezza, C., Bifulco, M., and Di Marzo, V. (1998) The endogenous cannabinoid anandamide inhibits human breast cancer cell proliferation, *Proc Natl Acad Sci U S A 95*, 8375-8380.
52. Pisanti, S., Borselli, C., Oliviero, O., Laezza, C., Gazzerro, P., and Bifulco, M. (2007) Antiangiogenic activity of the endocannabinoid anandamide: correlation to its tumor-suppressor efficacy, *J Cell Physiol 211*, 495-503.
53. Zhang, G. D., Kodani, S., and Hammock, B. D. (2014) Stabilized epoxygenated fatty acids regulate inflammation, pain, angiogenesis and cancer, *Progress in Lipid Research 53*, 108-123.
54. Rani Sagar, D., Burston, J. J., Woodhams, S. G., and Chapman, V. (2012) Dynamic changes to the endocannabinoid system in models of chronic pain, *Philos Trans R Soc Lond B Biol Sci 367*, 3300-3311.
55. Newman, J. W., Morisseau, C., and Hammock, B. D. (2005) Epoxide hydrolases: their roles and interactions with lipid metabolism, *Progress in Lipid Research 44*, 1-51.
56. Long, J. Z., LaCava, M., Jin, X., and Cravatt, B. F. (2011) An anatomical and temporal portrait of physiological substrates for fatty acid amide hydrolase, *J Lipid Res 52*, 337-344.
57. Chen, C. T., Domenichiello, A. F., Trepanier, M. O., Liu, Z., Masoodi, M., and Bazinet, R. P. (2013) The low levels of eicosapentaenoic acid in rat brain phospholipids are maintained via multiple redundant mechanisms, *J Lipid Res 54*, 2410-2422.
58. Iliff, J. J., Jia, J., Nelson, J., Goyagi, T., Klaus, J., and Alkayed, N. J. (2010) Epoxyeicosanoid signaling in CNS function and disease, *Prostag Oth Lipid M 91*, 68-84.
59. Tomar, S., Zumbrun, E. E., Nagarkatti, M., and Nagarkatti, P. S. (2015) Protective Role of Cannabinoid Receptor 2 Activation in Galactosamine/Lipopolysaccharide-Induced Acute

Liver Failure through Regulation of Macrophage Polarization and MicroRNAs, *Journal of Pharmacology and Experimental Therapeutics 353*, 369-379.

60. Dai, M. Y., Wu, L. J., He, Z. W., Zhang, S. S., Chen, C., Xu, X. Z., Wang, P. H., Gruzdev, A., Zeldin, D. C., and Wang, D. W. (2015) Epoxyeicosatrienoic Acids Regulate Macrophage Polarization and Prevent LPS-Induced Cardiac Dysfunction, *Journal of Cellular Physiology 230*, 2108-2119.
61. Fitzpatrick, F. A., Ennis, M. D., Baze, M. E., Wynalda, M. A., McGee, J. E., and Liggett, W. F. (1986) Inhibition of cyclooxygenase activity and platelet aggregation by epoxyeicosatrienoic acids. Influence of stereochemistry, *J Biol Chem 261*, 15334-15338.
62. Braud, S., Bon, C., Touqui, L., and Mounier, C. (2000) Activation of rabbit blood platelets by anandamide through its cleavage into arachidonic acid, *Febs Lett 471*, 12-16.
63. Baldassarri, S., Bertoni, A., Bagarotti, A., Sarasso, C., Zanfa, M., Catani, M. V., Avigliano, L., Maccarrone, M., Torti, M., and Sinigaglia, F. (2008) The endocannabinoid 2-arachidonoylglycerol activates human platelets through non-CB(1)/CB(2) receptors, *J Thromb Haemost 6*, 1772-1779.
64. Ye, D., Zhang, D., Oltman, C., Dellsperger, K., Lee, H. C., and VanRollins, M. (2002) Cytochrome p-450 epoxygenase metabolites of docosahexaenoate potently dilate coronary arterioles by activating large-conductance calcium-activated potassium channels, *J Pharmacol Exp Ther 303*, 768-776.

APPENDIX A: LIPOPROTEIN NANOPLATELETS, BRIGHTLY FLUORESCENT, ZWITTERIONIC PROBES WITH RAPID CELLULAR UPTAKE

Sung Jun Lim,[1,2] Daniel R. McDougle,[3,4] Mohammad U. Zahid,[1,2] Liang Ma,[2,5] Aditi Das,[1,3,6,7]* and Andrew M. Smith[1,2,5]*
[1]Department of Bioengineering, University of Illinois at Urbana-Champaign, Urbana, Illinois 61801, USA
[2]Micro and Nanotechnology Laboratory, University of Illinois at Urbana-Champaign, Urbana, Illinois 61801, USA
[3]Department of Comparative Biosciences, University of Illinois at Urbana-Champaign, Urbana, Illinois 61802, USA
[4]College of Medicine, University of Illinois at Urbana-Champaign, Urbana, Illinois 61801, USA
[5]Department of Materials Science, University of Illinois at Urbana-Champaign, Urbana, Illinois 61801, USA
[6]Department of Biochemistry, University of Illinois at Urbana-Champaign, Urbana, Illinois 61801, USA
[7]Beckman Institute for Advanced Science and Technology, University of Illinois at Urbana-Champaign, Urbana, Illinois 61801, USA

A.1 ABSTRACT

Semiconductor nanoplatelets are planar nanocrystals that have recently attracted considerable attention due to their quantum well-like physics, atomically precise thickness, and unique photophysical properties such as narrow-band fluorescence emission. These attributes are of potential interest for applications in biomolecular and cellular imaging, but it has been challenging to colloidally stabilize these nanocrystals in biological media due to their large dimensions and tendency to aggregate. Here we introduce a new colloidal material that is a hybrid between a nanoplatelet and an organic nanodisc composed of phospholipids and lipoproteins. We find that phospholipids adsorb to flat surfaces on the nanoplatelet and lipoproteins bind to sharp edges to enable efficient encapsulation of single nanoplatelets with long-term stability in biological buffers and high salt solutions. The lipoprotein–nanoplatelets are highly fluorescent with brightness comparable to wavelength-matched quantum dots at the ensemble level and at the single-molecule level. They also exhibit a unique feature of rapid and efficient internalization into living cells, after which they retain their fluorescence. These unique properties suggest that lipoprotein–nanoplatelets are particularly well suited for applications in live-cell single-molecule imaging and multiplexed cellular labeling.

Reprinted, with permission, from Lim SJ, McDougle DR, Zahid MU, Ma L, Das A*, Smith AM. Lipoprotein Nanoplatelets: Brightly Fluorescent, Zwitterionic Probes with Rapid Cellular Uptake. JACS. 2016 13;138(1):64-7. PMID: 26687504

A.2 MATERIALS & METHODS

Materials for Nanoplatelet Synthesis. Cadmium oxide (CdO, 99.99+%), cadmium acetate hydrate ($Cd(Ac)_2 \cdot H_2O$, 99.99+%), selenium powder (Se, ~100 mesh, 99.99%), ammonium sulfide ($(NH_4)_2S$, 40–48 wt.% in H_2O), tetramethylammonium hydroxide solution (TMAH, 25 wt.% in methanol), 3-mercaptopropionic acid (MPA, >99%), tributylphosphine (TBP, 97%), sodium chloride (NaCl), bromocresol green (ACS Reagent, dye content 95%), and dimethyl sulfoxide (DMSO, >99.9%, anhydrous) were purchased from Sigma-Aldrich. 1-octadecene (ODE, 90% tech.), oleic acid (OAc, 90% tech.), and oleylamine (OLA, 80–90% C18-content) were purchased from Acros Organics. Tris base (99%) and hydrochloric acid (37% in water) were purchased from Fisher Scientific. *N*-methylformamide (NMF, >99%) was obtained from Tokyo Chemical Industry. Other solvents including chloroform, hexane, methanol, ethanol, ethyl acetate, acetone, phosphate buffered sailine (PBS) were purchased from various suppliers including Acros Organics, Fisher Scientific, Macron Fine Chemicals.

Materials for Polymeric ligand synthesis. Tris(carboxyethyl)phosphine (TCEP, 98%), polyacrylic acid (PAA, MW 1.8 kDa), dimethylethylenediamine (DMDA, 99%), *N*,*N*-diisopropylethylamine (DIPEA, 99.5%), *N*,*N*,*N*′,*N*′-tetramethyl-*o*-(1*H*-benzotriazol-1-yl)uronium hexafluorophosphate (HBTU, 98%), 1-hydroxybenzotriazole hydrate (HOBt, 97%), 1,3-propanesultone (98%), trifluoroacetic acid (TFA, 99%), phenol (99%), triisopropylsilane (TIPS, 98%) were purchased from Sigma-Aldrich. Dimethylformamide (DMF, 99.8% anhydrous) was purchased from Alfa Aesar. All chemicals were used as received. S-trityl-protected cysteamine was prepared according to the literature.(*1*) 40% octylamine-modified polyacrylic acid (amphipol, MW ~2.9 kDa) was synthesized using methods described in the literature.[2]

Materials for lipoprotein coatings, labeling, and surface modification. The phospholipids 1,2-dimyristoyl-*sn*-glycero-3-phosphocholine (DMPC) and 1-palmitoyl-2-oleoyl-*sn*-glycero-3-phosphocholine (POPC) were purchased from Avanti Polar Lipids. Decyl maltoside (C10M) and ultrapure sodium cholate (≥ 97%) was purchased from Affymetrix.

Membrane scaffold protein (MSP1E3D1) was expressed and purified as previously described (3). Texas Red® 1,2-dihexadecanoyl-*sn*-glycero-3-phosphoethanolamine, triethylammonium salt (Texas Red® DHPE) and Alexa Fluor® 680 NHS ester, bis(triethylammonium salt) (Alexa Fluor® 680 NHS) were obtained from ThermoFisher Scientific. Mono-Sulfo-NHS-Nanogold® (*d* ~1.4

nm) was purchased from Nanoprobes. α-Methoxy-ω-NHS ester (PEG-NHS, 2 kDa) was purchased from Rapp Polymere.

Materials for negative staining TEM. Sodium phosphotungstate hydrate (PTA, >99.9%) was purchased from Sigma-Aldrich. ***Polymer 1.*** PAA (116.67 mg, 1.62 mmol COOH), HBTU (910.17 mg, 2.4 mmol), HOBt (356.98 mg , 2.31 mmol) were dissolved in DMF (5 mL). DIPEA (846 µL, 4.8 mmol) was added to activate the carboxylic acid and 10 minutes later S-trityl-protected cysteamine (181.8 mg, 0.57 mmol) and DMDA (120 µL, 1.1 mmol) were added. The mixture was stirred overnight at room temperature. The product was precipitated with the addition of 10 mM NaOH solution (250 mL) and collected by centrifugation. The product was redissolved in acetone, mixed with anhydrous Na_2SO_4, filtered, and dried under vacuum. Finally, the viscous oil was washed with ether to remove any residual solvent to yield the product **1** as a yellow powder. Yield: 40%. 1H NMR (d_6-DMSO, δ, ppm, 500 MHz): 7.1-7.4 (Ar-*H*, br), 3.25-3.6 (br), 2.84 (-S-CH_2, br), 2.75 and 2.4 (-CH_2-N<, m), 2.0-2.4 (CH_3, br).

***Polymer 2*. 1** (100 mg, 0.7 mmol) was treated with 1,3-propanesultone (129 mg, 1.05 mmol) in dry propylene carbonate (1.5 mL) under continuous stirring for 24 hours at room temperature, followed by 24 hours at 80°C. The product **2** was precipitated from the reaction mixture with ether (40 mL) to obtain a white powder. The product was then rinsed with ether and dried under vacuum. Yield: 70%. ^{1}H NMR (D_2O, δ, ppm, 500 MHz): 6.5-7.51 (Ar-*H*, br), 3.25-3.75 (br), 3.0-3.2 (br), 2.4-3.0 (br), 1.8-2.3 (br).

***Poly(thiol and sulfobetaine) (PTSB)*. 2** (10 mg, 11 µmol SH) and TCEP (3.2 mg, 11 µmol) was treated with TFA/phenol/TIPS (38:2:1 v/v/v, 1 mL) under N_2 for 5 hours. The solid PTSB product was precipitated with ether (10 mL) and collected by centrifugation at 7,000 g/5 min.

Nanoplatelet (NPL) synthesis

***Core CdSe NPL*.** CdSe NPLs were synthesized and purified using literature methods with slight modifications.[4] In a typical synthesis, CdO (0.6 mmol), OAc (1.2 mmol), and ODE (15 mL) were mixed in a 50-mL round bottom flask (r.b.f.) and heated to ~200°C under Ar until the mixture became clear and colorless due to the formation of cadmium oleate. The solution was cooled to 140°C and Se powder (0.6 mmol) was added. Then the temperature was quickly raised to 240°C at a rate of ~20°C/min. At 190°C, $Cd(Ac)_2$ (0.6 mmol) was swiftly added into the mixture to initiate NPL growth. After reaching 240°C, the mixture was heated for an additional 10 min and the reaction was quenched by removing the heating mantle. When cooled to ~130°C, OAc (1 mL) was

added to stabilize the NPL dispersion. The reaction yielded a mixture of NPLs with the first exciton λ_{abs} at 510 nm as well as quantum dots (QDs). For purification, the reaction mixture was diluted with hexane (~15 mL), divided into two 50-mL centrifuge tubes, and sonicated for ~5 min before adding ethanol (~30 mL) containing TBP (1 mL) into each tube and centrifuged at 7,000g for 5 min to precipitated all nanocrystals (NPLs and QDs). Precipitates were redispersed in hexane (20 mL per tube) with sonication, then only NPLs were precipitated by adding ethanol (5 mL per tube) and centrifuging. Finally, pure NPLs were redispersed in hexane and stored as a stock solution.

Core/shell CdSe/CdS NPLs. CdS shells were grown layer-by-layer on purified CdSe NPLs by following the colloidal atomic layer deposition protocol developed by Ithurria and Talapin[4c] with slight modifications. In a typical reaction, a biphasic mixture of CdSe NPLs in hexane (top phase; band edge absorbance ~4, 2 mL) and NMF (bottom phase; 2 mL) was prepared in a glass vial with magnetic stir bar. While gently stirring the mixture, a drop of $(NH_4)_2S$ solution (20 μL) was added into the top phase. This induced a sudden color change from yellow to dark orange followed by the flocculation of NPLs due to the deposition of sulfide layer on the NPL surface. The aggregates were eventually homogeneously dispersed into the bottom NMF phase. After complete phase transfer in 1–2 min, the top phase was discarded and the bottom phase was washed with hexane twice. The NPLs were isolated from excess sulfide ions by precipitation with ethyl acetate and centrifugation at 7,000g for 5 min. Sulfide-coated NPLs were redispersed in pure NMF (2 mL) and a solution of $Cd(Ac)_2$ in NMF (0.1 M, 50 μL) was added, which induced a color change to dark red due to the growth of a monolayer (ML) of CdS shell on the NPL surface. After a few minutes, NPLs were isolated from the excess Cd ions by precipitation with ethyl acetate. These NPLs were redispersed in NMF and an additional monolayer of CdS shell was grown through another cycle of $(NH_4)_2S$ addition – precipitation – redispersion in NMF – $Cd(Ac)_2$ addition – precipitation – redispersion in NMF. The final core/shell NPLs were transferred back to organic phase by adding OAc (~100 μL) and OLA (~100 μL) in a biphasic mixture of NPL solution in NMF (bottom phase) and hexane (top phase; 2 mL) while gently stirring the mixture for ~10 min. After complete phase transfer, the bottom phase was discarded and the NPLs were purified by precipitation with excess methanol. Finally, pure core/shell NPLs were dispersed in $CHCl_3$ and stored in the dark until use.

Lipoprotein–nanoplatelet (L–NPL) preparation and purification

***L–NPL assembly*.** In a typical synthesis, a CdSe/CdS core/shell NPL stock in $CHCl_3$ (~100 nM, $\square_{@350nm}$ ~5×10^7 $cm^{-1}M^{-1}$, 1 mL) was sonicated for 10 min and phospholipids (DMPC or POPC) dispersed in $CHCl_3$ were added in a 10,000:1 lipid:NPL molar ratio. The mixture was sonicated for 10 min and $CHCl_3$ was evaporated under a steady stream of N_2. The dry product was stored under vacuum to ensure complete $CHCl_3$ removal. The NPL–phospholipid mixture was reconstituted in PBS or Tris (0.1M, pH 7.4) containing detergents (sodium cholate or C10M) (10 mM, 1 mL) and sonicated for 10 min before rocking at 22°C for 30 min. Next, MSP (MSP1E3D1) was added in a 100:1 MSP:NPL molar ratio and the mixture was rocked at 22°C for 6–8 hours to form a macromolecular assembly between the NPL, phospholipids, and MSPs, yielding L–NPL hybrids as well as a large excess of empty nanodiscs. The as-prepared L–NPL hybrid solution was filtered through a syringe filter (0.2 μm pores) to remove any aggregates, then the clear dispersion was dialyzed in the same buffer (PBS or Tris) for 1 day using a 50 kDa molecular weight cutoff (MWCO) dialysis tube (Spectrum Laboratories, Inc.) to remove excess lipids and detergents and concentrated using a 50 kDa MWCO centrifugal filter (Amicon® Ultra, EMD Millipore). Excess nanodiscs remaining after dialysis were removed using density gradient centrifugation.

***NaCl density gradient centrifugation*.** A saturated NaCl solution (~6.5 M, d = 1.20 g/mL, 10 mL) was prepared by dissolving NaCl in distilled water at room temperature. A series of lower density solutions (d = 1.17, 1.14, 1.10, 1.07, and 1.03 g/mL) were prepared by diluting the saturated NaCl stock. In a 14-mL ultracentrifugation tube (Ultra-Clear™, Beckman Instruments, Inc.), a NaCl density gradient medium was prepared by carefully stacking NaCl layers with successively decreasing densities (~1 mL per layer, see Figure A.6). This discontinuous density gradient medium was then centrifuged at 26,000 g for 20 min to form a continuous density gradient medium. Then, 0.1-0.2 mL of concentrated L–NPL stock was loaded on top of the density gradient medium and centrifuged at 26,000 g for 2 hours. The denser L–NPLs migrated into the medium whereas the lighter nanodiscs remained at the top of the medium. After ultracentrifugation, the location of L–NPLs was identified by the absorption color (brown) and the fluorescence under UV light (red). The portion of medium containing L–NPLs was recovered and dialyzed (50 kDa membrane, in PBS or Tris) to remove excess NaCl.

Dye-labeled lipoprotein and nanodisc synthesis

Dye-labeled MSP. For quantification of MSP number per L-NPL, Alexa Fluor® 680-labeled MSP was prepared using amine-reactive Alexa Fluor® 680 NHS. A solution of the dye in anhydrous DMSO was added dropwise to a stirring solution of MSPE3D1 (50 uM) in 0.1 M sodium carbonate buffer (pH 8.3). The dye:MSP1E3D1 molar ratio was 10:1. The reaction was stirred at room temperature for 4 hours and the protein product was purified using a G-25 column (GE Healthcare). The number of dyes per MSP was measured spectroscopically by absorbance of MSP at 280 nm (ε = 29,400 cm^{-1} M^{-1}) and absorbance of the dye at 683 nm (ε = 184,000 cm^{-1} M^{-1}). See Figure A.8a for the results.

Dye-labeled nanodisc. Dye-labeled nanodiscs containing were prepared by incorporating a dye-labeled lipid during synthesis using previously described methodology.[5] Briefly, Texas Red® 1,2-Dihexadecanoyl-sn-Glycero-3-Phosphoethanolamine (DHPE) and DMPC were suspended in a solution of cholate (50 mM) in potassium phosphate buffer (KPi, pH 7.4) at a 3:97 molar ratio and sonicated for 5 min. Next, phospholipids were added to MSP1E3D1 at a 130:1 lipid:MSP molar ratio and equilibrated for 30 min. Assembly of the Texas Red® DHPE-containing nanodiscs was initiated upon addition of Amberlite Biobeads for detergent removal and the mixture was gently rocked overnight at 22°C. Biobeads were removed and the homogenous labeled nanodiscs were purified using size exclusion chromatography with a Superdex 200 10/300 column (GE Healthcare) coupled to an HPLC (Waters Alliance 2695), running 100 mM KPi (pH 7.4) buffer at a 0.5 mL/min flow. Collected fractions of fluorescent nanodiscs were pooled and concentrated using Amicon Ultra (10,000 MWCO) centrifugal filters (Millipore).

L–NPL labeling and PEGylation

L–NPLs with dye-labeled MSPs. L–NPLs were prepared and purified by following the steps described above using dye-labeled MSPs instead of normal (unlabeled) MSPs. The average number of MSPs per L–NPLs was determined based on the relative absorbance contributions from the dye and NPL. See Figure A.8b for the results.

Nanogold-labeled L–NPL. A purified L–NPL solution in PBS (~1.45 nM, 1 mL) was mixed with freshly prepared solution of Mono-Sulfo-NHS-Nanogold® in PBS at a 500:1 nanogold:L–NPL ratio. The mixture was incubated for 1 hour at room temperature, then excess nanogold was removed by multiple cycles of centrifugal filtration using a 100kDa MWCO filter (Amicon® Ultra, EMD Millipore). As a negative control, purified L–NPLs were mixed with non-functional

nanogold prepared by quenching Mono-Sulfo-NHS-Nanogold® with Tris (10^5 molar excess) for 12 hours.

L–NPL PEGylation. A purified L–NPL dispersion in PBS (~1 nM, 0.5 mL) was mixed with PEG-NHS in DMSO (~0.625 mM, 50 μL) and incubated at room temperature for 2 hours. Excess PEG and DMSO were removed by multiple cycles of centrifugal filtration using a 50 kDa MWCO filter.

Polymer-coated NPLs and QDs

Amphipol-coated core/shell CdSe/CdS NPLs. A $CHCl_3$ solution of amphipol (~150 mg/mL, 0.2 mL) was added dropwise to a NPL dispersion in $CHCl_3$ (~1 μM, 2 mL) with vigorous stirring. The amphipol:NPL ratio was ~5,000:1. While stirring, the solvent was slowly evaporated in a vacuum desiccator. The dried film was redispersed in NaOH solution (0.1 M, 2 mL) with stirring and sonication. Any aggregates were removed using a 0.2 μm syringe filter.

Zwitterionic PTSB-coated QDs. Purified red-emitting QDs (λ_{em} 600 nm) in hexane were phase transferred into NMF by adding TMAH (100 equivalents of QD surface atoms). PTSB dissolved in NMF (0.5 mL) was mixed with the OH^--coated QDs in NMF (1 μM, 0.4 mL) (5:1 thiol to QD surface atom) and purged with N_2 for 2 min. The mixture was stirred at 110°C for 4 hours and then diluted with 50 mM sodium borate buffer (pH 8.5, 4 mL). QDs were purified using centrifugal filtration (Amicon Ultra 50 kDa MWCO) in 50 mM sodium borate buffer (pH 8.5). The dilution – filtration cycle was performed five times.

Single-molecule imaging, diffusion, and cell interaction studies. For single-molecule brightness and blinking analysis, a dilute suspension of L–NPLs or QDs in PBS (~4 pM for L–NPLs and ~100 pM for QDs, 100 μL) were spin-coated on a glass coverslip (2,500 rpm, 30 s) and a solution of dye-labeled nanodisc (1 nM, 100 μL) was drop-and-dried on a coverslip to achieve similar particle density. Then fluorescence was immediately measured under ambient conditions using a Zeiss epifluorescence/total internal reflectance fluorescence (TIRF) microscope. To determine brightness values from single-particle fluorescence videos, the method of Arnspang et al. was used (6). Briefly, the center positions (x,y) of emitting spots were determined using the detection/estimation/deflation algorithm of Serge et al.[7] and the intensities of 3x3 points centered on these spots were measured. Intensity histograms were then plotted for each emitter, which were fit to a sum of a symmetric Gaussian function (the background signal) and an asymmetric Gaussian function (the emitter signal) using the least squares method. These two Gaussian centroid positions

were compiled into histograms for each particle sample and plotted in Figure A.10. Because the emission wavelengths of the NPLs and QDs were similar, no scaling factor was needed to account for the wavelength dependent sensitivity of the detector.

For single-molecule diffusion studies, 0.5 nM L–NPLs were dispersed in a 50% (w/w) mixture of glycerol and aqueous sodium borate buffer (50 mM, pH 8.5). 100 μL of this solution was then transferred to a #1.5 coverglass and imaged using highly inclined and laminated optical sheet (HILO) microscopy. Emitter position centroids were determined using the methods of Serge et al.[7] to calculate mean squared displacements per time increment. The first 3-5 points from MSD plots were fitted to a line with slope equal to 2D, where D is the diffusion coefficient.

For cell interaction studies, A431 cells (ATCC) were seeded at a density of 30,000–35,000 cells/cm^2 in CellView glass dishes (Greiner Bio-One) 24 hours before incubation with nanoparticles (1 nM) in phenol red-free serum-free DMEM (Cell Media Facility, UIUC). Incubation was allowed to proceed for 5 min, 15 min, 1 hour, or 24 hours at 37°C. After the respective incubation times, the cells were rinsed with PBS three times in order to remove free nanoparticles. The cells were then stained sequentially with 3,3'-dioctadecyloxacarbocyanine perchlorate (DiO) (Santa Cruz Biotechnology) to label the membrane (10 min at 37°C) and Hoechst 33258 (Life Technologies) to label the nuclei (15 min at 4°C). After staining, the cells were fixed using paraformaldehyde (electron Microscopy Sciences) freshly diluted to 4% in PBS for 10 min at room temperature.

To study the effect of L–NPL surface PEGylation on cellular uptake, A431 cells (ATCC) were seeded at a density of 30,00–35,000 cells/cm^2 in CellView glass dishes (Greiner Bio-One, Kremsmünster, Austria) 24 hours before addition of nanoparticles (0.076 nM) in phenol red-free serum-free DMEM (Cell Media Facility, UIUC). Incubation was allowed to proceed for 24 h at 37°C. The cells were then rinsed with PBS three times in order to remove the free nanoparticles, and then stained and fixed using the same procedures described above.

Optical spectroscopy and fluorescence quantum yield (QY) measurements. Absorption spectra were obtained with an Agilent Cary 5000 UV–Vis–NIR spectrometer and fluorescence spectra were acquired using a Horiba NanoLog spectrofluorometer. For fluorescence QY measurements, the solution was diluted to give NPL absorption of ~0.1 at 490 nm. QY was calculated relative to a reference dye (fluorescein in 1mM NaOH, QY=92%).

Transmission electron microscopy (TEM). TEM images were obtained using a JEOL 2010 LaB_6 high-resolution microscope in the Frederick Seitz Materials Research Laboratory Central Research Facilities at University of Illinois. For NPLs in organic solvents, samples were prepared by placing a drop of dilute NPL solution in hexane on a ultrathin carbon film TEM grid (Ted Pella; Product # 01824) and then wicking the solution off with a tissue. For L–NPLs, a drop of sample solution in buffer was added to the grid and allowed to incubate for 5 min before wicking off the liquid with a tissue. Then a drop of 1% PTA solution in DI water (pH 7) was loaded and wicked off after 30–40s.

Elemental analysis and NPL extinction coefficient calculation. Elemental analysis was performed using a PerkinElmer Optima 2000DV ICP–optical emission spectrometer. Detailed protocols for sample preparation and NPL extinction coefficient calculation can be found in our previous work (8).

^{1}H NMR. ^{1}H NMR spectra were recorded using a Varian U500 MHz or VXR-500 MHz spectrometer.

Zeta potential. For zeta potential measurement, a sample dispersion (L–NPLs, nanodiscs, or QDs) in high-salt buffer (e.g. PBS) was dialyzed against phosphate buffer (10 mM, pH 7.4) for 1 day. Zeta potential was measured using a Malvern Zetasizer.

Ultracentrifugation. For density gradient centrifugation of L–NPL samples, ultracentrifugation was performed using a Beckman Coulter Optima^{TM} L-90K Ultracentrifuge equipped with a SW 40 Ti swinging bucket rotor.

Fluorescence microscopy. For single molecule imaging and diffusion studies, samples were imaged via wide-field illumination on a Zeiss Axio Observer.Z1 inverted microscope with a 100x 1.45 NA alpha Plan-Fluar oil immersion microscope objective with excitation from a 488nm/100mW OPSL laser set in epifluorescence excitation mode. Excitation light was filtered using a 482/18 laser-line bandpass filter (Semrock Inc., Rochester, NY), and emission light was filtered with a 624/40 bandpass filter (Semrock Inc.). Images were acquired using a Photometrics eXcelon Evolve 512 EMCCD using Zeiss Zen software. Single molecule imaging was performed with epi-illumination of the sample and diffusion studies were performed using a HILO angle. Single-molecule brightness movies were collected at a rate of ~16 frames/s, while diffusion coefficient measurement movies were collected at a rate of ~7.6 frames/s.

For cell interaction studies, fixed cell samples were imaged using a Zeiss LSM 700 confocal microscope with a 63x/1.40NA oil immersion objective at the Core Facilities at the Carl R. Woese Institute for Genomic Biology. The L–NPLs, QDs, and fluorescent nanodiscs were excited using a 555-nm laser line, DiO was excited using a 488-nm laser line, and Hoechst was excited with a 405-nm laser line. Z-stacks of all three channels were acquired with slice spacing of ~0.74 μm spanning the entire height of the cell or cell cluster.

A.3 INTRODUCTION, RESULTS AND DISCUSSION

Semiconductor nanocrystals have recently been the subject of extensive multidisciplinary studies due to their unique physical, optical, and electronic properties (*2-4*). Their primary emergent property is bright, stable fluorescence emission that is tunable across a broad range of wavelengths. This characteristic has enabled diverse applications as imaging agents and molecular probes in cells and tissues (*2*) as well as light-emitting components of diodes and display devices (*3, 4*). These particles have become especially useful in single-molecule imaging applications where their unique combination of high photon emission rate and compact size has facilitated the discovery of a host of new biomolecular phenomena (*5, 6*).

The prototypical materials used in these applications are either quasi-spherical quantum dots (QDs) or elongated nanorods (NRs) (*7-10*). But recently a new class of semiconductor nanocrystal has emerged called nanoplatelets (NPLs) with a variety of unusual structural and optical properties (*8, 11, 12*). NPLs are thin crystalline sheets with atomically flat surfaces, tunable from 1.2 to 2.8 nm in thickness (*11, 13, 14*) and roughly 5 to 700 nm in lateral dimensions (*15*) and thus are colloidal analogues of quantum wells. Their fluorescence emission bandwidth is exceptionally narrow (8–20 nm full-width at half maximum, FWHM) compared to QDs (typically 25–35 nm FWHM) and organic fluorophores (typically 35–45 nm FWHM). Their light collecting efficiency can be very large; a single CdSe NPL with 1.5 nm thickness and 30 nm lateral dimensions has a molar extinction coefficient near 5×10^7 M^{-1} cm^{-1}, roughly 1,000-times that of green fluorescent protein. In addition, unlike QDs, NPLs have high surface-area-to-volume ratios, which may facilitate efficient transfer of energy and charge and efficient modulation of their optical properties by changes in their local environment. Together, these properties could allow multiplexed imaging with reduced spectral crosstalk as well as enhanced sensitivity for analyte detection. Recently CdSe-based NPLs have been coated with CdS shells resulting in greatly enhanced fluorescence

quantum yield, (*16-18*) which is a critical step forward in the production of bright NPLs suitable for imaging in oxidizing environments.

However it is an outstanding current challenge to stabilize NPLs in aqueous solutions compatible with cells and tissues. Like QDs and NRs, these materials are synthesized in organic solvents at high temperature, and the resulting colloids are coated with aliphatic ligands (e.g. oleic acid) that render them insoluble in polar solvents. We found that conventional phase transfer techniques used for core/shell CdSe/CdS QDs, such as ligand exchange with hydrophilic thiolates, can damage the NPL structure and/or quench fluorescence entirely (see Figure A.4).

Here we demonstrate the production of a new class of water-stable NPLs encapsulated in lipoproteins. These lipoprotein–nanoplatelets (L–NPLs) derive from lipoprotein nanodiscs. Nanodiscs are nanoscale analogues of plasma membranes consisting of a phospholipid bilayer stabilized by helical, amphipathic membrane scaffold proteins (MSPs) that encircle the nanodisc like a belt (*19-22*). Nanodiscs are used to solubilize integral and transmembrane proteins in aqueous solution and encapsulate hydrophobic drugs (*21, 23, 24*), suggesting that they may be able to encapsulate and stabilize NPLs in aqueous solution. Lipid-encapsulation is a versatile strategy to transform hydrophobic colloidal nanoparticles into biocompatible nanostructures (*25, 26*). However it is critical to geometrically match the nanoparticle morphology with the native self-assembled lipid structure to generate stable and individually coated nanoparticles. For example, spherical nanoparticles such as QDs and gold colloids are successfully encapsulated by amphiphilic polymers (*27, 28*), polyethylene glycol (PEG)-containing phospholipids (*25, 26*) and globular lipoproteins (*29, 30*) that individually self-assemble into spherical colloids in water. This is due to a high volume ratio of the polar head domain to the nonpolar tail domain, or a large packing parameter, which matches the high surface curvature of the encapsulated isotropic particles (*31*). We found that PEG-phospholipids can encapsulate flat NPLs, but their fluorescence entirely quenched, likely due to sparse lipid packing on the flat surfaces (see Figure A.4). Instead, lipids with small packing parameters are geometrically ideal for flat NPLs, however they have a tendency to form large liposomes entrapping multiple nanoparticles (*32, 33*). We therefore hypothesized that nanodisc components, which include phospholipids with packing parameters that yield flat structures and MSPs that stabilize the truncated edges with high curvature, are ideal for encapsulation of flat NPLs.

L–NPLs were synthesized in a three step process schematically depicted in Figure A.1a, comprising (1) colloidal synthesis of CdSe core NPLs, (2) growth of a CdS shell, and (3) encapsulation of CdSe/CdS core/shell NPLs with nanodisc components (see Methods). CdSe was used for the core due to robust syntheses that allow independent tuning of lateral dimensions and thickness, as well as narrow-band fluorescence emission in the visible spectrum (*11, 13*). Figure A.1b shows an example of uniform rectangular-shaped CdSe NPLs with 41 nm × 11 nm lateral dimensions and 1.8 nm thickness, as measured by transmission electron microscopy (TEM). These thin nanocrystals are flexible and form stacks of twisted NPLs (see inset). Layer-by-layer shell growth techniques were recently introduced for deposition of CdS, which has a wider bandgap (2.5 eV) than the core CdSe material (1.76 eV) (*16-18*). The shell boosts quantum yield and allows better preservation of fluorescence in aqueous media (see below). Figure A.1c shows that after 2 monolayers (ML) of growth, the lateral dimensions were similar (42 nm × 12 nm), but the thickness increased to 3.0 nm. Twisted and stacked NPLs were no longer observed (see inset) indicating that shell growth increased structural rigidity. Finally, these core/shell NPLs were encapsulated in lipoprotein nanodisc components through an evaporation–encapsulation process described below (*20*). Counter-stained TEM images in Figure A.1d show individual core/shell NPLs uniformly surrounded by a 3–4 nm organic coating, a thickness consistent with an inner layer of oleate ligands bound to the NPL surface and an outer layer of phospholipids and MSPs.

Efficient encapsulation of NPLs required three components: phospholipids, detergents, and MSPs (see Figure A.5). To generate L–NPLs, NPLs were dispersed in chloroform and self-assembled with excess phospholipids through slow solvent evaporation followed by dispersion in phosphate buffered saline (PBS) containing a mixture of detergents (sodium cholate or *n*-decyl-β-maltoside) and amphipathic MSPs (e.g. MSP1E3D1). Zwitterionic phospholipids were used to optimize biocompatibility and dispersion stability, and were chosen to have a packing parameter near 1 for dense assembly on the flat NPL surfaces; we used 1,2-dimyristoyl-*sn*-glycero-3-phosphocholine (DMPC) or 1-palmitoyl-2-oleoyl-*sn*-glycero-3-phosphocholine (POPC). Eliminating any one of the three components significantly reduced the phase transfer efficiency and stability of NPLs in aqueous solution. Phospholipids alone natively self-assemble into larger liposomal structures (*34, 35*), yielding a low percentage of NPLs transferred into aqueous buffer (most products were insoluble aggregates). Detergents dissociate liposomal structures into smaller metastable micelles (*34*); this increased the phase transfer efficiency of NPLs but aggregation was still substantial.

However the addition of MSPs caused NPLs to readily disperse in water without substantial aggregates. These L-NPLs were stable for more than one month after extensive dialysis and density gradient centrifugation in high salt (even in > 4 M NaCl solution) to remove empty nanodiscs and expel detergents (Figure A.6). MSPs also eliminated fluorescence quenching from detergents that strip off oleate ligands from the NPL (Figure A.7).

We characterized L-NPLs using multiple analytical methods and determined that the structure is consistent with the schematic in Figure A.1a, in which lipids cover flat NPL surfaces and MSP proteins adsorb to sharp edges. For L–NPLs made from NPLs with average dimensions of 37 nm × 10 nm × 3 nm, it was determined that there was an average of 1,193 DMPC lipids per NPL based on elemental analysis of cadmium (which is only in the CdSe/CdS NPL core) and phosphorous (only in the phospholipid). Assuming that DMPC adopts a similar area as in nanodiscs (0.69 nm^2 $DMPC^{-1}$) (*20*), this quantity is consistent with a monolayer coating of the flat top and bottom of the NPL (740 nm^2 surface area, or 1,070 lipids) and some of the sides (282 nm^2 surface area, or 409 lipids). The slight deficiency is likely covered by MSP proteins. We calculated an average of 7.7 MSPs per L–NPL by spectral analysis of L–NPLs prepared with dye-labeled MSP (see Figure A.8). MSPs likely localize to edges to interact with lipid tail sides where they reside analogously in nanodiscs. This is consistent geometrically, as MSP1E3D1 extends to a length of 38 nm in a nanodisc (circumference of a nanodisc with 13 nm diameter) (*20*), so theoretically at least 5.0 MSPs are needed to cover both top and bottom edges of the NPL (total perimeter length of 188 nm), only slightly less than the measured value of 7.7. Deviations may arise from protein conformation differences on the circular nanodisc versus the rectangular NPL. This model was further justified by an imaging study to localize MSPs using TEM. We conjugated gold colloids activated with *N*-hydroxylsuccinimide (NHS) to L-NPLs. Because only the MSP protein contains primary amines with which NHS will conjugate, gold should only localize to the protein. TEM showed that NHS-gold was almost exclusively localized around the L–NPL perimeter, as opposed to the particle center (see Figure A.1d inset and Figure A.9).

The optical properties of CdSe core and CdSe/CdS core/shell NPLs before and after coating with lipoprotein/MSP are shown in Figure A.2. The crystalline CdS shell was necessary for maintaining fluorescence in water, as core-only NPLs completely quenched after lipoprotein/MSP encapsulation, despite a quantum yield (QY) of 2.3% in organic solvents. With CdS shell growth, QY increased significantly in organic solvents, and could reach 80% with thick shells (7–8 ML)

(*18*). Unlike core-only NPLs, the fluorescence of core/shell NPLs was preserved after encapsulation, but the QY partially decreased in a manner dependent on the CdS shell thickness. For a 2-ML shell (the structure used in cells below) a 4.3% QY in hexane resulted in a 1.6% QY in water (Figure A.2b, top). Thinner shells yielded more substantial QY loss while thicker shells provided greater QY retention. While a shell is necessary to maintain fluorescence, increasing thickness diminishes the unique optical attributes of NPLs as well as their potential for environmental sensitivity and flexibility. For example, CdSe-only NPLs have exceptionally narrow emission bands (FWHM = 9 nm for λ_{em} = 515 nm), but they monotonically broaden with shell growth, likely due to increasing structural heterogeneity or/and increased electron–phonon coupling (*18*). We find that at intermediate shell thickness (2–3 ML), bands are still much more narrow (FWHM = 21 nm at λ_{em} = 626 nm) than those of spectrally-matched QDs (FWHM = 25–35 nm at λ_{em} = 600–650 nm), so we focused on this structural set for further investigations.

To investigate the potential of L–NPLs as fluorescent imaging probes, we measured their optical and diffusive behavior at the single-particle level using fluorescence microscopy. L–NPLs and QDs with similar emission wavelengths were spin-coated from dilute aqueous solutions on a glass coverslip. Individual emitters were readily distinguished by fluorescence intermittency (blinking) and homogeneous intensity levels in the blinking "on" state. L–NPLs exhibited longer "off"-times and shorter "on"-times (see Figure A.10). The "on"-time brightness values were measured for at least 250 single particles using the method of Lagerholm (see Methods) (*36*). Average relative single-particle brightness values were similar for L–NPLs ($B_{rel,sp}$ = 2.06 ± 0.98) and QDs ($B_{rel,sp}$ = 1.94 ± 0.90), with L–NPLs being slightly brighter (by 6%). At the ensemble level, absolute brightness values were calculated from the relation $B_{rel} = QY \cdot \varepsilon$, where ε is the extinction coefficient calculated from the particle core volume from TEM and the CdSe concentration derived from elemental analysis (*37*). Ensemble brightness values were similar for L–NPLs ($B_{rel,en}$ = 4.0 × 10^5 cm^{-1} M^{-1}) and QDs ($B_{rel,en}$ = 4.7 × 10^5 cm^{-1} M^{-1}), with L–NPLs being slightly dimmer (by 14%). The small mismatch between ensemble and single-particle brightness values may originate from errors in extinction coefficient calculations due to anisotropic NPL structure, the possible presence of "dark" L–NPLs not counted in single-particle analyses, or preferential alignment on the substrate. These results confirmed that L–NPLs are bright single-molecule emitters, comparable to QDs, but with substantially narrower bandwidths.

The diffusion of L–NPLs was probed through single-particle fluorescence imaging in dilute solutions. By fitting mean squared displacements of 429 single particle trajectories to a model of Brownian motion, the mean center-of-mass diffusion coefficient was calculated to be 1.55 ± 0.71 $\mu m^2\ s^{-1}$ in 50% (w/w) glycerol–sodium borate buffer (Figure A.10). By the Stokes-Einstein equation, the diameter of an equivalent sphere is 46.1 nm, which is close to many QDs in common use and thus appropriate for cellular and molecular imaging applications (*38*).

Finally, we investigated the interactions of L–NPLs with living A431 human epidermoid carcinoma cells to evaluate their potential for use as single-molecule imaging probes and cellular labels (see Figure A.3). We compared L–NPLs directly with two chemically analogous nanoparticles: nanodiscs composed of the same lipid and lipoprotein components labeled with a fluorescent dye (Texas Red) and zwitterionic QDs. All three had similar red emission wavelengths. After casting on glass coverslips, all three were readily visible at the single-particle level under identical excitation conditions (Figure A.3a). Zeta potential measurements in phosphate buffered solution indicated that all nanoparticles were anionic; the L–NPLs and nanodiscs were similar (–25 to –30 mV) but the zwitterionic QDs, which had no protein component, had a lower charge (–11 mV) (Figure A.3b). When added to cells at equal particle concentrations (1 nM), cells exposed to L–NPLs showed a much higher level of intracellular red fluorescence (Figure A.3c–e) compared to control cells and cells exposed to nanodiscs or QDs (Figure A.3f–h). We tracked this process over time via confocal microscopy and stained cells with a nuclear dye (blue) and a plasma membrane dye (green). We observed that internalization is rapid, with L–NPLs colocalizing with the membrane within 5 minutes of exposure, and becoming internalized within 15 minutes. After 24 hours, uptake was substantial, consisting of bright punctate cytosolic spots of L-NPLs likely in endosomal vesicles. It is surprising that among three chemically similar panicles, only L–NPL structures exhibited substantial uptake. Zwitterionic components were shared by all particles, so they likely did not contribute. The MSP protein was also not likely the contributor, since MSP-containing nanodiscs did not exhibit substantial uptake. A change in protein conformation is also not likely the source, as the result was similar when MSP was PEGylated to block protein-mediated association with cells (see Figure A.11). We believe that strong uptake arises from the very high surface area and low curvature of L-NPLs, for which multiple weak adsorption events can become substantial in strength through multivalency effects. Overall these observations suggest that L–

NPLs are a promising class of fluorophore for intracellular imaging and for efficient fluorescence tagging of cells.

In conclusion, we engineered a new composite nanocrystal comprising a quantum well-like nanoplatelet encapsulated within phospholipid and lipoprotein components of a nanodisc, yielding colloidally stable fluorophores with bright emission at the ensemble and single particle level. Employing geometrically compatible materials is critical, and extensive studies in nanodisc engineering (*19-24*) set the stage for diverse chemistries and biological functionality of L–NPLs. The unique shapes and optical properties of these materials are intriguing in the context of single-molecule imaging, optical cellular tagging, and even drug delivery, as high aspect ratio particles have been observed to have enhanced permeation through crowded tissues and unique delivery capabilities in living animals (*39, 40*). To our knowledge, these studies are the first example of a colloidal fluorescent quantum well employed in biological systems. The unique finding of rapid cellular entry suggests that these materials may be immediately useful for cellular labeling applications to allow highly multiplexed spectral encoding of cellular identity. Furthermore this new material composite opens the door to reveal how 2-dimensional materials interact with biological systems at the single-particle level.

A.4 ACKNOWLEDGMENTS

AMS acknowledges support from the NIH (R00CA153914 and R21NS087413) and the UIUC College of Engineering Strategic Research Initiatives Program. LM acknowledges support from the NIEHS (T32ES007326). DRM and AD acknowledge support from the American Heart Association (14PRE20130015 and 15SDG25760064). We acknowledge Ms. Yelena Grinkova, Dr. Mark McLean and the Sligar lab for assistance with MSP production and labeling, and Core Facilities at the Carl R. Woese Institute for Genomic Biology for microscopy assistance

A.5 FIGURES

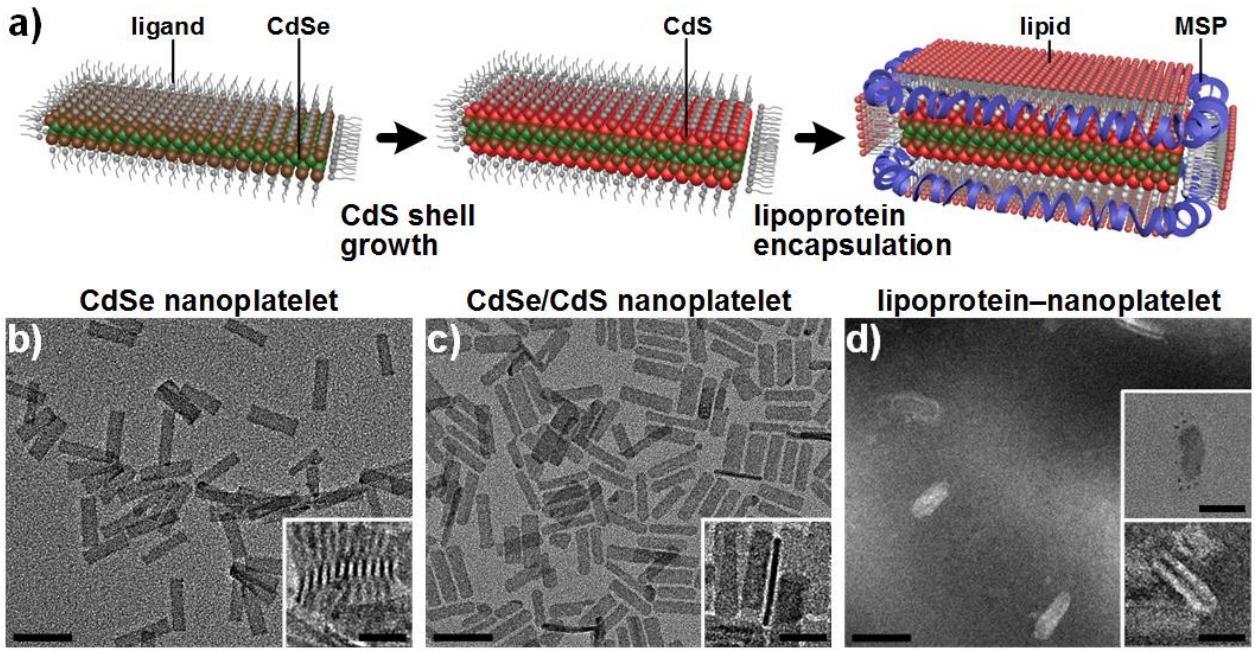

Figure A.1. Synthesis and structure of lipoprotein–nanoplatelets. (a) Schematic illustration of synthesis steps. TEM images depict (b) CdSe core NPLs (unstained), (c) CdSe/CdS core/shell NPLs (unstained), and (d) L–NPL hybrids (counter-stained). Insets show side-views of the structures. Top inset in (d) shows L–NPLs after MSP conjugation to gold colloids. Scale bars = 50 nm in wide-field images and 20 nm in insets.

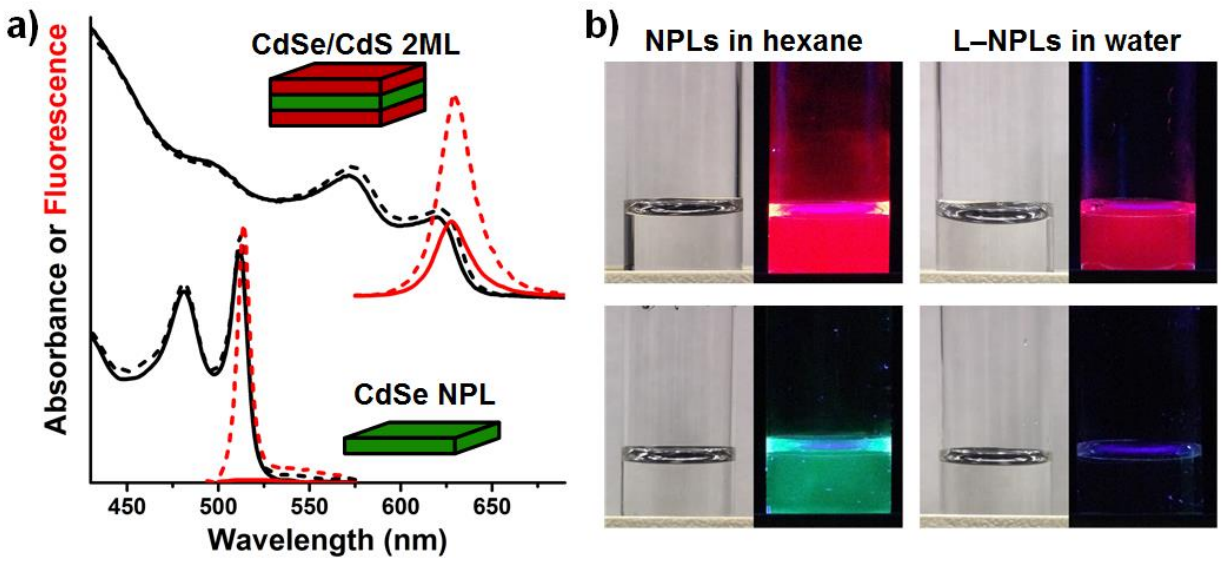

Figure A.2. Optical properties of CdSe and CdSe/CdS L–NPLs. (a) Visible absorption (black) and fluorescence (red) spectra of CdSe core (bottom) and CdSe/CdS core/shell (top) NPLs in hexane (dotted lines) and corresponding L–NPL structures in PBS (solid lines). (b) Photographs of sample solutions under room light (left) or 366-nm lamp excitation (right).

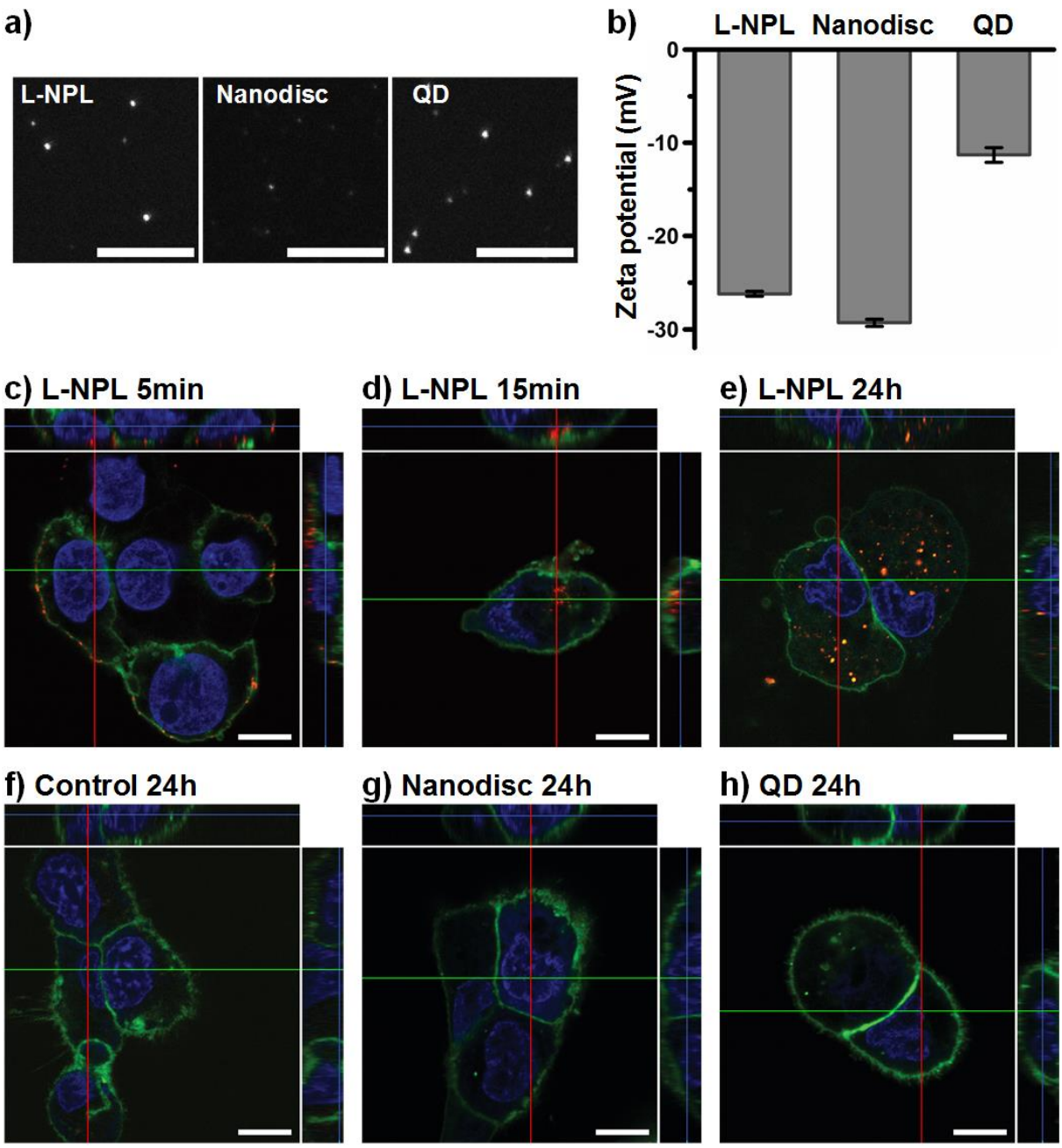

Figure A.3. (a) Single-particle fluorescence images of L-NPLs, dye-labeled nanodiscs, and QDs cast from aqueous solution. **(b)** Zeta potential measurements of the three samples. **(c-h)** Fluorescence confocal microscopy images of A431 cells as 3D z-stack projections of three color channels. Blue = nuclear dye, Green = membrane dye, Red = L-NPL, nanodisc, or QD. Duration of exposure to each nanoparticle is given for each image. Uptake was only significant for L-NPLs. All scale bars = 10 μm.

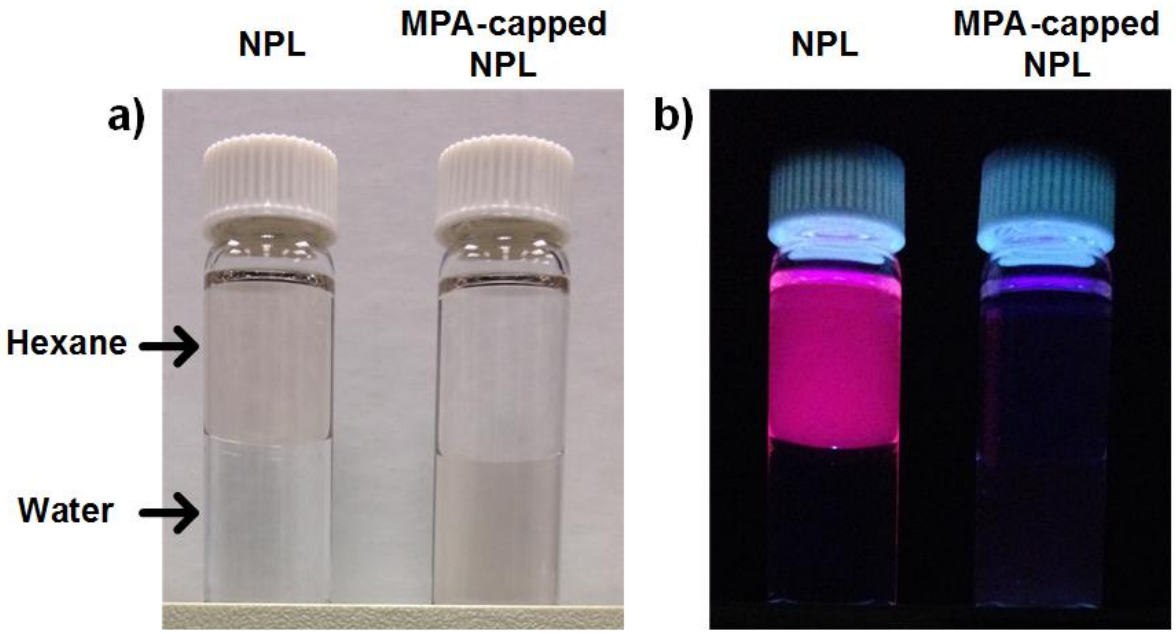

Figure A.4. Photos of CdSe/CdS core/shell NPL dispersions **(a)** under room light and **(b)** under 366-nm UV excitation. As-synthesized organic-dispersed NPLs show strong fluorescence in hexane (top phase) whereas MPA-capped aqueous NPLs show no fluorescence in water (bottom phase).

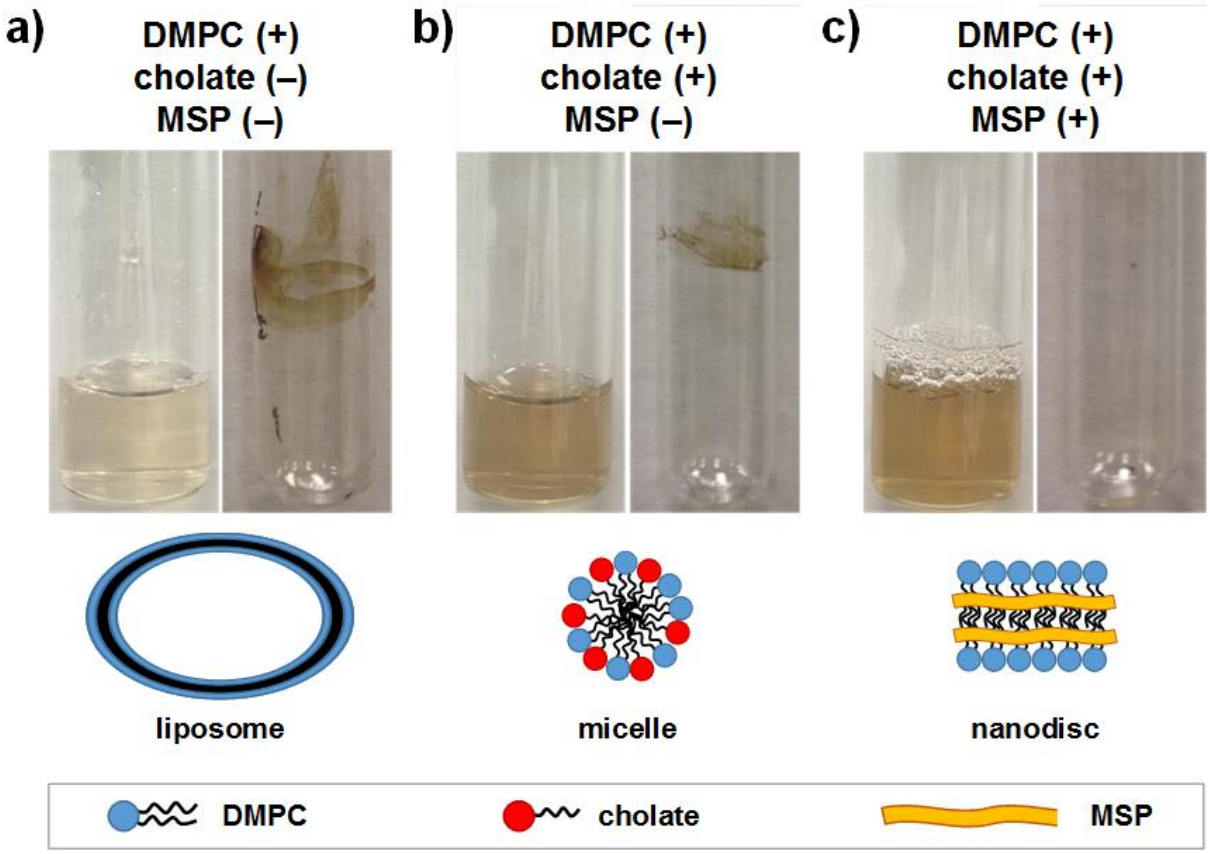

Figure A.5. Effects of lipid composition on the encapsulation efficiency of NPLs. Photographs depict vials containing NPLs dispersed in PBS (left) and corresponding reaction tubes containing insoluble NPL aggregates (right). NPLs were mixed with **(a)** DMPC, **(b)** DMPC with cholate, or **(c)** DMPC, cholate, and MSP. The primary structures of the corresponding self-assembled lipids without NPLs are depicted below, showing liposomes, micellar mixtures, and lipoprotein nanodiscs.

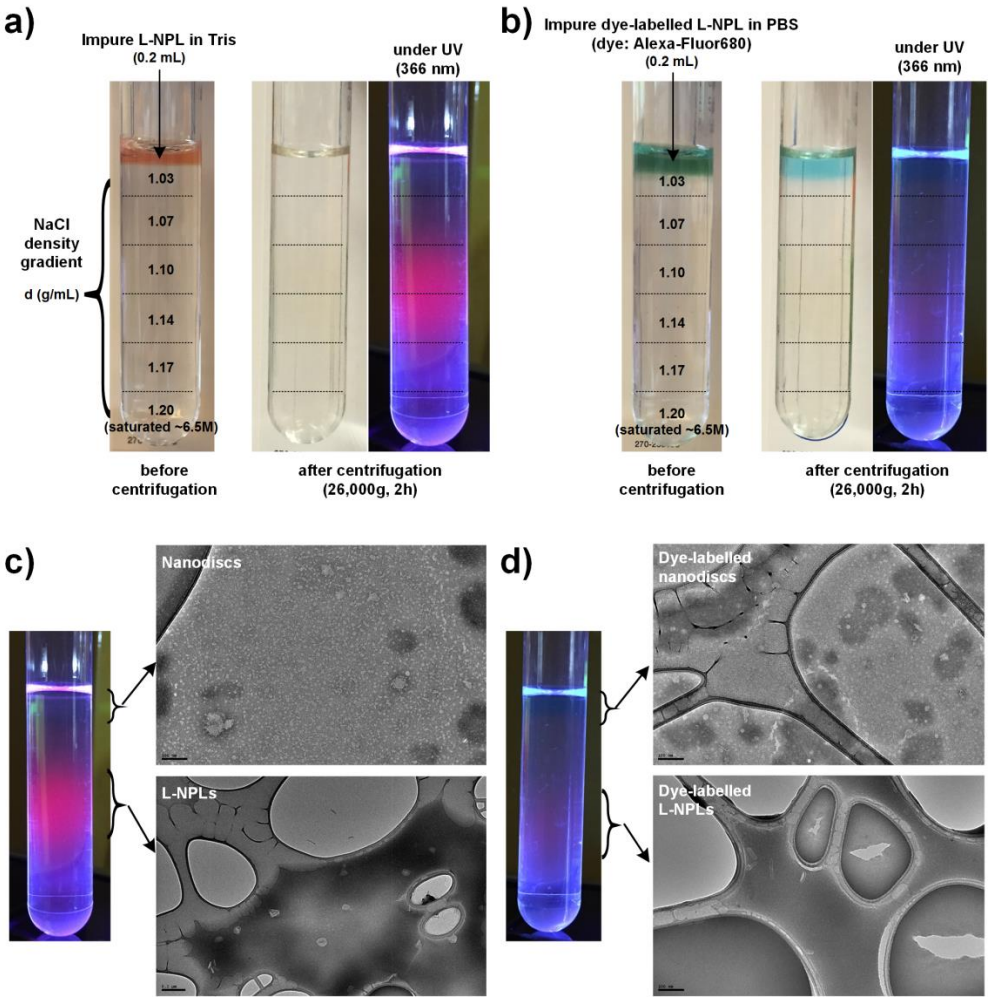

Figure A.6. L–NPL purification by NaCl density gradient centrifugation. **(a,b)** Photos of ultracentrifugation tubes containing NaCl density gradient media with (a) impure L–NPLs in Tris buffer and **(b)** impure Alexa Fluor® 680-labeled L–NPLs in PBS loaded at the top. Photos on the left show the density gradient media before ultracentrifugation. The numbers indicate densities of different NaCl layers and the horizontal dotted lines show their initial boundaries. Photos on the right show the same tubes after ultracentrifugation at 26,000 g for 2 hours. L–NPLs migrated downward into heavier NaCl media and can be located both by pale brown region under room light (left) and red fluorescence under UV light (right). **(c,d)** Negative-stained TEM images of aliquots obtained at the top and at the middle regions in the density gradient media (indicated by the braces) after ultracentrifugal purification of **(c)** L–NPLs and **(d)** Alexa Fluor® 680-labeled L–NPLs. TEM images of the top phase show numerous small white spots on the stained background verifying the presence of empty nanodiscs. TEM images of the middle phase show L–NPLs placed on solid dark backgrounds without any small white spots indicating the successful separation of L–NPLs from empty nanodiscs.

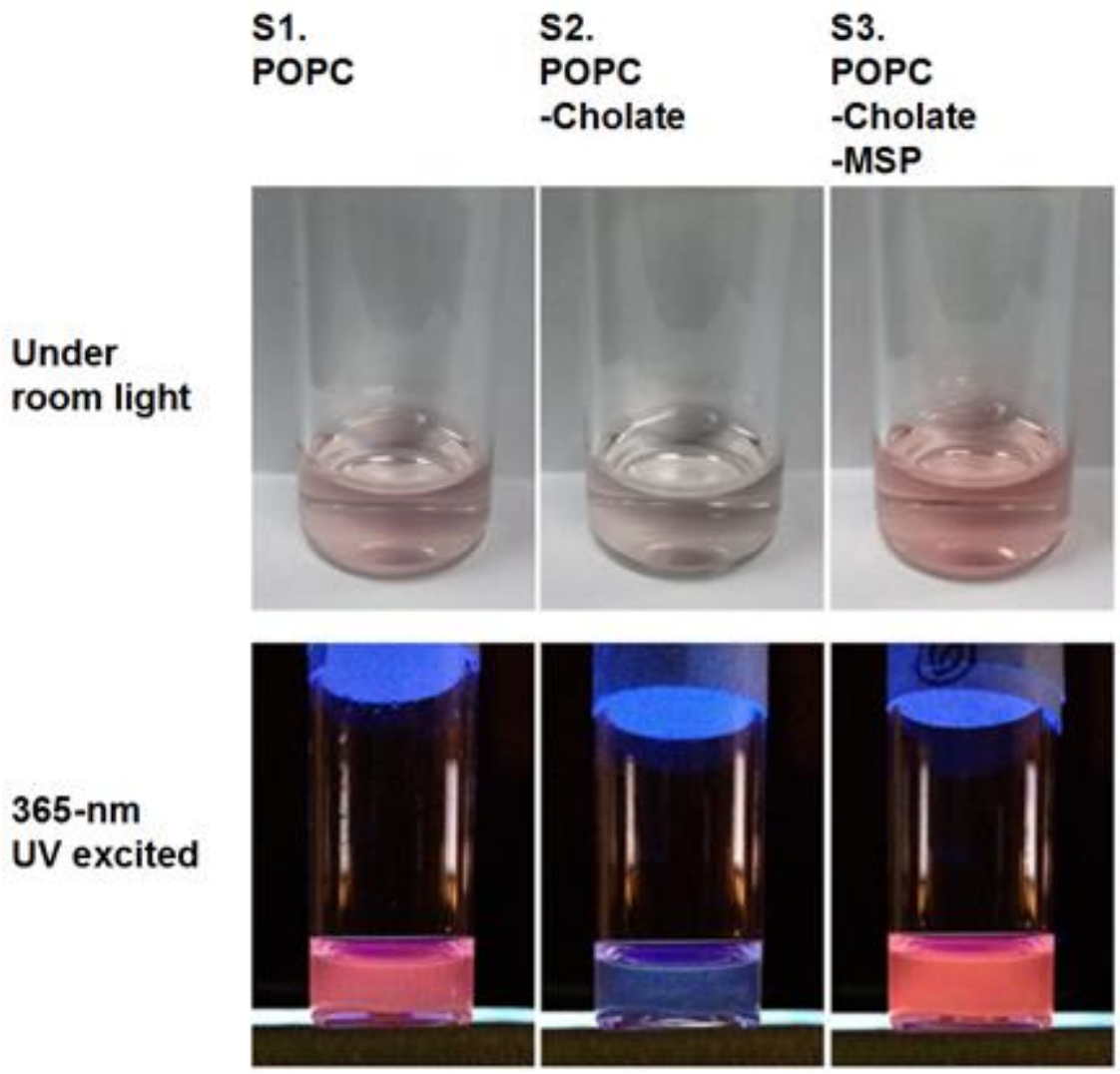

Figure A.7. Photographs of CdSe/CdS core/shell L–NPL solutions in PBS under room light (top) and under 366-nm UV excitation (bottom). NPLs encapsulated with POPC alone showed strong fluorescence in water **(S1)**, but these POPC-encapsulated NPLs lost their fluorescence when cholate was added **(S2)**. Adding MSPs eliminated cholate-enduced fluorescence quenching **(S3)** due to the formation of L–NPLs.

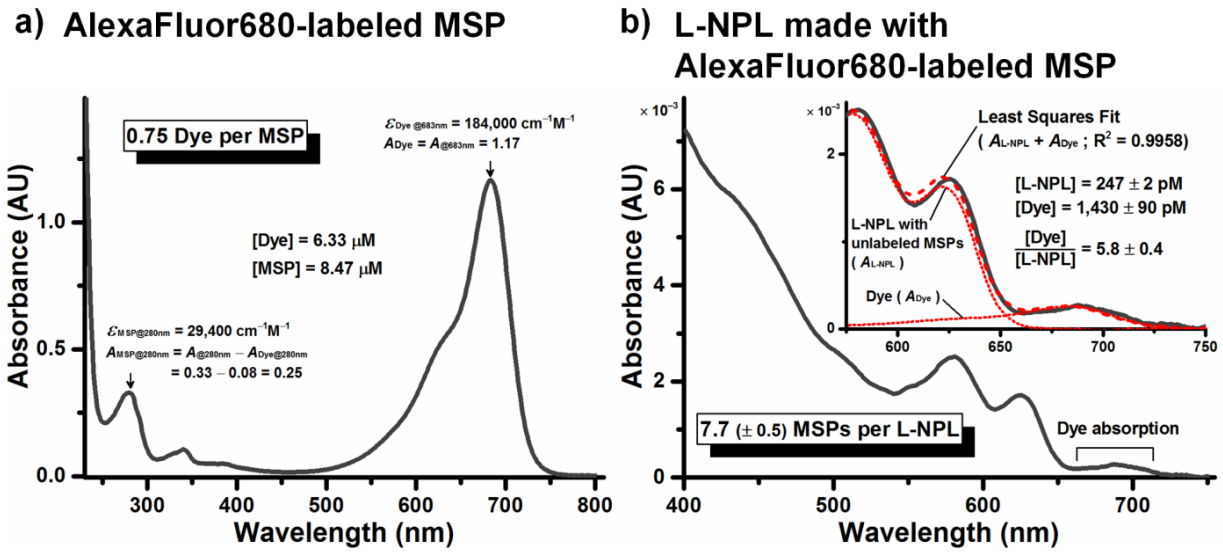

Figure A.8. Quantification of MSPs in L–NPLs. **(a)** Absorption spectrum of Alexa Fluor® 680-labeled MSPs, indicating an average number of 0.75 dye per MSP. **(b)** Absorption spectrum of purified L–NPLs prepared with Alexa Fluor® 680-labeled MSPs. Inset shows the least squares fitted curve (red dashed line) comprising a linear combination of the absorption spectra of Alexa Fluor® 680-labeled MSPs and L–NPLs prepared with unlabeled MSPs (red dotted lines). The results show an average number of 7.7 MSPs per L–NPL.

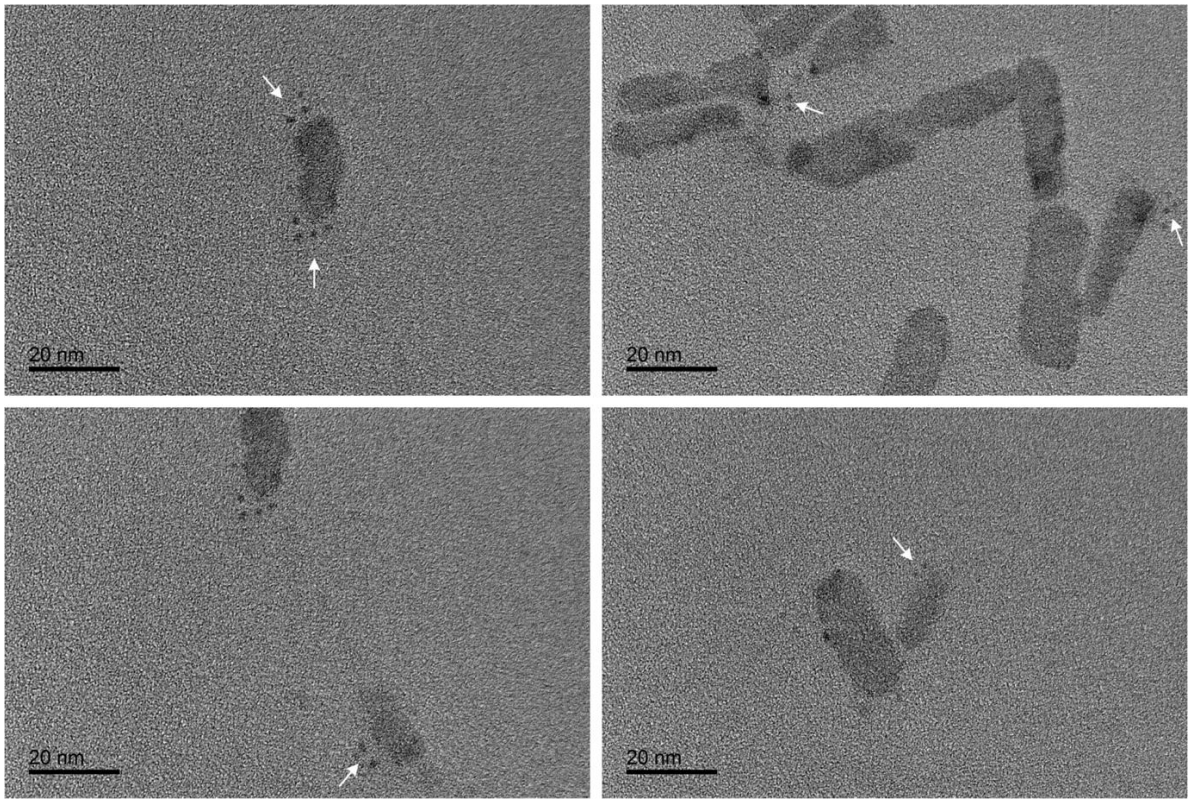

Figure A.9. Close-up images of L–NPLs conjugated to gold colloids through NHS-reactions with primary amines on the MSP lipoprotein. White arrows locate gold colloids.

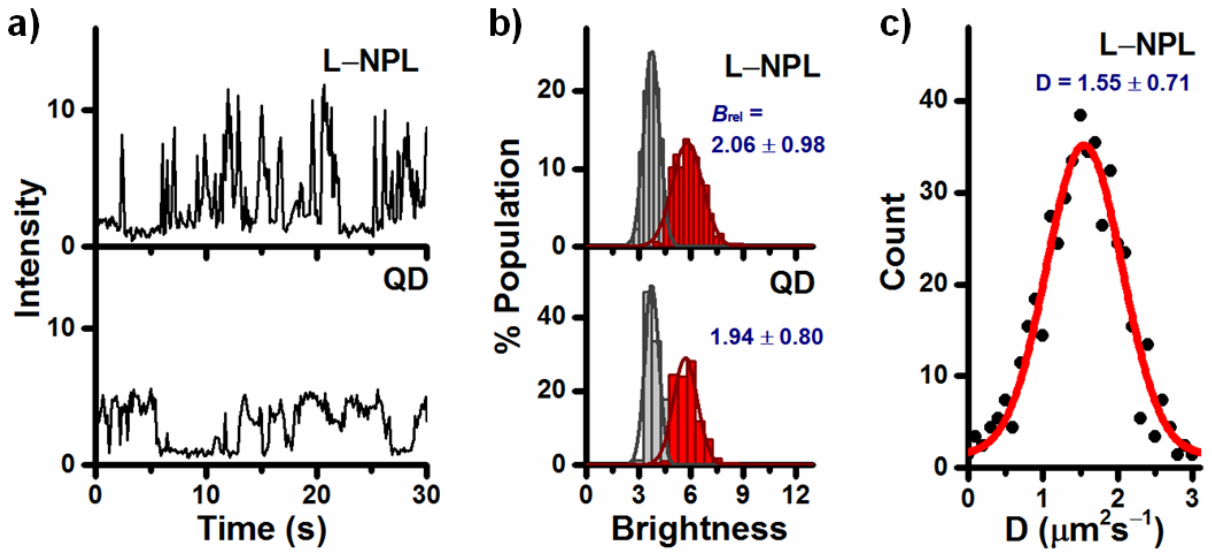

Figure A.10. (a) Representative single-particle blinking traces of L–NPLs (top) and QDs (bottom). **(b)** Relative single-particle brightness values (B_{rel}) of L–NPLs (top) and QDs (bottom). **(c)** Single-particle diffusion coefficient histogram of L–NPLs in a glycerol-water solution.

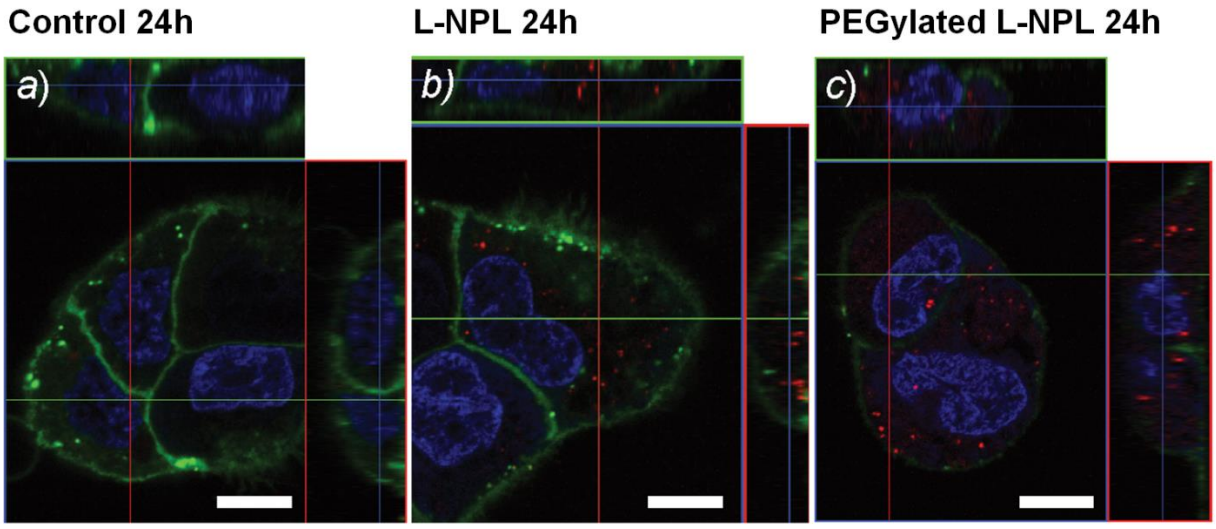

Figure A.11. Confocal microscope images with z-stacks of A431 cells after 24-hour incubation **(a)** without L–NPLs, **(b)** with L–NPLs, and **(c)** with PEGylated L–NPLs, showing no major impact of PEGylation on cellular uptake.

A.6 REFERENCES

1. Mazzier, D., Mba, M., Zerbetto, M., and Moretto, A. (2014) Bulky toroidal and vesicular self-assembled nanostructures from fullerene end-capped rod-like polymers, *Chemical Communications 50*, 4571-4574.
2. Kairdolf, B. A., Smith, A. M., Stokes, T. H., Wang, M. D., Young, A. N., and Nie, S. (2013) Semiconductor Quantum Dots for Bioimaging and Biodiagnostic Applications, *Annual Review of Analytical Chemistry 6*, 143-162.
3. Talapin, D. V., Lee, J. S., Kovalenko, M. V., and Shevchenko, E. V. (2010) Prospects of Colloidal Nanocrystals for Electronic and Optoelectronic Applications, *Chemical Reviews 110*, 389-458.
4. Mashford, B. S., Stevenson, M., Popovic, Z., Hamilton, C., Zhou, Z., Breen, C., Steckel, J., Bulovic, V., Bawendi, M., Coe-Sullivan, S., and Kazlas, P. T. (2013) High-efficiency quantum-dot light-emitting devices with enhanced charge injection, *Nat Photon 7*, 407-412.
5. Zahid, M. U., and Smith, A. M. (2014) Single molecule imaging with quantum dots, In *Optical Nanoscopy and Novel Microscopy Techniques* (Xi, P., Ed.), CRC Press.
6. Pinaud, F., Clarke, S., Sittner, A., and Dahan, M. (2010) Probing cellular events, one quantum dot at a time, *Nature Methods 7*, 275-285.
7. Smith, A. M., and Nie, S. (2010) Semiconductor Nanocrystals: Structure, Properties, and Band Gap Engineering, *Accounts of Chemical Research 43*, 190-200.
8. Lim, S. J., Smith, A., and Nie, S. (2014) The more exotic shapes of semiconductor nanocrystals: emerging applications in bioimaging, *Current Opinion in Chemical Engineering 4*, 137-143.
9. Fu, A., Gu, W. W., Boussert, B., Koski, K., Gerion, D., Manna, L., Gros, M. L., Larabell, C. A., and Alivisatos, A. P. (2007) Semiconductor quantum rods as single molecule fluorescent biological labels, *Nano Letters 7*, 179-182.
10. Yong, K. T., Qian, J., Roy, I., Lee, H. H., Bergey, E. J., Tramposch, K. M., He, S. L., Swihart, M. T., Maitra, A., and Prasad, P. N. (2007) Quantum rod bioconjugates as targeted probes for confocal and two-photon fluorescence imaging of cancer cells, *Nano Letters 7*, 761-765.
11. Ithurria, S., Tessier, M. D., Mahler, B., Lobo, R., Dubertret, B., and Efros, A. (2011) Colloidal nanoplatelets with two-dimensional electronic structure, *Nature Materials 10*, 936-941.
12. Bouet, C., Tessier, M. D., Ithurria, S., Mahler, B., Nadal, B., and Dubertret, B. (2013) Flat Colloidal Semiconductor Nanoplatelets, *Chemistry of Materials 25*, 1262-1271.
13. Ithurria, S., and Dubertret, B. (2008) Quasi 2D Colloidal CdSe Platelets with Thicknesses Controlled at the Atomic Level, *Journal of the American Chemical Society 130*, 16504-16505.
14. Son, J. S., Wen, X.-D., Joo, J., Chae, J., Baek, S.-i., Park, K., Kim, J. H., An, K., Yu, J. H., Kwon, S. G., Choi, S.-H., Wang, Z., Kim, Y.-W., Kuk, Y., Hoffmann, R., and Hyeon, T. (2009) Large-Scale Soft Colloidal Template Synthesis of 1.4 nm Thick CdSe Nanosheets, *Angewandte Chemie International Edition 48*, 6861-6864.

15. Bouet, C., Mahler, B., Nadal, B., Abecassis, B., Tessier, M. D., Ithurria, S., Xu, X. Z., and Dubertret, B. (2013) Two-Dimensional Growth of CdSe Nanocrystals, from Nanoplatelets to Nanosheets, *Chemistry of Materials 25*, 639-645.
16. Ithurria, S., and Talapin, D. V. (2012) Colloidal Atomic Layer Deposition (c-ALD) using Self-Limiting Reactions at Nanocrystal Surface Coupled to Phase Transfer between Polar and Nonpolar Media, *Journal of the American Chemical Society 134*, 18585-18590.
17. Mahler, B., Nadal, B., Bouet, C., Patriarche, G., and Dubertret, B. (2012) Core/Shell Colloidal Semiconductor Nanoplatelets, *Journal of the American Chemical Society 134*, 18591-18598.
18. Tessier, M. D., Mahler, B., Nadal, B., Heuclin, H., Pedetti, S., and Dubertret, B. (2013) Spectroscopy of Colloidal Semiconductor Core/Shell Nanoplatelets with High Quantum Yield, *Nano Letters 13*, 3321-3328.
19. Bayburt, T. H., Grinkova, Y. V., and Sligar, S. G. (2002) Self-Assembly of Discoidal Phospholipid Bilayer Nanoparticles with Membrane Scaffold Proteins, *Nano Letters 2*, 853-856.
20. Denisov, I. G., Grinkova, Y. V., Lazarides, A. A., and Sligar, S. G. (2004) Directed Self-Assembly of Monodisperse Phospholipid Bilayer Nanodiscs with Controlled Size, *Journal of the American Chemical Society 126*, 3477-3487.
21. McDougle, D. R., Palaria, A., Magnetta, E., Meling, D. D., and Das, A. (2013) Functional studies of N-terminally modified CYP2J2 epoxygenase in model lipid bilayers, *Protein Science : A Publication of the Protein Society 22*, 964-979.
22. Roy, J., Pondenis, H., Fan, T. M., and Das, A. (2015) Direct Capture of Functional Proteins from Mammalian Plasma Membranes into Nanodiscs, *Biochemistry 54*, 6299-6302.
23. Bayburt, T. H., Grinkova, Y. V., and Sligar, S. G. (2006) Assembly of single bacteriorhodopsin trimers in bilayer nanodiscs, *Archives of Biochemistry and Biophysics 450*, 215-222.
24. Das, A., Zhao, J., Schatz, G. C., Sligar, S. G., and Van Duyne, R. P. (2009) Screening of Type I and II Drug Binding to Human Cytochrome P450-3A4 in Nanodiscs by Localized Surface Plasmon Resonance Spectroscopy, *Analytical Chemistry 81*, 3754-3759.
25. Dubertret, B., Skourides, P., Norris, D. J., Noireaux, V., Brivanlou, A. H., and Libchaber, A. (2002) In vivo imaging of quantum dots encapsulated in phospholipid micelles, *Science 298*, 1759-1762.
26. Mulder, W. J. M., Koole, R., Brandwijk, R. J., Storm, G., Chin, P. T. K., Strijkers, G. J., Donega, C. D., Nicolay, K., and Griffioen, A. W. (2006) Quantum dots with a paramagnetic coating as a bimodal molecular imaging probe, *Nano Letters 6*, 1-6.
27. Pellegrino, T., Manna, L., Kudera, S., Liedl, T., Koktysh, D., Rogach, A. L., Keller, S., Radler, J., Natile, G., and Parak, W. J. (2004) Hydrophobic nanocrystals coated with an amphiphilic polymer shell: A general route to water soluble nanocrystals, *Nano Letters 4*, 703-707.
28. Smith, A. M., and Nie, S. M. (2008) Nanocrystal synthesis in an amphibiouis bath: spontaneous generation of hydrophilic and hydrophobic surface coatings, *Angewandte Chemie International Edition 47*, 9916-9922.
29. Skajaa, T., Zhao, Y., van den Heuvel, D. J., Gerritsen, H. C., Cormode, D. P., Koole, R., van Schooneveld, M. M., Post, J. A., Fisher, E. A., Fayad, Z. A., de Mello Donega, C.,

Meijerink, A., and Mulder, W. J. M. (2010) Quantum Dot and Cy5.5 Labeled Nanoparticles to Investigate Lipoprotein Biointeractions via Förster Resonance Energy Transfer, *Nano Letters 10*, 5131-5138.

30. McMahon, K. M., Mutharasan, R. K., Tripathy, S., Veliceasa, D., Bobeica, M., Shumaker, D. K., Luthi, A. J., Helfand, B. T., Ardehali, H., Mirkin, C. A., Volpert, O., and Thaxton, C. S. (2011) Biomimetic High Density Lipoprotein Nanoparticles For Nucleic Acid Delivery, *Nano Letters 11*, 1208-1214.
31. Israelachvili, J. N. (2011) *Intermolecular and Surface Forces, 3rd Edition*, Academic Press, Boston, MA.
32. Gopalakrishnan, G., Danelon, C., Izewska, P., Prummer, M., Bolinger, P.-Y., Geissbühler, I., Demurtas, D., Dubochet, J., and Vogel, H. (2006) Multifunctional Lipid/Quantum Dot Hybrid Nanocontainers for Controlled Targeting of Live Cells, *Angewandte Chemie International Edition 45*, 5478-5483.
33. Al-Jamal, W. T., Al-Jamal, K. T., Tian, B., Lacerda, L., Bomans, P. H., Frederik, P. M., and Kostarelos, K. (2008) Lipid−Quantum Dot Bilayer Vesicles Enhance Tumor Cell Uptake and Retention in Vitro and in Vivo, *ACS Nano 2*, 408-418.
34. Johnsson, M., and Edwards, K. (2003) Liposomes, Disks, and Spherical Micelles: Aggregate Structure in Mixtures of Gel Phase Phosphatidylcholines and Poly(Ethylene Glycol)-Phospholipids, *Biophysical Journal 85*, 3839-3847.
35. Nagarajan, R. (2002) Molecular Packing Parameter and Surfactant Self-Assembly: The Neglected Role of the Surfactant Tail†, *Langmuir 18*, 31-38.
36. Arnspang, E. C., Brewer, J. R., and Lagerholm, B. C. (2012) Multi-Color Single Particle Tracking with Quantum Dots, *PLoS ONE 7*, e48521.
37. Jasieniak, J., Smith, L., Embden, J. v., Mulvaney, P., and Califano, M. (2009) Re-examination of the Size-Dependent Absorption Properties of CdSe Quantum Dots, *The Journal of Physical Chemistry C 113*, 19468-19474.
38. Smith, A. M., and Nie, S. M. (2009) Next-generation quantum dots, *Nature Biotechnology 27*, 732-733.
39. Chauhan, V. P., Popovic, Z., Chen, O., Cui, J., Fukumura, D., Bawendi, M. G., and Jain, R. K. (2011) Fluorescent nanorods and nanospheres for real-time in vivo probing of nanoparticle shape-dependent tumor penetration, *Angewandte Chemie-International Edition 50*, 11417-11420.
40. Lane, L. A., Qian, X. M., Smith, A. M., and Nie, S. (2015) Physical chemistry of nanomedicine: understanding the complex behaviors of nanoparticles in vivo, *Annual Review of Physical Chemistry 66*, 521-547.

APPENDIX B: METHODS FOR INCORPORATION OF CYCLOOXYGENASE-2 IN THE MEMBRANE BILAYERS OF NANODISCS

B.1 ABSTRACT

Cyclooxygenases (COX-1 and COX-2) oxygenate arachidonic acid (AA) to generate prostaglandins. The enzymes associate with one leaflet of the membrane bilayer. We utilized nanodisc technology to investigate the function of human (hu) COX-2 and murine (mu) COX-2 in a lipid bilayer environment. huCOX-2 and muCOX-2 were incorporated into nanodiscs composed of POPC, POPS, DOPC, or DOPS phospholipids. Size-exclusion chromatography and negative stain electron microscopy confirm that a single COX-2 homodimer is incorporated into the nanodisc scaffold. Nanodisc-reconstituted COX-2 exhibited similar kinetic profiles for the oxygenation of AA, eicosapentaenoic acid, and 1-arachidonoyl glycerol compared to those derived using detergent solubilized enzyme. Moreover, changing the phospholipid composition of the nanodisc did not alter the ability of COX-2 to oxygenate AA or to be inhibited by various nonselective NSAIDs or celecoxib. The cyclooxygenase activity of nanodisc-reconstituted COX-2 was reduced by aspirin acetylation and potentiated by the nonsubstrate fatty acid palmitic acid to the same extent as detergent solubilized enzyme, independent of phospholipid composition. The stabilization and maintenance of activity afforded by the incorporation of the enzyme into nanodiscs generates a native-like lipid bilayer environment to pursue studies of COX utilizing solution-based techniques that are otherwise not tractable in the presence of detergents.

Reprinted, with permission, from Orlando BJ, McDougle DR, Lucido MJ, Eng ET, Graham LA, Schnedier C, Stokes DL, Das A, Malkowski MG. Cyclooxygenase-2 catalysis and inhibition in lipid bilayer nanodiscs. Arch Biochem Biophys. 2014 15;546:33-40. PMID: 24503478

B.2 METHODS

Incorporation of COX-2 into nanodiscs. COX-2 was reconstituted into nanodiscs comprised of POPC, POPS, DOPC, or DOPS phospholipids. Briefly, stock phospholipids were dissolved in chloroform, their concentrations were determined by total phosphate analysis using the manufacturer's protocol, followed by resuspension in 50 mM TRIS, pH 7.4, 150 mM NaCl, and sodium cholate for use in nanodisc assembly. The sodium cholate concentration was at a concentration twice that of the phospholipid. The resulting mixtures were chilled on ice prior to the addition of MSP1E3D1(+) and detergent solubilized COX-2 to achieve a final phospholipid:MSP1E3D1(+):COX-2M ratio of 1950:15:1. The volume of the incorporation mixture was designed such that the final concentration of sodium cholate was at least 20 mM and twice the concentration of the phospholipid. The mixtures utilizing POPC, DOPC, and DOPS were incubated at 4 °C for 1 h, followed by the addition of 0.8 g of BioBeads per mL of reconstitution mixture. For POPS, the mixture was incubated at room temperature for 1 h, followed by BioBeads addition. Incorporation mixtures were incubated with BioBeads overnight to initiate detergent removal and concomitant nanodisc assembly. The BioBeads were subsequently removed and the resulting sample was dialyzed for 4 h at 4 °C against 1L 50 mM TRIS, pH 7.4, 150 mM NaCl. For purification of nanodisc-reconstituted COX-2, the dialyzed sample was loaded onto a column (2.5 cm × 10 cm) containing 10 mL of Anti-FLAG M2 affinity resin, washed with 10 column volumes of 50 mM TRIS, pH 7.4, 150 mM NaCl, and eluted with wash buffer containing 100 μg/mL FLAG peptide. The elution fractions from the FLAG affinity column were pooled and loaded onto a 1 mL HiTrap Chelating HP column. The column was washed with 10 column volumes of 50 mM TRIS, pH 7.4, 150 mM NaCl, followed by 10 column volumes of 50 mM TRIS, pH 7.4, 150 mM NaCl, 35 mM imidazole. Nanodisc-reconstituted COX-2 was eluted from the column with 50 mM TRIS, pH 7.4, 150 mM NaCl, 350 mM imidazole. Fractions were pooled and dialyzed overnight at 4 °C against 25 mM TRIS, pH 7.4, 150 mM NaCl. For size-exclusion chromatographic analysis, dual affinity purified muCOX-2 reconstituted into POPC nanodiscs was loaded onto a Superdex 200 10/300 GL column equilibrated in 50 mM TRIS, pH 7.4, 100 mM NaCl.

B.3 FIGURES

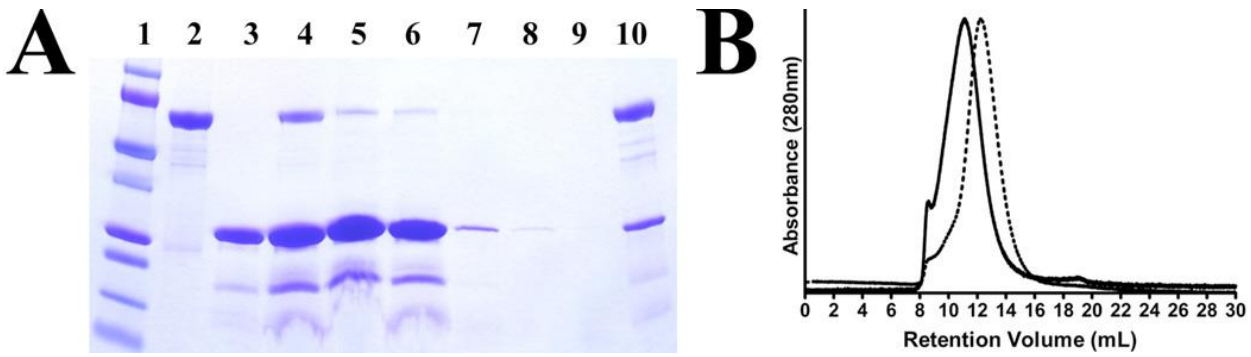

Figure B.1. Biophysical characterization of POPC:muCOX-2. (A) SDS-PAGE gel depicting the results from the dual affinity purification of nanodisc-reconstituted COX-2. Lane 1, molecular weight marker; lane 2, detergent solubilized COX-2 control; lane 3 MSP1E3D1(+) control; lane 4, crude nanodisc incorporation mixture following detergent removal with BioBeads; lane 5, FLAG column flow through; lanes 6–9, FLAG affinity column wash fractions; lane 10, purified nanodisc-reconstituted COX-2 eluted from IMAC affinity column. **(B)** SEC Analysis of incorporation: muCOX-2 reconstituted into POPC nanodiscs (solid line); empty POPC nanodiscs (dotted line).

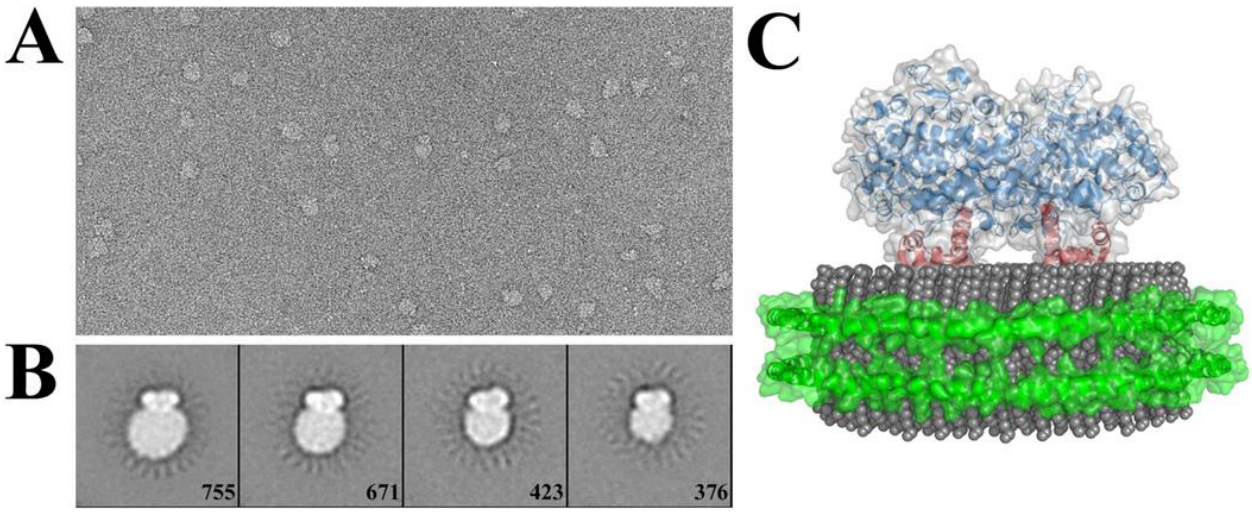

Figure B.2. Negative Stain EM Analysis of POPC:muCOX-2. **(A)** Representative negative-stain EM micrograph of POPC:muCOX-2. **(B)** 2D k-means class averages of POPC:muCOX-2 particles. 6,069 particles were windowed into 150 × 150 pixel individual images, aligned to each other, and subjected to ten cycles of multireference alignment and k-means classification. The numbers at the bottom right designate the number of particles used in each average and the box size of each image is 44nm × 44nm. The images suggest that the COX-2 homodimer lies at the edge of the nanodisc scaffold. However, this is due to the nature of the sample preparation for negative-stain EM analysis, which flattens the sample prior to analysis. **(C)** Model depicting muCOX-2 (PDB id 3HS5) bound to one leaflet of the POPC nanodisc. Nanodisc scaffold proteins and POPC lipids are colored green and gray, respectively. The muCOX-2 homodimer is colored blue, with the MBD of each monomer colored red.